

The copyright of this thesis vests in the author. No quotation from it or information derived from it is to be published without full acknowledgement of the source. The thesis is to be used for private study or non-commercial research purposes only.

Published by the University of Cape Town (UCT) in terms of the non-exclusive license granted to UCT by the author.



Preparation of Nano and Ångström sized Cobalt Ensembles and their Performance in the Fischer-Tropsch Synthesis

by

Nico Fischer

Dipl. Chem. Ing., University of Karlsruhe, Germany

Thesis presented to the University of Cape Town
in the fulfilment of the requirements
for the degree of

Doctor of Philosophy

Centre for Catalysis Research
Department of Chemical Engineering
University of Cape Town

Cape Town
August 2011

“Why are things as they are and not otherwise?”

-Johannes Kepler

University of Cape Town

Acknowledgements

This work was completed in the time from September 2007 to June 2011 at the Centre for Catalysis Research in the Department of Chemical Engineering at the University of Cape Town, South Africa.

First and foremost, my thanks go to my supervisors, Prof. Michael Claeys and Prof. Eric van Steen, for giving me the opportunity and the trust to conduct this study in their laboratories and for their continuous support throughout my time in Cape Town. A special thanks to Prof. Michael Claeys for all the time he made available for discussions, thesis corrections and for generally generating a nurturing environment in which one was free to develop any idea and was only held back by oneself.

During my time at the Centre for Catalysis Research I worked with numerous people who supported me along the way and made every day of work so much more enjoyable, Christian, Theresa, Elvira, Cathrin, Jako, You Qi, Marc, Stephen, Waldo just to mention a few. I do not have the space to list all of them, but they all contributed to this great experience and I wish you all the best for your future work at the Centre for Catalysis Research and beyond.

I also want to thank the researchers and scientists I had the pleasure to collaborate with: Prof. Frank Rößner and Robert Henkel from the University of Oldenburg for the possibility to take part in an exchange programme and to spend time in their laboratories, Dr. Gregory Smith and Prinessa Chellan from the Organometallic Research Group for their support in the synthesis of organometallic cobalt complexes, Dr. Esna du Plessis from SASOL for the time she took to introduce me to the 'art' of XRD and Rietveld Refinement, Prof. Neil Coville and Matthew Rayner from the University of Witwatersrand for the possibility to use their in-situ FTIR equipment, Prof. Michael Bäumer and Melanie Minnemann from the University of Bremen for the support with XPS measurements and last but not least the staff of the in-house analytical laboratory, Mrs. Helen Divey and Mrs. Suzanna Vasic and of the Electron Microscope Unit at the University of Cape Town Mr. Mohammed Jaffer, for the countless samples analysed together.

I would also want to thank the DST-NRF Centre of Excellence in Catalysis c*change for their financial support throughout the thesis and the Catalysis Society of South Africa (CATSA) for their contributions towards attending local as well as international conferences.

Without the long lasting support from my family: Gabi, Uli and Felix, and my friends over the years, in whichever situation I found myself in, I would not be where I am now. I will be forever thankful.

My final thanks go to Nicole. For having the trust and love to follow me to South Africa, to support me in whichever way possible, to pretend to be interested when sitting in a group of ten chemical engineers talking only about mass transfer limitations, for proof-reading pages and pages of drafts, for a thousand other things and for generally just being there!

Synopsis

In the Fischer-Tropsch synthesis carbon monoxide and hydrogen are converted in a surface polymerisation reaction over a heterogeneous catalyst to mainly long chain hydrocarbons and water. Although all group VIII metals are reported to show activity in this carbon monoxide hydrogenation, only iron and cobalt are used on an industrial scale due to availability and costs. In order to minimise the costs of these catalysts it is generally important to increase the mass specific active surface area by dispersing the active material on an inert carrier. However recent studies on nano sized iron, cobalt, ruthenium and rhodium crystallites indicate that below a certain crystallite size the catalysts display a decrease in surface specific activity. There is still disagreement on the causes for this decrease and the concurring effects of crystallite size on the selectivity of the various Fischer-Tropsch product classes. In the published studies on cobalt most of the catalysts were not fully characterised and effects of different loadings and metal support interactions might have clouded the obtained results.

This work aims to study the crystallite size effect of cobalt, supported on an industrially relevant carrier material, on activity and selectivity in the Fischer-Tropsch synthesis. A special focus is put on the time on stream behaviour and the initial changes (first 30-50 minutes under Fischer-Tropsch conditions) in the product spectrum.

To obtain a set of model catalysts suited for this study a novel **catalyst preparation** method was developed based on the reverse micelle technique. With this technique model catalysts with well distributed nano sized cobalt crystallites (average sizes from 2 to 11 nm), with narrow size distributions supported on an alumina carrier, were prepared. Extensive characterisation of the catalyst in the oxidic state, the reduced/activated state and after exposure to Fischer-Tropsch conditions showed that these model catalysts are remarkably stable against crystallite growth making them ideal for the use in this study. In-situ characterisation showed oxidation (aluminate formation) of very small cobalt crystallites at conditions of high synthesis gas conversions. In order to achieve further insight regarding the activity and selectivity of sub 2 nanometer cobalt clusters/ensembles, a cobalt carbonyl based organometallic complex was synthesised and supported on the alumina carrier.

The **Fischer-Tropsch activity and selectivity** of the prepared model catalysts was monitored throughout the experiment with a high temporal resolution. With decreasing crystallite size the surface specific activity was observed to decrease. Furthermore the selectivity towards methane as well as the selectivity of branched hydrocarbons increased with decreasing crystallite size while the selectivity towards longer hydrocarbons decreased. In contrast to previous studies, no influence of crystallite size on the olefin selectivity could be observed. As no crystallite growth or cobalt phase changes occurred during these studies the observed trends could unambiguously be linked to size effects highlighting structure sensitivity of the Fischer-Tropsch synthesis and the various product formation steps of the synthesis. The activity and selectivity results from the Fischer-Tropsch experiments with the supported cobalt organometallic complex, which decomposed over reaction time, extended the above mentioned trends for sub 2 nanometer clusters. An experiment with ^{13}C labelled carbon monoxide proved the incorporation of gaseous carbon monoxide into the Fischer-Tropsch products when the complex was used.

The high temporal resolution of product sampling and analysis allowed to follow changes of different active sites upon exposure of the model catalysts to Fischer-Tropsch conditions. It could be noticed that the secondary olefin isomerisation did only take place on the freshly reduced catalysts and was not detectable after 25 hours at Fischer-Tropsch conditions. However the secondary olefin hydrogenation to paraffins could be measured at initial stages as well as at steady state conditions. Effects of surface reconstruction have shown to play an important role in the time on stream behaviour of the catalysts as evidenced with catalysts subjected to CO pre-exposure.

University of Cape Town

Contents

Contents	i
List of Figures	v
List of Tables	xiii
Nomenclature	xv
1 Introduction	1
2 Literature review	5
2.1 Fischer-Tropsch synthesis	5
2.1.1 The Fischer-Tropsch reactions	6
2.1.2 Fischer-Tropsch reaction mechanisms	7
2.1.3 Fischer-Tropsch products	10
2.1.4 Heterogeneous Fischer-Tropsch catalysts	13
2.1.5 Homogeneous Fischer-Tropsch catalysts	14
2.2 Catalyst deactivation	15
2.2.1 Poisoning	16
2.2.2 Fouling	16
2.2.3 Thermal degradation	17
2.2.4 Vapour-solid and solid-solid reactions	17
2.2.5 Attrition	21
2.3 Effect of water in the Fischer-Tropsch synthesis	21
2.4 Effect of crystallite size in the Fischer-Tropsch synthesis	22
2.5 Conventional catalyst preparation techniques	27
2.5.1 Precipitation and co-precipitation	28
2.5.2 Impregnation	28
2.6 Microemulsion technique	29
2.6.1 Definition of a microemulsion	29
2.6.2 Preparation of nano-particles with the reverse micelle technique	31
3 Scope of the Thesis	41
4 Experimental Methodology	45
4.1 Synthesis of supported cobalt crystallites as model catalysts	45
4.1.1 Variation of support addition	46
4.1.2 Variation of precipitation agents	47
4.1.3 Composition of the microemulsion	47

4.2	Synthesis of organometallic cluster $(\text{CO})_9\text{Co}_3\text{CCOOH}$	49
4.3	Support material Al_2O_3	50
4.4	Characterisation of the w/o microemulsion	50
4.4.1	Determination of the influence of temperature on the stability region of the reverse micelle	50
4.4.2	Measurement of the size of the reverse micelles	50
4.5	Characterisation of supported cobalt crystallites	51
4.5.1	Transmission electron microscopy (TEM)	51
4.5.2	Powder X-ray diffraction (PXRD)	52
4.5.3	Atomic absorption spectroscopy (AAS)	52
4.5.4	Raman spectroscopy	53
4.5.5	X-ray photoelectron spectroscopy (XPS)	53
4.5.6	Temperature programmed reduction (TPR)	53
4.5.7	Degree of reduction (DOR)	54
4.5.8	Temperature programmed desorption (TPD)	54
4.5.9	In-situ powder X-ray diffraction (in-situ PXRD)	55
4.5.10	Magnetic measurements	55
4.6	Characterisation of organometallic cluster $(\text{CO})_9\text{Co}_3\text{CCOOH}$	57
4.6.1	Mass spectroscopy (MS)	58
4.6.2	Elemental analysis	58
4.6.3	Diffuse reflectance infrared Fourier transform spectroscopy (DRIFTS)	58
4.6.4	In-situ powder X-ray diffraction (in-situ PXRD)	58
4.6.5	In-situ Fourier transform infrared spectroscopy (FTIR)	58
4.6.6	Magnetic measurements	59
4.7	Fischer-Tropsch synthesis experiments	59
4.7.1	Test unit set-up	59
4.7.2	Reactor set-up	59
4.7.3	Experimental procedure for FT experiments with supported cobalt crystallite catalysts	60
4.7.4	Experimental procedure for FT experiments with supported organometallic cobalt complex	61
4.7.5	Experimental procedure for FT experiments with supported organometallic cobalt complex with ^{13}CO	61
4.7.6	Off-line sampling technique	62
4.8	Fischer-Tropsch experiments with in-situ magnetic measurements	64
4.8.1	Test unit set-up	64
4.8.2	Reactor set-up	65
4.8.3	Experimental procedure	65
4.8.4	Magnetic measurement procedure	67
4.9	Product analysis	67
4.9.1	Conversion, yield and selectivity	68
4.9.2	Turn-over frequency (TOF)	70

5	Characterisation of the w/o Microemulsion	73
5.1	Influence of temperature on the stability of reverse micelles	73
5.2	Influence of composition on the size of the reverse micelle	75
5.2.1	Model size predictions for reverse micelles	77
5.3	Influence of temperature on the size of the reverse micelle	80
6	Characterisation of the Preparation Methods of supported Co/Co₃O₄ Crystallites	83
6.1	Atomic absorption spectroscopy (AAS)	84
6.2	Raman spectroscopy	85
6.3	Powder X-ray diffraction (PXRD)	85
6.4	X-ray photoelectron spectroscopy (XPS)	87
6.5	Temperature programmed reduction (TPR)	87
6.6	In-situ powder X-ray diffraction (PXRD)	89
6.7	Variation of precipitation agent	93
6.8	Conclusion and summary of method variations	94
7	Characterisation of Model Catalysts	97
7.1	Cobalt oxide & cobalt crystallites	97
7.1.1	Atomic absorption spectroscopy	98
7.1.2	Temperature programmed reduction (TPR) and degree of reduction (DOR)	98
7.1.3	Transmission electron microscopy (TEM)	101
7.1.4	Conventional and in-situ powder X-ray diffraction (PXRD)	106
7.1.5	CO temperature programmed desorption (CO-TPD)	110
7.1.6	Magnetic in-situ studies on supported cobalt crystallite model catalysts	113
7.1.7	Conclusion and summary of the characterisation results of cobalt/cobalt oxide crystallites	119
7.2	Organometallic cobalt complex	120
7.2.1	Elemental analysis	120
7.2.2	Mass spectroscopy	120
7.2.3	Fourier transform infra red spectroscopy (FTIR)	121
7.2.4	Magnetic measurements	123
7.2.5	In-situ X-ray diffraction (PXRD)	124
7.2.6	Conclusion and summary of the characterisation results of the organometallic cobalt complex	125
8	Fischer-Tropsch Performance of the Model Catalysts	129
8.1	Supported nano-sized cobalt crystallites	129
8.1.1	Fischer-Tropsch activity and characterisation of the spent catalysts	129
8.1.2	Methane formation and chain growth	138
8.1.3	Olefin formation	143
8.1.4	Formation of branched hydrocarbons	149

8.1.5	Formation of oxygenates	150
8.1.6	Conclusions and summary of the FT performance of the supported nano-sized cobalt crystallites	151
8.2	Supported organometallic complex	153
8.2.1	Fischer-Tropsch activity and characterisation of the spent catalyst	153
8.2.2	Methane formation and chain growth	155
8.2.3	Olefin formation	155
8.2.4	Activation of gaseous ^{13}C	156
8.2.5	Conclusions and summary of the FT performance of the supported organometallic complex	158
8.3	Consolidation of FT results of supported $(\text{CO})_9\text{Co}_3\text{CCOOH}$ and supported cobalt crystallites	158
9	Summary and Conclusions	165
10	Recommendations and Future Work	169
Appendix		171
A1	Composition of reverse micelles for stability measurements	171
A2	Calibration of magnetometer	173
A3	Conditions for off-line GC-FID analysis	174
A4	Calculation of Kovats indices	174
A5	Calculation of total and exposed cobalt atoms for specific crystallite sizes	177
A6	Crystallite size distributions from TEM analysis	178
A7	In-situ PXRD scans	181
A8	In-situ magnetic measurements	182
A9	Selected results of the FT testing	183
A10	List of chemicals	185
A11	Curriculum vitae	186
A12	List of publications	187

List of Figures

2.1	Proposed alkyl mechanism (adapted from [38]).	8
2.2	Proposed mechanisms for the formation of branched hydrocarbons in the FTS (adapted from [38]).	8
2.3	Proposed alkenyl mechanism (adapted from [38]).	9
2.4	Proposed enol mechanism (adapted from [38]).	10
2.5	Proposed CO-insertion mechanism (adapted from [38]).	11
2.6	Ideal chain growth mechanism with one class of products (Pr) and one class of surface species (Sp) (N: carbon number, g: growth, d: desorption) (adapted from [38]).	12
2.7	Chain growth mechanism with paraffins (Par), olefins (Ol) and oxygenates (Ox) as product classes and one class of surface species (Sp) (N: carbon number, g: growth) (adapted from [38]).	12
2.8	Schematic pathways of crystallite growth due to sintering (adapted from [75]).	18
2.9	Thermodynamic stability region of metallic cobalt nano-crystallites in presence of product water in the Fischer-Tropsch synthesis (recalculated from [84]).	19
2.10	(a) STM image of a clean Co (0001) surface (prior to reaction) showing atomically flat terraces 150 nm (ca. 600 atoms) in width (tunnelling current $I_t = 2\text{ nA}$, sample bias $V = 0.05\text{ V}$). The smallest step visible is monoatomic in height, 0.205 nm being the expected single atom step height on Co (0001). (b) STM image of the Co (0001) surface after 1h exposure to high pressure CO hydrogenation conditions ($I_t = 0.5\text{ nA}$, $V = 0.5\text{ V}$). Insert: hard-sphere model of the bulk-terminated Co (0001) surface (from [92]).	20
2.11	(A) Ratio of different surface atoms over total number of surface atoms for fcc cobalt cubo-octahedron crystallites of different sizes (■ edge atoms; ▲ surface atoms; ▼ corner atoms); (B) Model of maximum number of B5 sites fcc cobalt cubo-octahedron crystallite ($d = 1.5\text{ nm}$) with position of B5 sites indicated; (calculated from [125]).	26
2.12	Schematic presentation of the ensemble theory (adapted from [134]).	27
2.13	Schematic ternary phase diagram of a microemulsion system with stability regions of the micelle and the reverse micelle.	30
2.14	Schematic representation of a reverse micelle.	31
2.15	Schematic representation of the precipitation of nano-particles from a w/o microemulsion. (A) Through combination of two reverse micelle solutions, one containing the dissolved metal precursor, the other the precipitation or reduction agent. (B) Through addition of a precipitation or reduction agent to a reverse micelle solution containing the dissolved metal precursor [156].	32
4.1	Schematic representation of catalyst preparation methods A & B.	47
4.2	Schematic representation of catalyst preparation methods C & D.	48
4.3	Ternary phase diagram of microemulsion system with compositions of synthesised reverse micelles. Stability region for reverse micelles at 25°C shaded.	49

4.4	Schematic representation of the behaviour of superparamagnetic particles in an external magnetic field (adapted from [23])	57
4.5	Schematic representation of the temperature/crystallite size dependency of remnant magnetisation (adapted from [23]).	57
4.6	Flow sheet of the test unit set-up for the Fischer-Tropsch synthesis experiments.	60
4.7	Schematic drawing of U-tube reactor with catalyst packing.	60
4.8	Flow sheet of the test unit set-up for the Fischer-Tropsch synthesis experiments with ¹³ CO.	62
4.9	Schematic drawing of off-line ampoule sampler.	63
4.10	Calculated fractions of n-alkanes (A) and α -olefins (B) from a theoretical Fischer-Tropsch product spectrum at 10% CO conversion in the gas (■) and liquid (▲) phase.	63
4.11	Flow sheet of the test unit set-up for the Fischer-Tropsch synthesis experiments with in-situ magnetic characterisation.	64
4.12	Fixed bed reactor set-up for in-situ magnetic characterisation: (A) front view; (B) top view; (C) side view.	66
5.1	Ternary phase diagram indicating all mixtures studied to establish the stability region of the reverse micelles at 10, 25 and 40°C.	73
5.2	Ternary phase diagram indicating stability regions of the reverse micelle at 10 (red), 25 (blue) and 40°C (green).	74
5.3	Measured sizes of water cores at 25°C from selected microemulsion mixtures. For exact composition see table 5.1.	76
5.4	Schematic representation of a spherical reverse micelle.	76
5.5	Calculation of the solubility of PEGDE in n-hexane at 25°C. Water core (wc) sizes were measured using DLS.	77
5.6	Comparison of measured water core sizes (black) (see figure 5.3 and table 5.1) and calculated water core sizes using different models applied to sample compositions (red).	79
5.7	Water core size (d_{wc}) in the reverse micelle as function of water to surfactant mass ratio (ω) at constant total volume and constant n-hexane mass ratio at 10°C (▲) and 25°C (■).	80
6.1	Raman spectra of studied catalyst samples and spectra of Co ₃ O ₄ as reference material.	85
6.2	XRD spectra of samples CAT A-D, pure Al ₂ O ₃ and reference patterns of Co ₃ O ₄ and CoO ($\lambda = 0.178897$ nm).	86
6.3	High resolution XPS Co 2p _{3/2} spectra with curve fitting according to table 6.4.	88
6.4	TPR spectra of studied catalyst samples (CAT A-D).	89
6.5	Schematic representation of the combination of precipitate/Co ₃ O ₄ crystallites and alumina support in preparation method C & D. Residual surfactant hinders the cobalt hydroxide particles to enter the pore structure of the support (method C). Calcined Co ₃ O ₄ crystallites can enter the pore structure and undergo stronger interactions with the support (method D).	89

6.6	In-situ PXRD scans of CAT C. A: diffraction patterns, 3D view; B: diffraction patterns, on-top view; C: crystallite sizes of Co ₃ O ₄ (▲), CoO (■), hcp Co (▼) and fcc Co (●) as function of temperature obtained via Rietveld refinement using PONKCS approach.	91
6.7	In-situ PXRD scans of CAT D. A: diffraction patterns, 3D view; B: diffraction patterns, on-top view; C: crystallite sizes of Co ₃ O ₄ (▲), CoO (■), hcp Co (▼) and fcc Co (●) as function of temperature obtained via Rietveld refinement using PONKCS approach.	92
7.1	TPR spectra of synthesised model catalysts normalised for the respective cobalt loading (heating rate 10°C/min).	99
7.2	(A) formation of carbonaceous species during the TPR experiment of CAT 9.6 (H ₂ ■, CO ■, CO ₂ ■, CH ₄ ■); (B) formation of methane during the activation/reduction of CAT 9.6.	100
7.3	TEM and HRTEM micrographs of CAT 9.6, CAT 5.9 and CAT 3.1 in the calcined state. Identified cobalt crystallites are encircled.	102
7.4	TEM and HRTEM micrographs of CAT 9.6, CAT 5.9 and CAT 3.1 after reduction and passivation in CO ₂ . Identified cobalt crystallites are encircled.	103
7.5	EDX maps of STEM micrograph of CAT 9.6 in calcined state: (A) STEM micrograph; (B) cobalt map of boxed area in (A); (C) aluminium map of boxed area in (A).	104
7.6	Crystallite size distributions (number based) of selected model catalysts calculated from a minimum of 300 crystallites (■ calcined; ■ reduced and passivated).	105
7.7	PXRD spectra of Co ₃ O ₄ crystallites prior to their deposition on the Al ₂ O ₃ support. Co ₃ O ₄ diffraction pattern given as reference. Crystallite sizes were obtained via Rietveld refinement. For exact reference peak positions see table 7.7.	106
7.8	PXRD spectra of selected model catalysts in the calcined state with spectrum of pure Al ₂ O ₃ and Co ₃ O ₄ diffraction pattern as reference. For exact reference peak positions see table 7.7.	107
7.9	PXRD spectra of selected model catalysts in the reduced and passivated state with spectrum of pure Al ₂ O ₃ and fcc Co and hcp Co diffraction pattern as reference. For exact reference peak positions see table 7.7.	107
7.10	In-situ PXRD scans of CAT 9.6. A: diffraction patterns, 3D view; B: diffraction patterns on-top view; C: crystallite sizes of Co ₃ O ₄ (▲), CoO (■), hcp Co (▼) and fcc Co (●) as function of temperature obtained via Rietveld refinement using PONKCS approach.	109
7.11	TCD reading and MS results from CO-TPD studies of Al ₂ O ₃ , CAT 9.6 (d _{num,red} = 9.3 nm) and CAT 5.9 (d _{num,red} = 4.7 nm). All scans normalised to 1 gram of model catalyst. Scales are indicated for B-D in the graph. A: TCD reading; B: CO flow (m/z = 28); C: H ₂ flow (m/z = 2); D: H ₂ O flow (m/z = 18).	111
7.12	MS results from CO-TPD studies of CAT 9.6 (d _{num,red} = 9.3 nm), CAT 8.6 (d _{num,red} = 8.2 nm), CAT 6.8 (d _{num,red} = 6.0 nm), CAT 5.9 (d _{num,red} = 4.7 nm) and CAT 4.0 (d _{num,red} = 3.7 nm). All scans normalised to 1 gram of metallic cobalt. Scales are indicated in the graph.	112

7.13	(A) Degree of reduction as a function of temperature for CAT 9.6 (■) and CAT 4.4 (▲) as calculated from the magnetic measurements; (B) Magnetisation relative to magnetisation at the end of the reduction process for CAT 9.6 (■) and CAT 4.4 (▲).	114
7.14	Relative magnetisation of CAT 9.6 (-■-) and CAT 4.4 (-▲-) as a function of external field strength (hysteresis). (A) full hysteresis; (B) cut-out at no external field (H = 0 kOe).	115
7.15	Crystallite size distribution of superparamagnetic sample CAT 4.4 calculated via superimposing Langevin functions.	115
7.16	Relative magnetisation (normalised) as a function of time on stream for CAT 9.6 (■) and CAT 4.4 (▲) as calculated from the magnetic measurements under FT conditions and under FT conditions with co-fed water.	116
7.17	Percentage of ferromagnetic material as a function of time on stream for CAT 9.6 (■) and CAT 4.4 (▲) as calculated from the magnetic measurements under FT conditions and under FT conditions with co-fed water.	116
7.18	Crystallite size distribution of superparamagnetic sample CAT 4.4 calculated via superimposing Langevin functions (A) after 25 hours under conditions; (B) after 3 hours of additional co-feeding of 6 bar water.	117
7.19	PXRD spectra of spent catalyst samples CAT 4.4 and CAT 9.6 as well as Al ₂ O ₃ , with AlO(OH), CoAl ₂ O ₄ , CoO and fcc Co diffraction patterns as reference.	118
7.20	HRTEM image of CAT 4.4 after exposure to elevated water pressures under FT conditions. Examples of AlO(OH) and Al ₂ O ₃ crystallites are indicated.	119
7.21	Ball and stick model of cobalt carbonyl complex (CO) ₉ Co ₃ CCOOH (Co blue, C grey, O red, H white).	120
7.22	MS spectrum of synthesised cobalt carbonyl complex.	121
7.23	Diffuse reflectance FTIR spectra of freshly prepared (CO) ₉ Co ₃ CCOOH (A) and alumina supported (CO) ₉ Co ₃ CCOOH (B).	122
7.24	In-situ diffuse reflectance FTIR spectra of supported (CO) ₉ Co ₃ CCOOH at 6 bar and 40 ml/min (STP) N ₂ flow. Heating rate 2°C/min.	122
7.25	In-situ diffuse reflectance FTIR spectra of supported (CO) ₉ Co ₃ CCOOH at 6 bar and 40 ml/min (STP) H ₂ flow. Heating rate 2°C/min.	122
7.26	Saturation magnetisation (▲, at 20 kOe external magnetic field strength) and remnant magnetisation (▼, at 0 kOe external magnetic field strength) of the supported cobalt complex sample as function of temperature.	123
7.27	Percentage of ferromagnetic material in the supported cobalt complex sample as function of temperature.	124
7.28	(A) (CO) ₉ Co ₃ CCOOH freshly supported on alumina carrier; (B) supported (CO) ₉ Co ₃ CCOOH after exposure to high temperatures in synthesis gas in set-up for magnetic measurements.	124
7.29	In-situ PXRD of supported (CO) ₉ Co ₃ CCOOH at 6 bar and 30 ml/min synthesis gas flow (H ₂ /CO = 2). Heating rate 2°C/min.	125
8.1	Turn over frequency (TOF) as a function of time on stream (TOS) for CAT 9.6 (◇) and CAT 3.1 (□). (Reaction conditions: T = 190°C, PP _{syn.gas} = 9.9 bar, SV = 7.2 ml _{syn.gas} /g _{catalyst} ·min (STP)).	130

- 8.2 Turn over frequency (TOF) as a function of time on stream (TOS) for CAT 7.3 after normal activation process (\diamond) and CAT 7.3 after activation process followed by pre-exposure to 3.3 bar CO at 190°C for 1.5 hours. (\diamond). (Reaction conditions: T = 190°C, $PP_{\text{syn.gas}} = 9.9$ bar, $SV = 7.2 \text{ ml}_{\text{syn.gas}}/\text{g}_{\text{catalyst}} \cdot \text{min}$ (STP)). 132
- 8.3 TEM and HRTEM micrographs of CAT 9.6, CAT 5.9 and CAT 3.1 after 25 hours under Fischer-Tropsch conditions and passivation in CO₂. Identified cobalt crystallites are encircled. 133
- 8.4 Crystallite size distributions (number based) of selected model catalysts determined from a minimum of 300 crystallites (\blacksquare reduced and passivated, \blacksquare after 25 hours at Fischer-Tropsch conditions and passivated). 134
- 8.5 PXRD spectra of spent model catalysts, i.e. after 25 hours at Fischer-Tropsch conditions followed by passivation. The diffraction spectrum of Al₂O₃ and the reference patterns of face-centred cubic and hexagonal closest packed cobalt metal are given as reference. 135
- 8.6 TOF as a function of average cobalt crystallite size; (A) at maximum activity versus the crystallite size of the freshly reduced catalyst; (B) at steady state versus the crystallite size of the spent catalyst, i.e. after 25 hours under Fischer-Tropsch conditions. (Reaction conditions: T = 190°C, $PP_{\text{syn.gas}} = 9.9$ bar, $SV = 7.2 \text{ ml}_{\text{syn.gas}}/\text{g}_{\text{catalyst}} \cdot \text{min}$ (STP)). 137
- 8.7 Mass specific activity as a function of average cobalt crystallite size; (A) at maximum activity versus the crystallite size of the freshly reduced catalyst; (B) at steady state versus the crystallite size of the spent catalyst, i.e. after 25 hours under Fischer-Tropsch conditions. (Reaction conditions: T = 190°C, $PP_{\text{syn.gas}} = 9.9$ bar, $SV = 7.2 \text{ ml}_{\text{syn.gas}}/\text{g}_{\text{catalyst}} \cdot \text{min}$ (STP)). 138
- 8.8 Schematic representation of the formation of methane and chain growth according to the alkyl mechanism (see chapter 2.1.2) (adapted from [40]). 139
- 8.9 Methane selectivity as a function of time on stream (TOS) of CAT 9.6 (\diamond) and CAT 3.1 (\square). Note that the methane selectivity is calculated based on the conversion obtained via product formation rates (extrapolated to a carbon number of 50) and is expressed as percentage carbon in this extrapolated product stream. (Reaction conditions: T = 190°C, $PP_{\text{syn.gas}} = 9.9$ bar, $SV = 7.2 \text{ ml}_{\text{syn.gas}}/\text{g}_{\text{catalyst}} \cdot \text{min}$ (STP)). 140
- 8.10 Selectivity towards hydrocarbons with a carbon chain length of five and higher ($S_{C_{5+}}$) as a function of time on stream (TOS) of CAT 9.6 (\diamond) and CAT 3.1 (\square). Note that $S_{C_{5+}}$ is calculated based on the conversion obtained via product formation rates (extrapolated to a carbon number of 50) and is expressed as percentage carbon in this extrapolated product stream. (Reaction conditions: T = 190°C, $PP_{\text{syn.gas}} = 9.9$ bar, $SV = 7.2 \text{ ml}_{\text{syn.gas}}/\text{g}_{\text{catalyst}} \cdot \text{min}$ (STP)). 141
- 8.11 Methane selectivities in the first 2 hours of the FT experiment. (A) CAT 7.3; (B) CAT 7.3 after pre-exposure to 3.3 bar of CO at 190°C for 1.5 hours after reduction and prior to exposure to FT conditions. (Reaction conditions: T = 190°C, $PP_{\text{syn.gas}} = 9.9$ bar, $SV = 7.2 \text{ ml}_{\text{syn.gas}}/\text{g}_{\text{catalyst}} \cdot \text{min}$ (STP)). 142

- 8.12 ((A) Methane selectivities (S_{CH_4}) and (B) selectivities towards hydrocarbons of a carbon number of 5 and higher ($S_{\text{C}_{5+}}$) over cobalt crystallite sizes at initial maximum TOF (\circ) and after 25 hours under Fischer-Tropsch conditions (\circ). Note that both types of selectivities are calculated based on the extrapolated (to a carbon number of 50) FT product spectrum. (Reaction conditions: $T = 190^\circ\text{C}$, $\text{PP}_{\text{syn.gas}} = 9.9$ bar, $\text{SV} = 7.2$ $\text{ml}_{\text{syn.gas}}/\text{g}_{\text{catalyst}} \cdot \text{min}$ (STP)). 142
- 8.13 Proposed chain termination steps in the FTS according to the alkyl mechanism (see chapter 2.1.2) forming the primary products, α -olefins (predominant with 70-90 mol% [49, 51, 52, 53]) and n-paraffins (adapted from [40]). 143
- 8.14 Non trivial surface polymerisation with chain growth, chain termination as n-paraffin (Par) and termination as α -olefin (Ol) and re-adsorption of α -olefins (adapted from [40]). 143
- 8.15 Selectivity (in C%) towards olefins in the C_1 - C_8 fraction as a function of time on stream for CAT 9.3 with different phases of the experiment indicated. (I) initial: high hydrogen concentration of the catalyst surface resulting in high methane selectivities and strong olefin hydrogenation; (II) surface reconstruction with increasing suppression of secondary olefin reactions resulting in an increase in olefin selectivity; (III) steady state. (Reaction conditions: $T = 190^\circ\text{C}$, $\text{PP}_{\text{syn.gas}} = 9.9$ bar, $\text{SV} = 7.2$ $\text{ml}_{\text{syn.gas}}/\text{g}_{\text{catalyst}} \cdot \text{min}$ (STP)). 145
- 8.16 Selectivity (in C%) towards olefins in the C_1 - C_8 fraction as a function of time on stream for CAT 7.3 without CO pre-exposure (\diamond) and with CO pre-exposure (\diamond) at different phases of the experiment. (I) initial: high hydrogen concentration of the catalyst surface resulting in high methane selectivities and strong olefin hydrogenation; (II) surface reconstruction with increasing suppression of secondary olefin reactions resulting in an increase in olefin selectivity; (III) steady state. (Reaction conditions: $T = 190^\circ\text{C}$, $\text{PP}_{\text{syn.gas}} = 9.9$ bar, $\text{SV} = 7.2$ $\text{ml}_{\text{syn.gas}}/\text{g}_{\text{catalyst}} \cdot \text{min}$ (STP)). 145
- 8.17 Carbon number dependent olefin fraction in the linear hydrocarbons for CAT 9.3 and CAT 3.1 at maximum TOF (\square) and after 25 hours under Fischer-Tropsch conditions (\diamond). (Reaction conditions: $T = 190^\circ\text{C}$, $\text{PP}_{\text{syn.gas}} = 9.9$ bar, $\text{SV} = 7.2$ $\text{ml}_{\text{syn.gas}}/\text{g}_{\text{catalyst}} \cdot \text{min}$ (STP)) 146
- 8.18 Molar ratio of olefins to paraffins for carbon numbers of 2, 3 and 5 as function of crystallite size at maximum TOF (\circ) and after 25 hours under Fischer-Tropsch conditions (\circ). (Reaction conditions: $T = 190^\circ\text{C}$, $\text{PP}_{\text{syn.gas}} = 9.9$ bar, $\text{SV} = 7.2$ $\text{ml}_{\text{syn.gas}}/\text{g}_{\text{catalyst}} \cdot \text{min}$ (STP)). 147
- 8.19 Schematic representation of the re-adsorption of an α -olefin and subsequent double bond isomerisation. 147
- 8.20 Molar content of primarily formed α -olefins in the fraction of C_5 olefins as function of crystallite size at maximum TOF (\circ) and after 25 hours under Fischer-Tropsch conditions (\circ). (Reaction conditions: $T = 190^\circ\text{C}$, $\text{PP}_{\text{syn.gas}} = 9.9$ bar, $\text{SV} = 7.2$ $\text{ml}_{\text{syn.gas}}/\text{g}_{\text{catalyst}} \cdot \text{min}$ (STP)) 148
- 8.21 Schematic representation of proposed formation routes of branched hydrocarbons (adapted from [40]). 149

8.22	Molar content of branched hydrocarbons (HCs) in the C ₅ fraction in mol% at maximum TOF (◊) and after 25 hours under Fischer-Tropsch conditions (○). (Reaction conditions: T = 190°C, PP _{syn.gas} = 9.9 bar, SV = 7.2 ml _{syn.gas} /g _{catalyst} ·min (STP))	150
8.23	Turn over frequency (TOF) as function of time on stream (TOS) for alumina supported (CO) ₉ Co ₃ CCOOH.	153
8.24	Diffuse reflectance FTIR spectra of fresh alumina supported (CO) ₉ Co ₃ CCOOH (A) and the spent catalyst after 5 hours under Fischer-Tropsch conditions (B).	154
8.25	Methane (A) and C ₅₊ (B) selectivity in carbon % as function of time on stream.	155
8.26	(A): Olefin selectivity in C% over time on stream; (B) Carbon number dependent olefin fraction in the linear hydrocarbons mol% at 1 h (◇), 3 h (□) and 5h (○) on stream.	156
8.27	(A) Turn over frequency (TOF) as a function of time on stream; (B) Methane selectivity in C% as function of time on stream.	157
8.28	Mass over charge (m/z) ratio of 17 as a function of time on stream.	158
8.29	Steady state turn over frequency of supported crystallites (○) with extended trend and populated with turn over frequencies of supported organometallic cobalt complex (□). (A) full view, (B) detailed view.	159
8.30	Selectivities of methane (A) and C ₅₊ (B) for supported cobalt crystallites at maximum TOF (◊) and after 25 hours under FT conditions (○) as well as for supported organometallic cobalt complex (□). For clarity only the values of the organometallic complex experiment at 1 hour and at 5 hours TOS are shown.	159
A2.1	Linear relationship of measured magnetisation at 20 kOe against amount of metallic cobalt.	173
A5.1	Model of a fcc cubo-octahedron with 4 edge atoms.	177
A6.1	Crystallite size distributions (number based) of model catalysts (<i>top</i> CAT 8.6, <i>bottom</i> CAT 7.3) determined from a minimum of 300 crystallites (■ calcined; ■ reduced and passivated; ■ after 25 hours at FT conditions and passivated).	178
A6.2	Crystallite size distributions (number based) of model catalysts (<i>top</i> CAT 6.8, <i>bottom</i> CAT 4.8) determined from a minimum of 300 crystallites (■ calcined; ■ reduced and passivated; ■ after 25 hours at FT conditions and passivated).	179
A6.3	Crystallite size distributions (number based) of model catalysts (<i>top</i> CAT 4.4, <i>bottom</i> CAT 4.0) determined from a minimum of 300 crystallites (■ calcined; ■ reduced and passivated; ■ after 25 hours at FT conditions and passivated).	180
A7.1	In-situ PXRD scans of CAT 3.1. A: diffraction patterns, 3D view; B: diffraction patterns on-top view; C: crystallite sizes of Co ₃ O ₄ (▲), CoO (■), hcp Co (▼) and fcc Co (●) as function of temperature obtained via Rietveld refinement using PONKCS approach.	181
A8.1	Relative magnetisation of CAT 9.6 (-■-) and CAT 4.4 (-▲-) as a function of external field strength (hysteresis). (A) after 25 hours under FT conditions; (B) after 3 hours of additional co-feeding of 6 bar water.	182

List of Tables

2.1	Influence of experimental conditions on the product distribution in the FTS [56].	13
2.2	Selected melting, Hüttig and Tamman temperatures.	17
2.3	Observed effects and proposed role of water on cobalt based Fischer-Tropsch synthesis.	22
2.4	Parameters influencing the precipitate [136].	28
2.5	Catalytic reactions studied with catalysts synthesised with the microemulsion technique [155].	30
4.1	Composition of the microemulsions used to obtain nano-sized supported cobalt crystallites.	48
4.2	Reduction conditions for supported nano-sized cobalt model catalysts.	54
4.3	Magnetic properties of bulk cobalt species.	56
5.1	Composition of microemulsions measured using dynamic light scattering (DLS).	75
5.2	Water to surfactant ratio at the interface of the reverse micelles and solubility of PEGDE in n-hexane.	77
5.3	Composition of microemulsions for measurement of size of reverse micelles using dynamic light scattering (DLS) at 10 and 25°C.	80
6.1	Composition of the microemulsions used to obtain samples CAT A-D.	83
6.2	Cobalt loading (wt% cobalt) of four catalyst samples obtained from AAS analysis.	84
6.3	Average Co ₃ O ₄ crystallite size obtained from Rietveld refinement using PONKCS approach.	86
6.4	Fitted XPS binding energies of Co(OH) ₂ and Co ₃ O ₄ [13].	87
6.5	Reference diffraction patterns of Co ₃ O ₄ , CoO, hcp Co and fcc Co in the relevant 2 θ range for a cobalt X-ray source ($\lambda = 1.78897 \text{ \AA}$). Values from International Centre for Diffraction Data PDF-2 database.	93
7.1	Composition of the microemulsions used to obtain nano-sized cobalt oxide crystallites.	97
7.2	Cobalt loadings of synthesised model catalysts measured via AAS.	98
7.3	Reduction conditions of supported nano-sized cobalt model catalysts under a flow of 40 ml/min (STP) H ₂ per gram catalyst.	99
7.4	Degree of reduction (DOR) and content of metallic cobalt after activation/reduction.	100
7.5	Average crystallite size and standard deviation of cobalt oxide/cobalt crystallites in model catalysts calculated from a minimum of 300 crystallites in the calcined and in the reduced and passivated states. To allow comparison with values obtained from XRD analysis the volume weighted mean crystallite sizes are also given.	104
7.6	Crystallite sizes obtained via Rietveld refinement of PXRD scans of the calcined (d_{cal}) and reduced and passivated (d_{red}) model catalysts.	108

7.7	Reference diffraction patterns of Co ₃ O ₄ , CoO, hcp Co and fcc Co in the relevant 2 θ range for a cobalt X-ray source ($\lambda = 1.78897 \text{ \AA}$). Values from International Centre for Diffraction Data PDF-2 database.	110
7.8	Onset temperatures for desorption peaks of CO ₂ and CH ₄ .	113
7.9	Calculated composition of spent model catalysts CAT 4.4 and CAT 9.6 obtained via Rietveld refinement (excluding alumina support).	118
7.10	Carbon and hydrogen content of synthesised sample and theoretical contents of the desired cobalt complex and other common cobalt carbonyls.	120
8.1	Average crystallite sizes and standard deviations of model catalysts calculated from a minimum of 300 crystallites in the spent state (after 25 hours at Fischer-Tropsch conditions and passivation with CO ₂). For comparison with values obtained from PXRD analysis the volume weighted mean crystallite sizes are also given.	132
8.2	Relative crystallite growth (in %) during exposure to Fischer-Tropsch conditions, based on average crystallite sizes obtained from Rietveld refinement of PXRD spectra.	136
8.3	Chain growth probabilities for tested model catalysts at maximum turn over frequency and at steady state. The chain growth probabilities are calculated via linear regression from the ASF distribution (C ₃ to C ₈) of the measured FT products at the respective times.	141
A1.1	Composition of w/o microemulsions used to establish the reverse micelle stability region in the ternary phase diagram at 10, 25 and 45°C.	171
A2.1	Calibration data obtained from magnetic measurements of various metallic cobalt masses.	173
A3.1	Off-line GC-FID conditions.	174
A4.1	Reference Kovats indices utilised in this study for most common FTS products up to a carbon number of 10.	174
A9.1	Selected characterisation and FT activity and selectivity results for supported nano-sized cobalt crystallites at initial stages, i.e. maximum TOF (Reaction conditions: T = 190°C, PP _{syn.gas} = 9.9 bar, SV = 7.2 ml _{syn.gas} /g _{catalyst} ·min (STP)).	183
A9.2	Selected characterisation and FT activity and selectivity results for supported nano-sized cobalt crystallites at steady state, i.e. after 25 hours under Fischer-Tropsch conditions (Reaction conditions: T = 190°C, PP _{syn.gas} = 9.9 bar, SV = 7.2 ml _{syn.gas} /g _{catalyst} ·min (STP)).	184
A10.1	Table of chemicals used for the synthesis of model catalysts and for FT experiments.	185

Nomenclature

Abbreviations

3WV	Three way valve
4WV	Four way valve
AAS	Atomic absorption spectroscopy
AOT	Sodium bis (2-ethylhexyl)sulphosuccinate
ASF	Anderson-Schulz-Flory
BET	Brunauer-Emmett-Teller
BPR	Back pressure regulator
BTL	Biomass to liquid
CMC	Critical micelle concentration
CO-TPD	Carbon monoxide temperature programmed desorption
CTAB	Cetyltrimethylammonium bromide
CTL	Coal to liquid
cyclo-C6	Cyclohexane
d	Desorption
DFT	Density functional state theory
DLS	Dynamic light scattering
DOR	Degree of reduction
DRIFTS	Diffuse reflectance Fourier transform infra-red spectroscopy
EDX	Energy dispersive X-ray spectroscopy
EXAFS	Extended X-ray absorption fine structure
fcc	Face-centred cubic
FID	Flame ionisation detector
FT	Fischer-Tropsch
FTIR	Fourier transformed infra-red spectroscopy
FTS	Fischer-Tropsch synthesis
g	Growth
GC	Gas chromatography
GTL	Gas to liquid
HC	Hydrocarbon
hcp	Hexagonal closest packed
HOMO	Highest occupied molecular orbital
HRTEM	High resolution transmission electron microscopy
HTFTS	High temperature Fischer-Tropsch synthesis
LTFTS	Low temperature Fischer-Tropsch synthesis
LUMO	Lowest unoccupied molecular orbital
MFC	Mass flow controller
MS	Mass spectroscopy
NP-X	Poly(oxyethylene) _x nonylphenol ether

NV	Needle valve
OI	Olefins
Ox	Oxygenates
Par	Paraffins
PEGDE	Penta-ethyleneglycol-dodecylether
PONKCS	Partial or not known crystal structure
PR	Pressure regulator
PXRD	Powder X-ray diffraction
SMSI	Strong metal support interactions
Sp	Surface species
STEM	Scanning transmission electron microscopy
STM	Scanning tunnelling microscopy
STP	Standard temperature and pressure (25°C and 1.013 bar)
TCD	Thermal conductivity detector
TEM	Transmission electron microscopy
THF	Tetrahydrofuran
TPR	Temperature programmed reduction
UHV	Ultra high vacuum
w/o	Water in oil
wc	Water core
WGS	Water gas shift
XPS	X-ray photoelectron spectroscopy
XRD	X-ray diffraction

Chemical formulas

$(\text{Co})_9\text{Co}_3\text{CCOOH}$	Aceto alkylidynetricobalt nonacarbonyl
^{13}CO	Carbon 13 isotope labelled carbon monoxide
Al_2O_3	Aluminium oxide (Alumina)
Ar	Argon
C	Carbon
CCl_3COEt	Ethyl-trichloro-ethanoate
CH_2	Alkenyl group
CH_3	Alkyl group
CH_4	Methane
Co	Cobalt
CO	Carbon monoxide or carbonyl
$\text{Co}(\text{NO}_3)_2 \cdot 6\text{H}_2\text{O}$	Cobalt nitrate hexahydrate
$\text{Co}(\text{OH})_x$	Cobalt hydroxide species
CO_2	Carbon dioxide
Co_3O_4	Cobalt oxide
CoAl_2O_4	Cobalt aluminate
CoC_2	Cobalt carbide

CoO	Cobalt oxide
Fe	Iron
Fe ₂ O ₃	Iron oxide
H ₂	Hydrogen
H ₂ O	Water
H ₂ SO ₄	Sulfuric acid
HCl	Hydrochloric acid
HClO ₄	Perchloric acid
HF	Hydrofluoric acid
HNO ₃	Nitric acid
KBr	Potassium bromide
MgSO ₄	Magnesium sulfate
N ₂	Nitrogen
N ₂ H ₄	Hydrazine
NH ₃	Ammonia
Ni	Nickel
O ₂	Oxygen
Pd	Palladium
Pt	Platinum
Rh	Rhodium
Ru	Ruthenium
SiC	Silicon carbide
SiO ₂	Silicon oxide (Silica)
TiO ₂	Titanium dioxide (Titania)
Y ₂ O ₃	Yttrium oxide
ZrO ₂	Zirconium dioxide

Notations

A	Area in chromatogram	-
d	diameter	nm
f	Response factor	-
H	Enthalpy or external magnetic field	kJ/mol or Oe
I	Current	A
k	Bolzman constant, $1.38065048 \cdot 10^{-16}$	erg/K
KI	Kovats index	-
L	Loading	wt%
M	Molecular mass of a formula unit or magnetisation	g or emucgs
m	Mass or number of edge atoms	g or -
\tilde{M}	Molar mass	g/mol
m/z	Mass over charge ratio	-
\dot{n}	Molar flow rate	mol/min
N _A	Avogadro's number, $6.022141 \cdot 10^{23}$	mol ⁻¹

P	Pressure	bar
PP	Partial pressure	bar
r	Ratio or radius	mol/(min·g) or m
S	Selectivity	%
S	Mass specific surface	m ² /g
SV	Space velocity (STP, per gram of catalyst)	ml/min·g
T	Temperature	°C or K
TOF	Turn over frequency	s ⁻¹
TOS	Time on stream	h
V	Volume or unit cell volume	m ³
W	Weight fraction	%
x	Concentration	mg/l
X	Conversion	%
Y	Yield	%
Z	Number of units in a unit cell	-

Greek notations

γ	Percentage of ferromagnetic material	%
η	Viscosity	cP
Θ	Diffraction angle	°
ρ	Density	g/cm ³
σ	Mass specific magnetisation or standard deviation	emu _g /g or nm
ω	Water to surfactant mass ratio	-
α	Chain growth probability	%
λ	Wavelength	Å
ϕ	Volume fraction of particles in an emulsion	vol%

Subscript abbreviations

agg	Aggregation
aq	Dissolved in water
BET	Brunauer-Emmet-Teller
C	Carbon or Curie
C5+	Hydrocarbons with a carbon number of 5 and higher
CH ₄	Methane
CO	Carbon oxygen bond
Co	Cobalt
cryst	Crystallite
d	Desorption
exp	Exposed metal atoms

g	Growth
i	Compound i
in	Flow in
interf	Interface
n	Carbon number
N	Néel or carbon number
noO	No oxygen
num	Number weighted
out	Flow out
rem	Remnant
S	Saturation
s	Surfactant
TEM	Transmission electron microscopy
total	Total metal atoms
vol	Volume weighted
W	Water
wc	Water core
XRD	X-ray diffraction

University of Cape Town

Chapter 1

Introduction

Since its discovery in the early 1920s [1-7] the Fischer-Tropsch synthesis (FTS) has been in the focus of heterogeneous catalysis research as well as industrial applications. The extent of this interest varied over the decades with the varying knowledge about availability of cheap crude oil [8]. In the 21st century, with the crude oil reserves further diminishing, the Fischer-Tropsch synthesis returned into the focus of research. In 2007 Shafiee and Topal [9] calculated the reserves of the common fossil fuels to be depleted in 30-40 years in the case of crude oil, 35-70 years for natural gas and 100-200 years for coal. However according to the World Energy Outlook 2007 the demand for crude oil based fuels is estimated to still increase till the year 2030. This is where the Fischer-Tropsch synthesis can play an important role in meeting these demands. Not only can the FT synthesis convert natural gas and coal via reforming or gasification, respectively, into liquid hydrocarbons and therefore into replacements for crude oil derived fuels, it can also convert biomass into these sought after products. In times of increased awareness of the environmental impact of burning fossil fuels this option of converting biomass to liquid hydrocarbons (BTL) via the FT synthesis is not only economically but also ecologically and ethically highly interesting.

The Fischer-Tropsch synthesis consists of a network of catalytic surface polymerisation reactions leading to a non selective product distribution [10-13]. Through a series of primary and secondary reactions the Fischer-Tropsch synthesis converts a mixture of hydrogen and carbon monoxide (synthesis gas) in an overall highly exothermic process to mainly n-paraffins, n-olefins and, as a main by-product, water. Further reported products include carboxylic acids, aldehydes, primary alcohols, branched hydrocarbons and aromatic compounds.

Most group VIII metals show activity for the Fischer-Tropsch synthesis [14, 15]. However due to cost, availability, level of activity as well as selectivity differences only cobalt and iron are used on an industrial scale [8, 16, 17]. Ruthenium, rhodium, nickel and even gold are also under study by the scientific community to either shed more light on the mechanistic pathways of the FTS or for possible use in niche applications including the formation of valuable fine chemicals.

In recent years aspects of surface sensitivity of the FT synthesis have become a strong research focus. For surface insensitive reactions the activity per gram of catalytically active material depends solely on the surface area available. This results in higher activity for decreasing crystallite sizes [18, 19]. For high cost catalytic material the specific activity can therefore be improved and costs for the

catalyst can be decreased by increasing the dispersion of the active material. In the case of the Fischer-Tropsch synthesis several studies on iron, ruthenium, rhodium and cobalt have shown a decrease in surface specific activity for the carbon monoxide hydrogenation, for crystallite sizes below 10 nanometers. This shows that at least some of the reactions occurring during the Fischer-Tropsch synthesis do behave surface sensitive [20-26]. Although all reports agree on the decrease of activity with decreasing crystallite size there are discrepancies on the proposed origin of this decrease as well as on the influence of crystallite size on the selectivities of the various product groups formed in the Fischer-Tropsch synthesis (e.g. decrease of methane selectivity with an increase in crystallite size). At the current stage to our best knowledge no detailed study on the crystallite size effect of cobalt on the Fischer-Tropsch synthesis has been conducted which focuses on time resolved activity and selectivity trends as well as detailed characterisation of the model catalysts prior and after the Fischer-Tropsch synthesis experiments so as to shed more light on site requirements for the various reactions in the Fischer-Tropsch regime.

The model catalysts suited for studies of the crystallite size dependency can not be prepared with commonly used methods. Catalysts with a wide range of cobalt crystallite sizes with a very narrow size distribution are required. Furthermore they should not change their sizes upon reduction and reaction due to sintering but still be highly reducible and not show strong or any metal support interactions [27]. The method chosen to obtain these model catalysts in this study is the microemulsion technique [28-33]. This method has been previously reported to be suited to yield differently sized metal and metal oxide crystallites in the nanometer range with a particularly narrow size distribution [20-23, 26, 32, 33]. A major part of this project includes the adaptation of previously reported microemulsion techniques for the cobalt system and to develop a preparation technique suitable for the experimental objectives of this thesis.

As metal crystallites prepared via a microemulsion technique hardly ever exhibit sizes below 2 nanometers ([32, 33] and citations therein) an organometallic cobalt complex was synthesised as a model compound to study the sub 2 nanometer size range. Previous studies on ruthenium [20, 34-36] utilised organometallic complexes with varying numbers of ruthenium atoms (1 to 6) to simulate differently sized active centres/ensembles for the Fischer-Tropsch synthesis. In this work a cobalt carbonyl complex containing 3 cobalt atoms was synthesised and tested under Fischer-Tropsch conditions. As it has previously been reported, that cobalt carbonyls decompose at elevated temperatures to form metal clusters and then metal crystallites via sintering [37-39], the time on stream study of the activity and selectivity does result in information of a range of crystallite sizes less than 2 nanometers and therefore represent the FT performance of crystallites in this size range.

References

- [1] F. Fischer, National Petroleum News, 18 (1926) 49.
- [2] F. Fischer and H. Tropsch, International Conference on Bituminous Coal 1926.
- [3] F. Fischer and H. Tropsch, Brennstoff-Chemie, 7 (1926) 299.
- [4] F. Fischer and H. Tropsch, Berichte der Deutschen Chemischen Gesellschaft B, 59B (1926) 923.
- [5] F. Fischer and H. Tropsch, Berichte der Deutschen Chemischen Gesellschaft B, 59B (1926) 830.
- [6] F. Fischer, H. Tropsch and P. Dilthes, Brennstoff-Chemie, 6 (1925) 265.
- [7] F. Fischer, H. Tropsch and W. Ter-Nedden, Berichte der Deutschen Chemischen Gesellschaft B, 60B (1927) 1330.
- [8] M.E. Dry, Catalysis Today, 71 (2002) 227.
- [9] S. Shafiee and E. Topal, Energy Policy, 37 (2009) 181.
- [10] M.E. Dry, Catalysis Letters, 7 (1990) 241.
- [11] J. Gaube and H.F. Klein, Journal of Molecular Catalysis A: Chemical, 283 (2008) 60.
- [12] H. Schulz, Topics in Catalysis, 26 (2003) 73.
- [13] M. Claeys and E. van Steen, Studies in Surface Science and Catalysis, 152 (2004) 601.
- [14] M.A. Vannice, Journal of Catalysis, 50 (1977) 228.
- [15] M.A. Vannice, Journal of Catalysis, 37 (1975) 449.
- [16] M.E. Dry and A.P. Steynberg, Studies in Surface Science and Catalysis, 152 (2004) 406.
- [17] H. Schulz, Applied Catalysis A: General, 186 (1999) 3.
- [18] M. Boudart and M.A. McDonald, Journal of Physical Chemistry, 88 (1984) 2185.
- [19] R.A. van Santen, Accounts of Chemical Research, 42 (2008) 57.
- [20] C.A. Welker, Ruthenium based Fischer-Tropsch synthesis on crystallites and clusters of different sizes, Department of Chemical Engineering, PhD, University of Cape Town, 2007.
- [21] E.I. Mabaso, Nanosized iron crystallites for Fischer-Tropsch synthesis, Department of Chemical Engineering, PhD, University of Cape Town, Cape Town, 2005.
- [22] V. Cheang, Effect of crystallite size and water partial pressure on the activity and selectivity of low temperature iron-based Fischer-Tropsch catalysts, Department of Chemical Engineering, PhD, University of Cape Town, Cape Town, 2009.
- [23] M. Ojeda, S. Rojas, M. Boutonnet, F.J. Pérez-Alonso, F. Javier García-García and J.L.G. Fierro, Applied Catalysis A: General, 274 (2004) 33.
- [24] G.L. Bezemer, J.H. Bitter, P.C.E. Kuipers Herman, H. Oosterbeek, J.E. Holewijn, X. Xu, F. Kapteijn, A.J. van Dillen and K.P. de Jong, Journal of the American Chemical Society, 128 (2006) 3956.
- [25] J.P. den Breejen, P.B. Radstake, G.L. Bezemer, J.H. Bitter, V. Froseth, A. Holmen and K.P. de Jong, Journal of the American Chemical Society, 131 (2009) 7197.
- [26] G. Prieto, A. Martínez, P. Concepción and R. Moreno-Tost, Journal of Catalysis, 266 (2009) 129.
- [27] S.J. Tauster, Accounts of Chemical Research, 20 (1987) 389.
- [28] V. Uskokovic and M. Drofenik, Surface Review and Letters, 12 (2005) 239.
- [29] V. Uskokovic and M. Drofenik, Advances in Colloid and Interface Science, 133 (2007) 23.

- [30] I. Lisiecki, *Journal of Physical Chemistry*, 109 (2005) 12231.
- [31] I. Lisiecki, *Colloids and Surfaces A: Physicochemical and Engineering Aspects*, 250 (2004) 499.
- [32] S. Eriksson, U. Nylen, S. Rojas and M. Boutonnet, *Applied Catalysis A: General*, 265 (2004) 207.
- [33] M. Boutonnet, S. Lögdberg and E. Elm Svensson, *Current Opinion in Colloid & Interface Science*, 13 (2008) 270.
- [34] C. Welker, J.R. Moss, E. van Steen and M. Claeys, *DGMK/SCI-Conference "Synthesis Gas Chemistry"*, 4 (2006) 223.
- [35] M. Claeys, M. Hearshaw, J.R. Moss and E. van Steen, *Studies in Surface Science and Catalysis*, 130B (2000) 1157.
- [36] M. Claeys, M. Hearshaw-Timme, J.R. Moss and E. van Steen, *DGMK/SCI-Conference "Synthesis Gas Chemistry"*, 3 (2000) 95.
- [37] V.c. Calvo-Perez, A.s. Vega C, P. Cortes and E. Spodine, *Inorganica Chimica Acta*, 333 (2002) 15.
- [38] X. Lei, M. Shang, T.P. Fehlner, R. Werner, W. Haase, D. Hautot and G.J. Long, *Journal of Organometallic Chemistry*, 541 (1997) 57.
- [39] M.J. Overett, R.O. Hill and J.R. Moss, *Coordination Chemistry Reviews*, 206-207 (2000) 581.

Chapter 2

Literature Review

2.1 Fischer-Tropsch synthesis

The Fischer-Tropsch synthesis (FTS) today looks back on a history of over 90 years of research and industrial application. These 90 years are governed by fluctuating interest in the process due to political, economical and, recently, ecological reasons as well as the unpredictability of the fossil fuel stocks and prices [1, 2].

The first carbon monoxide hydrogenation was reported by Sabatier and Senderens in 1902 [3, 4]. The extent and importance of this discovery was only realised by Franz Fischer and Hans Tropsch during their studies on the carbon monoxide hydrogenation to form petrol and diesel at the Kaiser Wilhelm Institute for Coal Research at Mühlheim an der Ruhr, Germany in the 1920s [1, 5-11]. This very productive work led to a quick commercialisation of the process, from then onwards known as Fischer-Tropsch synthesis [2]. By the 1940s a total of 9 commercial plants were operating in Germany producing over 600 Mt of FTS products derived from coal per year. After the Second World War, with the German industry destroyed, the allied forces, i.e. the UK and mainly the United States at the US Bureau of Mines [12-25], developed increased interest in the FTS as a viable alternative to the then believed soon to deplete crude oil reserves. This resulted in the commissioning of a FTS plant in Texas with an annual capacity of 360 Mt [2]. However, the discovery of vast oil fields in the Middle East [26] ended the immediate interest in the process, as crude oil derived fuels and other chemicals became available at a fraction of the cost using well known technology. Only in South Africa, where large amounts of coal could be mined cheaply and no crude oil reserves were available and due to political sanctions on the Apartheid regime, the Fischer-Tropsch synthesis provided a viable option and SASOL started large scale fuels and chemicals production using this technology in the 1950s.

In the 21st century the interest in the FTS increased again as the crude oil reserves became scarcer resulting in an immense increase in the price of this valuable commodity. Furthermore the relatively new approach to move from coal (CTL) or natural gas (GTL) as carbon feed stock for the FTS to biomass [27] has also improved the public perception of the process as it can in theory then produce carbon neutral liquid hydrocarbons. Also perceived as environmentally friendly are new technologies aimed to convert stranded natural gas, for example from oil platforms, which until today has usually been flared, via the FT process to high value and transportable liquid hydrocarbons.

This renewed interest is also reflected in the development of new large industrial FT plants in Qatar (SASOL and Shell) and Nigeria (SASOL), proposed plants in China, Australia and Indonesia and several pilot plants based on novel technologies in Great Britain, Germany, the United States and Brazil which add to the existing plants in Malaysia (Shell) and South Africa (SASOL and PetroSA) [28].

2.1.1 The Fischer-Tropsch reactions

The Fischer-Tropsch reaction is a highly exothermic catalytic surface polymerization reaction. The overall reaction can be described as the reaction of hydrogen and carbon monoxide to long chain hydrocarbons and water. Primary products of this reaction are, besides water, n-paraffins and α -olefins. Small amounts of oxygenates and branched hydrocarbons are also formed as a by-product.



A number of different reactions are required for Fischer-Tropsch chain growth to take place [1, 29]:

- adsorption of CO on the catalytic surface
- splitting of the carbon-oxygen bond
- dissociative adsorption of H₂
- reaction of 2 H atoms with the oxygen to form H₂O
- desorption of H₂O
- reaction of 2 H atoms with the carbon to form CH₂
- formation of a new carbon-carbon bond

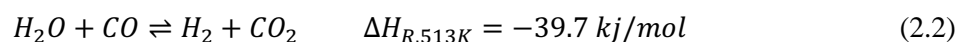
This illustrates how complex the reaction network in the FTS is. It has been proposed by Schulz [30-32] that the different reactions occurring on the catalyst surface, including those of product formation and desorption, may occur on different catalytic sites.

The chain length of the produced hydrocarbons, i.e. the chain growth probability, is strongly influenced by the choice of the catalyst and reaction conditions. Industrially two types of FT synthesis are distinguished. The High Temperature Fischer-Tropsch synthesis (HTFTS) is conducted on an iron based catalyst at 300-340°C. The chain growth probability at these conditions favours the formation of shorter hydrocarbon chains in the petrol carbon number range. The Low Temperature Fischer-Tropsch synthesis (LTFTS) on the other hand is conducted on cobalt or iron based catalysts at temperatures around 220 to 240°C and it is predominantly used to produce long chain hydrocarbons (predominantly wax) which are subsequently cracked to yield the required product fraction, i.e. mainly diesel [28], in a product upgrading step.

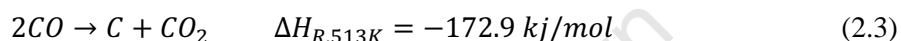
Several group VIII metals show activity for the hydrogenation of carbon monoxide. FT activity has been reported for Ni, Co, Fe, Ru and Rh [33, 34] with Ru reportedly displaying the highest activity. Due to performance, cost and availability only cobalt and iron are used industrially. Depending on the choice of the catalyst and the reaction conditions further side reactions can occur under FT conditions.

Iron also catalyses the water gas shift reaction (WGS) (see equation 2.2) under Fischer-Tropsch conditions. This reaction of water and carbon monoxide to hydrogen and carbon dioxide is normally

undesired in the context of the FTS as it results in the formation of CO_2 , an unwanted product [28]. For CO rich feed, i.e. synthesis gas with a $\text{H}_2:\text{CO}$ ratio smaller than 2, which can be derived from coal, the presence of the WGS is desired as it optimises the H_2/CO ratio for the FTS.



A further side reaction is the Boudouard reaction (see equation 2.3). This disproportionation of carbon monoxide to form carbon on the catalytically active surface and gaseous carbon dioxide is problematic in two ways. Firstly it also increases the ratio of $\text{H}_2:\text{CO}$ in the gas phase leading to a decrease in chain growth probability due to the increased hydrogenation probability of alkyl surface species. Secondly the surface carbon can form carbonaceous depositions on the catalyst surface therefore potentially blocking active sites for the Fischer-Tropsch reactions [35, 36].



2.1.2 Fischer-Tropsch reaction mechanisms

In order to form the Fischer-Tropsch products the mechanism of the synthesis has to account for several reactions (see also chapter 2.1.1). As a polymerisation reaction it needs to include the following steps:

- the adsorption of the reactants onto the catalyst surface
- the formation of a chain starter/initiator
- the growth of the chain (propagation step)
- the chain termination and desorption of the products

Several reaction pathways have been proposed in the nearly 90 years since the discovery of the FTS to explain the product spectrum. In order to account for the different product classes it is generally agreed that more than one single reaction pathway is present in the FTS [37]. Further difficulties in the postulation of reaction mechanisms are the possible secondary reactions that occur during the synthesis. Primarily formed α -olefins, for example, can re-adsorb on the catalyst surface and undergo further reactions, namely hydrogenation or double bond shift, but also act as chain starters. Claeys and van Steen [38] have reviewed the most accepted reaction mechanisms and presented the alkyl, the alkenyl, the enol and the CO-insertion mechanisms which will be further discussed in the following.

The **alkyl mechanism** (see figure 2.1) is the most widely accepted mechanism for the formation of long chain hydrocarbons in the FTS. The polymerisation monomer (CH_2 surface species) and the chain starter (CH_3 surface species) are both formed through the dissociative adsorption of carbon monoxide on the catalyst surface followed by the sequential hydrogenation of the surface carbon species. The chain propagation then occurs via the reaction of the surface CH_2 species with a surface alkyl chain. Several chain termination steps have been proposed. The β -hydrogen cleavage from a surface alkyl chain leads to an α -olefin, the main primary product. Hydrogen addition on the other hand yields an n-paraffin. The formation of oxygenates can not be explained by the alkyl mechanism but it has been postulated that the addition of surface hydroxyl species into the alky chain [39] may

account for oxygenate formation. Up to now no experimental evidence of this step has been reported in literature.

The alkyl mechanism is based on the proposed carbide mechanism originally proposed by Fischer and Tropsch [10]. In particular the chain propagation step in the alkyl mechanism has gained popularity due to experimental evidence provided by Brady and Pettit [40, 41] who showed that diazomethane reacted with hydrogen over a FT catalyst yields a FT product spectrum, while in absence of hydrogen ethane is the only product. This indicates that CH_2 species play an important role in the formation of hydrocarbon chains in the presence of hydrogen.

The formation of branched hydrocarbons can not be explained by the alkyl mechanism shown in figure 2.1. Schulz and co-workers [42, 43] proposed a reaction pathway explaining the formation of the branched hydrocarbons via the reaction of a surface alkylidene and a methyl species. Lee and Anderson [44] proposed a second mechanism based on the experimentally proven re-adsorption and subsequent secondary reaction of primarily formed α -olefins [45]. The latter mechanism was also confirmed by Schulz et al. [46] in experimental findings.

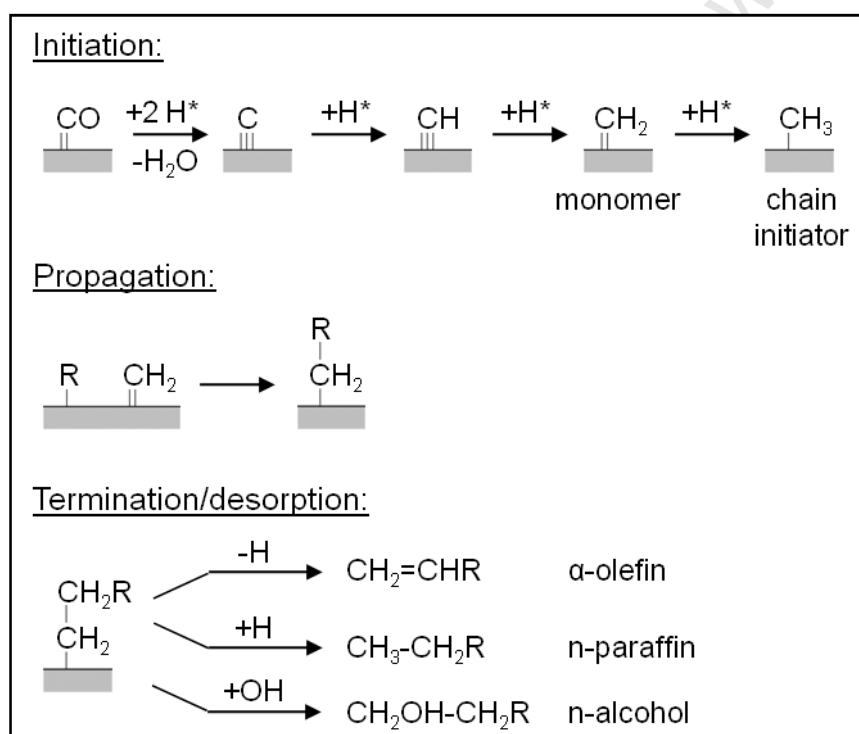


Figure 2.1: Proposed alkyl mechanism (adapted from [38]).

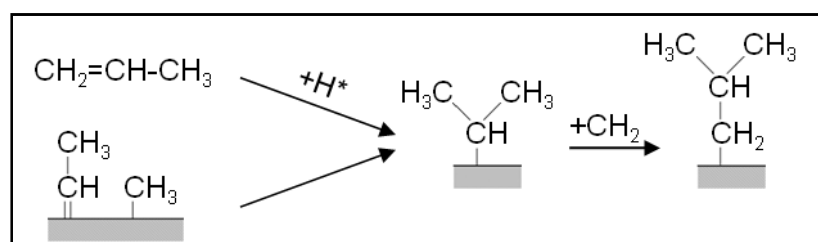


Figure 2.2: Proposed mechanisms for the formation of branched hydrocarbons in the FTS (adapted from [38]).

The **alkenyl mechanism** [47] (see figure 2.3) proposes a reaction pathway towards the formation of α -olefins. This mechanism is based on the same chain monomer and the same formation path as proposed in the alkyl mechanism. As chain initiator a surface vinyl species is identified which forms via a combination of a CH and a CH₂ surface species. The chain propagation occurs through the reaction of the vinyl species with a CH₂ species followed by a double bond shift isomerisation. The chain growth is terminated through hydrogenation of the α -carbon resulting in an α -olefin. This mechanism can not explain the formation of n-paraffins as primary product and therefore always requires a second parallel or consecutive mechanism to account for these product compounds.

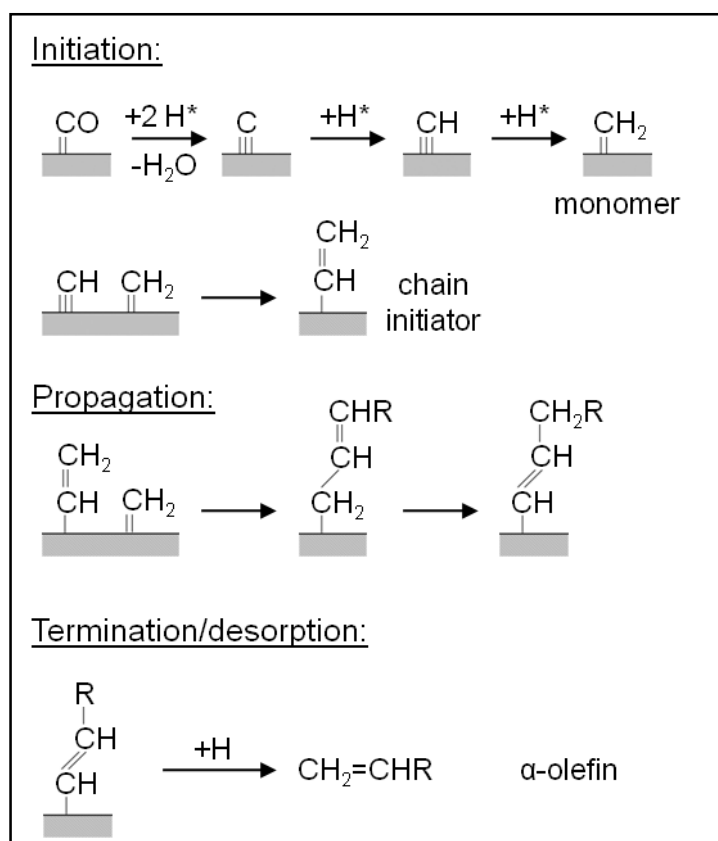


Figure 2.3: Proposed alkenyl mechanism (adapted from [38]).

A third reaction pathway, the **enol mechanism** (see figure 2.4), was proposed by researchers at the US Bureau of Mines [12] and it involves the reaction of oxygen containing surface species. This pathway provides an explanation for the formation of oxygenates during the FTS. The chain propagation step involves the condensation reaction of two 'enol' species under formation of water. The intermediate CH₂ROH could be the origin for the formation of branched hydrocarbons. Similar to the alkenyl mechanism the enol mechanism does not account for the formation of n-paraffins as primary product.

The last mechanism to be discussed here is the **CO-insertion mechanism** (see figure 2.5). This is the most accepted route to yield oxygenates in the Fischer-Tropsch synthesis. It was fully refined by Pichler and Schulz [48] and it is based on the CO insertion known from homogeneous catalysis. The monomer in this mechanism is the chemisorbed carbon monoxide which forms the chain starter, a

surface methyl species, via hydrogenation and formation of water. The chain propagation takes place via addition of a surface alkyl species and a chemisorbed CO. The CO is inserted into the chain and through subsequent hydrogenation and formation of water the alkyl chain grows by one carbon atom. Different chain termination steps starting from different surface species have been reported and can account for linear paraffins, α -olefins, aldehydes and alcohols as primary products.

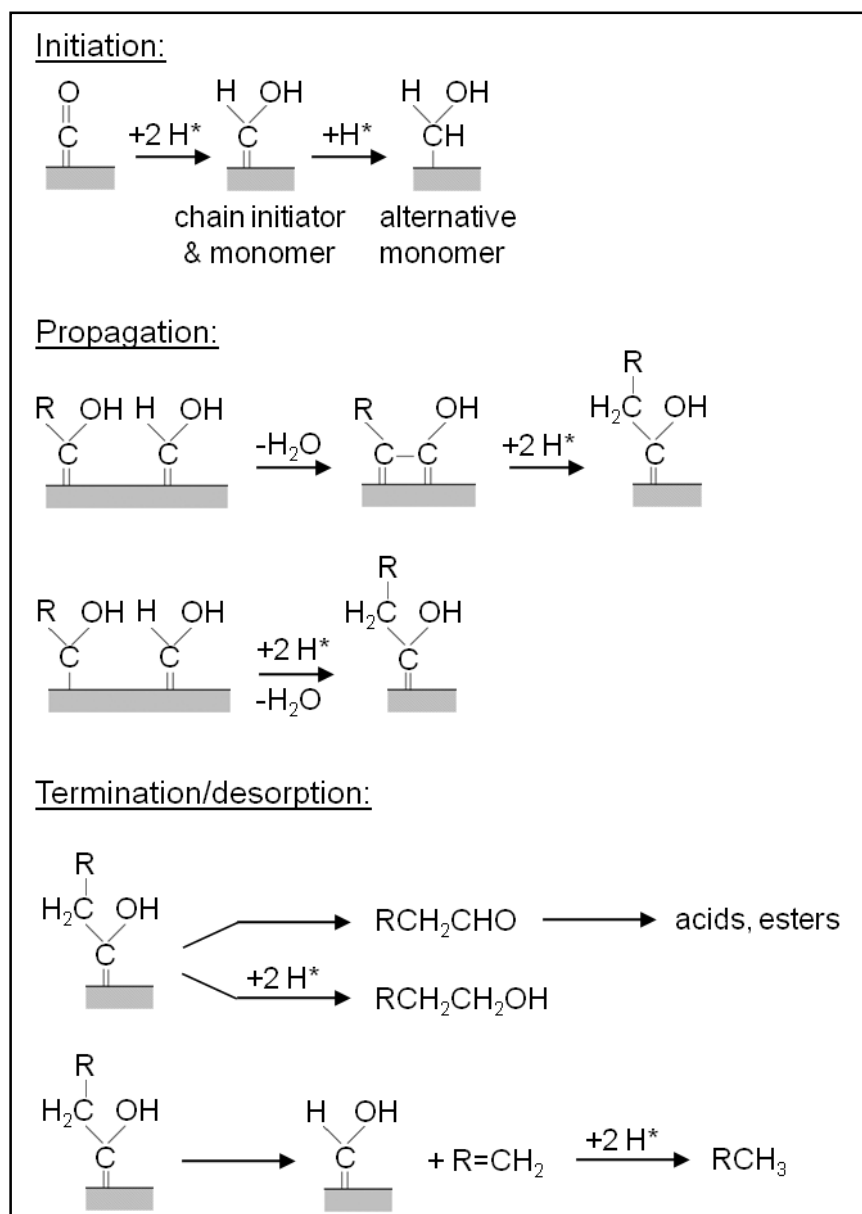


Figure 2.4: Proposed enol mechanism (adapted from [38]).

2.1.3 Fischer-Tropsch products

The Fischer-Tropsch synthesis is considered a surface polymerisation reaction (see chapter 2.1.2) and, as such, it is not very selective. A large variety of products is formed in the proposed reactions. In the classical FTS the main products include n-paraffins and n-olefins [38]. The n-olefins are mainly α -olefins, considered the main primary product, but also olefins with internal double bonds can be

formed through the re-adsorption of the α -olefins followed by a double bond shift. Typical FT product spectra also contain, although in smaller amounts, linear oxygenates (1-alcohols, aldehydes, ketones and carboxylic acids) as well as branched (mainly mono-methyl alkanes) and aromatic compounds. The latter are only found in the product of the high temperature Fischer-Tropsch synthesis. The composition of the product spectrum varies with the reaction conditions (reactor system, temperature, pressure, residence time, synthesis gas composition) (see table 2.1), but it also depends on the choice of catalyst. Irrespective of these influences the product distribution in the FTS follows a clear pattern. This is owed to the step wise growth of the product with the possibility of product desorption after each growth step.

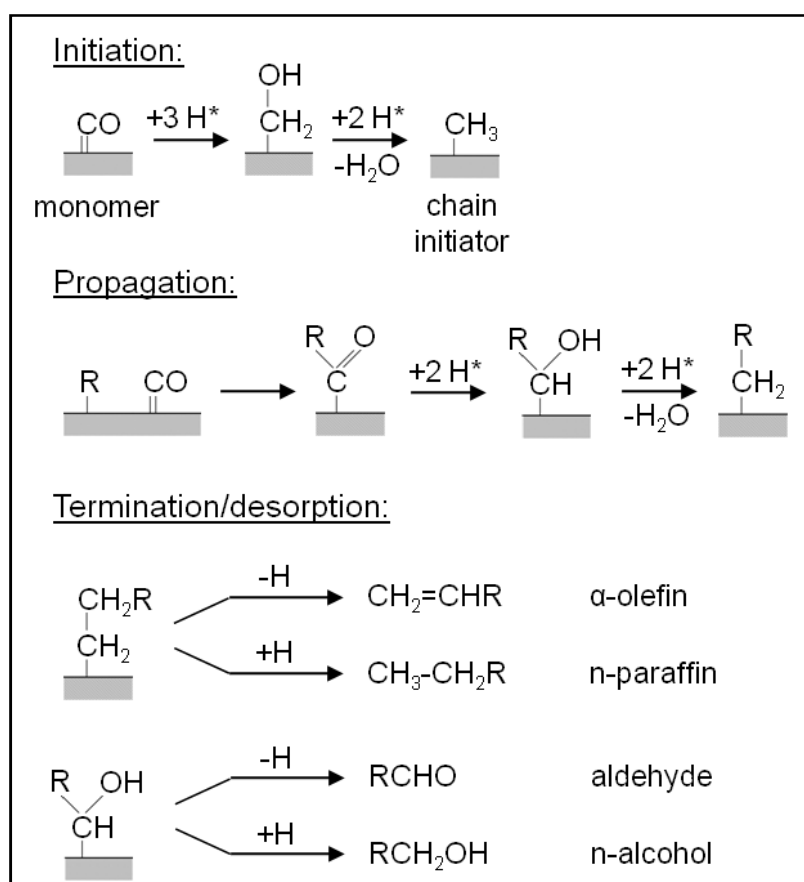


Figure 2.5: Proposed CO-insertion mechanism (adapted from [38]).

Figure 2.6 illustrates this ideal polymerisation behaviour with the possibility of chain growth or chain termination and desorption of the product at each step. The probability for chain growth, or chain growth probability (α), can therefore be expressed as:

$$\alpha = \frac{r_g}{r_g + r_d} \quad (2.4)$$

Where r_g is the rate of chain growth and r_d the rate of product desorption. Assuming an ideal polymerisation reaction the product distribution of the FTS can then be expressed mathematically with the Anderson-Schulz-Flory (ASF) distribution:

$$\log \frac{W_{N_C}}{N_C} = N_C \cdot \log \alpha + \log \frac{1-\alpha}{\alpha} \quad (2.5)$$

Where

W_{N_C} is the weight fraction of a product with a certain carbon number.

N_C is the respective carbon number.

The Anderson-Schulz-Flory distribution indicates that the product distribution of the FTS is very wide and the molar content of the products decreases exponentially with increasing carbon number. Methane, an undesired product, always has the highest molar yield. In fact methane is the only product that can be synthesised selectively by tuning the operation conditions to achieve a chain growth probability of zero.

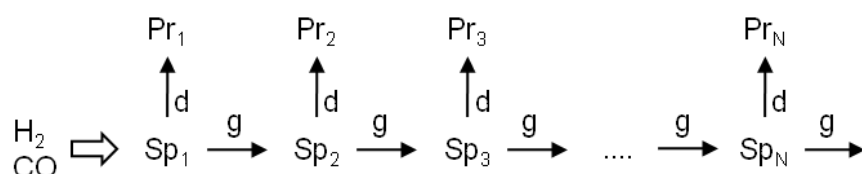


Figure 2.6: Ideal chain growth mechanism with one class of products (Pr) and one class of surface species (Sp) (N: carbon number, g: growth, d: desorption) (adapted from [38]).

Real Fischer-Tropsch product distributions however often deviate from the ideal ones based on Anderson-Schulz-Flory kinetics. In contrast to the ideal chain growth shown in figure 2.6 the FT product range includes several compounds (paraffins, olefins and oxygenates) which need to be studied separately due to their different behaviour as desorbed species. It is for example well established that the primarily formed α -olefins can re-adsorb dependent on their carbon number on the catalyst surface [38, 45, 49] to undergo a variety of secondary reactions including chain growth, hydrogenation and double bond shift. Similar to the behaviour of the α -olefins the primarily formed oxygenates (mainly 1-alcohols and aldehydes) [38] can also undergo re-adsorption and further reaction [50-55]. If we include all these reactions and their chain length dependency (see figure 2.7) in the proposed chain growth mechanism (neglecting the formation of branched hydrocarbons and the possibility of different surface species and different active sites) the model explains some of the experimentally observed deviations from ideal AFS distribution such as the higher methane and lower C_2 content.

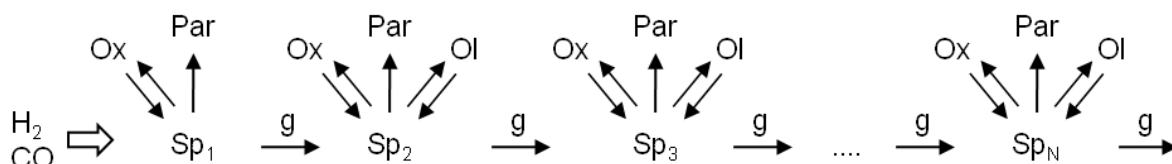


Figure 2.7: Chain growth mechanism with paraffins (Par), olefins (Ol) and oxygenates (Ox) as product classes and one class of surface species (Sp) (N: carbon number, g: growth) (adapted from [38]).

The experimental factors influencing the methane selectivity and the chain growth probability listed in table 2.1 can also be explained by the proposed chain growth mechanism. Higher temperature

does increase the rate of desorption of surface species relative to that of chain growth, therefore increasing the yield of short chain hydrocarbons and methane. An increasing H_2 to CO ratio in the feed gas increases the availability of atomic hydrogen on the catalyst surface therefore increasing the product formation of hydrocarbons with a high H:C ratio, i.e. CH_4 and paraffins versus olefins and oxygenates. In addition, secondary product hydrogenation and corresponding formation of paraffins are preferred at these conditions. Chain branching and carbon deposition are also enhanced by high temperatures, the latter reaction being further facilitated at low H_2 :CO ratios. The influence of total pressure is due to a combination of effects of partial pressures of feed and product gases. The effect of product water on the product distribution as well as catalyst stability is complex and is dealt with in detail in chapter 2.3.

Table 2.1: Influence of experimental conditions on the product distribution in the FTS [56].

	Temperature	Pressure	H_2 :CO	Residence Time
CH_4 selectivity	+	-	+	+
Chain growth	-	+	-	~
Chain branching	+	-	~	~
Olefin selectivity	~	~	-	-
Oxygenate selectivity	-	+	-	-
Carbon deposition	+	~	-	~
+	increase with increasing parameter			
-	decrease with decreasing parameter			
~	no clear effect			

2.1.3 Heterogeneous Fischer-Tropsch catalysts

Various group VIII metals (Ru, Rh, Co, Fe, Ni) show activity for the CO hydrogenation and subsequent formation of long chain products from synthesis gas. Ruthenium is reported to show the highest activity [1, 33, 34, 57, 58] forming high molecular weight products at very low temperatures. Due to its high costs and very limited availability it is not utilized on an industrial scale. Rhodium does not only show activity for the Fischer-Tropsch synthesis but also displays very high selectivity towards oxygenates [59-61]. As the Fischer-Tropsch synthesis can also be utilised as a path to valuable chemicals, these very valuable oxygenates, mainly short chain ones, are of great interest. Again the high costs and minimal resources of rhodium have prevented it to be used as a FT catalyst on an industrial scale. Nickel catalysts have not been used on an industrial scale for the FTS due to their tendency to form volatile nickel carbonyls under Fischer-Tropsch conditions [62] and their very high methanation activity leading to high yields of the undesired product CH_4 [1, 28]. For industrial applications only iron and cobalt based catalysts are used, both metals already being mentioned in the very early publications on CO hydrogenation [10, 63].

Iron catalysts have been reported to be more versatile than cobalt catalysts. They are utilised not only in the Low Temperature Fischer-Tropsch synthesis (LTFTS) but also in the High Temperature Fischer-Tropsch synthesis (HTFTS) (see chapter 2.1.1) [1, 2, 28, 64, 65]. Iron is less expensive than cobalt and less affected by sulphur poisoning. Iron catalysts promote the water gas shift reaction (WGS) (see equation 2.2) which produces the undesired product CO_2 . This however allows the feed

gas composition to be low in hydrogen, as is the case in synthesis gas obtained from the gasification of coal, as extra hydrogen is formed through the WGS reaction during the FT process. The active phase in iron based catalysts is not the reduced metallic phase which is present after hydrogen pre-treatment of the oxidic catalyst precursor. It rather forms under Fischer-Tropsch conditions and comprises a mixture of iron carbides with iron oxides and so some extend metallic iron being present as well [1, 64, 66, 67]. Generally iron catalysts are chemically promoted by the addition of small amounts of potassium to increase the activity and stability of the active phase and to affect the product selectivity [1, 64, 66, 68]. Metals such as copper can be added as reduction promoters to decrease the reduction temperature of the iron oxide. Low temperature based iron Fischer-Tropsch catalysts further contain SiO₂ as a structural promoter. The product distribution varies depending on the reaction conditions from short chain high value chemicals with high yields of α -olefins in the HTFTS to long chain liquid paraffins in the LTFTS for the use as diesel fuel.

Cobalt catalysts were chosen for the first ever industrial plants operated in Germany in the 1930s [12]. Cobalt displays a significantly higher activity than iron catalysts and can be operated at higher per pass conversion levels. Furthermore cobalt catalysts have a longer life time in industrial reactors (approximately 5 years as opposed to 8 weeks for an iron based catalyst in the HTFTS) [1, 2, 64, 66]. Due to its higher costs in industrial catalysts, cobalt is usually supported on an inert metal oxide carrier (Al₂O₃, SiO₂, TiO₂, etc.) to increase and maintain its mass specific surface area. The active phase in cobalt based catalysts is believed to be the metallic phase with active sites on the surface of the nanometer sized metallic crystallites. Due to the absence of any significant WGS activity cobalt catalysts are most suitable for hydrogen rich synthesis gas (H₂:CO = 2:1) as obtained from natural gas. Cobalt catalysts have a high selectivity towards long chain hydrocarbons and a high affinity towards olefin re-adsorption, making them ideal to produce paraffinic wax which is then hydrocracked to the desired product composition in a product upgrading step [2, 28, 64, 65].

2.1.4 Homogeneous Fischer-Tropsch catalysts

Homogeneously catalysed Fischer-Tropsch synthesis has not been demonstrated to be feasible to date and consequently it does not play any role in industrial Fischer-Tropsch synthesis. However, organometallic complexes of the group VIII metals have frequently been used as model catalysts to get insight into the reaction mechanism or single steps of a proposed mechanism for the product formation in the FTS. In a recent review Overett and co-workers [69] summarize the efforts made to find experimental prove of elemental steps in the proposed alkyl and alkenyl mechanisms (see chapter 2.1.1). Although valuable information on the Fischer-Tropsch reaction pathways could be extracted from work done on unsupported organo-metallic complexes, the reaction conditions were normally far from industrially relevant ones.

Recent developments in the field of heterogeneous or rather heterogenised model systems for the Fischer-Tropsch synthesis have focused on the combination of the very well defined geometry and chemical properties of organometallic complexes with conventional heterogeneous catalysis. To achieve this, some complexes from the well studied ruthenium carbonyl chemistry were selected, supported on conventional carriers (SiO₂ and Al₂O₃) and tested in fixed bed reactors for their activity and selectivity in the Fischer-Tropsch synthesis [70-73]. These studies showed that a Fischer-Tropsch product spectrum, although at very low chain growth rates, could in principle be observed with

ruthenium complexes containing two and more adjacent Ru atoms. For a monoatomic ruthenium complex no activity for product formation could be detected, leading to the hypothesis that in order to display FT activity on ruthenium at least two metal atoms are required. Furthermore DFT calculations support the principle feasibility that FT chain growth is indeed possible on Ruthenium compounds with at least two Ru atoms [74]. However in none of the studies it could conclusively be shown whether the observed product spectrum was obtained from the incorporation of gas phase carbon monoxide into the hydrocarbon product or whether the product originated from the CO ligands present in the complexes. The known decomposition of the ruthenium clusters at Fischer-Tropsch conditions further increased the difficulty to clearly conclude on the activity of the original complex. Welker [73] not only reported hydrocarbons in the product spectrum originating from ligands (rather than from FT activity) but also volatile ruthenium compounds were found.

The choice of the ligand system (which included non carbonyl groups such as cyclo-pentadiene rings and derivatives thereof) further seems to influence the activity for product formation immensely complicating the evaluation of obtained results. Welker [73] synthesised three di-ruthenium complexes varying only slightly in their ligand composition. However, the measured surface specific product formation activity per ruthenium atom of those three complexes varied by a factor of 3. An increase of the nuclearity, i.e. the number of ruthenium atoms, of those compounds used with carbonyl ligands only suggested an increase of product formation activity and a decrease of methane selectivity with cluster size. It must again be highlighted that no catalytic cycle including gas phase CO activation could be proven, but nonetheless important conclusions regarding site requirements for FT product formation (methane, chain growth) could be drawn.

2.2 Catalyst deactivation

Ideally a catalyst has an infinite lifetime during which it retains its activity and selectivity. This is however generally not the case and catalysts undergo a deactivation over time on stream. This deactivation can be tolerated as long as the process is still profitable but eventually replacement of the catalyst bed and/or the regeneration of the catalyst, be it in-situ or ex-situ [75], is necessary. The time of deactivation varies between catalytic systems and it ranges from seconds (in the case of fluid catalytic cracking) to months and even years. Not only can these catalyst changes result in downtime of an operation but also in high costs to renew the catalyst. Understanding of the processes that lead to the catalyst deactivation helps to develop more resistant catalysts resulting in extended performance. The importance of this aspect is reflected in the large number of publications including general reviews [75-77] and specific studies and reviews on supported cobalt catalysts in the Fischer-Tropsch synthesis [35, 36, 78]. From these publications the most relevant deactivation mechanisms for cobalt based catalysts in the FTS are:

- poisoning by sulphur, nitrogen alkali compounds
- fouling by deposition of carbonaceous species
- thermal degradation by sintering
- vapour-solid and solid-solid reactions by oxidation, sub-surface carbon, surface reconstruction, cobalt carbide formation and cobalt-support interaction
- attrition by mechanical force in the reactor

2.2.1 Poisoning

Poisoning is defined as the strong adsorption of impurities on otherwise catalytically active sites which then leads to a decrease in activity [75-77]. Not only impurities can block or affect active sites through adsorption, desired feed components as well as reaction products can also inhibit reaction through so called competitive adsorption. The difference to poisoning is the relative weak and reversible interaction these species undergo with the catalytic surface. Two different types of poisoning are distinguished: selective and non-selective poisoning [75]. In the case of selective poisoning the catalyst poison adsorbs specifically only on the catalytically active material or even only on the active site, while non-selective poisons adsorb on the catalyst including its carrier.

Poisoning in the context of the Fischer-Tropsch synthesis was already identified as a problem in the earliest stages of research in this field in the late 1920s and early 1930s [79]. For cobalt based FTS the main poisons to be encountered are sulphur and nitrogen containing compounds [35, 36]. Both are typically present in the feed stream originating from the various carbon sources, especially if biomass is used to obtain synthesis gas. Saib and co-workers [35] report very high adsorption energies at a low sulphur coverage on closest packed cobalt surfaces while sulfur was reported not to be a specific poison for the other cobalt surfaces. Due to combination of steric and electronic effects, one sulphur atom does not only influence one cobalt atom but also its nearest neighbours [77]. However, they further conclude that the poisoning through sulphur is not problematic on an industrial scale as sulphur containing compounds can easily be removed from the feed stream by using zinc- or lead-oxide guard beds.

The poisoning of cobalt FT catalysts via nitrogen containing compounds such as NH_3 and HCN has also been reported. The mechanism of inhibition here is assumed to be competitive adsorption and as such much weaker than sulphur poisoning [35]. However, there are studies in literature focusing on intentionally co-feeding ammonia to the Fischer-Tropsch synthesis in order to obtain nitrogen containing hydrocarbons as a part of the Fischer-Tropsch product spectrum [50-52] thus underlining the rather weak poisoning effect of this compound.

2.2.2 Fouling

According to Moulijn et al. [75] fouling includes all deactivation processes in which the catalytic surface is covered with a deposit. This does not have to originate from the catalytic reaction but can also be due to dust or other residues. Regardless where the deposit originates from, it does affect the catalyst activity by simply blocking the active site or the access to it and it is therefore more a physical phenomenon than a chemical one.

In the Fischer-Tropsch synthesis the main source of fouling is the carbon originating from the dissociative adsorption of carbon monoxide (see chapter 2.1.2) [35, 36, 38]. This carbon can form inactive polymeric carbon at elevated temperatures which is located on the catalytic surface as well as on the support. In a recent study [80] it was shown that the amount of polymeric carbon, which was distinguished from other surface carbon species through combined temperature controlled hydrogenation/oxygenation and electron microscopy studies, increases with increasing time on stream.

2.2.3 Thermal degradation

Thermal degradation includes all physical processes which change the morphology of the active phase and therefore the activity/selectivity due to exposure to elevated temperatures. These effects can occur during all phases of the catalyst life, including calcination and activation at higher temperatures, during reaction (hot spots) and during regeneration [75].

The most commonly observed type of thermal degradation is the growth of the crystallites of the active phase due to a process known as sintering. Sintering is often based on the effect of surface diffusion and is as such dependent on the nature of the support, its porosity, its surface structure, the metal crystallite size but mainly on the temperature. Figure 2.8 schematically illustrates the pathways of crystallite growth from highly dispersed metal clusters/crystallites to larger metal crystals. The closer the temperature of the reaction is to the melting temperature of the catalytic phase the higher is the probability for surface diffusion and crystallite growth due to sintering. Two component specific temperatures are defined in respect to the process of sintering. The Hüttig temperature is the temperature at which atoms at defect sites or kinks become mobile while bulk atoms gain mobility at the Tamman temperature.

$$T_{\text{Hüttig}} = 0.3 \cdot T_{\text{melting}} \quad (2.6)$$

$$T_{\text{Tamman}} = 0.5 \cdot T_{\text{melting}} \quad (2.7)$$

These temperatures are to be used as indicators only, as other factors (see above) also influence the affinity towards sintering of a catalyst system. Especially the presence of water is known to induce and facilitate sintering of metallic crystallites [77, 81]. Table 2.2 shows selected melting, Hüttig and Tamman temperatures for the catalytic system relevant to this study. The high temperatures for alumina indicate its stability against sintering, a reason why it is used as a catalyst support/carrier. In order to minimise effects of sintering, cobalt crystallites are usually bonded to the stable support so as to further reduce the possibility of metal migration.

Table 2.2: Selected melting, Hüttig and Tamman temperatures.

	T_{melting} (K)	T_{Tamman} (K)	$T_{\text{Hüttig}}$ (K)
Co ^a	1733	877	526
CoO ^b	2073 ^c	1037	622
Co ₃ O ₄ ^b	1223 ^c	612	369
Al ₂ O ₃ ^a	2318	1159	695

^a from [75]

^b from [82]

^c decomposes at this temperature

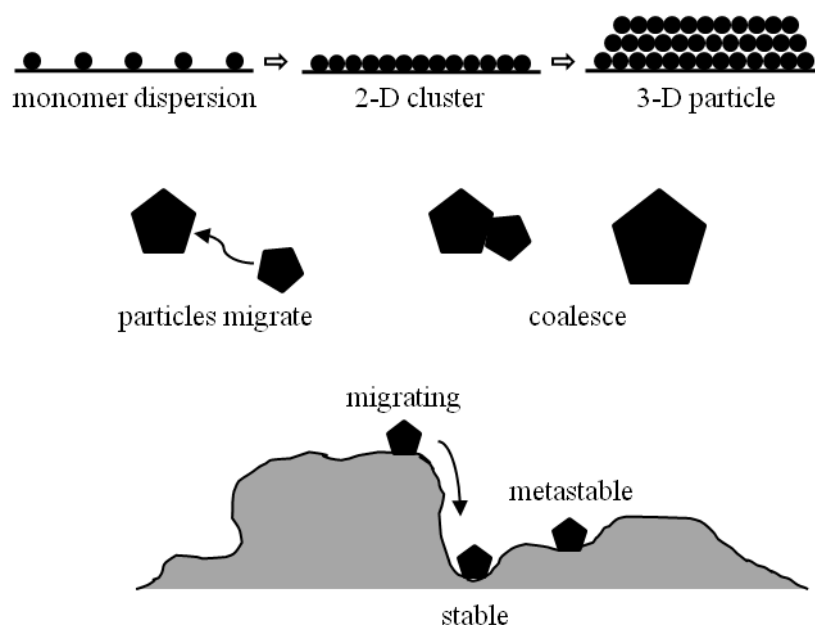


Figure 2.8: Schematic pathways of crystallite growth due to sintering (adapted from [75]).

2.2.4 Vapour-solid and solid-solid reactions

Vapour-solid and solid-solid reactions include all chemical and crystal structure related changes of the catalytically active material induced by gaseous reactants/products or adsorbed surface species. In the context of cobalt based Fischer-Tropsch synthesis we can encounter several of these reactions which typically have a detrimental effect on the catalyst performance:

- re-oxidation of the active phase through the presence of product water
- formation of strong metal support interactions
- surface reconstruction under Fischer-Tropsch conditions
- formation of Fischer-Tropsch inactive cobalt carbides
- formation of subsurface carbon

The **re-oxidation of metallic cobalt to CoO** is often regarded as a possible deactivation mechanism of cobalt based Fischer-Tropsch catalysts in literature. However, different studies report conflicting results on the presence or absence of oxidic cobalt resulting from re-oxidation ([78] and citations therein). Theoretical thermodynamic studies evaluated the possibility of oxidation of metallic fcc cobalt crystallites in the presence of water (the main product in the Fischer-Tropsch synthesis) at 220°C [83, 84] (see figure 2.9). These calculations indicate that with increasing water partial pressure, i.e. PP_{H_2O}/PP_{H_2} , or increasing, conversion X_{CO} , respectively, the tendency of metallic cobalt to oxidise increases. For realistic Fischer-Tropsch conditions (170-240°C, 20 bar, $H_2:CO = 2$, $X_{CO+H_2} = 50-70\%$ [78]) the re-oxidation has indeed been shown to occur for cobalt crystallites below a crystallite size of 4.5 nm.

A solid-solid reaction of supported cobalt catalysts in the Fischer-Tropsch synthesis is the formation of so called **strong metal support interactions** (SMSI) [85]. In this reaction cobalt atoms/ions diffuse into the support matrix and are therefore not longer available for the catalytic reaction. This

process is well known for cobalt supported on alumina [78, 86] and although the formation of so called cobalt aluminates is kinetically not favourable under FTS conditions [35] the presence of water has been reported to enhance the formation of these spinel structured compounds [87-91].

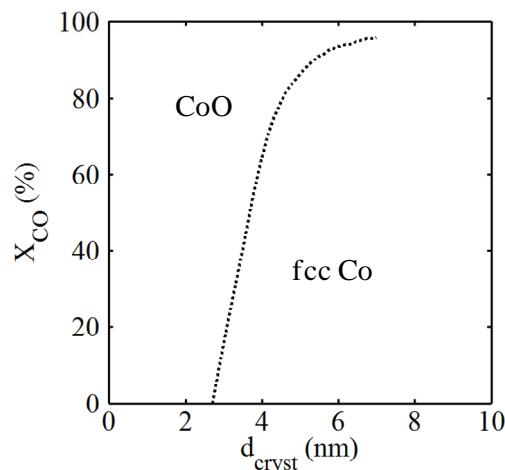


Figure 2.9: Thermodynamic stability region of metallic cobalt nano-crystallites in presence of product water in the Fischer-Tropsch synthesis (recalculated from [84]).

Surface reconstruction under carbon monoxide hydrogenation conditions was convincingly proven by Wilson and de Groot [92] with scanning tunnelling microscopy (STM) imaging of a clean cobalt (0001) surface prior and after one hour of exposure to CO hydrogenation conditions (see figure 2.10). The reconstructed surface (see (b) in figure 2.10) shows a much increased surface roughness. It is therefore highly probable that the nature and geometry of the active sites for the Fischer-Tropsch synthesis change during the course of the reaction. Schulz and co-workers [93] indeed hypothesised that a carbon monoxide induced surface reconstruction plays a role in the creation of the Fischer-Tropsch regime on the catalyst surface.

Density Functional State Theory (DFT) calculations by Ciobîcă et al. [94] on the role of different adsorbates present in the Fischer-Tropsch synthesis, i.e. O, CO, CH₂, CH and C, indicate that only the molecular carbon (coverage of 50%), resulting from the carbon monoxide dissociation, has the potential to induce a surface reconstruction of a fcc cobalt (111) surface to the more open fcc cobalt (100) surface. This (100) surface can then further undergo a so called clock reconstruction, again induced by adsorbed carbon. Both types of surface reconstruction have been previously experimentally proven to take place on nickel surfaces [95, 96].

Direct experimental evidence on the influence of surface reconstruction on the activity loss of cobalt catalysts, i.e. deactivation, and/or selectivity changes is, at this stage, not available.

Several research groups report the formation of **cobalt carbide** [97-100] believed to be inactive in the Fischer-Tropsch synthesis. This phase was observed mainly with in-situ and conventional powder X-ray diffraction techniques (PXRD). The formation of carbide phases under FT conditions was detected in carbon monoxide rich conditions or upset conditions with temporary hydrogen depletion. The presence of cobalt carbide reportedly resulted in a decrease of the CO hydrogenation activity with a parallel increase in methane selectivity [97, 101]. The carbide phases have been reported to easily decompose during mild treatment with hydrogen [99, 100, 102], interestingly under the formation of

pure hcp cobalt which in turn has been reported to display a higher Fischer-Tropsch activity than the fcc cobalt phase [99, 103]. Therefore a regeneration of cobalt catalysts deactivated by the formation of bulk cobalt carbide in hydrogen should not only recover the initial activity but it may even surpass it.

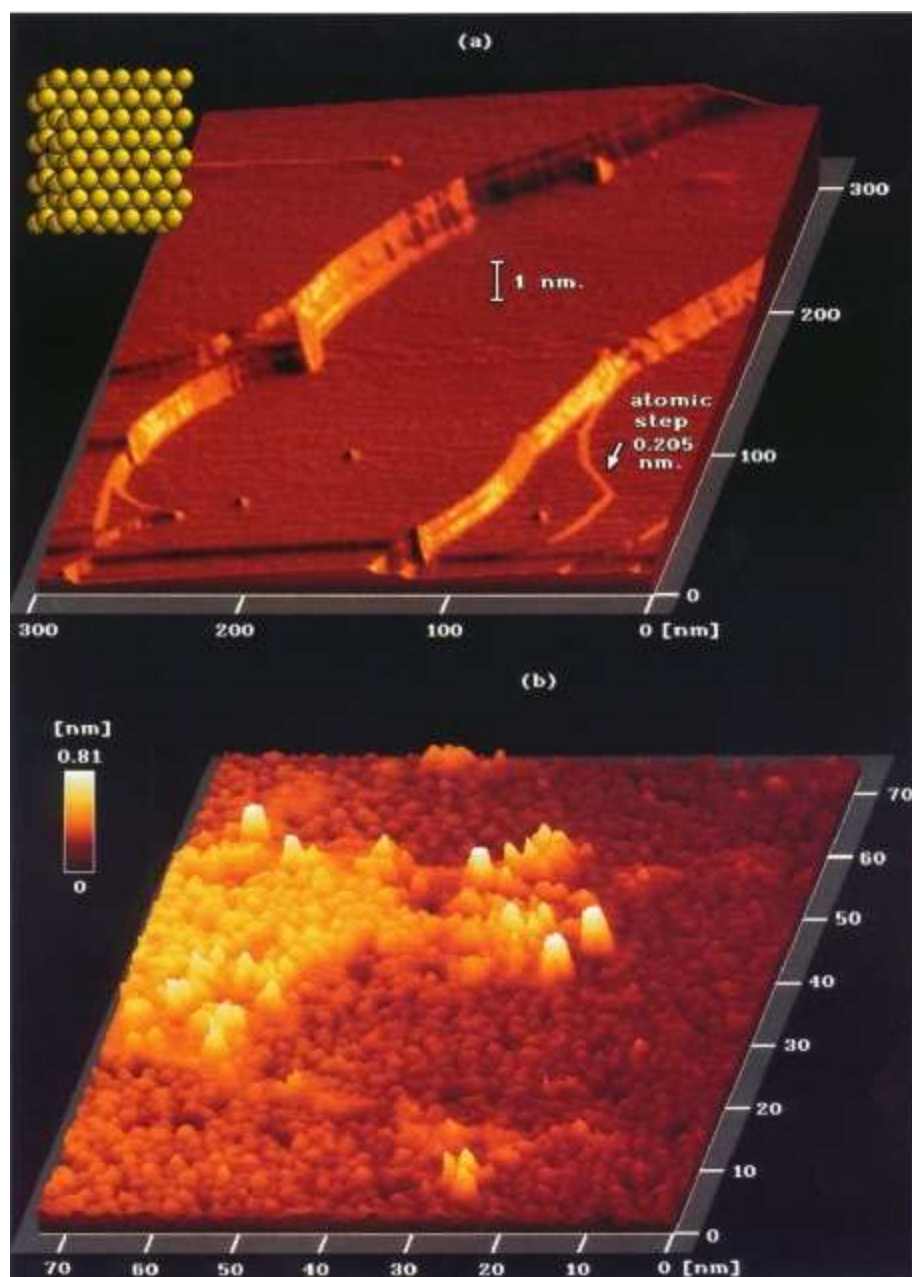


Figure 2.10: (a) STM image of a clean Co (0001) surface (prior to reaction) showing atomically flat terraces 150 nm (ca. 600 atoms) in width (tunnelling current $I_t = 2\text{ nA}$, sample bias $V = 0.05\text{ V}$). The smallest step visible is monoatomic in height, 0.205 nm being the expected single atom step height on Co (0001). (b) STM image of the Co (0001) surface after 1h exposure to high pressure CO hydrogenation conditions ($I_t = 0.5\text{ nA}$, $V = 0.5\text{ V}$). Insert: hard-sphere model of the bulk-terminated Co (0001) surface (from [92]).

Besides the formation of bulk cobalt carbides, atomic carbon is also reported to diffuse into the surface-near metallic lattice and form so called **subsurface carbon** [35]. The most favourable

position of this carbon is on an octahedral site positioned right below the fcc adsorption site. Calculations have shown that in the presence of these subsurface carbon atoms the strength of the metal-CO bond as well as the negative influence of the metal on the strength of the C-O bond is weakened. Overall this leads to a decrease in the CO adsorption strength as well as decreased activity towards CO dissociation [104].

2.2.5 Attrition

Attrition is the mechanical breakage of catalyst particles during their use in the Fischer-Tropsch synthesis [77]. This phenomenon is understandably more pronounced in reactor configurations in which the catalyst is in motion like in fluidised bed reactors and slurry bubble column reactors [105]. The thermal strain, i.e. expansion, of catalysts in a fixed bed reactor as well as swelling, an effect observed on iron catalysts originating from excessive carbon formation, can also lead to attrition [36].

The fines formed through attrition can be carried out of the reactor and therefore cause activity loss through loss of catalyst, but it can also cause mechanical problems including blockages and therefore an increase in reactor pressure [77]. To counteract the effects of attrition the catalyst stability can be increased through changes of the support system and the use of binders, changes in loading of the active phase and introduction of promoters [106].

2.3 Effect of water in the Fischer-Tropsch synthesis

In an attempt to improve control of the temperature in the highly exothermic Fischer-Tropsch synthesis (see equation 2.1), Fischer and Pichler conducted FT tests with the catalyst suspended in an aqueous slurry phase in the late 1930s [107]. They identified cobalt and ruthenium as the only suitable Fischer-Tropsch active materials in this medium due to their resistance against oxidation in water. Since then several studies have been conducted on supported and unsupported cobalt catalysts in presence of co-fed water mainly to simulate higher conversions. In 1991 Yates and Satterfield ([108] and citations therein) summarised the most accepted kinetic rate expressions for the carbon monoxide conversion in the FTS over cobalt catalysts and in none of the expressions the water partial pressure plays a role. Therefore from this kinetic point of view no activity changes upon addition of water should be observed in the FTS.

Schulz and co-workers [109] exposed a cobalt catalyst promoted with ruthenium and ZrO_2 and supported on aerosol (SiO_2) in a slurry reactor to various water pressures ranging from 8 to 43 vol% while keeping the hydrogen and carbon monoxide partial pressures constant. As expected from the published rate expressions ([108] and citations therein) no effect on the rate of reaction could be measured. The selectivity towards methane (S_{CH_4}) decreased strongly with increasing water partial pressure. Along with this decrease the selectivity towards higher hydrocarbons ($S_{C_{5+}}$) and the chain growth probability (α) increased. The product distribution further changed towards higher yields of oxygenates and olefins (mainly α -olefins) indicating the suppression of secondary reactions. All these effects were completely reversible upon removal of the co-fed water and replacement with an inert gas.

Li et al. [90, 91] studied two systems of supported cobalt catalysts: Co/SiO₂ and a platinum promoted Co/Al₂O₃ catalyst. For the silica supported catalyst an increase in CO conversion was observed upon increasing the water partial pressure. For water contents of 5 vol% this was completely reversible, while at higher water contents of 25 vol% the catalyst deactivated fast and irreversibly. A decrease in methane and an increase in C₅₊ selectivity was also observed, however no change in the olefin contents could be measured. For the alumina supported catalyst an immediate and irreversible deactivation upon exposure even to low water partial pressures was reported.

Rhenium promoted cobalt catalysts, supported on titania and unsupported, were studied at water contents of up to 57 vol% by Bertole and co-workers [110]. For the supported catalyst all trends previously reported by Schulz and co-workers [109] could be reproduced. Kinetic studies on the system indicated that the presence of water increases the dissociation activity of the adsorbed carbon monoxide but does not affect the chain growth, or the incorporation of the atomic carbon into the hydrocarbon chain respectively. This results in a higher concentration of atomic carbon on the surface and therefore decreases the hydrogen to carbon ratio favouring the formation of longer chain hydrocarbons over that of methane. The unsupported catalysts deactivated irreversibly upon exposure to elevated water partial pressure which was assigned to sintering effects and therefore loss of catalytic surface area which have been reported to be enhanced in the presence of water [81].

Similar to the unsupported catalysts reported by Bertole and co-workers [110] a group in Norway observed rapid deactivation of Rhenium promoted cobalt catalysts supported on alumina [111]. In this study the deactivation was attributed to the oxidation of the metallic cobalt nano-sized crystallites in presence of water and to water mediated formation of strong metal support interactions (SMSI) in form of cobalt aluminates. The role of water in the re-oxidation of metallic cobalt crystallites in the nanometer size range has previously been discussed as a possible deactivation mechanism in the FTS (see chapter 2.2.4).

In summary, several effects of water on the activity and selectivity in the Fischer-Tropsch synthesis have been observed and different roles of water have been proposed (see table 2.3).

Table 2.3: Observed effects and proposed role of water on cobalt based Fischer-Tropsch synthesis.

Observed Effect	Proposed Role of Water
increase of X_{CO} decrease of S_{CH_4} increase of $S_{C_{5+}}$	Increasing CO dissociation but not chain growth, leading to a high C:H ratio on the catalyst surface [110].
increase of S_{olefin}	Inhibiting secondary reactions [109]
deactivation	Enhancement of sintering [81] and formation of SMSI [87-91], re-oxidation to CoO [78, 83, 84].

2.4 Effect of crystallite size in the Fischer-Tropsch synthesis

In 1984 Boudart and McDonald proposed that a structure sensitive reaction requires a so-called multiple atom site or ensemble to show activity [112]. When comparing iron crystallites of average sizes between 1 and 17 nm in their FTS experiments they showed that the turnover rate for methane formation increased slightly with increasing crystallite size while the selectivity for C₂₊ hydrocarbons

decreased slightly. The different crystallite sizes were achieved via different metal loadings of the catalyst, varying from 0.5 to 2.8 wt%. The active phase was deposited onto the support by means of pH-controlled precipitation and impregnation. The authors noted that the observed changes were much less pronounced than effects typically observed with promoters, and they commented that changes in the active phase including carbide formation and sintering may have played a role.

In the same year Reuel and Bartholomew published a study on different supported cobalt catalysts and the effect of the crystallite size and the support on the FT activity and selectivity [113]. Like Boudart and McDonald [112] they used pH-controlled precipitation, impregnation and different metal loadings in their catalyst preparation. The results of their experiments showed that the activity of a catalyst and the turn over frequency (TOF), i.e. metal surface specific activity, increases with increasing loading or, respectively, with increasing average crystallite size. Furthermore the average hydrocarbon chain length increased with increasing average crystallite size. In a later publication Bartholomew et al. proposed, that their measured crystallite size effects on the CO conversion may have been clouded by effects of varied degrees of reduction of the cobalt phase in the different catalyst samples due to metal support interaction [114].

1990 Ho and co-workers tried to isolate the effect of the cobalt crystallite size from other variables [115]. For this purpose they used silica as support, to minimize metal support interactions, and completely reduced catalyst samples. The catalysts were prepared by incipient wetness impregnation with metal loadings from 1 to 10 wt% and average cobalt crystallite sizes of 4 to 10 nm were obtained. In this size range the experimental results showed no change of the TOF.

Iglesia and co-workers stated in 1992 that in a range of average cobalt crystallite sizes between 10 and 210 nm, no change in the TOF could be observed [116]. Earlier reported changes in TOF or in selectivity were attributed to either incomplete reduction of cobalt or to the reaction conditions which favoured the production of lighter products. According to Iglesia et al. effects of cobalt crystallite size would normally not play a role on catalyst performance at industrially relevant conditions while also stating that cobalt crystallites smaller than 5-6 nm might oxidise at the water rich conditions at high conversion [49]. The possibility of oxidation was later confirmed to be feasible for fcc cobalt crystallites smaller than 4-5 nm in a thermodynamic analysis [78, 83, 84]. A more recent theoretical study [83] corrected this threshold cobalt crystallite size for water induced re-oxidation to even smaller sizes (see chapter 2.2.4 and figure 2.9)

Recent publications from the group of de Jong [117-119] described a different observation than the one reported by Iglesia et al. [49]. In order to avoid metal support interactions in their studies the cobalt particles were loaded onto carbon nanofibers. The loading process was carried out by means of incipient wetness impregnation, ion adsorption and homogeneous deposition precipitation. The cobalt loading was varied between 0.8 and 22 wt% while the average cobalt crystallite size varied between 3 and 30 nm. By comparing the cobalt phase before and after the reaction it could be stated that no oxidation (neither bulk nor surface) of small crystallites had taken place as assumed by Iglesia [49]. Also no crystallite agglomeration or sintering could be observed in post-run catalyst analyses. The experiments were carried out at two different reaction conditions with pressures/temperatures of 1 bar/220°C and 35 bar/250°C. In both cases the results were very similar. While above a certain cobalt crystallite size (6 nm for 1 bar and 8 nm for 35 bar) the TOF remained unchanged, a sharp decrease of activity below these crystallite sizes was found. Furthermore it was reported that the methane selectivity as well as the paraffin to olefin ratio increased with smaller crystallite size which indicates

increased hydrogenation activity on these crystallites. A study by Prieto et al. [120] also reported a decreasing trend of activity with decreasing cobalt crystallite sizes. However, the results obtained for cobalt crystallite sizes below 6.8 nm might have been clouded by the formation of strong interactions between the cobalt species and the silylated ITQ-2 delaminated zeolite which was chosen as the support. The selectivity trends observed in this study are however inverse compared to previous results, with decreasing methane selectivity and increasing C₅₊ selectivity with a decrease in crystallite size. No explanation for this inverse trend was given by the authors and no further selectivities (for olefin, branched hydrocarbons and/or oxygenates) were reported.

Similar trends have recently also been described for other FT active metals. Mabaso [56], Mabaso et al. [121] and Barkhuizen et al. [122] reported a decrease of the turn over frequency for supported iron crystallites smaller than 6-8 nm. The model catalysts in this work were prepared by means of a novel reverse micelle precipitation method (see chapter 2.6) and crystallites with narrowly distributed sizes (between 2-16 nm on average) were prepared and deposited onto carbon and alumina supports. Similar to the study by Bezemer [117] increased methane selectivity was reported for smaller crystallites, while olefin to paraffin ratios remained apparently unaffected. It was noted that, although similar activity and selectivity patterns were observed over time-on-stream (i.e. at initial stages of testing and after several days), the results may have been affected by changes of iron phases and iron crystallite size (sintering) and no full post-run catalyst characterisation was reported. It was further noted that effects of unoptimised potassium promotion may have influenced their results. A follow-up study by Cheang [123] however conclusively showed that the effects reported by Mabaso [56] are indeed due to iron crystallite size, but they can further be influenced by water levels during the reaction.

Detailed studies on alumina supported ruthenium crystallites with average sizes between 2-11 nm by Welker [73], Welker et al. [72] and Barkhuizen et al. [122] also showed an increase of specific catalyst activity (TOF) with a simultaneous decrease of methane selectivity for increasing crystallite sizes. In these studies the catalysts were prepared via an impregnation method using reverse micelle systems and detailed pre- and post-run catalyst characterisation showed that effects of sintering did not impact on the results obtained. Effects of oxidation by water, which generally are considered unlikely on this noble metal, could also be excluded as some of the tests were done at very low synthesis gas conversion levels (< 0.1%). Like in the studies by Bezemer et al. [117], Welker [73] and Welker et al. [72] also observed decreasing olefin contents with smaller crystallite size. They also studied the formation of oxygenates and branched compounds but no clear trends with respect to crystallite size could be found. It was noted that activity and selectivity can change dramatically over time-on-stream, in particular in the very first minutes of catalyst testing. It was concluded that, since the crystallite sizes had not changed significantly during testing, surface reconstruction of the crystallites may have occurred upon exposure to synthesis gas, which is believed to cause dramatic performance changes of the model catalysts [93, 117]. In an attempt to understand site requirements for the formation of FT products, Welker [73] and Welker et al. [72] also used organo-metallic ruthenium complexes of varied nuclearity (2-6 metal atoms). It was shown that these compounds do indeed show C-C bond formation and C-O bond cleavage. All clusters showed high methane selectivity while the overall activity was dependent on the nuclearity and the different ligands used. In line with the trends observed for crystallites with a decreasing number of Ru atoms in the cluster the

TOF also decreased. It could not be proven whether gas phase CO was incorporated into the produced hydrocarbons.

In a study by Ojeda et al. [59] rhodium nano crystallites of different size (<5 to 30 nm on average) supported on alumina have been tested in CO hydrogenation. Again a reverse micelle method was applied in which the metal crystallites were prepared via reduction of the metal precursor followed by impregnation onto the support. Rhodium shows some FT activity [33], although generally shorter chains and higher oxygenate selectivities are obtained due to the lower tendency of this metal to promote C-O bond cleavage. Again smaller crystallites displayed lower specific activity and higher methane selectivity (60 C% for crystallites with a diameter of <5 nm compared to 42 C% for crystallites with a diameter of 30 nm). Interestingly greatly enhanced selectivity of valuable oxygenates was observed on the smaller crystallites (26 C% for crystallites with a diameter of <5 nm compared to 17 C% for crystallites with a diameter of 30 nm). It was shown that enhanced metal-support interaction of small crystallites lead to partially oxidised rhodium atoms which may be responsible for increased oxygenates formation. Alternatively it has been stated by Schulz [29] that sites of low coordination, which should preferably be present on corners and edges of small crystallites, might be responsible for CO insertion-type reactions [38, 48] (see chapter 2.1.2) leading to oxygen containing products. In particular metals like rhodium and cobalt are known to promote such reactions, and homogeneous complexes of these metals are effective catalysts for e.g. olefin hydroformylation [124].

Most published studies which report a change of TOF and selectivity with changing metal crystallite size are consistent regarding the resulting effects. With decreasing metal crystallite size the selectivity of methane increases with a concurrent decrease of the selectivity for higher hydrocarbons. In all these cases the TOF is lower for the smallest crystallites tested compared to the larger ones. The only exception is the publication by Boudart and McDonald [112] who report a decrease of the selectivity of higher hydrocarbons with increasing crystallite size. This might be due to the different definition of higher hydrocarbons as Boudart and McDonald [112] define C₂₊ selectivities while others referred to C₅₊ selectivities. Further differences might be the result of crystallite size and phase changes which were not detected due to incomplete catalyst characterisations.

The exact origin of these observed size effects is still under debate. Three main effects have been proposed:

1. Structural effect: At different metal crystallite sizes different surface sites are exposed leading to different activities and selectivities [70, 71, 112, 125, 126].
2. Electronic effect: At smaller crystallite sizes the activation energy for the dissociation of hydrogen is favoured over that of carbon monoxide resulting in changes in selectivity [73, 117, 119].
3. Oxidation effect: Smaller crystallites are easily re-oxidised under Fischer-Tropsch conditions leading to changes in activity due to a loss in active material [49, 78, 83, 84].

Structural effects have been proposed in the late 1960 by van Hardeveld and Hartog [125] to be responsible for changes in activity and selectivity in a number of catalytic reactions. With statistical

methods they developed equations to calculate the abundance of different surface sites on ideal crystallites in the nanometer size range (see figure 2.11 A). They further studied the number of so called B5 sites, an ensemble of 5 adjacent metal atoms in a specific geometry (see figure 2.11 B), which was proposed to enhance the activity of a metallic surface to catalyse reactions involving the breakage of π -bonds in diatomic molecules such as CO and N₂ [126]. As these B5 sites are only present on step or terrace sites and not on plain surfaces of an ideal crystallite, van Hardeveld and Hartog [125] developed a model crystallite with incomplete plains achieving a maximum number of B5 sites. The idea of the B5 sites gained popularity in the field of theoretical catalysis resulting in a number of Density Functional State Theory (DFT) studies on the subject [127-131], all indicating that indeed the geometry of the B5 site facilitates the π -bonds cleavage as required for carbon monoxide dissociation in the Fischer-Tropsch synthesis. It is further noted that B5 sites located at the edges of crystallites do display a higher activity than B5 sites at terraces on plains due to the larger number of uncoordinated cobalt atoms [126]. Saib et al. [35] also proposed that the number of B5 sites on cobalt crystallites increases upon reconstruction of its surface (see chapter 2.2.4) under Fischer-Tropsch conditions.

The structural effects on the activity of the Fischer-Tropsch synthesis are also known as the ensemble theory. This theory implies that a complex reaction like the FTS, or reaction steps therein respectively, can not be catalysed by a single metal atom but requires a certain number of adjacent atoms in a certain geometry to show activity [71, 132], the so called minimum required ensemble. By changing the crystallite size the number of these minimum required ensembles that can be ‘accommodated’ on the crystallite changes (see figure 2.12).

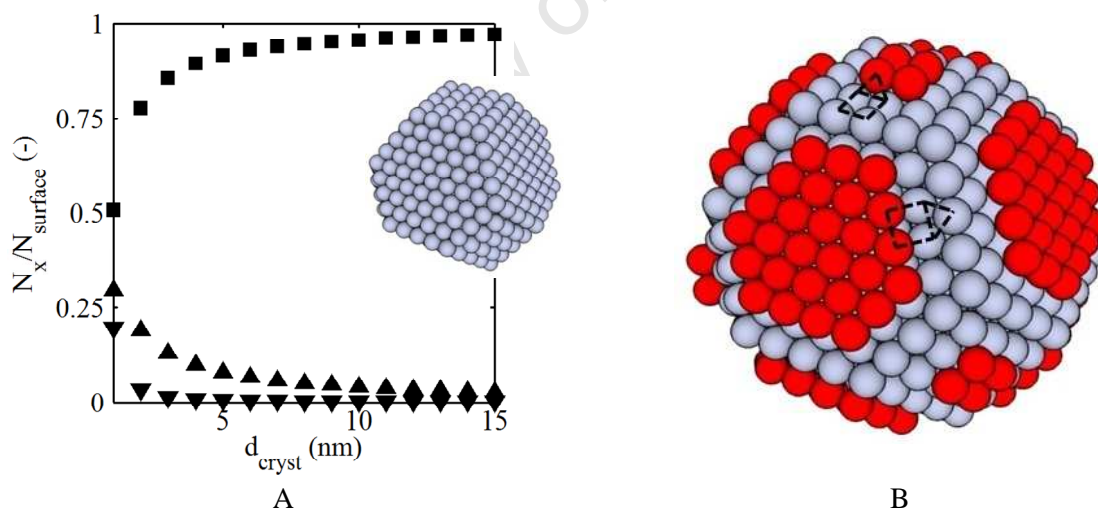


Figure 2.11: (A) Ratio of different surface atoms over total number of surface atoms for fcc cobalt cubo-octahedron crystallites of different sizes (\blacksquare edge atoms; \blacktriangle surface atoms; \blacktriangledown corner atoms); (B) Model of maximum number of B5 sites fcc cobalt cubo-octahedron crystallite ($d = 1.5$ nm) with position of B5 sites indicated; (calculated from [125]).

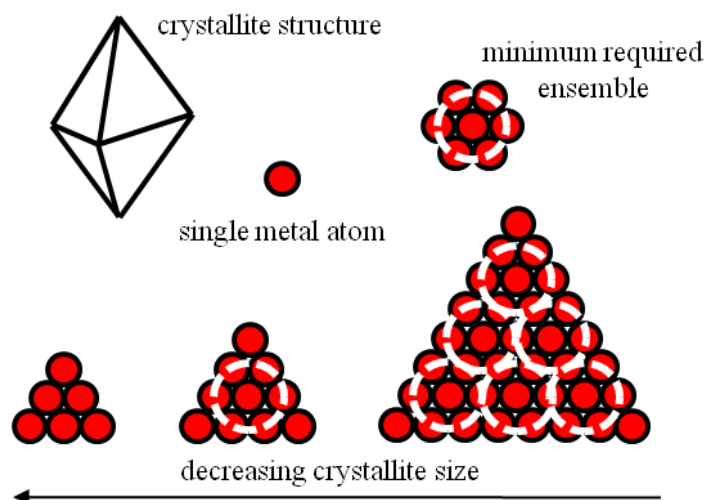


Figure 2.12: Schematic representation of the ensemble theory (adapted from [134]).

The **electronic effects** in the FTS are proposed to enhance the hydrogen dissociation but not the dissociation of carbon monoxide on smaller crystallites or to suppress the dissociation of carbon monoxide while not affecting hydrogen activation. Both cases result in a relative enrichment of atomic hydrogen on the catalytic surface therefore increasing methane selectivity and secondary hydrogenation reactions of the primarily formed α -olefins while decreasing the chain growth probability. These changes of product spectra were indeed reported for small nano-sized cobalt crystallites on carbon fibres as well as for ruthenium crystallites on an alumina support [73, 117, 121, 122, 133].

The third effect, the possibility of **re-oxidation of nano-sized metal crystallites** under Fischer-Tropsch conditions as based on thermodynamic calculations [78, 83, 84] and evidenced in some studies, is discussed in detail in chapter 2.2.4 as a possible deactivation mechanism.

2.5 Conventional catalyst preparation techniques

There are three common classes of heterogeneous catalysts being used in industrial processes [135]:

- Carrier free: Catalyst consists completely (or almost completely) of the catalytic material
- Supported catalysts: The catalytic material is dispersed in form of small crystallites on an inert carrier/support. Usually this type of catalyst is chosen for expensive raw materials to maximise the specific metal surface area.
- Coated catalysts: A very thin layer (few hundred micrometers) of catalytic active material is coated around an inert carrier, facilitating short contact times as required for kinetically rapid reactions.

The two main preparation techniques used on industrial scale to prepare these various types of catalyst are the precipitation and the impregnation technique.

2.5.1 Precipitation and co-precipitation

Precipitation is the formation of an insoluble solid from a homogeneous solution upon addition of a precipitation agent [136, 137]. Although the process of precipitation is well understood, it is a very complex process to be applied industrially due to its numerous factors that do influence not only the homogeneous starting solution but also the precipitation and the resulting precipitate (see table 2.4). Nevertheless several large scale industrial catalyst materials, including iron oxide (Fe_2O_3), Al_2O_3 , SiO_2 , TiO_2 , ZrO_2 are prepared via precipitation [136, 138]. By precipitating two different metal ions from a mixed solution, i.e. co-precipitation, it is possible to obtain very homogeneously mixed bimetallic crystals.

The very fine precipitate, mostly metal-hydroxides or carbonates, are usually amorphous. After washing of the solid to remove residual precipitation agent the precipitate is dried and heated to decompose the hydroxides/carbonates and to form the corresponding metal oxide. The so obtained catalysts, catalyst precursors or catalyst supports are usually of very small size (nanometer-range) and of high surface area [139]. Precipitation and co-precipitation are not suitable for the synthesis of the model catalyst required in this work as the control of the crystallite size is very difficult with this method.

Table 2.4: Parameters influencing the precipitate [136].

Parameter	Influence on precipitate
pH	Phase
Anion	Morphology & textural properties
Precipitation agent	Phase & homogeneity
Supersaturation	Particle size & rate of precipitation
Solvent	Textural properties & crystallinity
Mixing sequence	Precipitate composition & homogeneity
Temperature	Phase & textural properties
Additives	Textural properties
Aging	Purity, crystallinity & textural properties
Solution composition	Phase, purity, precipitate composition

2.5.2 Impregnation

Impregnation is the introduction of a homogeneous metal salt solution onto an existing support [137, 140]. The aim is to deposit the dissolved metal salt in the porous structure of the support and fixate it through temperature treatment. Two different impregnation techniques are distinguished depending on the state of the support.

The **capillary impregnation** is defined as the contact of the impregnating solution with a previously dried support [140]. Through the capillary effects the metal solution is taken up into the empty pores where it can be fixated through heating and crystallite formation. The often reported incipient wetness impregnation [141-150] is a type of capillary impregnation. In this case the volume of the metal solution matches that of the pore volume of the support so that after the process no solution remains

outside of the pore geometry [140]. Marceau et al. [140] list three physical effects to be considered with the capillary impregnation:

1. Exothermicity due to the exchange of a gas-solid with a liquid-solid interface.
2. Pressure in the pores due to the compression of the air in the pores.
3. The time required for the liquid to completely penetrate the pores.

While point three is just an experimental factor to be adjusted to obtain best results, the build-up of heat and pressure in the pores might actually alter and/or damage the support material as well as the metal precursor.

For the **diffusional impregnation** [140] the pore volume of the support is pre-filled with the pure solvent. Then the wet support is immersed in the metal precursor solution allowing the diffusional transport of the metal precursor into the pore system. Neither exothermicity nor pressure increase is observed with this impregnation method, however the diffusion time increases compared to capillary impregnation.

The drawback of any impregnation method are the rather low achievable metal loadings as well as a rather low dispersion of the catalytic material on the support. As the crystallite size is not easily tuneable and the crystallite size distribution is rather wide, impregnation techniques can not be used for the synthesis of model catalysts as they are required in this work.

2.6 Microemulsion technique

The concept of a microemulsion was first reported in 1949 by Schulman and co-workers [151], but it took until the 1970s-80s [152-154] for the catalysis community to identify this method as a viable synthesis route for the formation of nano-sized metal/metal oxide crystallites for the use as catalysts (see table 2.5). Since these early days numerous research groups adapted the concept of the microemulsion as novel approach for the production of model catalysts ([155, 156] and citations therein). The advantages over conventional catalyst preparation routes (see chapter 2.5) are the controllability of the obtained metal particle size with a very narrow size distribution by simply varying the composition of the microemulsion.

2.6.1 Definition of a microemulsion

According to the definition of Danielsson and Lindman [157] a microemulsion is a thermodynamically stable mixture of a polar solvent (usually an aqueous phase), a non-polar solvent and at least one amphiphilic phase, i.e. a surfactant. Several different surfactant types have been reported in literature ([155, 156] and citations therein), the most common ones being the ionic surfactants sodium bis (2-ethylhexyl)sulphosuccinate (AOT), cetyltrimethylammonium bromide (CTAB) and the non-ionic surfactants poly(oxyethylene)_x nonylphenol ether (NP-X) and penta-ethyleneglycol-dodecylether (PEGDE). Using ionic surfactants has the disadvantage that during heat treatment of the metal particles residual surfactant decomposes and possibly forms catalyst poisons including sulphur compounds (see chapter 2.2.1). Different levels of this poisoning might cloud activity and selectivity results obtained in the studied catalytic reaction. In addition it may be difficult to remove the inorganic counter ions (such as sodium) present in the ionic surfactant; these can also

negatively affect catalytic performance. For this reason the non-ionic surfactant penta-ethyleneglycol-dodecylether (PEGDE) was chosen in this study for the synthesis of the microemulsion. Besides the surfactant some authors report the usage of additional compounds like primary alcohols, i.e. co-surfactants, to tune the properties of the microemulsion [156, 158, 159].

The ternary mixture of a microemulsion has two distinct regions where a thermodynamically stable single phase forms, on a macroscopic scale (see figure 2.13). In the water rich area of the ternary phase diagram small oil droplets are stabilised by a surfactant layer forming so called micelles in the aqueous continuum. In the oil rich area of the phase diagram so called reverse micelles form, i.e. small water droplets are stabilised in the oil continuum (see figure 2.14). Reverse micelles are also referred to as water in oil (w/o) microemulsions. The region of stability of the micelles as well as the reverse micelles is very sensitive towards external influences such as temperature and stirring as well as towards pH and concentration of salts in the water phase [160, 161]. Outside of the stability regions a two or three phase system forms.

Table 2.5: Catalytic reactions studied with catalysts synthesised using the microemulsion technique [155].

Catalytic reactions
Combustion of methane
Fischer-Tropsch synthesis
Partial oxidation of methanol
Selective hydrogenation of unsaturated aldehydes
Selective oxidation of ammonia
Partial oxidation of methane
CO oxidation
NO reduction
Photocatalysis
Fuel cells

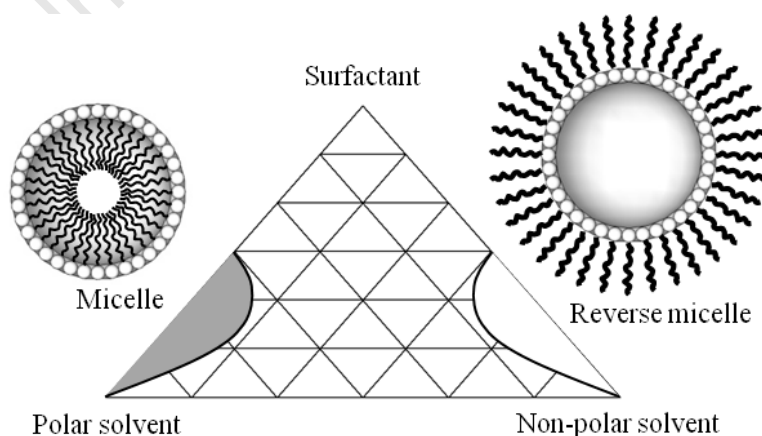


Figure 2.13: Schematic ternary phase diagram of a microemulsion system with stability regions of the micelle and the reverse micelle.

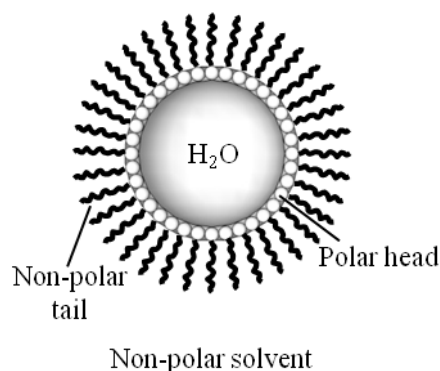


Figure 2.14: Schematic representation of a reverse micelle.

2.6.2 Preparation of nano-particles with the reverse micelle technique

In a reverse micelle solution the surfactant stabilised water droplets have a very specific geometry and a uniform internal diameter, in most microemulsion systems in the nanometer range. This uniformity makes it possible to use the structure of a reverse micelle as a reactor/template to form a nano-sized metal precipitate within the confined space of the micelle [156, 159-161]. The metal precursor is dissolved in the aqueous phase of the w/o microemulsion and is as such homogeneously distributed within the reverse micelles. The size of the resulting metal precipitate can be controlled by either changing the amount of metal precursor within a reverse micelle, i.e. the precursor concentration, or by changing the size of the reverse micelle [56, 121, 122, 162, 163]. The main factor reported to change the size of the reverse micelle is the mass ratio of the aqueous and the amphiphilic phase. By increasing the relative amount of water, the water core of the micelles increases in diameter, as the same amount of surfactant does stabilise a higher volume of water. It is assumed that the water droplet surface area occupied by one surfactant molecule stays constant. Correspondingly the relative increase of the amount of surfactant allows a higher water surface area to be stabilised, thus resulting in smaller water droplets. The size of the precipitate is further reported to be dependent on the drying procedure and the drying temperature [154-156, 159, 164].

Two different approaches to obtain the desired precipitate in the reverse micelle are reported [156] (see figure 2.15). For the first method two identical reverse micelle solutions are prepared. The metal precursor is dissolved in the aqueous phase of one microemulsion and the precipitation or reduction agent in the aqueous phase of the other one. By combining the w/o microemulsions, the reverse micelles interact by colliding and exchange matter [165]. This exchange of matter results in the formation of a precipitate in the confined geometry of the water droplet. For the second reported method the precipitation or reduction agent is added directly to a reverse micelle solution containing the metal precursor. Through the interaction with the reverse micelles and the uptake of precipitation agent the desired precipitate forms. Common precipitation agents include solutions of ammonia & ammonium salts or other weak bases such as hydrazine [56, 121, 154, 166, 167].

The nano-sized metal precipitates obtained with the microemulsion technique are commonly supported on inert carriers to be tested in heterogeneously catalysed reactions ([155, 156] and citations therein). Several techniques to deposit the precipitate on the support have been reported.

Kishida and co-workers [168] co-precipitated the support while destabilising the reverse micelle structures. This way the homogeneous distribution of the metal particles on and in the support is guaranteed. However, the in-situ formation of the support can lead to an encapsulation of the metal and therefore to a loss in catalytically active surface area and therefore catalyst activity. The support can also be pre-synthesised and then mixed with the precipitate, either directly in the reverse micelle solution by destabilising the microemulsion [56] or by re-suspending the collected precipitate in a solvent and combining the emulsion with the support [123]. In a third method the metal precursor is actually not precipitated at all. The reverse micelles are used as impregnation vessels. The selected support is mixed with the stable reverse micelle solution and via ionic interaction the dissolved metal precursor is taken up from the reverse micelles [73, 156, 164].

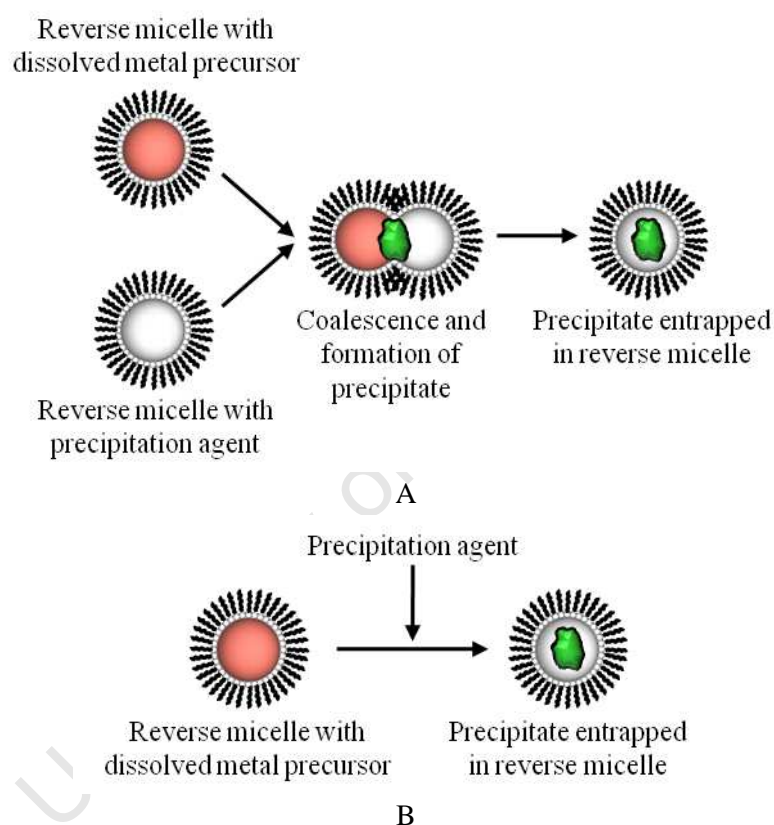


Figure 2.15: Schematic representation of the precipitation of nano-particles from a w/o microemulsion. (A) Through combination of two reverse micelle solutions, one containing the dissolved metal precursor, the other the precipitation or reduction agent. (B) Through addition of a precipitation or reduction agent to a reverse micelle solution containing the dissolved metal precursor [156].

References

- [1] H. Schulz, *Applied Catalysis A: General*, 186 (1999) 3.
- [2] M.E. Dry, *Catalysis Today*, 71 (2002) 227.
- [3] P. Sabatier and J.B. Senderens, *Comptes Rendus Hebdomadaires des Seances de l'Academie des Sciences*, 134 (1902) 689.
- [4] P. Sabatier and J.B. Senderens, *Comptes Rendus Hebdomadaires des Seances de l'Academie des Sciences*, 134 (1902) 514.
- [5] F. Fischer and H. Tropsch, *Brennstoff-Chemie*, 9 (1928) 39.
- [6] F. Fischer, H. Tropsch and W. Ter-Nedden, *Berichte der Deutschen Chemischen Gesellschaft B*, 60B (1927) 1330.
- [7] F. Fischer, H. Tropsch and P. Dilthes, *Brennstoff-Chemie*, 6 (1925) 265.
- [8] F. Fischer and H. Tropsch, *Berichte der Deutschen Chemischen Gesellschaft B*, 59B (1926) 830.
- [9] F. Fischer and H. Tropsch, *Berichte der Deutschen Chemischen Gesellschaft B*, 59B (1926) 923.
- [10] F. Fischer and H. Tropsch, *Brennstoff-Chemie*, 7 (1926) 299.
- [11] F. Fischer, *National Petroleum News*, 18 (1926) 49.
- [12] H.H. Storch, N. Golumbic and R.B. Anderson, *The Fischer-Tropsch and Related Syntheses* (John Wiley & Sons), (1951) 603.
- [13] H.H. Storch, *Chem. Petroleum Hydrocarbons* (Reinhold Publishing Corp., New York, N.Y.), 1 (1954) 631.
- [14] H.H. Storch, *Chemical Engineering Progress*, 44 (1948) 469.
- [15] H.H. Storch, *Journal of Industrial and Engineering Chemistry* (Washington, D. C.), 37 (1945) 340.
- [16] M.D. Schlesinger, J.H. Crowell, M. Leva and H.H. Storch, *Journal of Industrial and Engineering Chemistry* (Washington, D. C.), 43 (1951) 1474.
- [17] M.D. Schlesinger, H.E. Benson, E.M. Murphy and H.H. Storch, *Journal of Industrial and Engineering Chemistry* (Washington, D. C.), 46 (1954) 1322.
- [18] M. Leva, M. Grummer, M. Weintraub and H.H. Storch, *Chemical Engineering Progress*, 44 (1948) 707.
- [19] M.A. Elliott, E.L. Clark and H.H. Storch. 1953. Hydrocarbon-synthesis gas from coal, USA, Patent, U.S. 2534286.
- [20] H.E. Benson, J.H. Field, D. Bienstock, R.R. Nagel, L.W. Brunn, C.O. Hawk, J.H. Crowell and H.H. Storch, *Bull. - U. S., Bur. Mines*, 568 (1958) 72.
- [21] H.E. Benson, J.H. Crowell, J.H. Field and H.H. Storch, *Proc. 3rd World Petroleum Congress, Hague*, (1951) 38-56.
- [22] R.B. Anderson, J.F. Shultz, B. Seligman, W.K. Hall and H.H. Storch, *Journal of the American Chemical Society*, 72 (1950) 3502.
- [23] R.B. Anderson, J.F. Schultz, L.J.E. Hofer and H.H. Storch, *Bulletin - U. S., Bureau of Mines*, 580 (1959) 25.
- [24] R.B. Anderson, R.A. Friedel and H.H. Storch, *Journal of Chemical Physics*, 19 (1951) 313.

- [25] R.B. Anderson, J. Feldman and H.H. Storch, *Journal of Industrial and Engineering Chemistry* (Washington, D. C.), 44 (1952) 2418.
- [26] W.W.A. Ver, *North American Petroleum. A Complete Summary of Geological Information on the Occurrence of Oil and Gas in the United States and Canada, with a Concluding Chapter on the Oil Fields of the Middle East.* Municipal University, Department of Geology, (1957) 459.
- [27] S. Ahlgren, A. Baky, S. Bernesson, K. Nordberg, O. Noren and P.A. Hansson, *Biosystems Engineering*, 99 (2008) 145.
- [28] M.E. Dry and A.P. Steynberg, *Studies in Surface Science and Catalysis*, 152 (2004) 406.
- [29] H. Schulz, *Topics in Catalysis*, 26 (2003) 73.
- [30] H. Schulz, *C₁ Molecule Chemistry*, 1 (1985) 2312.
- [31] H. Schulz, E. van Steen and M. Claeys, *Topics in Catalysis*, 2 (1995) 2234.
- [32] H. Schulz, E. van Steen and M. Claeys, *Studies in Surface Science and Catalysis*, 81 (1994) 455.
- [33] M.A. Vannice, *Journal of Catalysis*, 50 (1977) 228.
- [34] M.A. Vannice, *Journal of Catalysis*, 37 (1975) 449.
- [35] A.M. Saib, D.J. Moodley, I.M. Ciobîca, M.M. Hauman, B.H. Sigwebela, C.J. Weststrate, J.W. Niemantsverdriet and J. van de Loosdrecht, *Catalysis Today*, 154 (2010) 271.
- [36] N.E. Tsakoumis, M. Rønning, Ø. Borg, E. Rytter and A. Holmen, *Catalysis Today*, 154 (2010) 162.
- [37] G.J. Hutchings, M. van der Riet and R. Hunter, *Journal of the Chemical Society, Faraday Transactions 1*, 85 (1989) 2875.
- [38] M. Claeys and E. van Steen, *Studies in Surface Science and Catalysis*, 152 (2004) 601.
- [39] P. Johnston and R.W. Joyner, *Studies in Surface Science and Catalysis* 75 (1993) 165.
- [40] R.C. Brady and R. Pettit, *Journal of the American Chemical Society*, 103 (1981) 1287.
- [41] R.C. Brady and R. Pettit, *Journal of the American Chemical Society*, 102 (1980) 6181.
- [42] H. Schulz, E. Erich, H. Gorre and E. van Steen, *Catalysis Letters*, 7 (1990) 157.
- [43] H. Schulz, K. Beck and E. Erich, *Proceedings of the 9th International Congress on Catalysis*, Calgary, Canada, (1988) 829.
- [44] C.B. Lee, and R.B. Anderson, *Proceedings of the 8th International Congress on Catalysis*, Bruxelles, Belgium, (1985) II15.
- [45] L.M. Tau, H.A. Dabbagh, B. Chawla and B.H. Davis, *Catalysis Letters* 7 (1990) 141.
- [46] H. Schulz, B.R. Rao and M. Elstner, *Erdoel Kohle, Erdgas, Petrochemie*, 23 (1970) 651.
- [47] P.M. Maitlis, R. Quayoum, H.C. Long and M.L. Turner, *Applied Catalysis A: General*, 186 (1999) 363.
- [48] H. Pichler and H. Schulz, *Chemie-Ingenieur-Technik*, 42 (1970) 1162.
- [49] E. Iglesia, *Applied Catalysis A: General*, 161 (1997) 59.
- [50] M. Claeys, E. van Steen, F. Roessner and A. Rausch, 2009, A process for the production of hydrocarbons including olefins from syntehsis gas, South Africa, PCT Patent Application PCT PCT/IB2009/005256.
- [51] M. Claeys, E. van Steen, F. Roessner and T. Sango, 2009, A process for the production of nitrogen or phosphorus containing compounds from synthesis gas, South Africa, PCT Patent Application PCT PCT/IB2009/005242.

- [52] T. Sango, Nitrogen-containing compounds from ammonia co-feed to the Fischer-Tropsch synthesis. Department of Chemical Engineering, Master of Science, University of Cape Town, Cape Town, to be submitted.
- [53] M. Claeys and H. Schulz, Preprints - American Chemical Society, Division Petroleum Chemistry, 49 (2004) 195.
- [54] B.H. Davis, Preprints - American Chemical Society, Division Fuel Chemistry, 47 (2002) 237.
- [55] L.M. Tau, R. Robinson, R.D. Ross and B.H. Davis, Journal of Catalysis, 105 (1987) 335.
- [56] E.I. Mabaso, Nanosized Iron Crystallites for Fischer-Tropsch Synthesis, Department of Chemical Engineering, PhD, University of Cape Town, Cape Town, 2005.
- [57] H. Pichler and H. Buffleb, Brennstoff-Chemie, 21 (1940) 257.
- [58] H. Pichler and H. Buffleb, Brennstoff-Chemie, 21 (1940) 273.
- [59] M. Ojeda, S. Rojas, M. Boutonnet, F.J. Pérez-Alonso, F. Javier García-García and J.L.G. Fierro, Applied Catalysis A: General 274 (2004) 33.
- [60] M.M. Bhasin, W.J. Bartley, P.C. Ellgen and T.P. Wilson, Journal of Catalysis, 54 (1978) 120.
- [61] W.J. Bartley, P.O. Ellgen, and T.P. Wilson. 1980. Two-carbon atom oxygenated compounds from synthesis gas with minimal production of methane.
- [62] W.M. Shen, J.A. Dumesic and C.G. Hill Jr., Journal of Catalysis, 68 (1981) 152.
- [63] F. Fischer and H. Tropsch, Brennstoff-Chemie, 7 (1926) 97.
- [64] H. Schulz, Studies in Surface Science and Catalysis, 163 (2007) 177.
- [65] M.E. Dry, Journal of Chemical Technology and Biotechnology 77 (2001) 43.
- [66] M.E. Dry, Catalysis Letters, 7 (1990) 241.
- [67] R.B. Anderson, L.J.E. Hofer, E.M. Cohn and B. Seligman, Journal of the American Chemical Society 73 (1951) 944.
- [68] A. Steynberg, M. Dry, Editors, Fischer-Tropsch Technology. [In: Stud. Surf. Sci. Catal.; 2004, 152]. Elsevier B.V., Amsterdam, 2004.
- [69] M.J. Overett, R.O. Hill and J.R. Moss, Coordination Chemistry Reviews, 206-207 (2000) 581.
- [70] M. Claeys, M. Hearshaw, J.R. Moss and E. Van Steen, Studies in Surface Science and Catalysis, 130B (2000) 1157.
- [71] M. Claeys, M. Hearshaw-Timme, J.R. Moss and E. van Steen, DGMK/SCI-Conference "Synthesis Gas Chemistry", 3 (2000) 95.
- [72] C. Welker, J.R. Moss, E. van Steen and M. Claeys, DGMK/SCI-Conference "Synthesis Gas Chemistry", 4 (2006) 223.
- [73] C.A. Welker, Ruthenium based Fischer-Tropsch synthesis on crystallites and clusters of different sizes, Department of Chemical Engineering, PhD, University of Cape Town, Cape Town, 2007.
- [74] C. Welker, N.S. Phala, J.R. Moss, M. Claeys and E. van Steen, Journal of Molecular Catalysis A: Chemical, 288 (2008) 75.
- [75] J.A. Moulijn, A.E. van Diepen and F. Kapteijn, Applied Catalysis A: General, 212 (2001) 3.
- [76] P. Forzatti and L. Lietti, Catalysis Today, 52 (1999) 165.
- [77] C.H. Bartholomew, Applied Catalysis A: General, 212 (2001) 17.
- [78] J. van de Loosdrecht, B. Balzhinimaev, J.A. Dalmon, J.W. Niemantsverdriet, S.V. Tsybulya, A.M. Saib, P.J. van Berge and J.L. Visagie, Catalysis Today, 123 (2007) 293.

- [79] F. Fischer and H. Tropsch, *Gesellschaftliche Abhandlungen zur Kenntnis der Kohle*, 10 (1932) 313.
- [80] D.J. Moodley, J. van der Loosdrecht, A.M. Saib, M.J. Overett, A.K. Datye and J.W. Niemantsverdriet, *Applied Catalysis A: General*, 354 (2009) 102.
- [81] G.L. Bezemer, T.J. Remans, A.P. van Bavel, and A.I. Dugulan, *Journal of the American Chemical Society*, 132 (2010) 8540.
- [82] R.H. Perry, D.W. Green, and Editors, *Perry's Chemical Engineers' Handbook*, 7th Edition. McGraw-Hill, 1997.
- [83] J.C.W. Swart, A theoretical view on deactivation of cobalt-based Fischer-Tropsch catalysts, Department of Chemical Engineering, PhD, University of Cape Town, Cape Town. 2008.
- [84] E. van Steen, M. Claeys, M.E. Dry, J. van de Loosdrecht, E.L. Viljoen and J.L. Visagie, *Journal of Physical Chemistry B*, 109 (2005) 3575.
- [85] S.J. Tauster, *Accounts of Chemical Research*, 20 (1987) 389.
- [86] A. Tavasoli, R.M. Malek Abbaslou and A.K. Dalai, *Applied Catalysis A: General*, 346 (2008) 58.
- [87] G. Jacobs, T.K. Das, P.M. Patterson, J. Li, L. Sanchez and B.H. Davis, *Applied Catalysis A: General*, 247 (2003) 335.
- [88] G. Jacobs, T.K. Das, Y. Zhang, J. Li, G. Racoillet and B.H. Davis, *Applied Catalysis A: General*, 233 (2002) 263-281.
- [89] G. Jacobs, P.M. Patterson, Y. Zhang, T. Das, J. Li and B.H. Davis, *Applied Catalysis A: General*, 233 (2002) 215-226.
- [90] J. Li, G. Jacobs, T. Das, Y. Zhang and B. Davis, *Applied Catalysis A: General*, 236 (2002) 67.
- [91] J. Li, X. Zhan, Y. Zhang, G. Jacobs, T. Das and B.H. Davis, *Applied Catalysis A: General*, 228 (2002) 203.
- [92] J. Wilson and C. de Groot, *Journal of Physical Chemistry*, 99 (1995) 7860.
- [93] H. Schulz, Z. Nie and F. Ousmanov, *Catalysis Today*, 71 (2002) 351.
- [94] I.M. Ciobîca, R.A. van Santen, P.J. van Berge and J. van de Loosdrecht, *Surface Science*, 602 (2008) 17.
- [95] C. Klink, I. Stensgaard, F. Besenbacher and E. Laegsgaard, *Surface Science*, 360 (1996) 171-.
- [96] J.E. Kirsch, and S. Harris, *Surface Science*, 522 (2003) 125.
- [97] V. Gruver, X. Zhan, J. Engman, H.J. Robota, S.L. Suib and M. Polverejan, *Preprints - American Chemical Society, Division Petroleum Chemistry*, 49 (2004) 192.
- [98] O. Ducreux, J. Lynch, B. Rebours, M. Roy and P. Chaumette, *Studies in Surface Science and Catalysis*, 119 (1998) 125.
- [99] H. Karaca, O.V. Safonova, S. Chambrey, P. Fongarland, P. Roussel, A. Griboval-Constant, M. Lacroix and A.Y. Khodakov, *Journal of Catalysis*, 277 (2011) 14.
- [100] S. Weller, L.J.E. Hofer and R.B. Anderson, *Journal of the American Chemical Society*, 70 (1948) 799.
- [101] J. Cheng, P. Hu, P. Ellis, S. French, G. Kelly, and C.M. Lok, *Journal of Physical Chemistry C*, 114 (2011) 1085.
- [102] O. Ducreux, B. Rebours, J. Lynch, M. Roy-Auberger and D. Bazin, *Oil Gas Science and Technology*, 64 (2009) 49.

- [103] D.I. Enache, B. Rebours, M. Roy-Auberger and R. Revel, *Journal of Catalysis* 205 (2002) 346.
- [104] M.C. Zonnevylle, J.J.C. Geerlings and R.A. van Santen, *Surface Science*, 240 (1990) 253.
- [105] C. Perego, R. Bortolo and R. Zennaro, *Catalysis Today*, 142 (2009) 9.
- [106] D. Wei, J.G. Goodwin, R. Oukaci, and A.H. Singleton, *Applied Catalysis A: General*, 210 (2001) 137.
- [107] F. Fischer and H. Pichler, *Brennstoff-Chemie*, 20 (1939) 247.
- [108] I.C. Yates and C.N. Satterfield, *Energy & Fuels*, 5 (1991) 168.
- [109] H. Schulz, M. Claeys and S. Harms, *Studies in Surface Science and Catalysis*, 107 (1997) 193.
- [110] C.J. Bertole, C.A. Mims and G. Kiss, *Journal of Catalysis*, 210 (2002) 84.
- [111] A.M. Hilmen, D. Schanke, K.F. Hanssen and A. Holmen, *Applied Catalysis A: General*, 186 (1999) 169.
- [112] M. Boudart and M.A. McDonald, *Journal of Physical Chemistry*, 88 (1984) 2185.
- [113] R.C. Reuel and C.H. Bartholomew, *Journal of Catalysis*, 85 (1984) 78.
- [114] C.H. Bartholomew, L.R. Neubauer and W.H. Lee, In *Eleventh North American Meeting of the Catalysis Society*, Dearborn, USA, 1989.
- [115] S.W. Ho, M. Houalla and D.M. Hercules, *Journal of Physical Chemistry*, 94 (1990) 6396.
- [116] E. Iglesia, S.L. Soled and R.A. Fiato, *Journal of Catalysis*, 137 (1992) 212.
- [117] G.L. Bezemer, J.H. Bitter, P.C.E.H. Kuipers, H. Oosterbeek, J.E. Holewijn, X. Xu, F. Kapteijn, A.J. van Dillen and K.P. de Jong, *Journal of the American Chemical Society*, 128 (2006) 3956.
- [118] G.L. Bezemer, P.B. Radstake, V. Koot, A.J. van Dillen, J.W. Geus and K.P. de Jong, *Journal of Catalysis*, 237 (2006) 291.
- [119] J.P. den Breejen, P.B. Radstake, G.L. Bezemer, J.H. Bitter, V. Froseth, A. Holmen and K.P. de Jong, *Journal of the American Chemical Society*, 131 (2009) 7197.
- [120] G. Prieto, A. Martínez, P. Concepción and R. Moreno-Tost, *Journal of Catalysis*, 266 (2009) 129.
- [121] E.I. Mabaso, E. van Steen and M. Claeys, *DGMK/SCI-Conference "Synthesis Gas Chemistry"*, 4 (2006) 93.
- [122] D. Barkhuizen, I. Mabaso, E. Viljoen, C. Welker, M. Claeys, E. van Steen and J.C.Q. Fletcher, *Pure Applied Chemistry*, 78 (2006) 1759.
- [123] V. Cheang, *Effect of crystallite size and water partial pressure on the activity and selectivity of low temperature iron-based Fischer-Tropsch catalysts*, Department of Chemical Engineering, PhD, University of Cape Town, Cape Town, 2009.
- [124] R.C. Ryan and C.U. Pittman Jr., *Journal of the American Chemical Society*, 99 (1977) 1986.
- [125] R. van Hardeveld and F. Hartog, *Surface Science*, 15 (1969) 189.
- [126] R.A. van Santen, *Accounts of Chemical Research*, 42 (2008) 57.
- [127] I.M. Ciobîca and R.A. van Santen, *The Journal of Physical Chemistry B*, 107 (2003) 3808.
- [128] J.J. Mortensen, L.B. Hansen, B. Hammer and J.K. Nørskov, *Journal of Catalysis*, 182 (1999) 479.
- [129] V. Pallassana, M. Neurock, L.B. Hansen, B. Hammer and J.K. Nørskov, *Physical Reviews B: Condensed Matter and Material Physics*, 60 (1999) 6146.

- [130] S. Dahl, A. Logadottir, R.C. Egeberg, J.H. Larsen, I. Chorkendorff, E. Tornqvist and J.K. Norskov, *Physical Reviews Letters*, 83 (1999) 1814.
- [131] I.M. Ciobica, F. Frechard, R.A. van Santen, A.W. Kleyn, and J. Hafner, *Journal of Physical Chemistry B*, 104 (2000) 3364.
- [132] J.W. Niemantsverdriet, *Applied Physics A: Materials Science & Processing*, 61 (1995) 503.
- [133] N.S. Phala, A theoretical Investigation in Heterogeneous Gold Catalysis, Department of Chemical Engineering, PhD, University of Cape Town, Cape Town, 2004.
- [134] J.W. Niemantsverdriet, *Catalysis, An Integrated Approach*, Netherlands Institute for Catalysis Research (NIOK).
- [135] E.F. Gallei, M. Hesse and E. Schwab, *Preparation of solid catalysts: development of industrial catalysts*, Wiley-VCH Verlag GmbH & Co. KGaA, Weinheim, 2008.
- [136] F. Schueth, M. Hesse and K.K. Unger, *Precipitation and coprecipitation*, Wiley-VCH Verlag GmbH & Co. KGaA., Weinheim, 2008.
- [137] J.W. Geus and J.A.R. van Veen, *Studies in Surface Science and Catalysis*, 79 (1993) 335.
- [138] E.B.M. Doesburg and J.H.V. van Hooff, *Studies in Surface Science and Catalysis*, 79 (1993) 309.
- [139] M.S. Spencer, in: M.V. Twigg, (Ed.), *Catalyst Handbook*, Wolfe Publishing Ltd. 17.
- [140] E. Marceau, X. Carrier, M. Che, O. Clause and C. Marcilly, *Ion exchange and impregnation*, Wiley-VCH Verlag GmbH & Co. KGaA., (2008) 467.
- [141] S.W. Chun, H.A. Hamilton and A.A. Montagna, 1973, Oxidative sweetening of hydrocarbons with a calcined composite of an alkali metal silicate, an iron salt, and a copper salt, USA, Patent, U.S. 481357.
- [142] P.E. Eberly, 1976, Aromatization process and catalysts, USA, Patent, U.S. 3758600.
- [143] S. Galvagno and G. Parravano, *Journal of Catalysis*, 57 (1979) 272.
- [144] Y.J. Huang and J.A. Schwarz, *Applied. Catalysis*, 32 (1987) 45.
- [145] W. Ji, S. Shen, S. Li and H. Wang, *Wuli Huaxue Xuebao*, 9 (1993) 311.
- [146] B.A. Kerns and O.A. Larson, 1969, Catalytic hydrodenitrogenation of petroleum fractions, USA, Patent, U.S. 432113.
- [147] B.S. Kwak and W.M.H. Sachtler, *Journal of Catalysis*, 141 (1993) 729.
- [148] M.G. Reichmann and A.T. Bell, *Langmuir*, 3 (1987) 563.
- [149] R.R. Soares, A. Frydman and M. Schmal, *Catalysis Today*, 16 (1993) 361.
- [150] A. Spozhakina, S. Damyanova, V. Sharkova, D. Shopov and T. Yurieva, *Heterogeneous Catalysis*, 6 (1987) 503-508.
- [151] J.H. Schulman and J.A. Friend, *Journal of Colloid Science*, 4 (1949) 497.
- [152] C. Corolleur, F.G. Gault, D. Juttard, G. Maire and J.M. Muller, *Journal of Catalysis*, 27 (1972) 466.
- [153] C. Corolleur, D. Tomanova and F.G. Gault, *Journal of Catalysis*, 24 (1972) 401.
- [154] M. Boutonnet, J. Kizling, P. Stenius and G. Maire, *Colloids and Surfaces*, 5 (1982) 209.
- [155] M. Boutonnet, S. Lögdberg and E. Elm Svensson, *Current Opinion in Colloid & Interface Science*, 13 (2008) 270.
- [156] S. Eriksson, U. Nylen, S. Rojas and M. Boutonnet, *Applied Catalysis A: General*, 265 (2004) 207.
- [157] I. Danielsson and B. Lindman, *Colloids and Surfaces*, 3 (1981) 391.

- [158] W.M. Targos, 1987, Method of making a catalyst composition comprising uniform-size metal components on a support, USA, US-4714693.
- [159] M.P. Pileni, *Journal of Physical Chemistry*, 97 (1993) 6961.
- [160] V. Uskokovic and M. Drofenik, *Surface Review and Letters*, 12 (2005) 239.
- [161] V. Uskokovic and M. Drofenik, *Advances in Colloid and Interface Science*, 133 (2007) 23.
- [162] I. Lisiecki, *Journal of Physical Chemistry*, 109 (2005) 12231.
- [163] I. Lisiecki, *Colloids and Surfaces A: Physicochemical and Engineering Aspects*, 250 (2004) 499.
- [164] P. Stenius, M. Boutonnet and J. Kizling, 1981, A liquid suspension of particles of a metal belonging to the platinum group, Sweden, Patent, EP-8102688.
- [165] U. Natarajan, K. Handique, A. Mehra, J.R. Bellare and K.C. Khilar, *Langmuir*, 12 (1996) 2670.
- [166] A. Bumajdad, J. Eastoe, M.I. Zaki, R.K. Heenan and L. Pasupulety, *Journal of Colloid and Interface Science*, 312 (2007) 68.
- [167] J. Eastoe, S. Stebbing, J. Dalton and R.K. Heenan, *Colloids and Surfaces A: Physicochemical and Engineering Aspects*, 119 (1996) 123.
- [168] M. Kishida, K. Umakoshi, J.-i. Ishiyama, H. Nagata and K. Wakabayashi, *Catalysis Today*, 29 (1996) 355.

Chapter 3

Scope of the Thesis

The Fischer-Tropsch synthesis is a catalytic surface polymerisation [1-3]. Its activity can therefore be assumed to be dependent on the available surface area of the catalytically active material. For a high cost material, as is the case with ruthenium, rhodium and even cobalt, it is therefore imperative to increase the mass specific activity by decreasing the metal crystallite size. Recent studies on the size effect of cobalt, iron, ruthenium and rhodium [4-10] however showed that with decreasing crystallite size the activity for the Fischer-Tropsch synthesis decreases and selectivity is also affected negatively. There is still disagreement on what the reasons for these performance changes are. In the published studies on cobalt most of the catalysts were not fully characterised and effects of different loadings and metal support interactions might have clouded the obtained results. To our best knowledge no study on cobalt crystallite size has been conducted focusing on the time resolved changes in activity and selectivity in the Fischer-Tropsch synthesis with thorough characterisation of the catalyst at its different stages (calcined, reduced and used).

This work aims to study the crystallite size effect of cobalt, supported on an industrially relevant carrier material, on the activity and selectivity in the Fischer-Tropsch synthesis with regard to time on stream. A special focus is put on the initial changes (first 30-50 minutes under Fischer-Tropsch conditions) of the product spectrum and its changes over time on stream in an attempt to understand crystallite size effects as function of time on stream.

The synthesis of the required model catalysts can be divided into two main parts. Firstly the development of a novel preparation technique based on the microemulsion system ([11, 12] and citations therein) to synthesise cobalt metal crystallites in the nanometer size range which are to be supported on an alumina carrier. The nature, composition, stability and reactivity of these model catalysts was characterised with several methods including electron microscopy, temperature programmed reduction (TPR), temperature programmed desorption of carbon monoxide (CO-TPD), in-situ and atmospheric powder x-ray diffraction (PXRD), atomic adsorption and Raman spectroscopy, X-ray photoelectron spectroscopy (XPS) and in-situ magnetic measurements. Most non in-situ characterisation techniques were applied at different stages of the catalyst life to obtain better understanding of the changes of the catalyst during reduction and reaction.

Secondly a cobalt carbonyl based organometallic cobalt cluster was synthesised as described in literature [13]. This complex and its decomposition products (small cobalt clusters and crystallites) offer an insight into the activity and selectivity of sub-nanometer sized cobalt ensembles in the

Fischer-Tropsch synthesis. Due to its tendency to decompose under Fischer-Tropsch conditions, the as synthesised organometallic complex as well as after immobilisation on an alumina carrier was characterised mainly by means of in-situ methods such as Fourier transform infra red spectroscopy (FTIR), powder X-ray diffraction (PXRD) and magnetic measurements.

All the synthesised model catalysts were studied in a laboratory scale fixed bed reactor at mild Fischer-Tropsch conditions for their activity and selectivity towards the various Fischer-Tropsch product classes as a function of cobalt crystallite/cluster size. A special emphasis was put on the changes with time on stream especially in the initial minutes of the Fischer-Tropsch synthesis. The mild conditions (190°C and 10 bar synthesis pressure) with conversion levels well below 10% were chosen to minimise the probability of water induced sintering of the nano-sized cobalt metal crystallites in the model crystallites [14, 15] as well as to slow down the decomposition of the cobalt carbonyl based complex [16].

University of Cape Town

References

- [1] M.E. Dry, *Catalysis Letters*, 7 (1990) 241.
- [2] H. Schulz, *Topics in Catalysis*, 26 (2003) 73.
- [3] M. Claeys and E. van Steen, *Studies in Surface Science and Catalysis*, 152 (2004) 601.
- [4] G.L. Bezemer, J.H. Bitter, P.C.E. Kuipers Herman, H. Oosterbeek, J.E. Holewijn, X. Xu, F. Kapteijn, A.J. van Dillen and K.P. de Jong, *Journal of the American Chemical Society*, 128 (2006) 3956.
- [5] J.P. den Breejen, P.B. Radstake, G.L. Bezemer, J.H. Bitter, V. Froseth, A. Holmen and K.P. de Jong, *Journal of the American Chemical Society*, 131 (2009) 7197.
- [6] G. Prieto, A. Martínez, P. Concepción and R. Moreno-Tost, *Journal of Catalysis*, 266 (2009) 129.
- [7] E.I. Mabaso, Nanosized iron crystallites for Fischer-Tropsch synthesis, Department of Chemical Engineering, PhD, University of Cape Town, Cape Town, 2005.
- [8] V. Cheang, Effect of crystallite size and water partial pressure on the activity and selectivity of low temperature iron-based Fischer-Tropsch catalysts, Department of Chemical Engineering, PhD, University of Cape Town, Cape Town, 2009.
- [9] C.A. Welker, Ruthenium based Fischer-Tropsch synthesis on crystallites and clusters of different sizes, Department of Chemical Engineering, PhD, University of Cape Town, 2007.
- [10] M. Ojeda, S. Rojas, M. Boutonnet, F.J. Pérez-Alonso, F. Javier García-García and J.L.G. Fierro, *Applied Catalysis A: General*, 274 (2004) 33.
- [11] S. Eriksson, U. Nylen, S. Rojas and M. Boutonnet, *Applied Catalysis A: General*, 265 (2004) 207.
- [12] M. Boutonnet, S. Lögdberg and E. Elm Svensson, *Current Opinion in Colloid & Interface Science*, 13 (2008) 270.
- [13] X. Lei, M. Shang, T.P. Fehlner, R. Werner, W. Haase, D. Hautot and G.J. Long, *Journal of Organometallic Chemistry*, 541 (1997) 57.
- [14] E. van Steen, M. Claeys, M.E. Dry, J. van de Loosdrecht, E.L. Viljoen and J.L. Visagie, *Journal of Physical Chemistry B*, 109 (2005) 3575.
- [15] G.L. Bezemer, T.J. Remans, A.P. van Bavel and A.I. Dugulan, *Journal of the American Chemical Society*, 132 (2010) 8540.
- [16] V.C. Calvo-Perez, A.S. Vega C, P. Cortes and E. Spodine, *Inorganica Chimica Acta*, 333 (2002) 15.

Chapter 4

Experimental Methodology

4.1 Synthesis of supported cobalt crystallites as model catalysts

To study the effects of cobalt crystallite size on the activity and selectivity in the Fischer-Tropsch synthesis a number of cobalt crystallite sizes in the nanometer range had to be synthesized and supported on an industrially relevant carrier for studies in a laboratory scale fixed bed reactor. In order to obtain average sizes between 2 and 10 nanometers with a very narrow size distribution, the w/o microemulsion technique was chosen.

The microemulsion system chosen in this study is a mixture of an organic non-polar phase (n-hexane), an anionic surfactant (penta-ethylene glycol-dodecylether, PEGDE) and an aqueous phase. The so called reverse micelles form in the oil rich area of the ternary phase diagram. The stability region of the reverse micelles and its temperature dependency was determined as part of this study (see chapter 5.1).

The reverse micelles are formed at room temperature (25°C) by mixing the oil and the surfactant in an appropriate glass vessel and stirring at room temperature for one hour. An aqueous cobalt nitrate solution is then added drop wise under stirring resulting in a clear pink solution. This solution is further stirred at 800 rpm on a magnetic stirring plate for 2 hours before it is left to rest for 12 hours. The final size of the cobalt crystallite is tuned by varying the water to surfactant ratio while keeping the oil to surfactant ratio constant. Changes of the resulting cobalt crystallite size can further be achieved by varying the cobalt nitrate concentration in the water core of the reverse micelle. The preparation of this reverse micelle solution is followed by a precipitation of the cobalt nitrate via addition of a 25 wt% ammonia solution and the deposition of the precipitate onto the alumina support (see chapter 4.1.1 for exact procedure) to obtain a cobalt loading of 5 wt% in the catalyst at its oxidic state.

To obtain well dispersed cobalt crystallites on the selected carrier material, paired with a high degree of reduction in the activation process prior to the Fischer-Tropsch synthesis, especially for very small crystallites, it is very important not to introduce strong metal support interactions in the catalyst preparation step. In the case of cobalt, as active phase, and alumina (for details see chapter 4.3), as carrier, these metal support interactions can result in the incorporation of Co^{2+} ions into the alumina matrix leading to non reducible cobalt species that do not show activity for the Fischer-Tropsch synthesis [1-3]. In an attempt to minimize this effect the point of addition of the support

during the preparation using the microemulsion technique was varied and the resulting cobalt on alumina model catalysts were characterised.

4.1.1 Variation of support addition

The addition of the support in the microemulsion technique was varied to ‘tune’ the ideal interaction of the active cobalt phase and the alumina carrier so as to allow to obtain high degrees of reduction, i.e. no formation of cobalt aluminates, while still introducing enough interaction to minimize cobalt movement/sintering during calcination, reduction and reaction. Four different methods of support addition were studied. Prior to usage the alumina support was calcined in a fluidized bed for 5 h at 450°C under air to remove water and other possible adsorbed species and then stored in an oven at 130°C. Methods A and B are presented in figure 4.1 and methods C and D are shown in figure 4.2.

Method A: The matching amount of dried alumina powder to obtain 5 wt% cobalt loading is added under stirring to the clear pink reverse micelle solution described in chapter 4.1. Contrary to the previously described ruthenium system [4] no colour change, which would indicate the direct uptake of the cobalt onto the support, was observed. Ammonia solution is added drop wise ($\text{NH}_3:\text{Co}^{2+}$ ratio of 4:1) resulting in an instant colour change from pink to light green due to the formation of cobalt hydroxide species. The cobalt hydroxide does not yet settle in the preparation vessel as it is still entrapped in the geometry of the reverse micelle. The reverse micelles encapsulating the precipitated $\text{Co}(\text{OH})_x$ are destabilised after 30 minutes of stirring via drop wise addition of acetone (volume of acetone to volume of microemulsion 1:1-2). The resulting precipitate/ Al_2O_3 mixture is washed thoroughly with acetone to remove residual surfactant. After decanting the residual acetone the solid is dried at 300 mbar at 60°C in a rotary evaporator. The dry powder is calcined in a fluidized bed under air (approximately 50 $\text{ml}_{\text{Air}}/\text{min}\cdot\text{g}$ (STP)) at 300°C for 4 hours (for schematic representation see figure 4.1).

Method B: The reverse micelle solution with the cobalt precursor is prepared as per method A. The NH_3 solution ($\text{NH}_3:\text{Co}^{2+}$ ratio of 4:1) is added drop wise, i.e. before the support addition, and the mixture is left to react for 30 minutes under stirring. As previously described the colour of the solution changes instantly from pink to light green but remains clear, indicating the formation of cobalt hydroxides in the confinement of the reverse micelles. After the 30 minutes of reaction the alumina is added followed by the drop wise addition of acetone to destabilize the reverse micelles. The resulting precipitate/ Al_2O_3 mixture is treated as described in method A (for schematic representation see figure 4.1).

Method C: The reverse micelle solution is prepared as described above and reacted with NH_3 solution. In contrast to method B the reverse micelles are destabilized via the addition of acetone without addition of alumina and the resulting $\text{Co}(\text{OH})_x$ precipitate is washed extensively with acetone. The obtained precipitate is resuspended in acetone in an ultrasonic bath and alumina (matching amount to obtain 5 wt% Co loading) is added. The mixture is heated to 50°C in an ultrasonic bath and dried under N_2 flow. The dry powder is calcined in a fluidized bed in air (approximately 50 $\text{ml}_{\text{Air}}/\text{min}\cdot\text{g}$ (STP)) at 300°C for 4 hours (for schematic representation see figure 4.2).

Method D: As described in method C the $\text{Co}(\text{OH})_x$ precipitate is formed and washed extensively. It is dried at 130°C in air for 12 hours followed by a calcination at 200°C in air for 5 hours. The obtained Co_3O_4 particles are resuspended in water under ultrasonication. Al_3O_4 is added to the slurry

and the mixture is dried at 200 mbar and 80°C in a rotary evaporator (for schematic representation see figure 4.2).

4.1.2 Variation of precipitation agents

The role of the precipitation agent was also investigated, by replacing the ammonia solution in method A described in chapter 4.1.1 with alternative precipitation agents:

- Gaseous NH_3 is bubbled through the microemulsion. To obtain a good mixture the gas is feed through a 0.5 μm frit positioned next to the stirrer in the solution.
- Hydrazine (N_2H_4) hydrate is added drop wise to the reverse micelle/alumina slurry until a colour change/precipitation is observed.

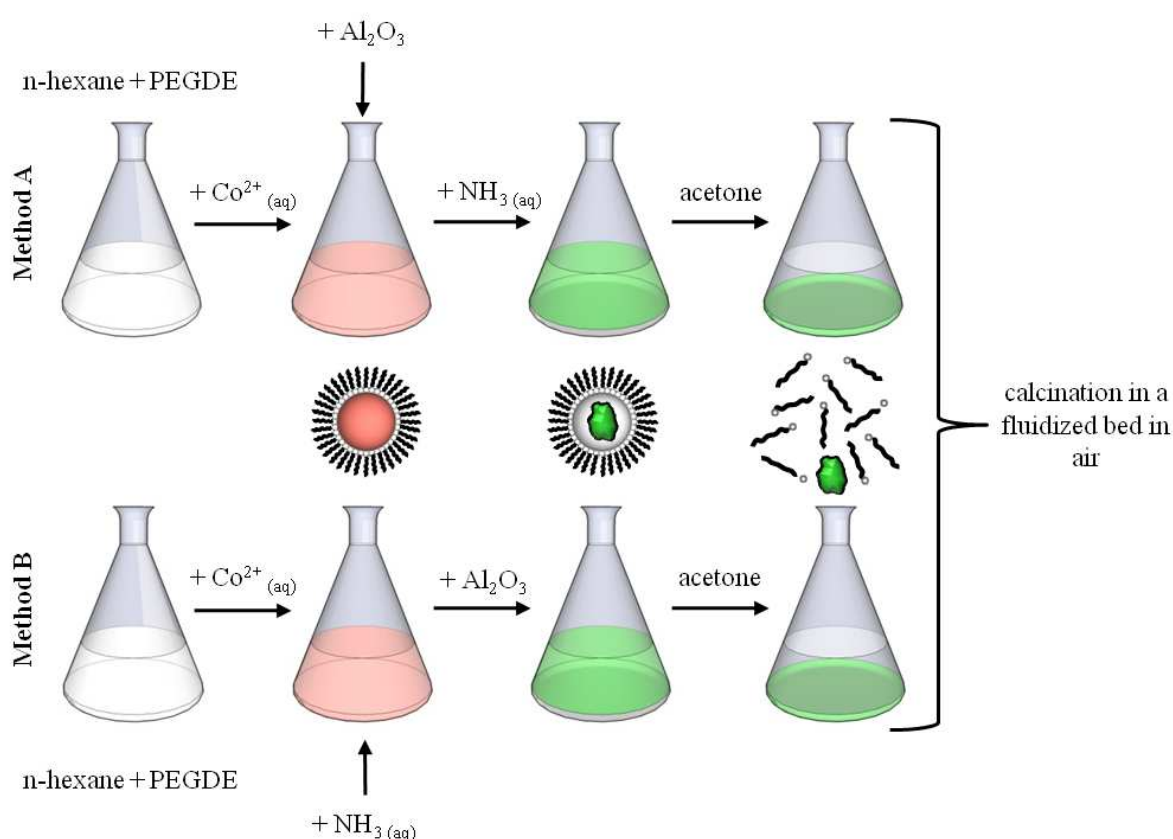


Figure 4.1: Schematic representation of catalyst preparation methods A & B.

4.1.3 Composition of the microemulsion

To target specific sizes of the final cobalt crystallites the sizes of the reverse micelles acting as templates/nano-reactors [5, 6] have to be 'tuned'. The sizes of the reverse micelles are strongly dependent on the composition of the microemulsion [7-10]. With an increasing mass ratio of the aqueous to the surfactant phase, also referred to as water to surfactant ratio or ω , the size of the reverse micelle, i.e. the water droplet diameter stabilized by the surfactant layer, increases and therefore the resulting crystallite size is reported to increase as well [8, 9, 11, 12]. As PEGDE is suspected to also dissolve partially in the organic phase, n-hexane in this work, the ratio of surfactant

to organic phase is kept constant for all experiments. In order to achieve very small cobalt crystallites the Co^{2+} concentration in the reverse micelles is also varied (see table 4.1 and figure 4.3). The total amount of cobalt in the microemulsions is kept constant. In table 4.1 the compositions of the reverse micelles for the preparation of the model catalysts with the selected preparation method D (see chapter 5) are given. The naming of the samples relates to the obtained volume weighted mean Co_3O_4 crystallite size (obtained from TEM analysis) in the calcined and supported state.

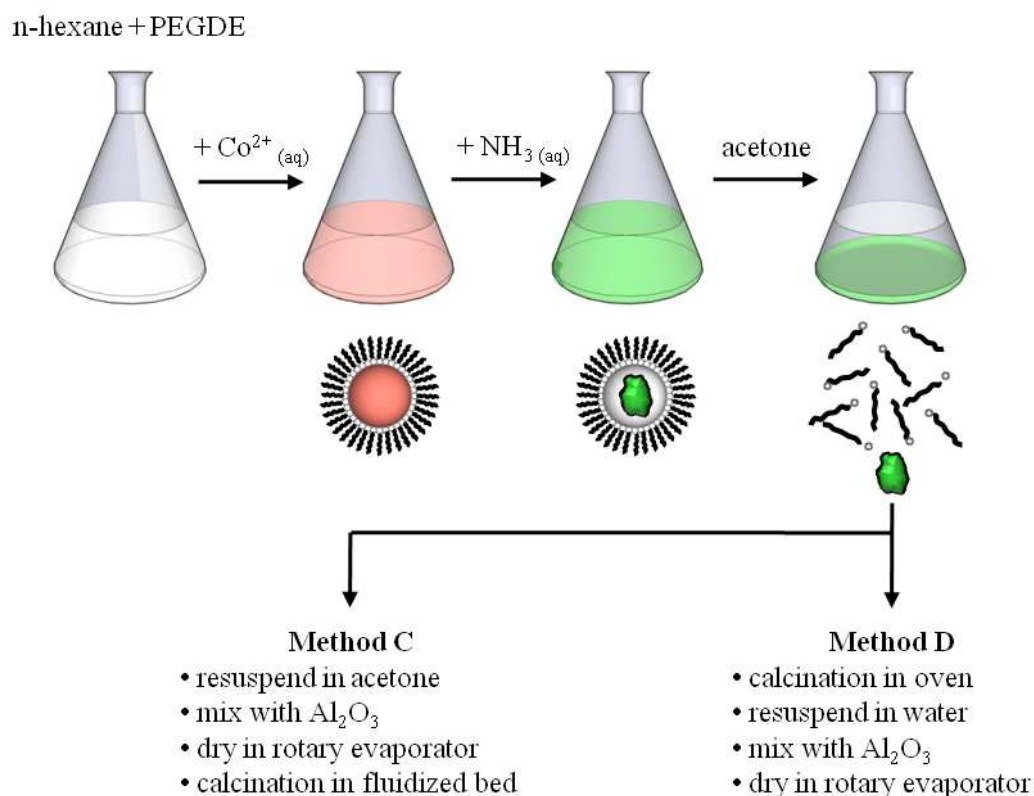


Figure 4.2: Schematic representation of catalyst preparation methods C & D.

Table 4.1: Composition of the microemulsions used to obtain nano-sized supported cobalt crystallites.

Catalyst	Hexane (g)	PEGDE (g)	Co-Sol. ^a (g)	Conc. ^b (mol/l)
CAT 9.6	500	68.4	29.24	0.15
CAT 8.6	1000	136.7	41.80	0.11
CAT 7.3	500	68.4	28.97	0.33
CAT 6.8	500	68.4	14.49	0.32
CAT 5.9	2000	273.6	14.46	0.32
CAT 4.8	1000	136.7	6.24	0.85
CAT 4.4	2000	273.6	55.50	0.08
CAT 4.0	500	68.4	7.62	0.67
CAT 3.1	4000	547.2	28.14	0.16

^a Aqueous cobalt solution.

^b Concentration of $\text{Co}(\text{NO}_3)_2 \cdot 6\text{H}_2\text{O}$ in the aqueous cobalt solution.

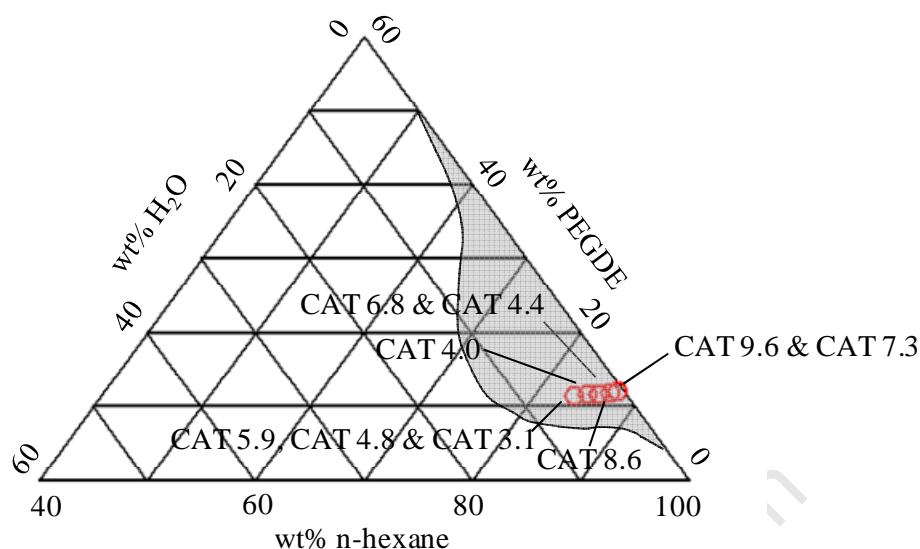


Figure 4.3: Ternary phase diagram of microemulsion system with compositions of synthesised reverse micelles. Stability region for reverse micelles at 25°C shaded.

4.2 Synthesis of organometallic cluster $(\text{CO})_9\text{Co}_3\text{CCOOH}$

To study the crystallite size effect on the activity and selectivity of the Fischer-Tropsch synthesis in the sub two nanometer size range an organometallic cobalt cluster with three adjacent cobalt atoms ($(\text{CO})_9\text{Co}_3\text{CCOOH}$) was synthesised for testing under Fischer-Tropsch conditions. The cobalt carbonyl based cluster was synthesised as described by Lei and co-workers [13].

Dicobaltoctacarbonyl (3 g) is dissolved in 15 ml of tetrahydrofuran (THF) under a nitrogen atmosphere. Ethyl-trichloro-ethanoate (CCl_3COOEt) (1.1 ml) is added drop wise to the mixture under stirring and N_2 flow. The solution is then slowly heated under stirring and N_2 flow to 45°C and held for 4 hours. After cooling down the organic solution is washed three times with 10% v/v HCl. The aqueous phase is kept while the organic phase is discarded. The aqueous layer is then washed three times with diethyl-ether and the resulting organic phase a further three times with water. To the organic phase 0.2 ml of acetic acid is added drop wise and the solution is left to dry over MgSO_4 for 8 hours. The solution is filtered through kieselguhr and the solvent removed under vacuum in a rotary evaporator resulting in purple crystals. These crystals are mixed with concentrated H_2SO_4 (20 ml) and stirred for 20 hours resulting in a brown solution. The brown solution is poured over crushed ice forming a brown powder. The water slurry is then extracted with dichloromethane and the organic layer washed with water until the aqueous layer becomes colourless. Then 0.5 ml of acetic acid is added to the organic phase which is subsequently dried over MgSO_4 for 8 hours. The mixture is filtered through kieselguhr and the solvent removed under reduced pressure resulting in black crystals. The obtained product was dried over night under vacuum to remove residual solvents and/or reagents.

The cobalt complex was immobilised by supporting it on the same alumina which was used in the synthesis of the nano-sized cobalt crystallites (see chapter 4.3). The organometallic compound is dissolved in acetone and mixed with the appropriate amount of alumina support to achieve a cobalt

loading of 3 wt%. Experimental results show, that the model catalysts prepared via the microemulsion technique do also show a cobalt loading of approximately 3 wt% (see chapter 6.1) due to losses in the multi step preparation procedure, and not the originally targeted 5 wt% (see chapter 4.1.1). The slurry is mixed under ultrasonication and dried slowly at 30°C under N₂ flow. The resulting powder is further dried under vacuum to remove residual acetone for 5 minutes. The supported complex seems to undergo decomposition relatively fast judging from the rapid colour change from black to grey (10-20 minutes in air at room temperature). The complex alone seems to be very stable in air at 4°C. Therefore the deposition of the complex onto the support is carried out directly before each experiment.

4.3 Support material Al₂O₃

Alumina (Puralox (Batch 9574), SCCa 5-150, Sasol Germany, $S_{\text{BET}} = 162\text{m}^2/\text{g}$, $V_{\text{pore}} = 0.47\text{ cm}^3/\text{g}$, $\bar{d}_{\text{pore}} = 11.5\text{ nm}$, particle size: 150-200 μm) was used as support material for the nano-sized cobalt crystallites as well as for the organometallic cobalt cluster.

4.4 Characterisation of the w/o microemulsion system

From previous studies [4, 11, 14], utilising the same microemulsion system, the approximate stability region of the reverse micelles in the ternary phase diagram was known. Using this as a starting point, the stability region of the reverse micelles was further investigated at different temperatures. The sizes of these micelles were also determined.

4.4.1 Determination of the influence of temperature on the stability region of the reverse micelle

Over 100 mixtures of n-hexane, surfactant and water were prepared (for exact compositions see appendix A1) starting from the region in the ternary phase diagram which is known to yield stable reverse micelles. These mixtures were equilibrated in a temperature controlled bath at 10, 25 and 40°C for 12 hours. Afterwards the stability was evaluated by visual inspection. Stable reverse micelles show a clear liquid without any phase separation or cloudiness. The stability region could be determined from these observations.

4.4.2 Measurement of the size of the reverse micelles

A selected number of microemulsions (for exact compositions see chapter 5.2) in the previously determined stability region of the reverse micelle were analysed using a Zetasizer Nano ZS (Malvern Instruments) based on dynamic light scattering. Dynamic light scattering measures the intensity fluctuations of the light reflected off the particles in solution, due to Brownian motion, and relates this to the size of the particles via the Stokes-Einstein equation [15]. The microemulsions are measured in a quartz cuvette at a constant temperature.

For the measurement of the size of the reverse micelle the absorption coefficient of the liquid (0 for clear samples as specified by the supplier), the refractive indices of n-hexane (1.38) and PEGDE (1.45) and the viscosity of the measured solution was required. The viscosity of the samples was measured in a Brookfield LVDV-I+ viscometer. The sample chamber for the viscosity measurements could be temperature controlled in order to avoid phase separation due to temperature effects.

4.5 Characterisation of supported cobalt crystallites

All synthesised model catalysts were extensively characterised using temperature programmed techniques viz. temperature programmed reduction (TPR), determination of the degree of reduction (DOR) and temperature programmed desorption (TPD), in-situ techniques including in-situ powder X-ray diffraction (in-situ PXRD) and magnetic measurements, ex-situ techniques including transmission electron microscopy (TEM), powder X-ray diffraction (PXRD) all applied at the different stages of the catalyst life and other spectroscopic techniques, i.e. atomic absorption spectroscopy (AAS), Raman spectroscopy and X-ray photoelectron spectroscopy (XPS).

4.5.1 Transmission electron microscopy (TEM)

The size distributions of the synthesised cobalt crystallites on the alumina support were determined using various transmission electron microscopes (TEM). These studies were conducted with the calcined, freshly reduced and with spent (after exposure to Fischer-Tropsch conditions for 25 hours) catalysts. The latter two sets of samples were passivated in flowing CO₂ at room temperature for 1 hour after the corresponding treatment/reaction step. Besides the size distribution, the shape and the dispersion of the cobalt crystallites on the support can be obtained by TEM studies.

For the determination of the size distributions a LEO 912 transmission electron microscope operated at 120 kV was used. The samples for this microscope were prepared using the resin method. A very small amount of powder sample is placed in a plastic vial which is filled with liquid resin. The mixture is stirred to remove all air bubbles between the catalyst particles. The resin was allowed to solidify at 60°C for 24 hours. The resulting solid sample was cut with glass knives to 0.1 µm slices using an Ultramicrotome Leica UltracutS machine. These slices were transferred onto copper grids for viewing in the TEM.

To gain information on the cobalt species and for better understanding of the particle geometry selected catalysts were further studied under a high resolution TEM (HRTEM) equipped with a field emission gun as electron source (FEI Technai F20) operated at 200 kV. This microscope also allowed studies in scanning transmission electron microscopy (STEM) mode and energy dispersive X-ray spectroscopy (EDX) for identification of the cobalt species on the support. The samples for the studies in the HRTEM were prepared by re-dispersing a small amount of catalyst in ethanol in an ultrasonic bath for 15 minutes. A drop of 2 µl is taken from the top layer of the liquid and placed on a holey carbon copper grid. After drying in a desiccator for 12 hours the grids were ready for viewing in the HRTEM.

All micrographs were analysed using the freeware IMAGEJ. For the crystallite size distributions a minimum of 300 crystallites per sample were measured to obtain representative cobalt size

distributions. The crystal lattices measured with the HRTEM were compared to lattice parameters listed in the International Centre for Diffraction Data PDF-2 database. The crystallite size distributions are calculated as number based (percentage of crystallites with one size of all measured crystallites) and volume based (percentage of crystallites with one volume; assuming spherical crystallites; of the total volume of all measured crystallites).

4.5.2 Powder X-ray diffraction (PXRD)

Powder X-ray diffraction patterns of the calcined, reduced and passivated and the spent (after exposure to Fischer-Tropsch conditions for 25 hours) catalysts were measured in a Bruker D8 Advance laboratory X-ray diffractometer equipped with a cobalt source ($\lambda = 1.78897 \text{ \AA}$) and a position sensitive detector (Bruker Vantec). For all samples the optics were set to parallel beam geometry so as to counteract possible peak shifts due to sample height difference (sample displacement). The scan range was 20 to 130° 2 θ (step size: 0.01151626°, time per step: 0.75 s, scan time: 2 hours 2.75 minutes).

All diffraction patterns were compared to known diffraction patterns from the International Centre for Diffraction Data PDF-2 database to determine the present species. To further identify phases and to obtain the average crystallite size Rietveld refinement utilising the programme Topas 4.2 was carried out. As the alumina support material used in this study is known to be present as a mixed phase of γ -Al₂O₃ and δ -Al₂O₃ and the crystal structure of δ -Al₂O₃ is not known at this stage, a novel approach for partial or not known crystal structures (PONKCS), first described by Scarlett and Madsen [16], was used. For this, firstly the pure alumina was measured under the chosen conditions. This scan was fitted in Topas as a plain peaks phase. Secondly a known mixture of 95 wt% alumina and 5 wt% yttrium oxide (Y₂O₃), calcined at 1200°C for four days to remove all strain in the crystallite before use, was measured under the same conditions. This scan was fitted with the known crystal phase of Y₂O₃ and the previously generated peaks phase for the alumina. In order to obtain a quantitative result from the scan, the factor ZMV (Z = number of units in a unit cell; M = molecular mass for formula unit; V = unit cell volume) utilised in the Topas calculation routine has to be manually adjusted until the right composition of 95% Al₂O₃ and 5% Y₂O₃ is obtained. This product of Z, M and V is specific for every species and once set it does not change. By modifying/adjusting this ZMV factor for the alumina peaks phase it loses all physical meaning but allows us to use it in combination with known crystallite phases for Rietveld refinement on the synthesised samples. For the investigated samples all possible crystalline cobalt species are allowed in the refinement, these are Co₃O₄ and CoO calcined state Co (fcc), Co (hcp), Co₃O₄ and CoO and in the reduced and spent state.

4.5.3 Atomic absorption spectroscopy (AAS)

To measure the achieved cobalt loading in the freshly synthesised and calcined samples atomic absorption spectroscopy was carried out using a Varian SpectraAA 110 instrument. For the sample preparation 50 mg of calcined catalyst was mixed with 10 ml of a 4:1 HCl/HF mixture and heated to boiling. At this stage 10 ml HNO₃ was added and the flask further heated to reduce the liquid volume to approximately 2 ml. A further 5 ml of HClO₄ was added and the volume reduced again to 2 ml under heating. A white cloud formed indicating that the reaction had taken place. The residual clear

solution was cooled down and then transferred into a 100 ml volumetric flask which was topped up with distilled water. The solution was then filtered through a Whatman No. 1 filter paper and sent for measurement in the AAS instrument. From the obtained cobalt concentration the loading on the catalyst can be calculated using equation 4.1.

$$L = \frac{x \cdot 10}{m} \quad (4.1)$$

With L being the loading in wt%, x the concentration of cobalt obtained from the AAS measurement in mg/l and m the mass of catalyst digested in mg.

4.5.4 Raman spectroscopy

With Raman spectroscopy the cobalt oxide species present in the calcined samples can be determined. The measurements were carried out in a combined FT-IR/Raman instrument (Thermo Scientific Nicolet 5700). To avoid sample heating of the dark coloured samples, a small amount was mixed with pure KBr and milled in an agate mortar. From the resulting light grey powder a tablet was pressed which was then studied in the Raman spectrometer. The obtained scans were compared to scans previously reported in literature for similar systems.

4.5.5 X-ray photoelectron spectroscopy (XPS)

The oxidation state of the cobalt oxide species in the calcined catalysts was studied using X-ray photoelectron spectroscopy. The studied powders were mounted on sticky carbon tape prior to insertion into the ultra high vacuum (UHV) chamber. The obtained binding energies were corrected using the carbon 1s signal as reference. The Co 2p_{3/2} signal was then compared to signals for Co(OH)₂, CoO(OH) and Co₃O₄ [17] as reported in literature and deconvoluted and fitted according to the reported peak positions.

4.5.6 Temperature programmed reduction (TPR)

The reduction behaviour of the synthesised model catalysts was studied by means of temperature programmed reduction (TPR) in a Micromeritics AutoChem 2950. An amount of 100 mg of sample was loaded into a quartz reactor tube and dried in argon at 120°C for two hours to remove excess water. The sample was cooled down to 60°C and then heated in 50 ml/min (STP) 5% H₂ in Ar mixture at a 10°C/min temperature ramp to 950°C or 1000°C. A thermal conductivity detector (TCD) measures the difference in thermal conductivity between the pure 5% H₂ in Ar and the exhaust gas of the reactor. From this measurement the hydrogen uptake due to cobalt oxide reduction can be measured as function of temperature. The TCD signal is calibrated by running a TPR of a known amount of pure Ag₂O and correlating the resulting peak area to the stoichiometrically required amount of H₂ for the complete reduction to metallic silver.

In order to get a better understanding of the surface of the catalysts during the reduction a Pfeiffer Omnistar GSD 300 mass spectrometer was attached to the exhaust gas stream to monitor the

formation of CH₄ ($m/z = 15$), CO₂ ($m/z = 44$) and CO ($m/z = 28$) due to the decomposition of residual surfactant during the reduction process. The overlapping of the $m/z = 28$ due to its presence in the pure CO₂ spectrum was accounted for by measuring the ratio of m/z 44:28 for pure CO₂ and correcting the experimental reading for this value.

4.5.7 Degree of reduction (DOR)

The degree of reduction (DOR) defined as the percentage of metallic cobalt present after a reduction relative to the total cobalt loading was measured using the same experimental set up described for the TPR measurements (see chapter 4.5.6). An amount of 100 mg catalyst was first exposed to its specific reduction condition (see table 4.2) under 40 ml/min (STP) H₂ and then further heated in 50 ml/min (STP) of the 5% H₂ in Ar mixture at a heating rate of 10°C/min to 950°C. The area of the TCD spectra measured during this ramping correlates to the amount of cobalt not reduced into the metallic form during the corresponding reduction procedure. The respective reduction procedure or reduction temperature respectively (see table 4.2), was chosen based on the slightly different peak positions in the TPR measurements. (see chapter 6.5). The ratio of the TCD spectra of the TPR measurement to the one of the DOR measurement equals the degree of reduction in each sample.

Table 4.2: Reduction conditions for supported nano-sized cobalt model catalysts.

Sample	Red. Temp (°C)	Hold. Time (h)	Ramp Rate (°C/min)
CAT 9.6; CAT 8.6; Cat 7.3; CAT 6.8; CAT 4.0	450	6	1
CAT 5.9; CAT 4.8; CAT 4.4; CAT 3.1	375	6	1

4.5.8 Temperature programmed desorption (TPD)

To study the interaction of the cobalt crystallite surfaces of different crystallite sizes with carbon monoxide (CO) temperature programmed desorption (TPD) studies were carried out. For this a Micromeritic AutoChem 2910 was connected with a Pfeiffer Omnistar GSD 300 mass spectrometer (MS). An amount of 500 mg of catalyst was reduced as specified in table 4.1. After the reduction the sample was flushed with 10 ml/min (STP) He and cooled down to 0°C. At 0°C it was exposed to one pulse of 1 ml CO in the helium stream followed by further 6 hours of flushing in He. The sample was then ramped in helium to 950°C at 10°C/min and held for 3 hours before being cooled down to 60°C at 10°C/min. During the heating up period the desorption of different species was monitored with the TCD and the MS detector (monitored masses H₂ $m/z = 2$; CH₄ $m/z = 15$; H₂O $m/z = 18$; CO $m/z = 28$; CO₂ $m/z = 44$). The overlapping of $m/z = 28$ due to CO and CO₂ in the MS-spectra was corrected as described in chapter 4.5.6.

After the cooling down to 60°C the sample was reheated to 950°C at 10°C/min and held for 3 hours under the flow of 5.1% O₂ in He to monitor the formation of carbon oxides from possible surface carbon depositions formed during the reaction of carbon monoxide to carbon dioxide. This allowed closing the carbon balance over the complete experiment.

4.5.9 In-situ powder X-ray diffraction (in-situ PXRD)

In-situ PXRD measurements were carried out in a XRK-900 reaction chamber (Anton-Paar, Austria) attached to laboratory XRD described above (see chapter 4.5.2). Samples were heated under different reaction gases (with gas flow through the catalyst sample) at the desired heating ramps and temperature holding steps were introduced in regular intervals to allow the collection of a diffraction pattern. To minimise effects of phase changes during a scan the scan time was kept very short and the scan range decreased to 40 to 95° 2 Θ (step size: 0.01151626°, time per step: 0.2 s, scan time: 16.5 minutes). The analysis of the obtained diffraction patterns was conducted as described in chapter 4.5.2.

4.5.10 Magnetic Measurements

The measurement of the total magnetisation of a catalyst sample can give insight into the catalyst composition and it can also provide information on the crystallite sizes and size changes of the magnetic phases. Three different types of magnetism are relevant for the material in this study: ferromagnetism, antiferromagnetism and superparamagnetism (see also table 4.3).

Ferromagnetic materials are attracted by an external magnetic field (H) via the alignment of the spins of the electrons and do retain a level of magnetism (remnant magnetisation M_{rem}) upon removal of the external field [18, 19]. Above the material specific Curie temperature (T_C) the thermal energy is too high to allow an alignment of the spins in an external field and no magnetism can be measured.

Antiferromagnetism [18, 19] is very similar in its physical nature to ferromagnetism with the difference that the interaction with the external field results from an anti-alignment of neighbouring spins. Antiferromagnetic material also does not show remnant magnetisation and loses its magnetic properties above the material specific Néel temperature (T_N).

Below a certain crystallite size ferromagnetic material changes its behaviour and becomes superparamagnetic. For cobalt this exact size is still under debate. At room temperature it has been reported to be in the range of 10-16 nm [20, 21]; theoretical studies have determined this critical diameter for hcp cobalt as being 8 nm and 28 nm for fcc cobalt [22]. In the case of superparamagnetism all crystallites behave like dipoles and their magnetic moments align in presence of an external magnetic field, but they return to random orientation upon the removal of this field. The strength of the field required to align superparamagnetic crystallites is strongly dependent on the crystallite size, requiring higher field strengths for smaller crystallites. The magnetisation at which the magnetic moments of all crystallites are aligned with the external field is called saturation magnetisation (M_s). Plotting the magnetisation of a completely superparamagnetic sample as a function of the field strength of an external magnetic field (H) (see figure 4.4) shows that at a lower external field strengths the magnetisation is mainly caused by larger crystallites while at a high external field the magnetisation is governed by the magnetisation of the smallest crystallites. Therefore from this conclusions regarding the crystallite sizes in the studied samples can be drawn. Dalmon [23] reports the relationship between crystallite size and relative magnetisation, i.e. magnetisation over saturation magnetisation, to follow a temperature dependent Langevin function behaviour and gives equation 4.2 to describe this behaviour for distinct crystallite sizes and temperatures. From comparison of experimental values and theoretical values for a number of

crystallite sizes (or via superimposing a number of Langevin equations [23]) a crystallite size distribution of the studied sample can be developed.

$$\frac{M}{M_s} = \coth\left(\frac{\rho \cdot \sigma_s \frac{\pi}{6} \cdot d^3 \cdot H}{k \cdot T}\right) - \frac{k \cdot T}{\rho \cdot \sigma_s \frac{\pi}{6} \cdot d^3 \cdot H} \quad (4.2)$$

Where $\frac{M}{M_s}$ is the ratio of sample magnetisation relative to the saturation magnetisation, ρ is the density of the magnetic material, d is the crystallite diameter of the crystallites of the magnetic material and H is the external field, σ_s is the mass specific saturation magnetisation of the magnetic material (for cobalt 168 emug^{-1} [24]). The saturation magnetisation is commonly accepted to be size independent [25].

For not purely superparamagnetic samples the so called Weil method [26] (see figure 4.5) can be employed in order to obtain crystallite size related information. The Weil method utilises the strictly temperature/crystallite size dependent ability to retain remnant magnetisation after the removal of the external magnetic field. At 0 K all crystallites show remnant magnetisation. Upon an increase in temperature first the smallest crystallites start losing their remnant magnetisation due to the increased thermal energy. By simply measuring the remnant magnetisation from very low temperatures on, one can draw conclusions on the crystallite sizes present in the studied sample.

Due to the difference in magnetic properties of the cobalt species (see table 4.3) and the resulting fact that at temperatures higher than 13°C (Néel temperature of CoO) [18] the only magnetic species is metallic cobalt it is possible to measure the degree of reduction in-situ by measuring the total magnetisation of the studied sample. By further measuring the remnant magnetisation it is possible to determine whether the crystallite size increases during the measurements. The percentage of ferromagnetic material (in wt%) can be calculated as being [20, 21, 23]

$$\gamma = \frac{2 \cdot M_{rem}}{M_s} \quad (4.3)$$

Where γ is the percentage of ferromagnetic material, M_{rem} the remnant magnetisation and M_s the saturation magnetisation.

All magnetic measurements were conducted in a novel magnetometer [27] (for further details see chapter 4.8) developed at the University of Cape Town for in-situ measurements under realistic Fischer-Tropsch conditions (up to 50 bar and 500°C). The magnetometer was calibrated with known amounts of metallic cobalt powder (see appendix A2).

Table 4.3: Magnetic properties of bulk cobalt species.

Compound	Magnetism	Curie/ Néel temperatures (K)
Co (metallic)	ferromagnetic	1403 [19]
CoO	antiferromagnetic	291 [18]
Co ₃ O ₄	antiferromagnetic	32 [28]

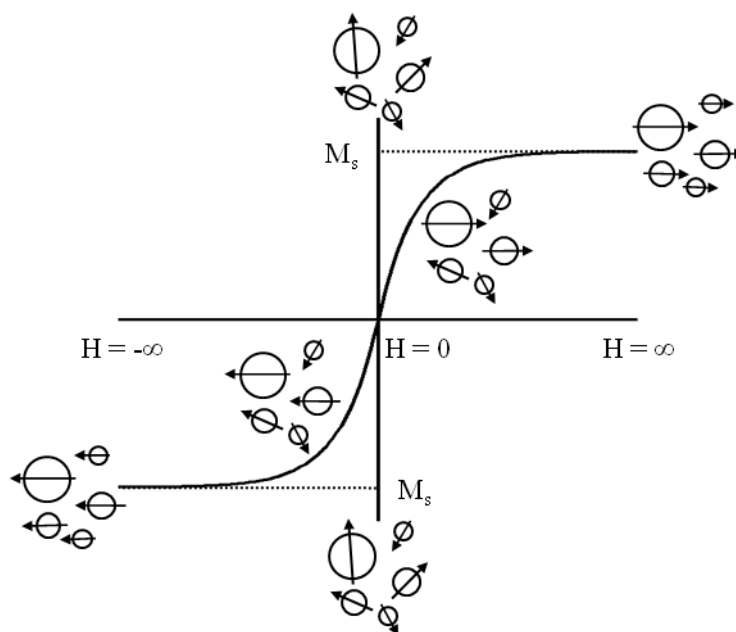


Figure 4.4: Schematic representation of the behaviour of superparamagnetic particles in an external magnetic field (adapted from [23])

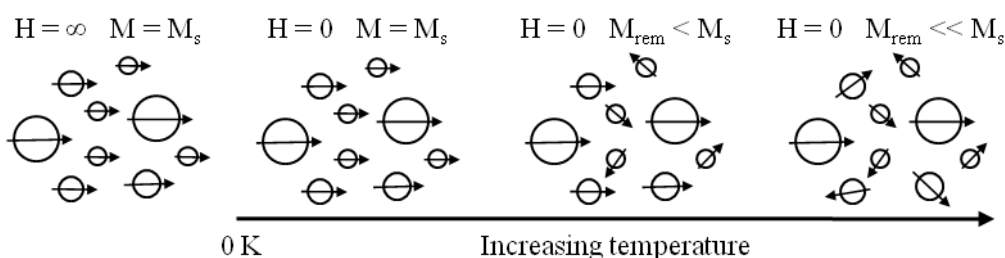


Figure 4.5: Schematic representation of the temperature/crystallite size dependency of remnant magnetisation (adapted from [23]).

4.6 Characterisation of organometallic cluster (CO)₉Co₃CCOOH

Cobalt carbonyl clusters and their derivatives are known to decompose in air at moderate temperatures. Therefore, mostly in-situ techniques were applied to characterise the synthesised complex and its decomposition. This includes magnetic measurements, in-situ powder X-ray diffraction (PXRD) and in-situ Fourier transform infrared spectroscopy (FTIR). The pure complex (not supported) was also analysed with mass spectroscopy, elemental analysis and diffuse reflectance infrared Fourier transform spectroscopy (DRIFTS).

4.6.1 Mass spectroscopy (MS)

The unsupported cobalt cluster was analysed in a JEOL JMS-GCMS-GCMAT II GCMS instrument. The obtained mass fractions were compared to the theoretical calculated mass fractions of the complex.

4.6.2 Elemental analysis

The mass ratio of C:O:H was determined for the unsupported cobalt cluster using an Elemental Analyser CHNS-O (Thermo). The obtained ratio was compared to the theoretical ratio calculated for the cobalt complex.

4.6.3 Diffuse reflectance infrared Fourier transform spectroscopy (DRIFTS)

Diffuse reflectance fourier transform spectroscopy (DRIFTS) was conducted in a Thermo Scientific Nicolet 5700 combined FT-IR/Raman instrument. The pure cobalt complex was placed into a sample pan. The background was taken against a polished gold mirror. The sample was scanned 200 times at a resolution of 4 cm^{-1} .

4.6.4 In-situ powder X-ray diffraction (in-situ PXRD)

The supported cobalt complex was placed in the in-situ chamber (see chapter 4.5.2 and 4.5.9) and exposed to a synthesis gas flow of 30 ml/min (STP), with a $\text{H}_2:\text{CO}$ ratio of 2:1 at atmospheric pressure. The temperature was ramped at $2^\circ\text{C}/\text{min}$ from 40°C to 600°C . PXRD spectra from 40 to $95^\circ 2\theta$ (step size: 0.01151626° , time per step: 0.2 s, scan time: 16.5 minutes) were taken at 25°C intervals; the temperature ramp was halted during the scans. The analysis of the obtained diffraction patterns was conducted as described in chapter 4.5.2.

4.6.5 In-situ Fourier transform infrared spectroscopy (FTIR)

The decomposition of $(\text{CO})_9\text{Co}_3\text{CCOOH}$ was studied in different gas environments as function of temperature by means of in-situ Fourier transform infrared spectroscopy on a Thermo Scientific Nicolet 5700 combined FT-IR/Raman instrument. This instrument is equipped with an in-situ chamber with water cooling, and can be used to heat samples up to 900°C under flow (over the sample) of different gases at atmospheric and elevated pressures ($< 10\text{ bar}$).

$(\text{CO})_9\text{Co}_3\text{CCOOH}$ was supported on alumina (as described in chapter 4.2) and placed in the in-situ cell. The sample was heated at $1^\circ\text{C}/\text{min}$ to 375°C at 6 bar and FTIR scans were continuously taken at a resolution of 8 cm^{-1} . This experiment was carried out under a 40 ml/min (STP) flow of N_2 and repeated under the same conditions but with hydrogen flow to study the difference between a reductive/reactive and an inert atmosphere. The pronounced carbonyl stretching frequencies at a wavenumber around 2000 cm^{-1} were used as an indicator of the state of the complex on the support..

4.6.6 Magnetic measurements

The decomposition of the organometallic cobalt complex was studied in the in-situ magnetometer (see chapter 4.5.10 and 4.8). The supported cobalt complex was placed in the reactor and exposed to the same conditions chosen for the Fischer-Tropsch experiments, i.e. $PP_{\text{syn.gas}} = 9.9$ bar, $SV = 7.2$ $\text{ml}_{\text{syn.gas}}/\text{g}_{\text{catalyst}} \cdot \text{min}$, $H_2/CO = 2$ (see chapter 4.7.3 & 4). The temperature was ramped at $2^\circ\text{C}/\text{min}$ from 40°C to 400°C . The magnetisation at 20 kOe and the remnant magnetisation at 0 kOe was measured at 10°C intervals, i.e. every 5 minutes. The measured signal was corrected for the signal obtained with the empty reactor under the same conditions.

4.7. Fischer-Tropsch synthesis experiments

4.7.1 Test unit set-up

Figure 4.6 shows a schematic set-up of the reactor used for Fischer-Tropsch testing. During reaction a synthesis gas mixture (60 mol% H_2 , 30 mol% CO and 10 mol% Ar) is fed via the mass flow controller 1 (MFC 1) (Brooks Instruments) into the reactor. The pressure in the rig is controlled by a continuous flow of argon which is controlled via the pressure regulator 4 (PR 4) and the needle valve (NV) prior to the reaction start; the total flow is set to a flow rate slightly higher than that of the synthesis gas mixture. Through the NV the pressure is reduced to atmospheric. After the pressure drop a constant stream of reference gas (0.015 mol% cyclohexane in N_2 mixture) is added with MFC 4 and its organic component (cyclohexane) is used as an internal standard for the off-line gas chromatograph which is equipped with a flame ionisation detector (GC-FID). Via the four way valve (4WV) the reactor (see chapter 4.7.2) can either be fed with inert argon or with the synthesis gas mixture. Due to the very low conversions no hot or cold trap to collect liquid products was needed. All lines downstream of the reactor were kept at 200°C while the reaction temperature was chosen to be 190°C .

4.7.2 Reactor set-up

A $1/4''$ stainless steel U-tube (ID = 3.8 mm) was used as a reactor (see figure 4.7). Two different ways of heating the reactor were employed. For the supported cobalt crystallites, which required a thermal treatment in H_2 for activation prior to the Fischer-Tropsch reaction, an insulated aluminium block with two heating cartridges and a centrally located thermocouple could be placed around the reactor. This allows slow and very controlled temperature ramping as required for the reduction process (see table 4.2). In the case of the supported cobalt complex no pre-treatment was required and the reactor had to be brought to reaction temperature as quickly as possible in order to avoid changes of the catalyst/complex structure during the heating up phase and prior to the actual Fischer-Tropsch reaction. Therefore in these cases the reactor was dipped into a pre-heated oil bath at 190°C on a stirring plate, this time defined the start of the Fischer-Tropsch experiment. This guaranteed the fastest possible heating rate and therefore minimised effects of complex decomposition during a slow heat up procedure. By applying this method the reaction temperature was reached within 30 seconds.

For both modes of heating the isothermal zone (i.e. $\pm 1^\circ\text{C}$), as determined by a previous study [11], allowed a loading of 1 g of catalyst. The outlet of the reactor was tightly packed with silane treated glass wool to avoid catalyst being carried out of the reactor into the downstream lines. The inlet is filled with silicon carbide (mesh size = 200-250 μm) which acts as a gas pre-heating zone and which is again topped with a plug of silane treated glass wool.

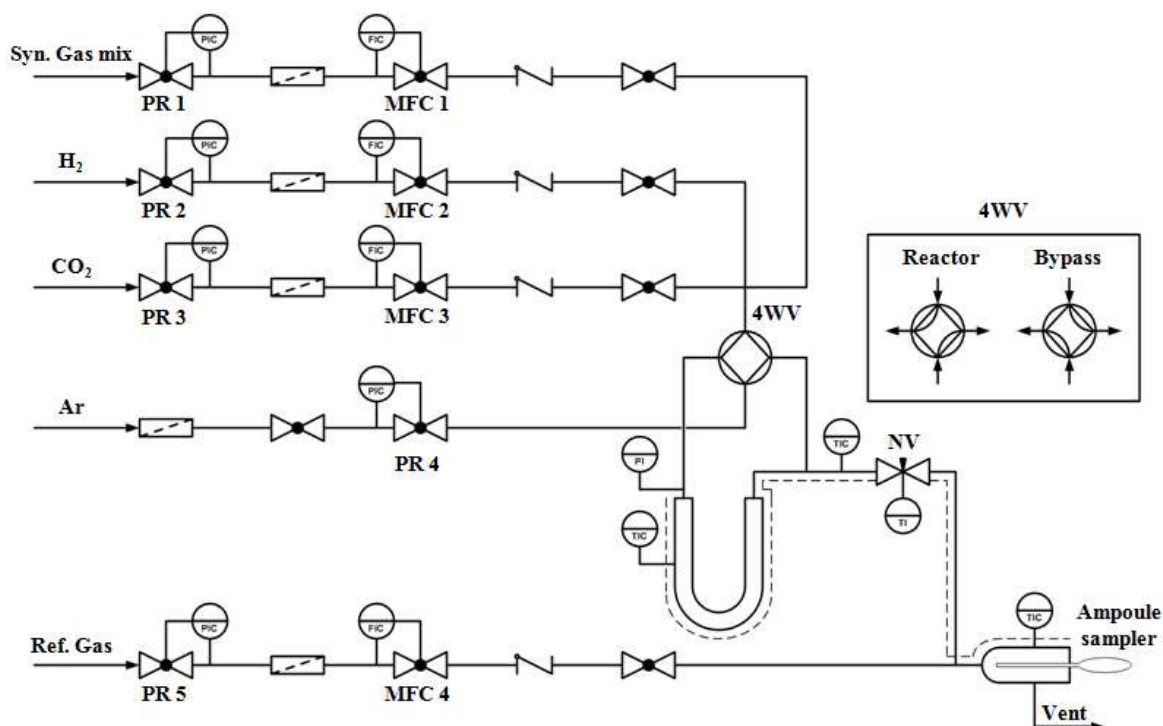


Figure 4.6: Flow sheet of the test unit set-up for the Fischer-Tropsch synthesis experiments.

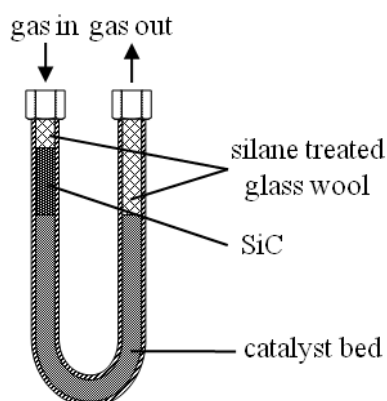


Figure 4.7: Schematic drawing of U-tube reactor with catalyst packing.

4.7.3 Experimental procedure for FT experiments with supported cobalt crystallite catalysts

Prior to the FT experiment the catalysts were reduced at atmospheric pressure in-situ in hydrogen at a space velocity of $40 \text{ ml/g}_{\text{catalyst}} \cdot \text{min}$ (4WV on reactor position) according to the temperature

specifications shown in table 4.2. After the reduction the reactor was cooled down under hydrogen flow to the reaction temperature 190°C.

Once the reaction temperature was reached, the 4WV was switched to bypass, the hydrogen flow was switched off and the argon pressure was set to 11 bar (absolute). The argon flow was regulated to 10-12 ml/min (STP) with the needle valve. Through the bypass the synthesis gas mix flow was set to 7.9 ml/min (STP) which correlates to a space velocity of $7.2 \text{ ml}_{\text{syn.gas}}/\text{g}_{\text{catalyst}} \cdot \text{min}$ at normal temperature and pressure. The partial pressures were: $PP_{\text{H}_2} = 6.6 \text{ bar}$, $PP_{\text{CO}} = 3.3 \text{ bar}$, $PP_{\text{Ar}} = 1.1 \text{ bar}$. These mild conditions, with low temperatures and relatively high space velocity, were chosen to obtain very low conversions and therefore low water partial pressure. This minimised the possibility of re-oxidation of cobalt crystallites to CoO due to the presence of product water (see chapter 2.2.4), and it reduced sintering due to very low levels of water and the lack of hot spots in the reactor. Via mass flow controller 4 a mixture of 0.015 mol% cyclohexane (cyclo-C₆) in nitrogen mixture was fed to the gas mixture at 3 ml/min (STP) as internal standard for the off-line GC-FID analysis. Once all gas flows had stabilised, the 4WV was switched to reactor which defined the start of the reaction. The product was sampled with the ampoule technique (see chapter 4.7.6) and stored for later analysis using the off-line GC-FID. The initial stages were of special interest so samples were taken at a relatively high frequency, i.e. every minute, while in later stages of the experiment, i.e. after 3 hours, samples were only taken every hour.

After 25 hours on stream the reaction was terminated by switching the 4WV back to bypass and shutting off the synthesis and reference gas flows. The reactor was allowed to cool down under pressure and argon flow. Once cooled down the rig was depressurised by opening the needle valve and decreasing the pressure of the argon line with PR 4. A flow of $30 \text{ ml}/\text{g}_{\text{catalyst}} \cdot \text{min}$ CO₂ was set, and by switching the 4WV to reactor, allowed to flow over the catalyst for 1 hour to passivate the reduced cobalt crystallites. After the passivation the catalyst could be removed and submitted to post run characterisation.

4.7.4 Experimental procedure for FT experiments with supported organometallic cobalt complex

The supported organometallic complex did not require any pre-treatment. As soon as the reactor was mounted the argon pressure/flow was set with the 4WV on the bypass position and the synthesis gas mix and reference gas were switched on as described in chapter 4.7.3. When the flows had stabilised the reactor was placed into the hot oil bath (see chapter 4.7.2) and the 4WV was switched to reactor. Immediately the reaction was started and ampoule samples were taken. Due to the decomposition of the cobalt complex the experiment was terminated after only 5 hours in the same fashion as described for the supported cobalt crystallites above.

4.7.5 Experimental procedure for FT experiments with supported organometallic cobalt complex with ¹³C

In order to investigate the carbon source in organic products that may form during the experiments with the complex, i.e. CO ligands versus gas phase CO, an experiment with ¹³C labelled CO was conducted. For FT studies the previously described test unit set-up (see chapter 4.7.1) was modified

slightly. The synthesis gas was now directly mixed with the mass flow controllers 1 and 2 (MFC 1 & 2) instead of using premixed synthesis gas. As ^{13}CO was not available at high pressures, the experiment was conducted at atmospheric pressure.

As described in chapter 4.7.6 the reactor with the supported organometallic cobalt complex was loaded and purged with Ar (at atmospheric pressure PR 3) with the 4 way valve in bypass position. The H_2 flow (via MFC 1) and the ^{13}CO flow (via MFC 2) were set to 4.8 and 2.4 $\text{ml/g}_{\text{catalyst}} \cdot \text{min}$ respectively. This results in the same space velocity as that used in the other Fischer-Tropsch experiments. The partial pressures in the experiment were $PP_{\text{H}_2} = 0.67 \text{ bar}$, $PP_{^{13}\text{CO}} = 0.33 \text{ bar}$. As soon as the gas flows stabilised, the reactor was placed in the hot oil bath (see chapter 4.7.2) and the 4WV switched to reactor. Immediately ampoule samples were taken. To study the incorporation of ^{13}C into the product spectrum the product gas was analysed on-line every 0.6 minutes with a Pfeiffer Omnistar GSD 300 mass spectrometer covering a mass range from $m/z = 1$ to 200. Due to the high costs of ^{13}CO and its limited availability the experiment was stopped after 3 hours.

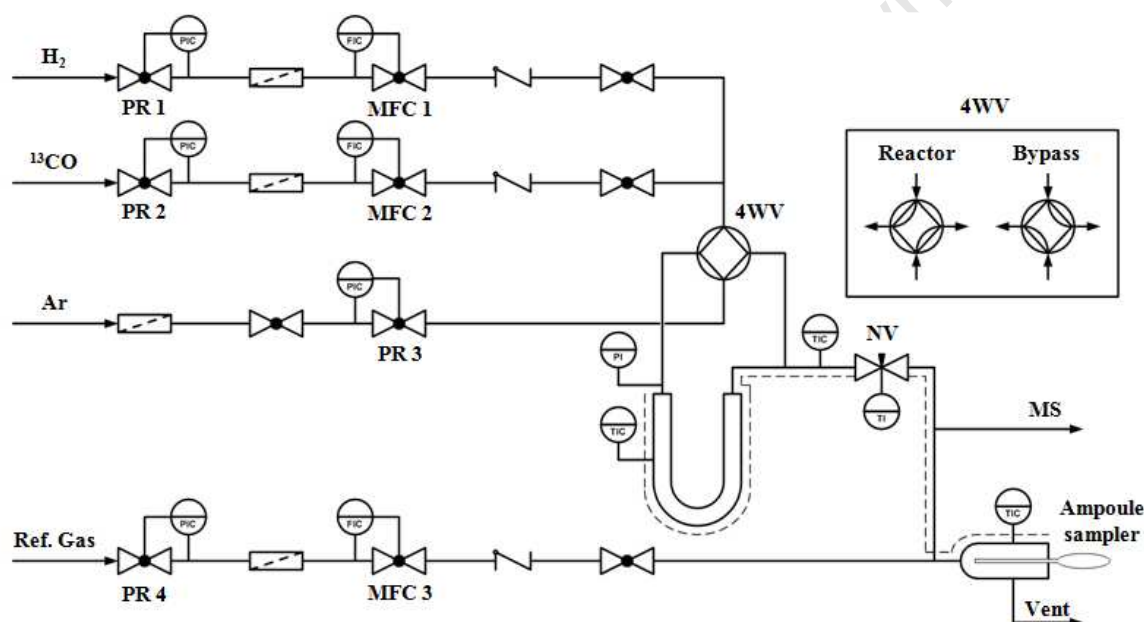


Figure 4.8: Flow sheet of the test unit set-up for the Fischer-Tropsch synthesis experiments with ^{13}CO .

4.7.6 Off-line sampling technique

Gaseous Fischer-Tropsch products and reaction gases were collected using the ampoule sampling method developed by Schulz and co-workers [29] at the Engler-Bunte Institute at the University of Karlsruhe. Ampoules were prepared from commercially available Pasteur pipettes. Under a butane/oxygen flame one side of the pipette was formed to a capillary and then sealed off. The pipette/ampoule was then evacuated with a vacuum pump and sealed. To collect a gas sample the capillary was inserted into the ampoule sampler (see figure 4.9) which was connected to the product stream and the tip was broken off by turning the breaking fork. Due to the vacuum in the ampoule product gas was collected and the ampoule was immediately sealed off. The ampoule was then stored for later injection into an off-line gas chromatograph equipped with a flame ionisation detector (GC-

FID) (for exact conditions see appendix A3). To study the condensation of possible long-chain Fischer-Tropsch product in the ampoule, which was stored at room temperature, a theoretical FT product stream corresponding to a 10% CO conversion level (based on the same experimental conditions described in chapter 4.7.3) was calculated in Aspen in a flash condenser from 200°C (line temperature in the test unit) to 20°C. A chain growth probability of 80% and an ideal ASF product distribution for carbon numbers of 3 and higher consisting only of n-alkanes and the corresponding α -olefins was assumed. The fraction of hydrocarbon in the gas and in the liquid phase was plotted over the carbon number (see figure 4.10). From the calculations it can be seen that up to a carbon number of 8 all hydrocarbons were present in the gas phase and no effect of the product distribution due to condensation is expected when injecting the content of the ampoule into a GC-FID at room temperature..

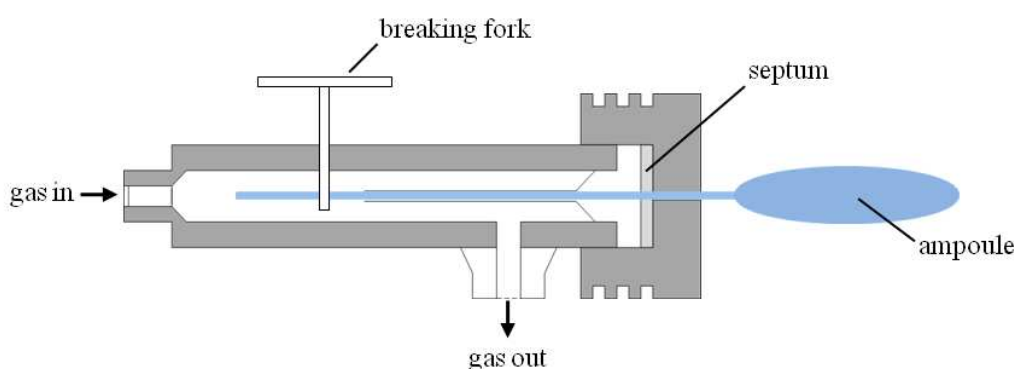


Figure 4.9: Schematic drawing of off-line ampoule sampler.

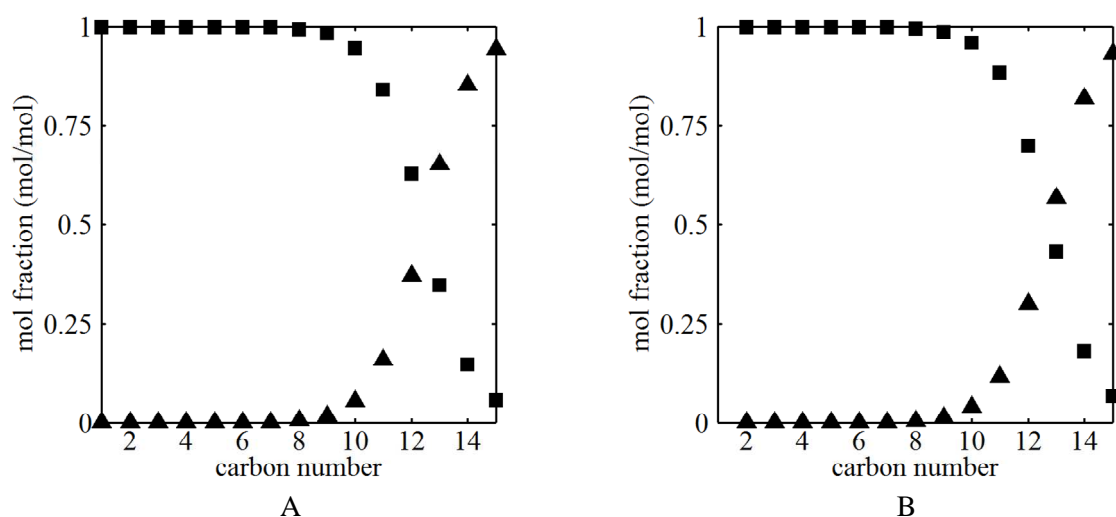


Figure 4.10: Calculated fractions of n-alkanes (A) and α -olefins (B) from a theoretical Fischer-Tropsch product spectrum at 10% CO conversion in the gas (■) and liquid (▲) phase.

4.8 Fischer-Tropsch experiments with in-situ magnetic measurements

4.8.1 Test unit set-up

The in-situ magnetic measurement were conducted in a newly developed magnetometer at the University of Cape Town (see figure 4.11) [27]. For the Fischer-Tropsch experiments a synthesis gas mixture (60 mol% H₂, 30 mol% CO and 10 mol% Ar) was fed via the mass flow controller MFC 1 (Brooks Instruments) into the reactor system. The pressure was set with a spring loaded backpressure regulator (BPR). The pressure set by the spring on a membrane controlled the gas pressure in the whole test unit. Besides a gas feed the set up allowed the co-feeding of water to simulate higher conversions and to study the effect of water on the sintering and oxidation of the catalyst crystallites. Liquid water was fed with an HPLC pump (P) into the evaporator which could be selected or bypassed with the main gas flow using the three way valves 3WV 2 & 3.

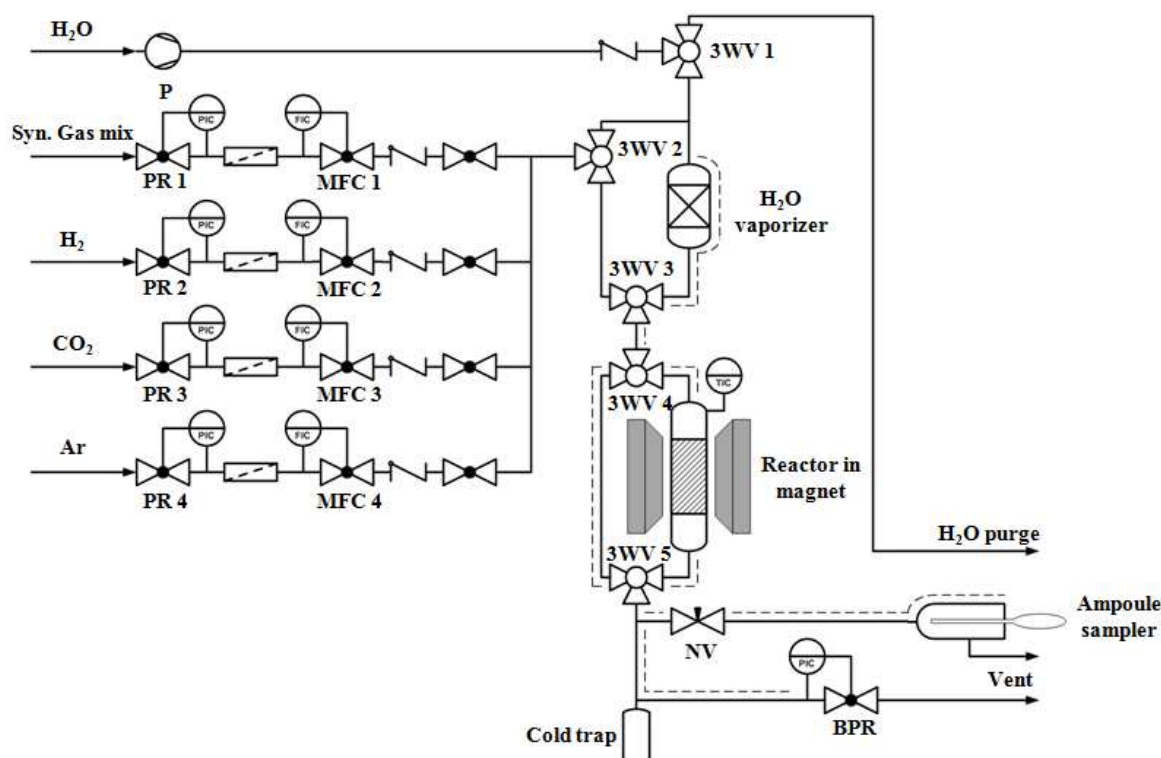


Figure 4.11: Flow sheet of the test unit set-up for the Fischer-Tropsch synthesis experiments with in-situ magnetic characterisation.

As the reactor a 1/2" stainless steel tube was used (ID = 9.7 mm). With the three way valves 3WV 4 & 5 the reactor could also be bypassed to stabilise the feed stream. Gaseous products could be collected via an ampoule sampler (see chapter 4.7.6). The product could be collected from the high pressure zone after the reactor and before the BPR. The flow to the sample point was regulated with a needle valve (NV). The water exiting the system was collected in a cold trap in the pressurised zone which was kept at room temperature to maximise the efficiency of water collection. Due to the very

low conversions (see chapter 4.7.3) no long chain hydrocarbon products, i.e. Fischer-Tropsch wax, had to be collected from a hot trap. All lines downstream of the water vaporizer were heated to 190°C to avoid condensation.

4.8.2 Reactor set-up

Figure 4.12 shows the schematic representation of the reactor used in the magnetic measurements and its positioning between the pole caps of the electro magnet. The ½” stainless steel reactor included a non magnetic brass frit to support the catalyst bed and to avoid catalyst loss through the reactor. On this brass frit a layer of glass wool was placed. Enough catalyst to obtain approximately 20 mg of cobalt in the reactor was then loaded. This layer is followed by a thin layer of glass wool. A non magnetic thermocouple (Pt 100 element) was placed with the tip in the catalyst layer. The thermocouple featured a star like guide to ensure the radially central position of the temperature sensor in the reactor bed. The reactor was topped up with a layer of SiC to facilitate a pre-heating zone for the reactive gases.

The loaded reactor was placed in the aluminium holding bracket equally distant from two infra red heaters which were used to heat the reactor. The electro magnet (Bruker Analytik GmbH; maximum field strength: 20 kOe) supplied a homogenous field which could be accurately controlled (field control). The control of the field strength from -20 to 20 kOe allowed the recording of a so called hysteresis (see figure 4.4). The reactor tube itself was painted with black high temperature paint to increase the heat absorption. For ideal signal strength it was of utmost importance that the catalyst bed was placed exactly in the centre of the detection coils which were placed on the pole caps of the magnet. In order to achieve this, the vertical position of the reactor could be adjusted in the aluminium holding bracket. This bracket was also used to realise the reactor movement (via an electromotor; amplitude: 4 cm, frequency: 2Hz) to induce the signal/voltage from the magnetised catalyst in the pick-up coils. To allow the movement of the reactor flexible 1/16” tubing is used for the gas in- and outlet. This tubing was heated to avoid condensation of co-fed water and reaction products.

The magnetisation of the sample is proportional to the induced signal measured by the pick up coils. The set up was calibrated with varied and known amounts of pure metallic cobalt powder.

4.8.3 Experimental procedure

To guarantee comparability the experimental conditions were chosen to be identical to the ones used for the Fischer-Tropsch studies in the U-tube reactor set up (see chapter 4.7.3). In addition to the previous runs however, in this set-up also the effect of water on selected catalysts (CAT 9.6 & 4.4) was studied via the addition of water to the feed gas stream, therefore simulating high conversion conditions (water level correlating to 66% CO conversion).

Prior to the Fischer-Tropsch synthesis the catalyst was reduced to its metallic form in 40ml/g_{catalyst}·min H₂ flow fed via the mass flow controller MFC 2. The reduction conditions are shown in table 4.2. After the reduction the reactor was cooled down to room temperature in Ar flow. The temperature was then set to 190°C and the pressure of the test unit including all bypasses, the reactor and the vaporizer was set to 11 bar (absolute) with the spring loaded back pressure regulator. The reactor was then isolated with the three way valves 3WV 4 & 5. The vaporizer was also bypassed

(3WV 2 & 3). The synthesis gas mix was set to a flow resulting in $7.2 \text{ ml}_{\text{syn.gas}}/\text{g}_{\text{catalyst}} \cdot \text{min}$ and partial pressures of 6.6 bar H_2 , 3.3 bar CO and 1.1 bar Ar . These are the same conditions used in the Fischer-Tropsch synthesis experiments in the U-tube reactor (see chapter 4.7.3). When the gas flows had stabilised, the three way valves 3WV 4 & 5 were switched to the reactor position and the reaction was started.

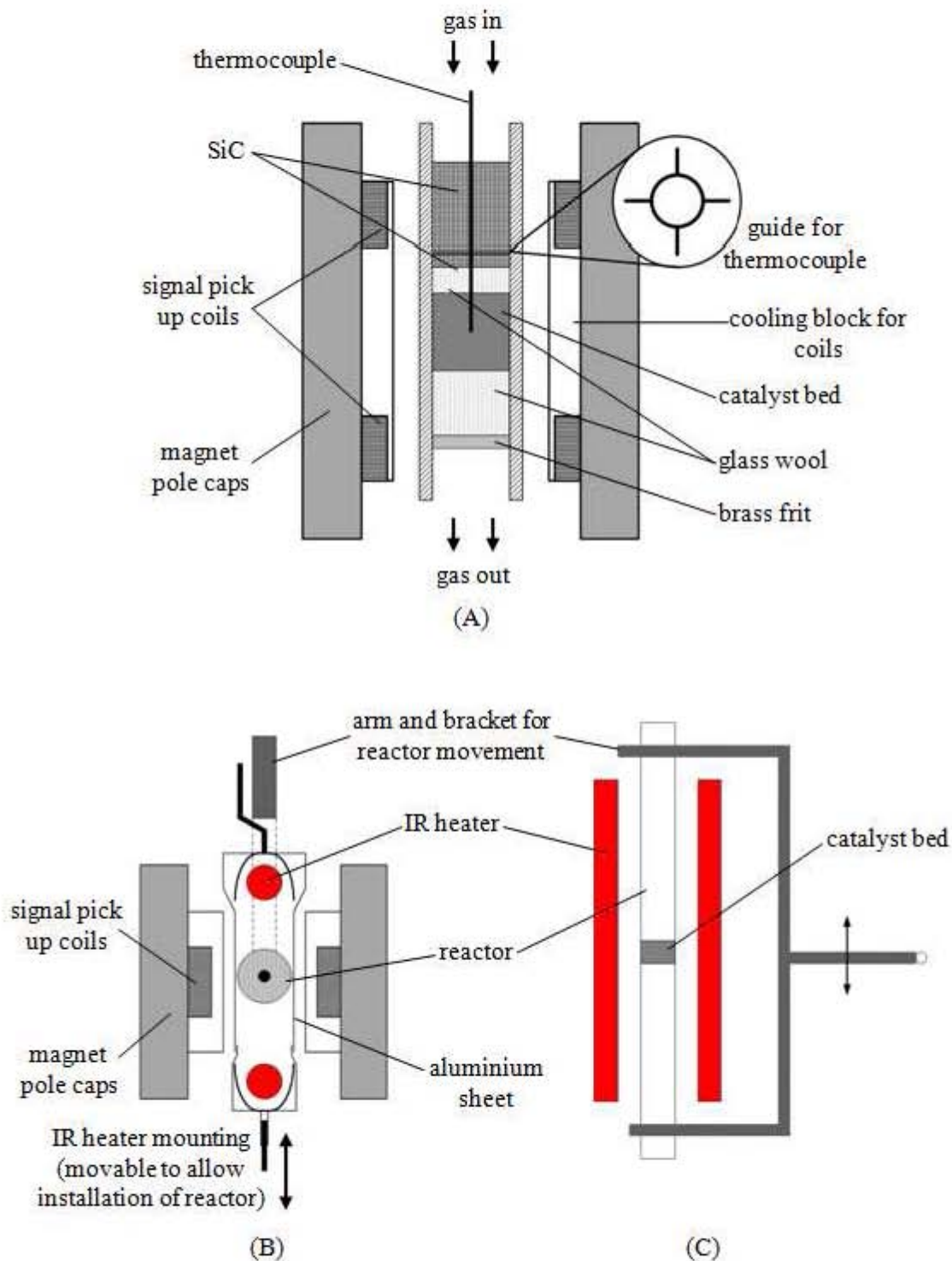


Figure 4.12: Fixed bed reactor set-up for in-situ magnetic characterisation: (A) front view; (B) top view; (C) side view.

The reaction was allowed to run for 25 hours, i.e. the same duration as studied in the U-tube reactor. After 25 hours the gas was switched back to inert Ar (MFC 4). The pressure in the whole test unit was then increased to 17 bar under argon. The reactor was isolated (3WV 4 & 5) and the gas flow was switched back to the synthesis gas mix. This time the gas stream was passed through the water vaporizer and the HPLC pump supplies the required water flow to supply 6 bar water partial pressure. This concentration of water simulates a 66% carbon monoxide conversion in the Fischer-Tropsch synthesis, assuming no water gas shift activity. The gas stream is switched back to the reactor after stabilisation and the reaction is allowed to run for 3 hours. After this time the vaporizer is bypassed and the gas switched to argon (MFC 4).

After completion of the run the gas was switched to argon flow (MFC 4), the system was depressurised and the reactor was cooled down. At room temperature the catalyst was passivated in the reactor by a $30 \text{ ml/g}_{\text{catalyst}} \cdot \text{min}$ flow of CO_2 for 60 minutes. The catalyst can then be extracted and is ready for further post-run characterisation.

4.8.4 Magnetic measurement procedure

During the reduction process the magnetisation of the catalyst sample was measured at an external field strength of 20 kOe followed by a measurement at 0 kOe to monitor the remnant magnetisation. These two measurements take approximately 2 minutes and they give information on the amount of metallic cobalt (from saturation magnetisation) and the amount of ferromagnetic material indicative for large crystallites ($2 \cdot M_{\text{rem}}/M_{\text{sat}}$) present. During the temperature ramping measurements were taken every 10 minutes. During the holding time samples were taken every 20 minutes until the magnetisation remained largely constant, then the sampling frequency was reduced. After the reduction a full hysteresis measurement was taken under argon flow, which consisted out of 53 readings starting from -20 kOe to 20 kOe and returning to -20 kOe. A further full hysteresis measurement was taken prior to the start of the FT run, i.e. at reaction temperature.

During the first hour of the Fischer-Tropsch synthesis 20 kOe/0 kOe measurements were taken every 10 minutes. Between 1 to 2 hours the sampling frequency was reduced to once every 15 minutes and further reduced after that. After 25 hours and after the switch to argon flow a full hysteresis was recorded again.

To study the influence of water 20 kOe/0 kOe measurements were taken every 10 minutes in presence of added water.

After the termination of the experiment a full hysteresis was measured again before the temperature is decreased in steps of 25°C to room temperature.

4.9 Product analysis

The ampoule samples taken during the Fischer-Tropsch experiments were injected into a gas chromatograph (GC) equipped with a flame ionisation detector (FID) (exact conditions see appendix A3). The flame ionisation detector is only sensitive to organic products and not to the permanent inorganic gases. However not all organic products give the same response in the FID. The signal strength is dependent on the number of carbon atoms in the molecule and the number of carbons

bonded to an oxygen atom. To account for these variations theoretical response factors for the different oxygenates were calculated using an increment method as published by Kaiser [30]. Carbon atoms which had only bonds to hydrogen or other carbon atoms were assigned an increment of 1. Carbon atoms with one single bonded oxygen an increment of 0.55 and carbon atoms with carbon oxygen double bond do not give any response. This resulted in a response factor which can be calculated for every compound of the Fischer-Tropsch product spectrum.

$$f_i = \left(\frac{N_{C,i}}{N_{C(noo)} + 0.55(N_{C(CO)})} \right) \quad (4.4)$$

Where f_i is the response factor for a specific compound i , $N_{C,i}$ is the total number of carbon atoms in the compound i , $N_{C(noo)}$ is the number of carbon atoms without bonds to oxygen and $N_{C(CO)}$ is the number of carbon atoms with a single bond to an oxygen atom.

The identification of the different species was conducted via comparison with known product spectra and calculation of compound specific Kovats indeces [31] (see appendix A4).

The molar flow rate of each compound could then be calculated using the co-fed cyclo-hexane (cyclo-C6), which was not a part of the Fischer-Tropsch product spectrum, as an internal standard.

$$\dot{n}_i = \left(\frac{N_{cyclo-C6}}{N_i} \right) \cdot \left(\frac{f_i \cdot A_i}{f_{cyclo-C6} \cdot A_{cyclo-C6}} \right) \cdot \dot{n}_{cyclo-C6} \quad (4.5)$$

Or on carbon basis:

$$\dot{n}_{iC} = N_{cyclo-C6} \cdot \left(\frac{f_i \cdot A_i}{f_{cyclo-C6} \cdot A_{cyclo-C6}} \right) \cdot \dot{n}_{cyclo-C6} \quad (4.6)$$

Where:

\dot{n}_i is the molar flow rate of compound i .

\dot{n}_{iC} is the molar flow rate of compound i on carbon basis.

$N_{cyclo-C6}$ is the number of carbon atoms in cyclo-C₆ (= 6).

N_i is the number of carbon atoms in compound i .

f_i is the response factor for compound i from equation 4.4.

A_i is the peak area of compound i in the chromatogram.

$f_{cyclo-C6}$ is the response factor for cyclo-C₆ from equation 4.4 (= 1).

$A_{cyclo-C6}$ is the peak area of cyclo-C₆ in the chromatogram.

$\dot{n}_{cyclo-C6}$ is the molar flow rate of cyclo-C₆.

4.9.1 Conversion, yield and selectivity

The conversion in the Fischer-Tropsch synthesis is usually given as conversion of carbon monoxide (CO) and is defined, under the assumption of negligible water gas shift activity, as:

$$X_{CO} = \frac{\dot{n}_{CO,in} - \dot{n}_{CO,out}}{\dot{n}_{CO,in}} \quad (4.7)$$

Where

X_{CO} is the conversion of CO.

$\dot{n}_{CO,in}$ is the molar flow rate of CO into the reactor.

$\dot{n}_{CO,out}$ is the molar flow rate of CO out of the reactor.

In this study the inorganic permanent gases downstream of the reactor were not analysed as the relative small changes of the gas concentrations (low conversions) would not allow for accurate conversion measurement. Therefore the conversion had to be calculated from the formation rates of the Fischer-Tropsch product. As we could measure hydrocarbons quantitatively only up to a carbon number of 8 without encountering condensation in the ampoule (see chapter 4.7.6) the Anderson-Schulz-Florry plot (see chapter 2.1.2) created from the measured products with carbon numbers from 3 to 8 was extrapolated to the carbon number of 50 (assuming constant chain growth probability) and summed up. This way we obtained the sum of molar flows of all Fischer-Tropsch products on a carbon basis which must equal the difference between the molar flow of CO into the reactor and out of the reactor. Therefore we could write:

$$X_{CO} = \frac{\sum_1^{50} \dot{n}_{iC}}{\dot{n}_{CO,in}} \quad (4.8)$$

Where

X_{CO} is the conversion of CO.

$\sum_1^{50} \dot{n}_{iC}$ is the sum of the carbon based flow rates of all Fischer-Tropsch products from carbon number 1 to 50.

$\dot{n}_{CO,in}$ is the molar flow rate of CO into the reactor.

The yield of one compound was defined as the ratio the molar flow rate of the compound formed to the molar flow rate of CO fed to the reactor and could be calculated as being:

$$Y_i = \frac{\dot{n}_i}{\dot{n}_{CO,in}} \quad (4.9)$$

Or on a carbon basis:

$$Y_{i,C} = \frac{\dot{n}_{i,C}}{\dot{n}_{CO,in}} \quad (4.10)$$

Where

Y_i is the yield of compound i .

$Y_{i,C}$ is the yield of compound i on a carbon basis.

\dot{n}_i is the molar flow rate of compound i .

$\dot{n}_{i,C}$ is the molar flow rate of compound i on carbon basis.

$\dot{n}_{CO,in}$ is the molar flow rate of CO into the reactor.

The selectivity (S_i) for compound i is defined as the ratio of the yield of compound i to the CO conversion.

$$S_i = \frac{Y_i}{X_{CO}} \quad (4.11)$$

Or on a carbon basis:

$$S_{i,C} = \frac{Y_{iC}}{X_{CO}} \quad (4.12)$$

4.9.2 Turn-over frequency (TOF)

The turn-over frequency is a surface specific activity and was defined as the number of converted CO molecules per mol exposed cobalt atoms on the catalyst surface.

$$TOF = \frac{X_{CO} \cdot \dot{n}_{CO,in}}{N_{exp,total}} \cdot N_A \quad (4.13)$$

Where

TOF is the turn-over frequency.

X_{CO} is the CO conversion.

$\dot{n}_{CO,in}$ is the molar flow rate of CO into the reactor.

$N_{exp,total}$ is the sum of all cobalt atoms on the surface of crystallites (exposed).

N_A is Avogadro's number ($6.022141 \cdot 10^{23} \text{ mol}^{-1}$).

The total number of cobalt surface atoms ($N_{exp,total}$) was calculated by multiplying the number of crystallites per sample (N_{cryst}) with the number of surface atoms per crystallite ($N_{exp,cryst}$). The number of crystallites was obtained by multiplying the cobalt loading (L_{Co}) (from AAS measurements) of the catalyst with the mass of the catalyst in the reactor (m_{cat}) and Avogadro's number and dividing this by the molar mass of cobalt (\tilde{M}_{Co}) and the total number of atoms in one crystallite ($N_{total,cryst}$). $N_{total,cryst}$ and $N_{exp,cryst}$ were obtained from statistical calculations with the experimentally (TEM) determined number weighted average crystallite size according to statistical calculations published by van Hardefeld and Hartog [32] (see calculations in appendix A5).

$$N_{exp,total} = N_{exp,cryst} \cdot N_{cryst} = N_{exp,cryst} \cdot \frac{L_{Co} \cdot m_{cat}}{\tilde{M}_{Co}} \cdot \frac{N_A}{N_{total,cryst}} \quad (4.14)$$

References

- [1] J. van de Loosdrecht, M. van der Haar, A.M. van der Kraan, A.J. van Dillen and J.W. Geus, *Applied Catalysis A: General*, 150 (1997) 365.
- [2] A. Sirijaruphan, A. Horvath, J.G. Goodwin Jr. and R. Oukaci, *Catalysis Letters*, 91 (2003) 89.
- [3] G. Jacobs, P.M. Patterson, Y. Zhang, T. Das, J. Li and B.H. Davis, *Applied Catalysis A: General*, 233 (2002) 215.
- [4] C.A. Welker, Ruthenium based Fischer-Tropsch synthesis on crystallites and clusters of different sizes, Department of Chemical Engineering, PhD, University of Cape Town, Cape Town, 2007.
- [5] V. Uskokovic and M. Drofenik, *Surface Review and Letters*, 12 (2005) 239.
- [6] V. Uskokovic and M. Drofenik, *Advances in Colloid and Interface Science*, 133 (2007) 23.
- [7] S. Eriksson, U. Nylen, S. Rojas and M. Boutonnet, *Applied Catalysis A: General*, 265 (2004) 207.
- [8] I. Lisiecki, *Journal of Physical Chemistry*, 109 (2005) 12231.
- [9] D. Barkhuizen, I. Mabaso, E. Viljoen, C. Welker, M. Claeys, E. van Steen and J.C.Q. Fletcher, *Pure Applied Chemistry*, 78 (2006) 1759.
- [10] T. Kinugasa, A. Kondo, S. Nishimura, Y. Miyauchi, Y. Nishii, K. Watanabe and H. Takeuchi, *Colloids and Surfaces A: Physicochemical and Engineering Aspects*, 204 (2002) 193.
- [11] E.I. Mabaso, Nanosized iron crystallites for Fischer-Tropsch synthesis, Department of Chemical Engineering, PhD, University of Cape Town, Cape Town, 2005.
- [12] E.I. Mabaso, E. van Steen and M. Claeys, *DGMK/SCI-Conference "Synthesis Gas Chemistry"*, 4 (2006) 93.
- [13] X. Lei, M. Shang, T.P. Fehlner, R. Werner, W. Haase, D. Hautot and G.J. Long, *Journal of Organometallic Chemistry*, 541 (1997) 57.
- [14] V. Cheang, Effect of crystallite size and water partial pressure on the activity and selectivity of low temperature iron-based Fischer-Tropsch catalysts, Department of Chemical Engineering, PhD, University of Cape Town, Cape Town, 2009.
- [15] D.F. Nicoli, *Proceedings SPIE-International Society for Optical Engineering*, 1430 (1991) 19.
- [16] N.V.Y. Scarlett and I.C. Madsen, *Powder Diffraction*, 21 (2006) 278.
- [17] J. Yang, H. Liu, W.N. Martens and R.L. Frost, *The Journal of Physical Chemistry C*, 114 (2009) 111.
- [18] C. Kittel, *Introduction to Solid State Physics*, John Wiley & Sons, Inc, London, 2005.
- [19] K.H.J. Buschow, in K.H.J. Buschow, Cahn, R. W., Flemings, M. C., Ilshner, B., Kramer, E. J., Mahajan, S. (Editor), *Encyclopedia of Materials: Science and Technology* Vol. 5, Elsevier, 2001.
- [20] A. Barbier, A. Hanif, J.-A. Dalmon and G.A. Martin, *Applied Catalysis A: General*, 168 (1998) 333.
- [21] A. Barbier, G.-A. Martin, P.R. de la Piscina and N. Homs, *Applied Catalysis A: General*, 210 (2001) 75.
- [22] C.P. Bean and J.D. Livingston, *Journal of Applied. Physics.*, 30 (1959) 120S.
- [23] J.A. Dalmon, in B. Imelick, Verdrine, J. (Editor), *Catalyst characterisation: Physical techniques for solid materials*, chapter 21, Plenum Press, New York, 1994.
- [24] H. Niu, Q. Chen, H. Zhu, Y. Lin and X. Zhang, *Journal of Materials Chemistry*, 13 (2003) 1803.
- [25] P.W. Selwood, *Chemisorption and Magnetization*, 2nd Ed, Academic, New York, 1975.
- [26] L. Weil, *Journal de Chimie Physique et de Physico-Chimie Biologique*, 51 (1954) 715.

- [27] M. Claeys, van Steen, E., Visage, J., van de Loosdrecht, J., 2010, A Magnetometer; a magnetometer for in-situ characterisation of ferromagnetic materials and catalysts, South Africa, PCT Patent Application PCT PCT/IB2009/006210.
- [28] T. Mousavand, T. Naka, K. Sato, S. Ohara, M. Umetsu, S. Takami, T. Nakane, A. Matsushita and T. Adschiri, *Physical Review B: Condensed Matter and Materials Physics*, 79 (2009) 144411/1.
- [29] H. Schulz, W. Böhringer, C. Kohl, N. Rahman and A. Will, *DGMK Forschungsbericht*, 3 (1984) 320.
- [30] R. Kaiser, *Methoden der Physikalischen Analyse*, 5 (1969) 357.
- [31] E.S. Kovats, *Fresenius' Zeitschrift für analytische Chemie*, 181 (1961) 351.
- [32] R. van Hardeveld and F. Hartog, *Surface Science*, 15 (1969) 189.

University of Cape Town

Chapter 5

Characterisation of the w/o Microemulsion

5.1 Influence of temperature on the stability of reverse micelles

Previous studies with the ternary system comprising n-hexane, water and penta-ethyleneglycol-dodecyl ether (PEGDE) [1-5] report that reverse micelles are only formed in the oil rich area of the ternary phase diagram below water weight fractions of 5%, PEGDE weight fractions of 15% and n-hexane weight fractions of at least 80%. It is further reported that the reverse micelle stability region in a ternary system, especially in presence of a non-ionic surfactant as in this work [6], is strongly temperature dependent [1, 7, 8]. However, to date no comprehensive study on the temperature dependency of the stability region has been conducted on the system used in this study.

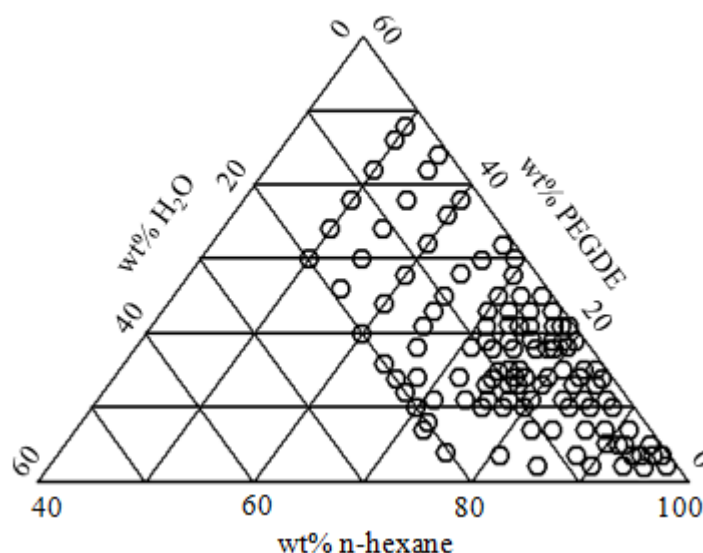


Figure 5.1: Ternary phase diagram indicating all mixtures studied to establish the stability region of the reverse micelles at 10, 25 and 40°C.

A stable reverse micelle solution is optically transparent. As soon as the mixture is modified and not longer located in the stable region for reverse micelles, the solution turns cloudy and/or a two or three phase system forms. In order to establish the stability region of the reverse micelles in the

ternary mixture, over 100 solutions were prepared in the oil rich area of the ternary phase diagram (see figure 5.1). After mixing the solutions were left to stabilise for 12 hours in a temperature controlled water bath at three different temperatures (10, 25 and 40°C). Via visual inspection the samples were classified as stable microemulsion or as multi-phase mixtures. From these classifications stability regions for the formation of reverse micelles at the three different temperatures can be drawn (see figure 5.2).

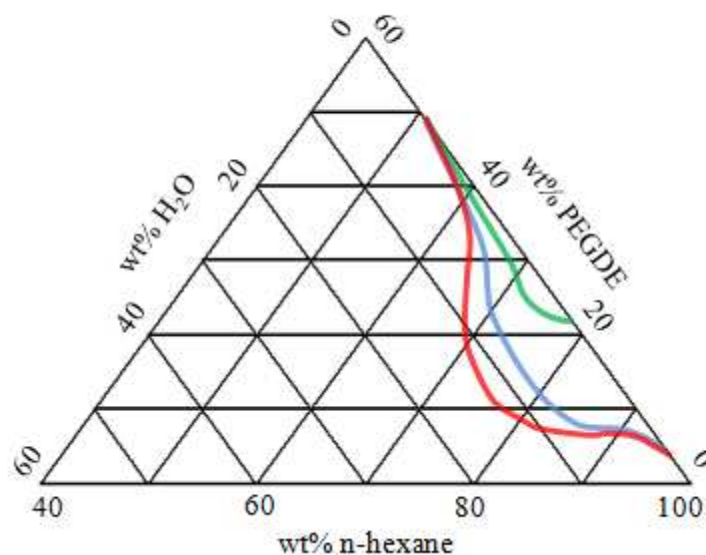


Figure 5.2: Ternary phase diagram indicating stability regions of the reverse micelle at 10 (red), 25 (blue) and 40°C (green).

Figure 5.2 clearly shows the changes of the stability region for the formation of reverse micelles with changing temperature which is qualitatively in line with previous reports [1, 7, 8]. With increasing temperature the area in the ternary phase diagram where stable reverse micelle solutions can be formed becomes smaller. While the decrease is small for a temperature increase from 10 to 25°C it is dramatic for a further increase to 40°C. At 40°C the minimum weight percentage of surfactant still resulting in a stable reverse micelle increases from 2-5% at lower temperatures to over 20%.

Several mechanisms have been proposed to cause the measured decrease of the stability region of the reverse micelles with increasing temperature. Clint [9] and Lawrence and co-workers [6] report an increase in solubility of the surfactant in the non-polar phase, i.e. n-hexane. The decreased availability of surfactant for the formation of reverse micelles results in a decreased stability region. Lawrence and Rees [6] termed this point of destabilisation of the reverse micelles (due to an increase of solubility of the surfactant in the non-polar phase and decrease of solubility in the polar phase) the cloud point. A similar effect has been reported by Inoue and co-workers [10] who observed a decreased hydration in the polar phase with increasing temperature resulting in an overall destabilisation of the reverse micelle structure when using polyoxyethylene as the surfactant.

Porter [11] reports that with increasing temperature the number of surfactant molecules required to form a micelle, i.e. critical micelle concentration (CMC), decreases. Therefore at higher temperatures

the number of micelles increases. A larger number of micelles results in more interactions between the micelles which is believed to lead to instability of the system [9, 12, 13].

5.2 Influence of composition on the size of the reverse micelle

It is well documented that the composition of the w/o microemulsion does influence the size of the reverse micelles formed [1, 7, 8, 14-17]. The resulting possibility to tune the sizes of a reverse micelle has led to their wide spread application in the synthesis of nano-particles as the particle sizes formed are dependent on the sizes of the reverse micelles they originate from [1, 14, 18, 19]. The most prominent factor determining the size of a reverse micelle is the water to surfactant weight ratio, or ω , in the corresponding ternary system. The effect of ω is based on the assumption that the number of surfactant molecules per surface area unit of the water core (wc), i.e. the aggregation number (n_{agg}), is constant. Hence an increase in water to surfactant ratio leads to less surfactant molecules stabilising a larger volume of water molecules. Assuming a constant aggregation number this can only be realised by increasing the diameter of the water core. The opposite effect is postulated when decreasing ω .

To study these effects in the water/PEGDE/n-hexane system six reverse micelle solutions were prepared at 25°C around one central/base case composition (see table 5.1) and the sizes of the water core were measured with dynamic light scattering (DLS). Variation of the water to surfactant ratio was achieved via, (a) compositions in which only the water content was changed (compositions 1 and 7 - ▼-) and (b) compositions in which only the surfactant content was changed (compositions 2 and 6 - ▲-). To study the effects of n-hexane compositions 3 (■) and 5 (◆) were prepared by changing the weight ratio of n-hexane from the base case composition (sample 4 ●).

Table 5.1: Composition of microemulsions measured using dynamic light scattering (DLS).

Composition No.	Water (g)	Surfactant (PEGDE) (g)	n-Hexane (g)	ω (-)	Viscosity (cP)
1	0.67	3.33	25.00	0.20	0.81
2	1.00	5.00	25.00	0.20	0.82
3	1.00	3.33	31.25	0.30	0.83
4	1.00	3.33	25.00	0.30	0.90
5	1.00	3.33	18.75	0.30	0.80
6	1.00	2.50	25.00	0.40	0.83
7	1.33	3.33	25.00	0.40	0.88

Figure 5.3 shows the water core sizes measured for the prepared reverse micelle compositions. As proposed in literature [1, 14, 18, 19] the size of the water core in the reverse micelle increases linearly with an increasing water to surfactant ratio. Interestingly this increase in size is different for the two cases of variation of ω , namely it is more pronounced where changes of ω were realised through changes in the amount of surfactant compared to variations of the amount of water. A decrease of the amount of surfactant by a factor of two (compositions 2,4,6) has a stronger impact than the increase of the water content by a factor of two (compositions 1,4,7). This different influence can be explained in terms of simple geometrical dependencies. Assuming an ideal spherical reverse micelle (see figure

5.4) an increase of the water fraction by a factor of two would increase the volume of the water core in the reverse micelle by a factor of two. On the other hand a decrease of the surfactant amount by a factor of 2 would lead to a decrease of the surface area of the water core, assuming a constant aggregation number, by a factor of two. From basic geometry it is known that the relationship between the radius of a sphere and its volume (see equation 5.1) is not the same as that between the radius and its surface area (see equation 5.2).

$$r \sim \sqrt[3]{V} \quad (5.1)$$

$$r \sim \sqrt{A} \quad (5.2)$$

Where r is the radius, V the volume and A the surface area of a sphere. From these simple geometrical considerations it is evident, that the influence of changing the surface area, i.e. the surfactant content, has a more pronounced influence on the reverse micelle size than changing the volume, i.e. the water content.

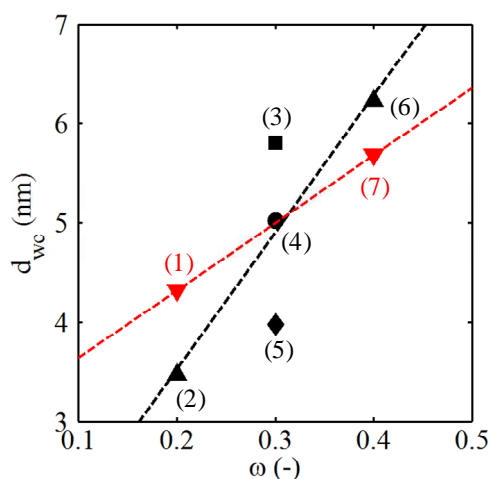


Figure 5.3: Measured sizes of water cores at 25°C from selected microemulsion mixtures. For exact compositions see table 5.1.

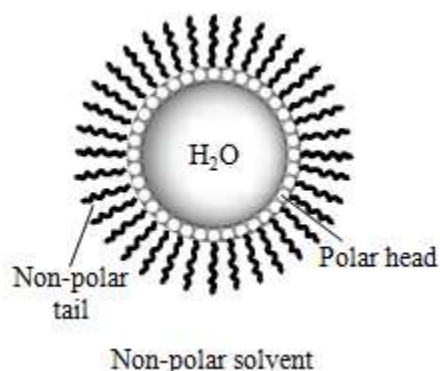


Figure 5.4: Schematic representation of a spherical reverse micelle.

The water to surfactant ratio of compositions 3 and 5 (see figure 5.3 and table 5.1) was not changed but the total amount of n-hexane was increased or decreased respectively compared to the base case composition 4. Upon an increase of the amount of n-hexane the water core size of the

reverse micelle increased while a decrease was observed when less n-hexane was present (see figure 5.3). This size effect can be explained by the solubility of PEGDE in n-hexane. The surfactant in the w/o microemulsion can dissolve in the non-polar phase (n-hexane in this work) to a certain extent. If the volume of the non-polar phase is increased, more surfactant can dissolve in this volume. Due to this effect only a smaller amount of surfactant is still available for the stabilisation of the aqueous phase leading to a higher water to surfactant ratio at the reverse micelle interface, i.e. ω_{interf} . This higher ω_{interf} therefore increases the micelle size as previously discussed. To obtain this new ω_{interf} and the solubility of PEGDE in n-hexane the compositions 3 and 5 are extrapolated to the linear trend obtained from compositions 2, 4 and 6 (see figure 5.5) (compositions 2-4 and 5-6 have all the same absolute amount of water, so that the solubility effect of the surfactant in the water phase does not play a role). The water to surfactant ratio at the reverse micelle interface (ω_{interf}) of compositions 3 and 5 is calculated assuming that the changes in n-hexane content only result in a de-/increase of the ω_{interf} . In this case the relation of the water core diameter (d_{wc}) to ω_{interf} should follow the linear trend given by compositions 2, 4 and 6. These calculations result in an average solubility of PEGDE in n-hexane of 0.12 g/g (see table 5.2).

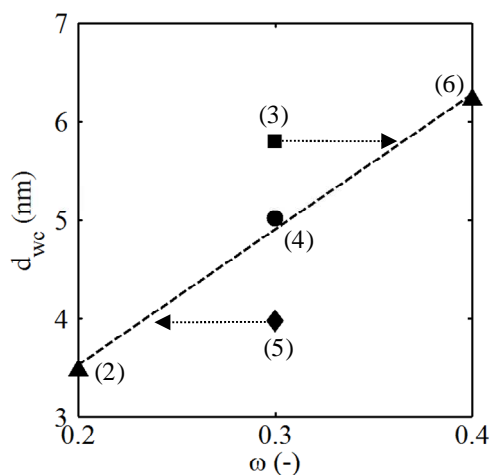


Figure 5.5: Calculation of the solubility of PEGDE in n-hexane at 25°C. Water core (wc) sizes were measured using DLS.

Table 5.2: Water to surfactant ratio at the interface of the reverse micelles and solubility of PEGDE in n-hexane.

Composition No.	ω (g/g)	ω_{interf} (g/g)	Dissolved PEGDE (g/g)
3	0.30	0.36	0.09
5	0.30	0.23	0.15

5.2.1 Model size predictions for reverse micelles

Several mathematical models have been proposed in literature to predict the sizes of micelles and reverse micelles in microemulsions. Two main theories, which led to equations to estimate the size/diameter of the water core (d_{wc}), are discussed here. Firstly the equation proposed by Kinugasa et al. [20] (see equation 5.3) and secondly the equation proposed by Mabaso [1] (see equation 5.4):

$$d_{wc} = 2 \left(\frac{V_W}{V_T} \right)^{\frac{1}{3}} \left(\frac{t_s}{\phi^{\frac{1}{3}} - \left(\frac{V_W}{V_T} \right)^{\frac{1}{3}}} \right) \quad (5.3)$$

$$d_{wc} = 2 \frac{t_s}{\left(\frac{\rho_W + \omega \rho_S}{\omega \rho_S} \right)^{\frac{1}{3}} - 1} \quad (5.4)$$

Where:

d_{wc} is the diameter of the water core in the reverse micelle in nm.

V_W is the total volume of the water phase.

V_T is the total volume of the total w/o microemulsion.

t_s (Å) = 1.5 + 1.265 · N_C [21] where N_C is the number of carbon atoms in the non-polar surfactant chain, i.e. 12 for PEGDE.

ϕ is the volume fraction of the suspended particles, i.e. the reverse micelles.

ρ_W is the density of water, i.e. 1 g/ml.

ρ_S is the density of the surfactant, i.e. 0.82 g/ml.

Several relationships between ϕ and the viscosity of the suspension have been proposed in literature [20, 22, 23]. The first relationship is based on work by Einstein in the early 1900s (see equation 5.5). This relationship does however not account for particle, i.e. reverse micelle, interactions and was revised by Cheng and Schachman in the 1950s (see equation 5.6) and Batchelor in the 1970s (see equation 5.7).

$$\frac{\eta - \eta_0}{\eta_0} = 2.5\phi \quad (5.5)$$

$$\frac{\eta - \eta_0}{\eta_0} = 2.5\phi + 14.1\phi^2 \quad (5.6)$$

$$\frac{\eta - \eta_0}{\eta_0} = 2.5\phi + 6.2\phi^2 \quad (5.7)$$

Where:

η is the viscosity of the solution (see table 5.1).

η_0 is the viscosity of the suspending medium, i.e. n-hexane = 0.294 cP.

Both the models proposed by Kinugasa [20] and by Mabaso [1] were applied for the compositions (see table 5.1) measured with dynamic light scattering and the results were compared with the experimental findings (see figure 5.6). For the model developed by Kinugasa the three different approaches to calculate the volume fraction of the reverse micelles are used (equation 5.5-7).

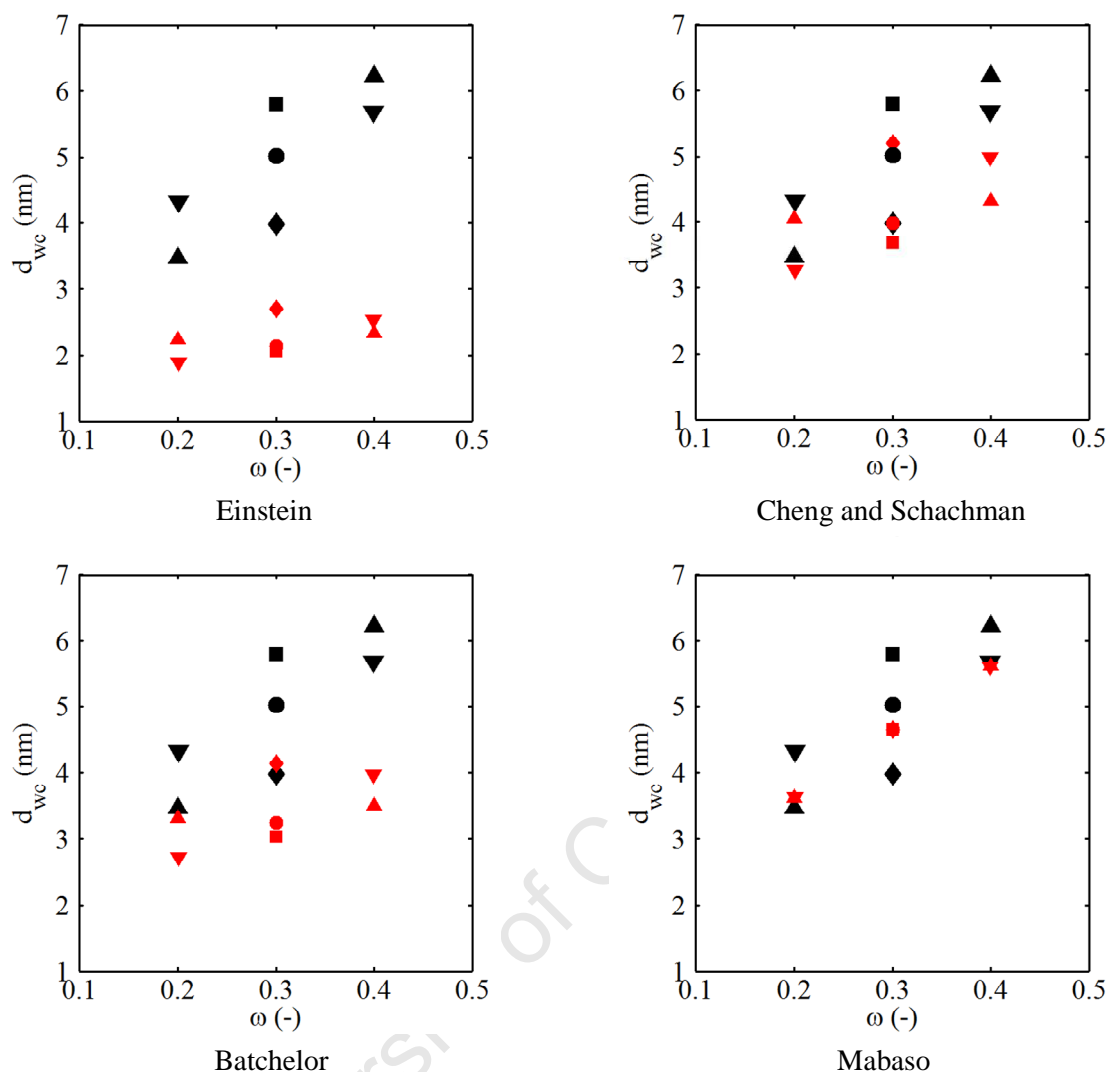


Figure 5.6: Comparison of measured water core sizes (black) (see figure 5.3 and table 5.1) and calculated water core sizes using different models applied to sample compositions (red).

In all three cases the Kinugasa model underestimates the sizes of the water cores in the reverse micelles (see figure 5.6, “Einstein”, “Cheng and Schachman” and “Batchelor”). The calculation using the approach to calculate the volume ratio of the reverse micelles proposed by Cheng and Schachman [22, 23] (see equation 5.6) gives the best fit with the measured data. None of the approaches, however, predict the trends discussed in chapter 5.2. Increases in water core size due to changes in the water to surfactant ratio due to an increase of water content (compositions 1,4,7; ▲) are estimated to be larger than changes due to a decrease of surfactant content (compositions 2,4,6; ▼) which is not in agreement with the experimentally observed results. Also in contrast to the experimental observations a decrease of the oil content (composition 5; ■) is modelled to yield larger reverse micelle water cores. These differences to the experimental results can be explained by the dependency of the Kinugasa model on the water volume fraction. The increase of the water to surfactant ratio as well as the decrease of the n-hexane content leads to an increase in the water volume fraction resulting in an increase in the calculated size of the water core. No solubility effects, as discussed in chapter 5.2, are incorporated in the model.

The model proposed by Mabaso [1] does predict the size range of the reverse micelles very well. However due to its sole dependency on the water to surfactant weight ratio, neither changes in n-hexane content nor differences in composition resulting in the same water to surfactant ratio are taken into account.

In conclusion the here discussed models can be applied to predict the water core size of a reverse micelle as a first estimate. Especially the model proposed by Mabaso [1] is suited for this purpose as it does not require any additional experimental values such as the viscosity of the microemulsion as is needed for the model by Kinugasa [20]. The Mabaso model can further be corrected by not utilising the overall water to surfactant ratio but by incorporating the solubility of the surfactant in the non-polar phase (see chapter 5.2) and use the water to surfactant ratio at the interface of the reverse micelle to predict water core sizes. Further investigation of the solubility behaviour of PEGDE in n-hexane would be required for this adjustment.

5.3 Influence of temperature on the size of the reverse micelle

In order to study the influence of temperature on the water core size (d_{wc}) of the reverse micelle, the water core size of four selected compositions (see table 5.3) was measured with dynamic light scattering at 10 and 25°C.

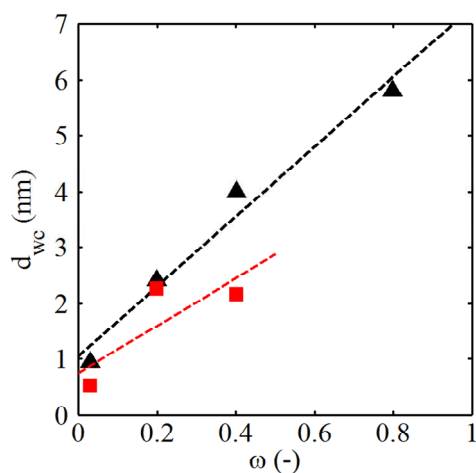


Figure 5.7: Water core size (d_{wc}) in the reverse micelle as function of water to surfactant mass ratio (ω) at constant total volume and constant n-hexane mass ratio at 10°C (\blacktriangle) and 25°C (\blacksquare).

Table 5.3: Composition of microemulsions for measurement of size of reverse micelles using dynamic light scattering (DLS) at 10 and 25°C.

Composition No.	Water (g)	Surfactant (PEGDE) (g)	n-Hexane (g)	ω (-)
1	0.18	5.96	28.85	0.03
2	1.02	5.11	28.85	0.20
3	1.76	4.38	28.86	0.40
4 ^a	2.72	3.41	28.86	0.80

^a Sample not stable at 25°C, only measured at 10°C.

An increase in temperature leads to a decrease in water core size in the reverse micelle (see figure 5.7). As discussed in chapter 5.1 it is reported that the critical micelle concentration, i.e. the minimum amount of surfactant molecules required to form a reverse micelle, decreases with increasing temperature [11]. This leads to smaller and more reverse micelles in the microemulsion at higher temperatures.

References

- [1] E.I. Mabaso, Nanosized iron crystallites for Fischer-Tropsch synthesis, Department of Chemical Engineering, PhD, University of Cape Town, Cape Town, 2005.
- [2] V. Cheang, Effect of crystallite size and water partial pressure on the activity and selectivity of low temperature iron-based Fischer-Tropsch catalysts, Department of Chemical Engineering, PhD, University of Cape Town, Cape Town, 2009..
- [3] C.A. Welker, Ruthenium based Fischer-Tropsch synthesis on crystallites and clusters of different sizes, Department of Chemical Engineering, PhD, University of Cape Town, Cape Town, 2007.
- [4] M. Boutonnet, J. Kizling, P. Stenius and G. Maire, *Colloids and Surfaces*, 5 (1982) 209.
- [5] W.M. Targos, 1987, Method of making a catalyst composition comprising uniform-size metal components on a support, USA, Patent, U.S. 4714693.
- [6] M.J. Lawrence and G.D. Rees, *Advances in Drug Delivery Reviews*, 45 (2000) 89.
- [7] V. Uskokovic and M. Drogenik, *Surface Review and Letters*, 12 (2005) 239.
- [8] V. Uskokovic and M. Drogenik, *Advances in Colloid and Interface Science*, 133 (2007) 23.
- [9] J.H. Clint, *Surfactant Aggregation*, Blackie Publishing Group, Glasgow London, 1992.
- [10] T. Inoue, H. Ohmura and D. Murata, *Journal of Colloid Interface Science*, 258 (2003) 374.
- [11] M. Porter, *Handbook of Surfactants*, Springer, London, 1994.
- [12] M.P. Pileni, *Journal of Physical Chemistry*, 97 (1993) 6961.
- [13] U. Natarajan, K. Handique, A. Mehra, J.R. Bellare and K.C. Khilar, *Langmuir*, 12 (1996) 2670.
- [14] I. Lisiecki, *Journal of Physical Chemistry*, 109 (2005) 12231.
- [15] D.J. Mitchell and B.W. Ninham, *Journal of the Chemical Society, Faraday Transactions 2: Molecular and Chemical Physics*, 77 (1981) 601.
- [16] S. Eriksson, U. Nylen, S. Rojas and M. Boutonnet, *Applied Catalysis A: General*, 265 (2004) 207.
- [17] M. Boutonnet, S. Lögdberg and E. Elm Svensson, *Current Opinion in Colloid & Interface Science*, 13 (2008) 270.
- [18] V. Agarwal, M. Singh, G. McPherson, V. John and A. Bose, *Langmuir*, 20 (2004) 11.
- [19] I. Lisiecki, *Colloids and Surfaces A: Physicochemical and Engineering Aspects*, 250 (2004) 499.
- [20] T. Kinugasa, A. Kondo, S. Nishimura, Y. Miyauchi, Y. Nishii, K. Watanabe and H. Takeuchi, *Colloids and Surfaces A: Physicochemical and Engineering Aspects*, 204 (2002) 193.
- [21] C. Tanford, *Journal of Physical Chemistry*, 76 (1972) 3020.
- [22] H.A. Barnes, J.F. Hutton and K. Walters, *An Introduction to Rheology*, Elsevier Science Publisher B.V., Amsterdam, 1989.
- [23] J. Ferguson and Z. Kemplowski, *Applied Fluid Rheology*, Springer, London, 1991.

Chapter 6

Characterisation of the Preparation Methods of Supported Co/Co₃O₄ Crystallites

To study the effect of the support addition at different stages in the reverse micelle technique, alumina supported cobalt oxide crystallites were prepared using four different methods (Method A-D, for details see chapter 4.1.1).

- Method A: Addition of Al₂O₃ support material to the reverse micelle solution; addition of precipitating agent (NH₃-solution); destabilisation of the reverse micelles with acetone; washing of precipitate with acetone; calcination in air in a fluidised bed.
- Method B: Addition of precipitating agent (NH₃-solution) to the reverse micelle solution; addition of Al₂O₃ support material; destabilisation of the reverse micelles with acetone; washing of precipitate with acetone; calcination in air in a fluidised bed.
- Method C: Addition of precipitating agent (NH₃-solution) to the reverse micelle solution; destabilisation of the reverse micelles with acetone; washing of precipitate with acetone; deposition of the precipitate onto the Al₂O₃ support material; calcination in air in a fluidised bed.
- Method D: Addition of precipitating agent (NH₃-solution) to the reverse micelle solution; destabilisation of the reverse micelles with acetone; washing of precipitate with acetone; calcination in air; deposition of the Co₃O₄ crystallites on the Al₂O₃ support material.

The composition of the reverse micelle systems and the water to surfactant weight ratio (ω) yielding the respective samples are given in table 6.1.

Table 6.1: Composition of the microemulsions used to obtain samples CAT A-D.

Catalyst	Hexane (g)	PEGDE (g)	Co-Sol. ^a (g)	Conc. ^b (mol/l)	ω (g/g)
CAT A	300	30.0	13.8	0.52	0.4
CAT B	400	40.0	17.0	0.20	0.4
CAT C	500	68.4	46.5	0.19	0.6
CAT D	500	68.4	29.2	0.15	0.4

^a Aqueous cobalt solution.

^b Concentration of Co(NO₃)₂·6H₂O in the aqueous cobalt solution.

The resulting samples were studied with different characterisation methods to determine the optimal preparation route to yield the desired cobalt model catalysts. For the present work the optimal catalyst must display well dispersed nano-sized cobalt crystallites (no agglomerates) with a very narrow size distribution so that possible trends in the Fischer-Tropsch activity and selectivity can be directly related to certain crystallite sizes. The catalysts should retain these characteristics throughout activation/reduction and the Fischer-Tropsch reaction. This stability of the active phase is often realised by the introduction of metal support interactions [1]. These interactions, which are well documented for the alumina/cobalt system [2-4], are introduced through the incorporation of cobalt ions in the alumina matrix at the metal-support interface resulting in non-reducible cobalt aluminates which can act as anchors for cobalt crystallites and therefore minimise crystallite mobility and thus prevent further crystallite growth via sintering [5]. The formation of these metal support interactions however results in a loss of active material for the FTS, which can not easily be quantified and therefore it can cloud obtained activity and selectivity results. Generally a high degree of reduction from the oxidic cobalt phase to a preferably pure metallic phase, i.e. no mixture of fcc and hcp crystal structures [6, 7], is desired as these may display different Fischer-Tropsch performances [8, 9] and their ratio may change during FT experiments. Samples prepared with all four methods were characterised using various methods to eliminate preparation methods yielding catalysts which do not comply with the above mentioned criteria.

6.1 Atomic absorption spectroscopy (AAS)

In all four preparation methods studied (see chapter 4.1.1) it was aimed to yield an alumina supported cobalt catalyst with a total cobalt loading of 5 wt%. In order to measure the obtained cobalt loading the prepared sample catalysts were digested in a mixture of hydrochloric acid (HCl), hydrofluoric acid (HF), nitric acid (HNO₃) and perchloric acid (HClO₄) (for exact ratios and procedure see chapter 4.5.3). The measured cobalt loadings are given in table 6.2.

Table 6.2: Cobalt loading (wt% cobalt) of four catalyst samples obtained from AAS analysis.

Sample	Co wt% (AAS)
CAT A	4.0
CAT B	5.1
CAT C	4.7
CAT D	5.0

Methods B-D yield catalyst samples with the desired cobalt loading of approximately 5 wt%. The slightly lower loading of CAT A might be the result of a more intense washing in this preparation procedure, resulting in the loss of cobalt hydroxide precipitate. However it is not too low for studies in the FTS.

6.2 Raman spectroscopy

Raman spectroscopy allows the identification of the cobalt oxide phases present on the four samples by comparison with the scans of known samples or with data from literature [10-13]. To avoid overheating of the black coloured catalysts by the Raman excitation laser, the samples are mixed with pure potassium bromide (KBr) powder and pressed into a pellet (see chapter 4.5.4).

The obtained spectra compare well to the reference material Co_3O_4 (obtained via the calcination of cobalt hydroxide (prepared via precipitation) at 500°C in air and characterised and identified with PXRD) as well as to Co_3O_4 spectra reported in literature [11-13]. No peaks for other cobalt phases including CoAl_2O_4 [10], $\text{Co}(\text{OH})_2$ [13] or CoO [11] could be observed. It can therefore be concluded that the predominant cobalt phase on the surface of all catalyst samples after calcinations is the spinel Co_3O_4 oxide.

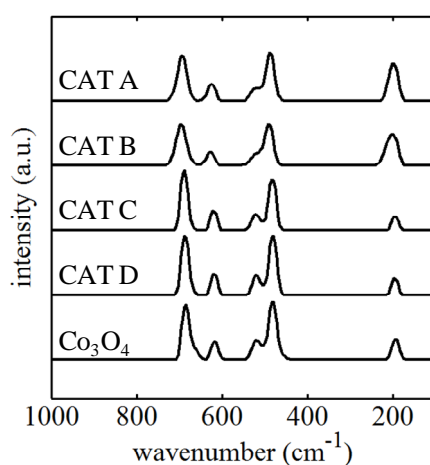


Figure 6.1: Raman spectra of studied catalyst samples and spectra of Co_3O_4 as reference material.

6.3 Powder X-ray diffraction (PXRD)

After the catalyst preparation the calcined samples were analysed using powder X-ray diffraction. From the diffraction patterns the different crystalline phases in a sample can be identified by comparison with known reference patterns. In addition to the amount of cobalt, the crystallite size does also influence the peak size and shape of the diffraction pattern of the metal oxide. Larger crystallites result in sharper and more intense peaks while smaller crystallites result in broad peaks with a low intensity. All four preparation methods tested here were aimed to yield cobalt oxide crystallites smaller than 15 nm. Due to the differences in the reverse micelle composition in the preparation process of the four studied samples (see table 6.1) we do not expect the same crystallite sizes. However, the crystallite size is at this stage only of secondary interest as the main focus lies on the nature of the cobalt phase and its behaviour during reduction/activation. A Rietveld refinement of the obtained experimental scans was conducted. This method entails the mathematical modelling of experimental diffraction patterns based on a convolution of known reference patterns/crystalline phases and instrument characteristics, and it allows quantify the phases compositions and average sizes of the different crystallite phases. It has to be noted that these average sizes are based on

spherical crystallites and they are to be compared with volume weighted average crystallite size obtained from other measurements. A further difficulty with the present cobalt oxide/alumina system is the partially unknown crystallite phase of the alumina support. Although mainly consisting of known and well studied γ - Al_2O_3 , it is suspected that the alumina used in this study also contains an unknown amounts of the previously not studied δ phase of alumina. Traditional Rietveld refinement requires the input of all present crystalline phases including their respective space groups. This can not be done for the alumina used in this study. Scarlett and Madsen [14] developed a novel approach to apply Rietveld refinement methods to partially or not known crystal structures (PONKCS) (for details see chapter 4.5.2). Adapting this approach the cobalt oxide/alumina system can be fully analysed.

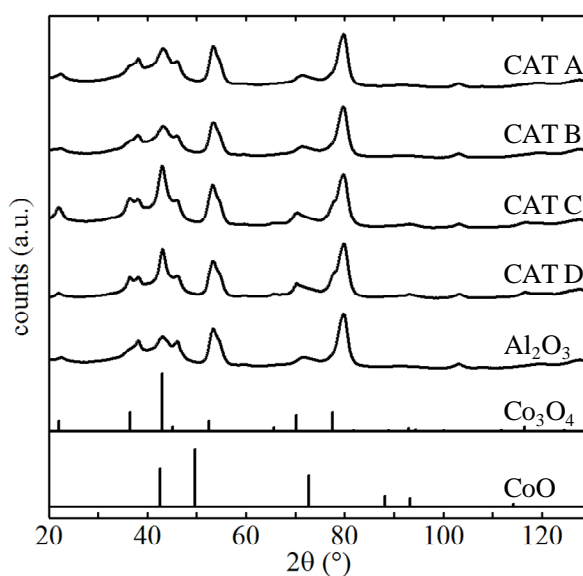


Figure 6.2: PXRD spectra of samples CAT A-D, pure Al_2O_3 and reference patterns of Co_3O_4 and CoO ($\lambda = 0.178897$ nm).

Table 6.3: Average Co_3O_4 crystallite size obtained from Rietveld refinement using PONKCS approach.

Sample	$d_{\text{Co}_3\text{O}_4}$ (nm)
CAT A	3.6
CAT B	3.4
CAT C	7.2
CAT D	9.9

Figure 6.2 and table 6.3 display the results obtained from XRD measurements and Rietveld refinement of the experimental spectra. Due to the low cobalt loadings, all scans are dominated by the diffraction pattern of the pure alumina support. From comparison of the experimental XRD traces with reported diffraction patterns, the only phase present besides the alumina support is Co_3O_4 . The most prominent diffraction line of this phase is found at 43° 2θ (cobalt X-ray source with a wavelength of $\lambda = 0.178897$ nm). Rietveld refinement of the experimental data confirms Co_3O_4 to be the only XRD visible phase present (i.e. crystalline and above critical crystallite size above ~ 1 - 2 nm).

The crystallite sizes shown in table 6.3 reflect the differences in peak shape in the experimental patterns, with CAT D having the largest average Co_3O_4 crystallite size, 9.9 nm, and therefore resulting in the sharpest and most intense peak and CAT B having the smallest average Co_3O_4 crystallite size, 3.2 nm.

6.4 X-ray photoelectron spectroscopy (XPS)

The oxidation state of the cobalt oxide species was further studied with X-ray photoelectron spectroscopy (XPS). In Co_3O_4 the cobalt cation is present in the Co^{2+} state, tetrahedrally coordinated to the O^{2-} , and in the Co^{3+} state which is coordinated octahedrally to the oxygen anions [11]. Yang and co-workers [13] synthesised Co_3O_4 and $\text{Co}(\text{OH})_2$, the latter as a reference compound in which the cobalt cation is present in the pure Co^{2+} state. Studying the two compounds with XPS they fitted the two Co 2p areas with a series of peaks varying in position and number (see table 6.4). By investigating the Co 2p region in catalysts CAT A-D and applying the curve fitting parameters proposed in literature, we were able to show differences in the oxidation states of the cobalt cations in the four samples. Although all samples showed a Co_3O_4 phase in the studies with Raman spectroscopy as well as XRD, only the Co 2p area of CAT C and D could be fitted with the proposed fitting parameters for Co_3O_4 . For samples CAT A and B the best fit was achieved by applying the peak positions proposed for $\text{Co}(\text{OH})_2$. This indicates the presence of a considerable amount of cobalt cations in the 2+ state. The Co^{2+} cations are known to incorporate into the alumina crystal lattice and form cobalt aluminates like CoAl_2O_4 [2-4]. It should however be borne in mind that XPS (as opposed to XRD and Raman) is a surface sensitive technique and the phases observed here are only present on the surface of the examined crystallites. Nonetheless, the presence of Co^{2+} cations may play an important role in the formation of metal support interactions.

Table 6.4: Fitted XPS binding energies of $\text{Co}(\text{OH})_2$ and Co_3O_4 [13].

Co 2p _{3/2} (eV)	
$\text{Co}(\text{OH})_2$	Co_3O_4
780.7	779.9
	781.2
782.5	782.5
786.3	785.5
790.7	789.8

6.5 Temperature programmed reduction (TPR)

The reduction behaviour of the four calcined catalyst samples was studied by means of temperature programmed reduction. The samples were heated in a constant flow of 5% H_2 in Ar with a temperature ramp of $10^\circ\text{C}/\text{min}$ to 1000°C and held for 1 h. Over the whole process the hydrogen consumption is measured with a thermal conductivity detector (TCD).

The TPR spectra of supported cobalt oxides have been studied extensively in literature [11, 15-19]. However, the peak identification is still discussed controversially. The TCD spectrum of the reduction of Co_3O_4 has been described by some as one peak [16, 19] while others consider two adjacent peaks [11, 15, 18] indicating the two step reduction from Co_3O_4 first to CoO followed by the reduction to metallic Co . Figure 6.3 shows the TPR spectra of catalysts CAT A-D.

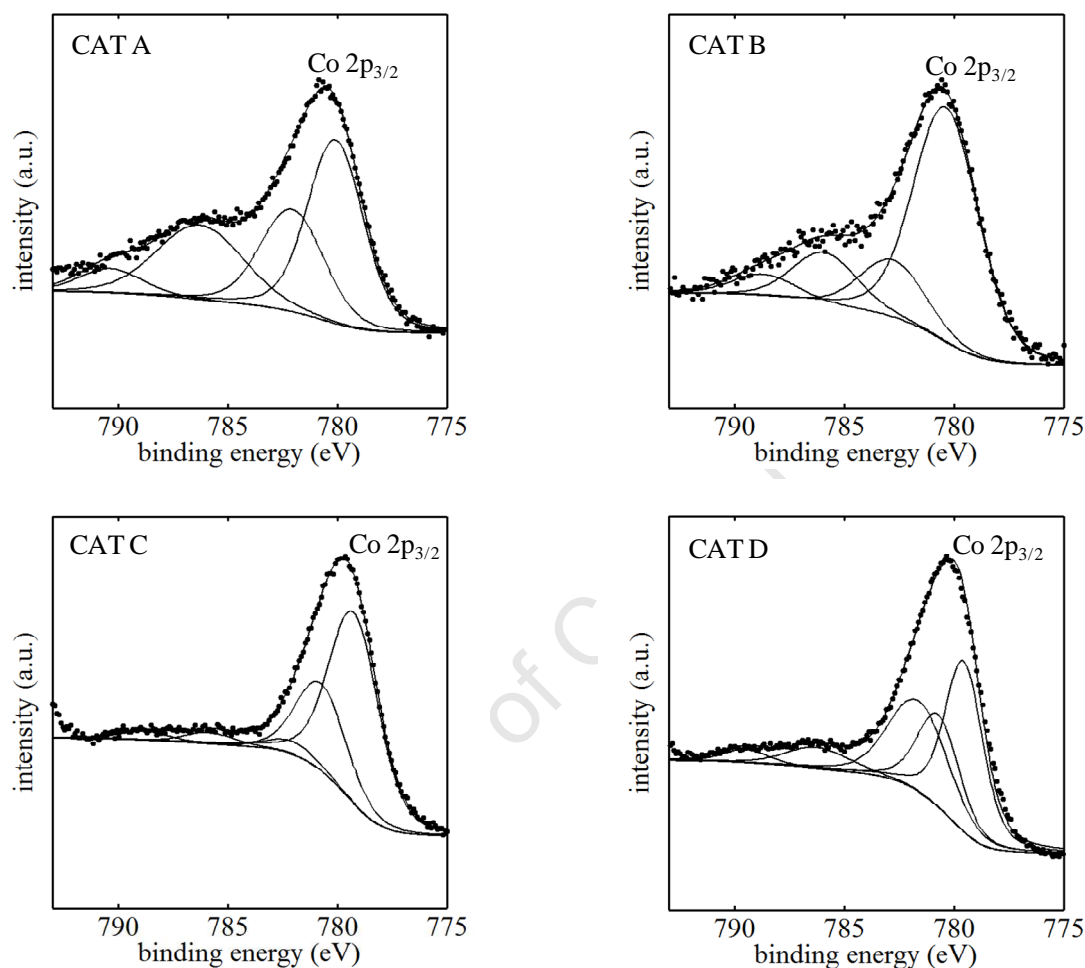


Figure 6.3: High resolution XPS $\text{Co } 2p_{3/2}$ spectra with curve fitting according to table 6.4.

Catalyst samples CAT A and B show only one low temperature reduction peak around 200°C . A second peak at temperatures above 750°C indicates the presence of strong interactions between Co^{x+} and the Al_2O_3 support [14, 17] as it is the case when cobalt is incorporated in the crystal lattice of alumina. Catalyst samples CAT C and D display two adjacent peaks between 200 and 500°C which can be assigned to the two step reduction process of Co_3O_4 . CAT C shows complete reduction at temperatures as low as 325°C while CAT D is only fully reduced at 500°C . This indicates a very low or no interaction of the alumina support with the cobalt phase in CAT C while some interaction seems to exist with sample CAT D. This difference in metal-support interaction can be explained by the differences in the preparation methods C & D. As figure 6.5 depicts, in the case of method C the support is contacted with the precipitated cobalt phase prior to calcination. Despite extensive washing the precipitate is likely to still be covered with residual surfactant (PEGDE) from the reverse micelle solution at this stage. These surfactant/cobalt hydroxide particles may have larger diameters than the

average pore diameter of the support of 11.5 nm [18]. This results in the cobalt particles being deposited on the outer surface of the support structure and therefore they only have minimal contact with the alumina (see figure 6.5). In method D the precipitate of the reverse micelle solution is calcined and forms sub 10 nm Co_3O_4 crystallites. When these are contacted and dispersed onto the support they have the possibility to enter the pore structure of the alumina and therefore be in closer contact with the carrier material without forming excessive strong metal support interactions (SMSI) [1] in the form of cobalt aluminates. The formation of cobalt aluminates seem to have dominated in methods A and B where the support was added directly to the reverse micelle system (before or after precipitation). Here a very intimate contact of the cobalt precursor and the alumina existed and may have caused the observed effect.

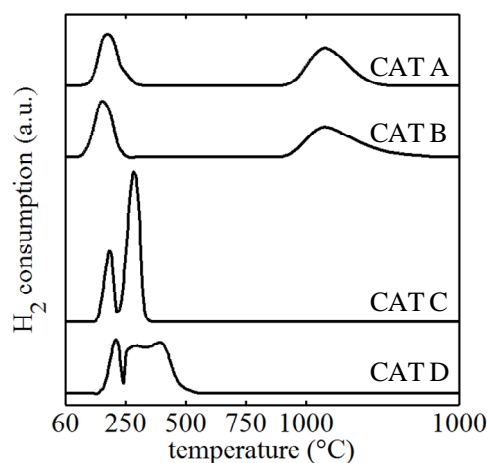


Figure 6.4: TPR spectra of studied catalyst samples (CAT A-D).

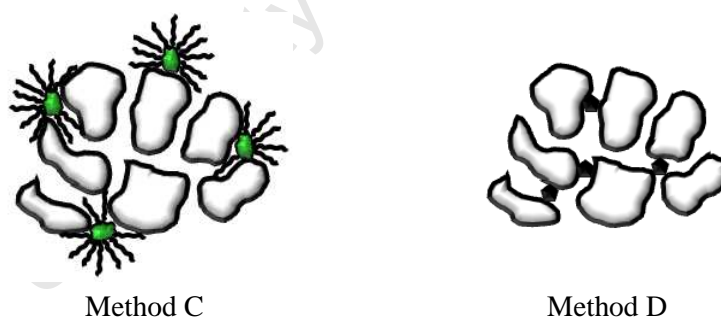


Figure 6.5: Schematic representation of the combination of precipitate/ Co_3O_4 crystallites and alumina support in preparation methods C & D. Residual surfactant hinders the cobalt hydroxide particles to enter the pore structure of the support (method C). Calcined Co_3O_4 crystallites can enter the pore structure and undergo stronger interactions with the support (method D).

6.6 In-situ powder X-ray diffraction (PXRD)

The two samples which did not show any signs of cobalt aluminate formation, i.e. CAT C & D, were tested for the stability of the cobalt phase under reduction conditions. The samples (approximately 500 mg) were heated in a constant flow of hydrogen (40 ml/min \cdot g_{cat} (STP)) at 1°C/min to 350°C, for CAT C, and to 450°C in the case of CAT D and then held at the respective temperature for four hours.

During the heating ramp every 25°C and during the holding step every 40 minutes a PXRD scan is taken. The temperature program was halted during the scans at the respective temperatures.

From figures 6.6 A & B and 6.7 A & B the reduction process of CAT C & D can be followed easily. Below temperatures of 200°C the behaviour of the two samples is very similar. Both display a Co_3O_4 phase at room temperature (diffraction lines at 43.07, 52.54, 70.20 and 77.50° 2 Θ , see table 6.5). At temperatures between 200 and 250°C this phase rapidly diminishes in the first reduction step and forms CoO (diffraction lines at 42.65, 49.66, 72.87 and 88.28° 2 Θ , see table 6.5). In the sample CAT C this phase is quickly, i.e. below 250°C, further reduced to metallic cobalt. In the case of CAT D the CoO diffraction pattern only diminishes slowly and it can still be observed at 300-375°C. The metallic phase in CAT C, which develops above 250°C, does consist of two crystalline phases: face-centred cubic (fcc) (most intense diffraction lines at 51.83 and 60.62° 2 Θ , see table 6.5) and hexagonal closed-packed (hcp) (most intense diffraction lines at 48.68 and 55.69° 2 Θ , see table 6.5). Both phases also show a diffraction line at 91.08 (fcc) and 91.10° (hcp) 2 Θ . The proximity of these two diffraction lines however makes them unsuitable for phase identification/distinction. A mixed crystallite phase is undesired in this study as selectivity results obtained from Fischer-Tropsch experiments can not be assigned to a single crystallite phase but would be clouded by potentially different performance of the two phases. Recently Enache et al. [20] published a study which shows increased FT activity for hcp cobalt in comparison to the fcc phase. This difference in catalytic activity would also interfere with data interpretation in this study. For sample CAT D only a fcc cobalt phase (diffraction lines at 51.83 and 60.62° 2 Θ , see table 6.5) could be observed. The distinct diffraction lines of hcp cobalt at 48.68 and 55.69° 2 Θ do not show. It is well documented in literature that the fcc phase in metallic cobalt is the stable phase at higher temperatures. Several studies have shown a phase change from hcp to fcc in a hydrogen atmosphere under heat treatment and found the phase transition temperature to be around 500°C for cobalt crystallites in the micrometer size range [6, 21, 22]. Kitakami and co-workers [23] describe the stable phase of metallic cobalt at room temperature to be size dependent. Below a crystallite diameter of 20 nm the stable phase is reported to be fcc while between 20 and 40 nm a mixed phase is present and above 40 nm cobalt behaves as reported for the bulk metal crystallising in a hcp phase. The combination of small crystallites and the elevated reduction temperature, i.e. higher temperature stability of CoO against reduction, in CAT D might result in the experimentally measured pure face-centred cubic phase for the metallic cobalt.

Figures 6.6 & 6.7 C show the obtained crystallite sizes as function of temperature and the degree of reduction. In both samples the crystallite size of Co_3O_4 decreases slightly upon the formation of the CoO phase, i.e. no crystallite growth takes place during the first step of reduction. Upon the reduction to metallic cobalt the crystallite sizes of the fcc cobalt phase in CAT C do increase by up to a factor of seven, from under 10 nm to approximately 50 nm, indicating the presence of extensive sintering during the second reduction step. The hcp cobalt phase does not undergo such an extensive crystallite growth and forms crystallites with an average diameter of 10 to 11 nm. In CAT D the crystallite size of the metallic phase does not increase significantly compared to the initial size of the Co_3O_4 crystallites. According to theory the crystallite size of Co_3O_4 should, in absence of crystallite growth processes, decrease by 25% after reduction to metallic cobalt due to the loss of oxygen. As this decrease in crystallite size is not observed, a moderate crystallite growth must also have taken place upon reduction of CAT D.

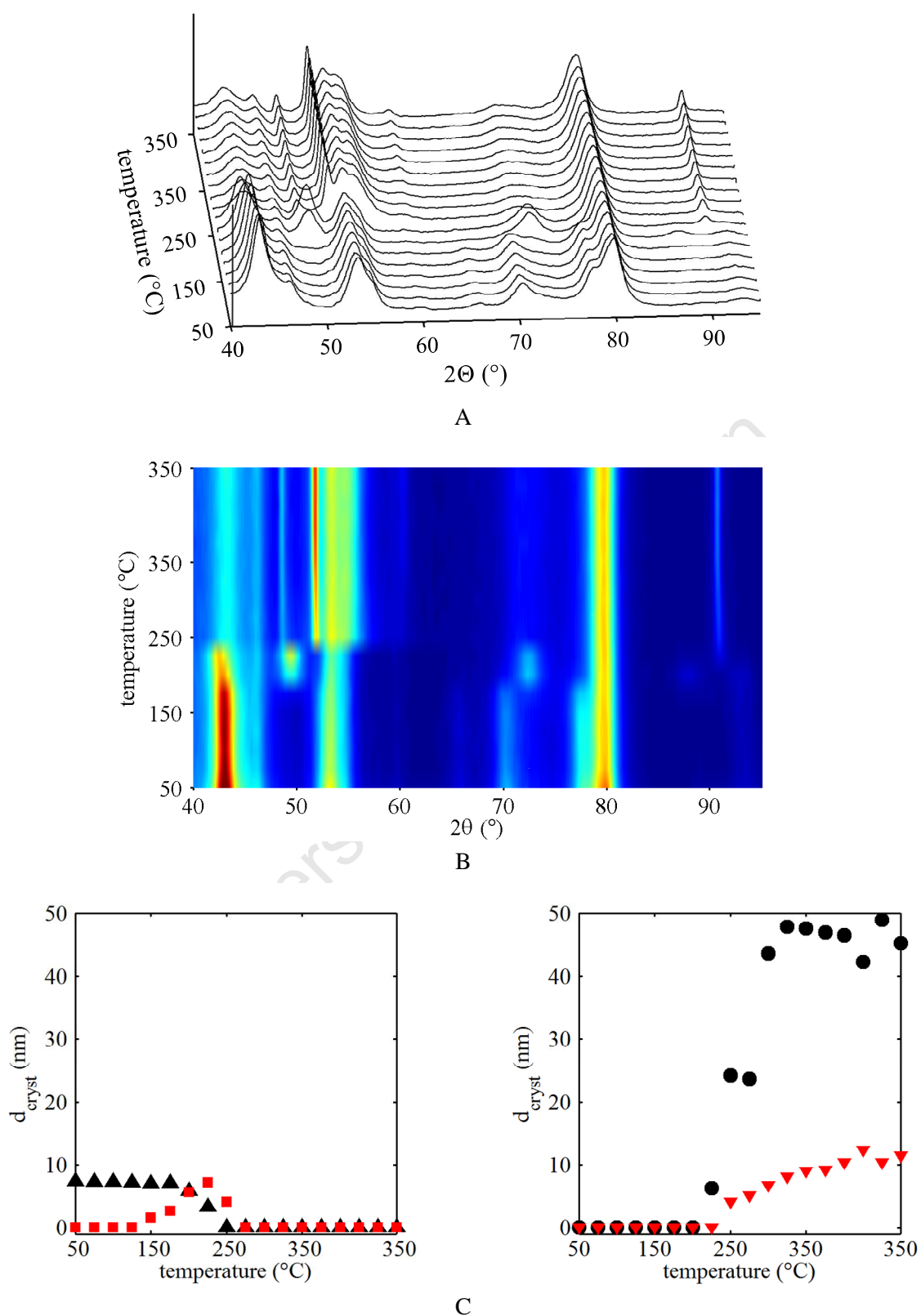


Figure 6.6: In-situ PXRD scans of CAT C. A: diffraction patterns, 3D view; B: diffraction patterns, on-top view; C: crystallite sizes of Co_3O_4 (▲), CoO (■), hcp Co (▼) and fcc Co (●) as function of temperature obtained via Rietveld refinement using POKKCS approach.

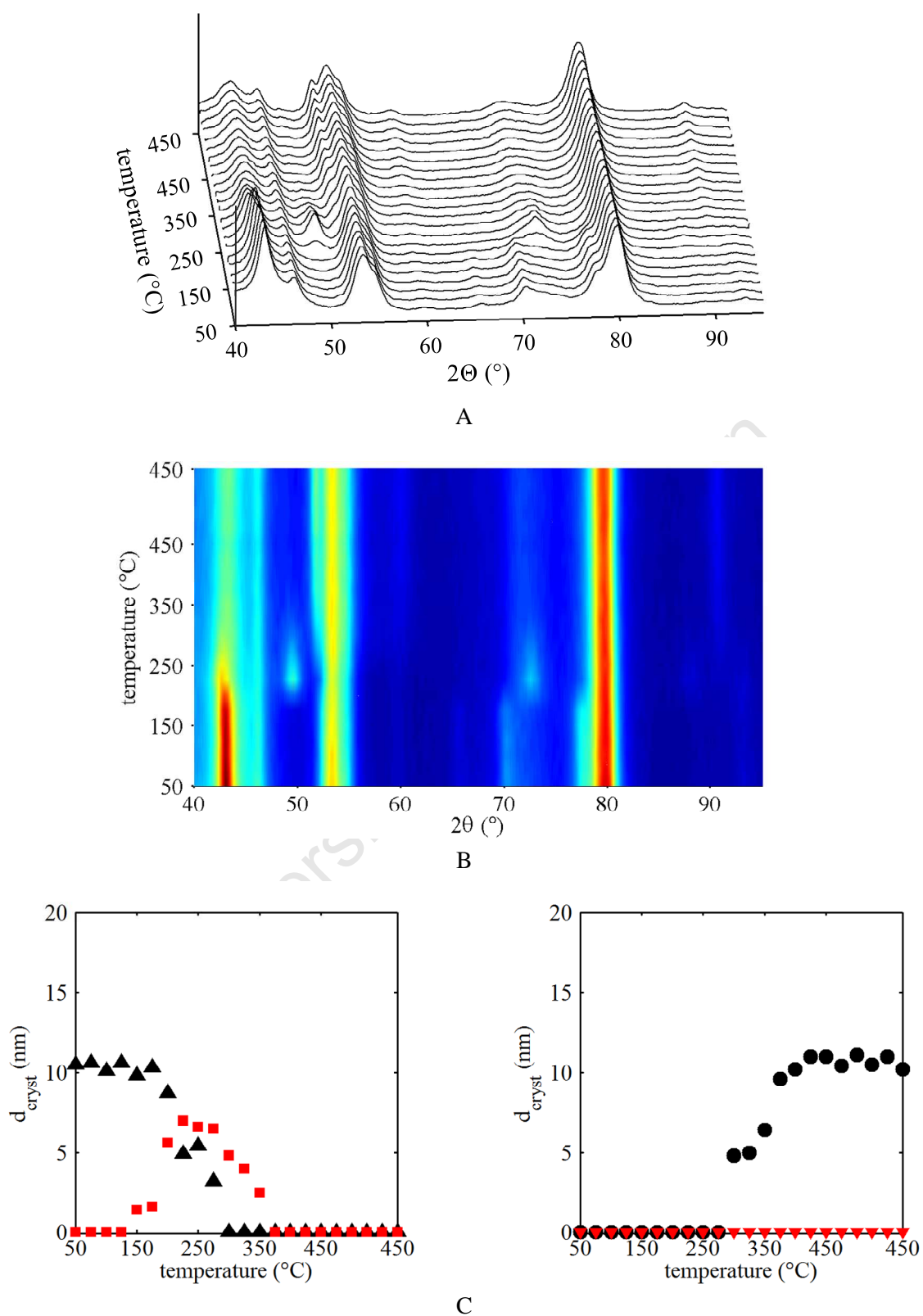


Figure 6.7: In-situ PXRD scans of CAT D. A: diffraction patterns, 3D view; B: diffraction patterns, on-top view; C: crystallite sizes of Co_3O_4 (▲), CoO (■), hcp Co (▼) and fcc Co (●) as function of temperature obtained via Rietveld refinement using POKKCS approach.

Table 6.5: Reference diffraction patterns of Co₃O₄, CoO, hcp Co and fcc Co in the relevant 2 Θ range for a cobalt X-ray source ($\lambda = 1.78897 \text{ \AA}$). Values from International Centre for Diffraction Data PDF-2 database.

Phase	2 Θ (°)	Int. (%) ^a	Phase	2 Θ (°)	Int. (%) ^a	Phase	2 Θ (°)	Int. (%) ^a	Phase	2 Θ (°)	Int. (%) ^a
Co ₃ O ₄	43.07	100	CoO	42.65	65	Co (hcp)	48.68	27	Co (fcc)	51.83	100
	45.07	9		49.66	100		52.16	28		60.62	40
	52.54	19		72.87	50		55.69	100		91.08	25
	65.65	8		88.28	20		74.12	11			
	70.20	29		93.33	13		91.10	10			
	77.50	34									
	81.78	2									
	88.82	2									
	93.03	7									
94.44	4										

^a relative intensities in %

6.7 Variation of precipitation agent

A short screening of different precipitation agents was conducted in preparation method A (see chapter 4.1.1-2). The 25 wt% NH₃ solution was replaced with gaseous NH₃ and hydrazine hydrate (N₂H₄).

The theoretical advantage of gaseous ammonia as a precipitation agent is the elimination of the additional aqueous phase, which is added in the precipitation step and which does change the overall w/o microemulsion composition as water is introduced with the precipitant. Gaseous ammonia bubbled through the reverse micelle solution did result in a very quick colour change from pink to green, indicating the successful precipitation of the cobalt nitrate. However, the dosage of the gas proved to be difficult. Too much NH₃ would change the pH of the reverse micelle solution so drastically that the stability of the w/o microemulsion was compromised. Furthermore the alumina support is reported to partially dissolve in basic environment [24, 25] increasing the probability of the formation of cobalt aluminates.

Hydrazine is generally known as a reducing agent and it has been claimed to be able to reduce cobalt precursors in reverse micelles directly to the metallic form [26-28], which eliminates the need for heat treatment of the synthesised catalyst during calcination and reduction steps which often result in crystallite size changes. In this study hydrazine was added drop wise at room temperature to the reverse micelle solution. Although a precipitation was observed (visually), the resulting precipitate did not consist of metallic cobalt as expected for a reduction, but most probably of cobalt hydroxide particles. The rapid colour change from pink to green was identical to the one observed during the precipitation of cobalt nitrate with gaseous or dissolved ammonia. The precipitate was collected and dried under nitrogen, to avoid possible re-oxidation of metallic cobalt crystallites, and studied with PXRD. The obtained material appeared amorphous, similar to the above reported precipitated cobalt hydroxide. It should be noted that hydrazine can act as an inorganic base with a similar basic strength

as ammonia ($pK_{b(N_2H_4)} = 6.05$, $pK_{b(NH_3)} = 4.75$ [29]). Due to the lack of improvement in the process and the increased risk associated with handling hydrazine compared to ammonia solution, hydrazine was not further used for the catalyst preparation.

6.8 Conclusion and summary of method variations

In an attempt to find the optimal method to prepare the desired model catalysts for this study, different precipitation agents (see chapter 4.1.2) and different methods of support material (Al_2O_3) addition were studied.

As none of the precipitation agents tested could surpass ammonia solution in effectiveness and usability, ammonia solution was selected as the precipitation agent of choice.

All four preparation methods for support addition (CAT A-D see chapter 4.1.1) yield an alumina powder approximately supporting the desired 5 wt% of cobalt. Although the cobalt after calcination is mostly present as Co_3O_4 , XPS and TPR studies indicate an increased amount of cobalt cations in the 2+ state prior to reduction and the presence of hard to reduce species in the samples CAT A & B. These results suggest the presence/formation of cobalt aluminates, which are undesired as they are inactive for the FTS and therefore result in a loss of active material. In samples CAT C & D these cobalt aluminates could not be detected. Both samples reduce in a two step reduction from Co_3O_4 to CoO to metallic cobalt. Due to the increased cobalt alumina interaction in CAT D, probably introduced through a lack of geometrical constraints in the precipitate loading step compared to method C (see figure 6.5), no extensive crystallite growth is detected upon complete reduction. A combination of stronger metal support interaction and higher reduction temperature might also lead to the pure face-centred cubic cobalt phase detected in CAT D compared to the mixed fcc/hcp phase in CAT C. It is concluded that method D is the ideal preparation route to yield the model catalysts required in this study.

References

- [1] S.J. Tauster, *Accounts of Chemical Research*, 20 (1987) 389.
- [2] A.M. Saib, A. Borgna, J. van de Loosdrecht, P.J. van Berge and J.W. Niemantsverdriet, *Applied Catalysis A: General*, 312 (2006) 12.
- [3] A.M. Saib, D.J. Moodley, I.M. Ciobîca, M.M. Hauman, B.H. Sigwebela, C.J. Weststrate, J.W. Niemantsverdriet and J. van de Loosdrecht, *Catalysis Today*, 154 (2010) 271.
- [4] A. Tavasoli, R.M. Malek Abbaslou and A.K. Dalai, *Applied Catalysis A: General*, 346 (2008) 58.
- [5] J.A. Moulijn, A.E. van Diepen and F. Kapteijn, *Applied Catalysis A: General*, 212 (2001) 3.
- [6] J. Ahmed, S. Sharma, K.V. Ramanujachary, S.E. Lofland and A.K. Ganguli, *Journal of Colloid and Interface Science*, 336 (2009) 814.
- [7] O. Ducreux, B. Rebours, J. Lynch, M. Roy-Auberger and D. Bazin, *Oil Gas Science and Technology*, 64 (2009) 49.
- [8] H. Karaca, J. Hong, P. Fongarland, P. Roussel, A. Griboval-Constant, M. Lacroix, K. Hortmann, O.V. Safonova and A.Y. Khodakov, *Chemical Communications*, 46 (2010) 788.
- [9] H. Karaca, O.V. Safonova, S. Chambrey, P. Fongarland, P. Roussel, A. Griboval-Constant, M. Lacroix and A.Y. Khodakov, *Journal of Catalysis*, 277 (2011) 14.
- [10] L.D. Kock and D.D. Waal, *Journal of Raman Spectroscopy*, 38 (2007) 1480.
- [11] C.-W. Tang, C.-B. Wang and S.-H. Chien, *Thermochimica Acta*, 473 (2008) 68.
- [12] V.G. Hadjiev, M.N. Iliev and I.V. Vergilov, *Journal of Physics C: Solid State Physics*, 21 (1988) L199.
- [13] J. Yang, H. Liu, W.N. Martens and R.L. Frost, *The Journal of Physical Chemistry C*, 114 (2009) 111.
- [14] N.V.Y. Scarlett and I.C. Madsen, *Powder Diffraction*, 21 (2006) 278.
- [15] E. van Steen, G.S. Sewell, R.A. Makhothe, C. Micklethwaite, H. Manstein, M. de Lange and C.T. O'Connor, *Journal of Catalysis*, 162 (1996) 220.
- [16] P. Arnoldy and J.A. Moulijn, *Journal of Catalysis*, 93 (1985) 38.
- [17] S. Todorova, V. Zhelyazkov and G. Kadinov, *Reaction Kinetics and Catalysis Letters*, 57 (1996) 105.
- [18] G.S. Sewell, E. van Steen and C.T. O'Connor, *Catalysis Letters*, 37 (1996) 255.
- [19] A. Sirijaruphan, A. Horvath, J.G. Goodwin Jr. and R. Oukaci, *Catalysis Letters*, 91 (2003) 89.
- [20] D.I. Enache, B. Rebours, M. Roy-Auberger and R. Revel, *Journal of Catalysis*, 205 (2002) 346.
- [21] J.E. Bidaux, R. Schaller and W. Benoit, *Acta Metallurgica*, 37 (1989) 803.
- [22] R. Speight, A. Wong, P. Ellis, P.T. Bishop, T.I. Hyde, T.J. Bastow and M.E. Smith, *Physical Reviews B: Condensed Matter and Material Physics*, 79 (2009) 54101.
- [23] O. Kitakami, H. Sato, Y. Shimada, F. Sato and M. Tanaka, *Physical Review B: Condensed Matter and Material Physics*, 56 (1997) 13849.
- [24] H. Al-Sheeha, M. Marafi and A. Stanislaus, *International Journal of Mineral Processing*, 88 (2008) 59.
- [25] H. Grénman, T. Salmi, D.Y. Murzin and J. Addai-Mensah, *Hydrometallurgy*, 102 (2010) 22.

- [26] M. Yashima, L.K.L. Falk, A.E.C. Palmqvist and K. Holmberg, *Journal of Colloid and Interface Science*, 268 (2003) 348.
- [27] J. Eastoe, S. Stebbing, J. Dalton and R.K. Heenan, *Colloids and Surfaces A: Physicochemical and Engineering Aspects*, 119 (1996) 123.
- [28] M. Boutonnet, J. Kizling, P. Stenius and G. Maire, *Colloids and Surfaces*, 5 (1982) 209.
- [29] A.K. Covington, in: D.R. Linde, (Ed.), *Handbook of Chemistry and Physics*, CRC Press, Inc., Boca Ranton, Ann Arbor, London, Tokyo, (1993).

University of Cape Town

Chapter 7

Characterisation of Model Catalysts

7.1 Cobalt oxide & cobalt crystallites

As discussed in chapter 6 the catalyst synthesis method D (see chapter 4.1.1) was chosen as the preparation method for the model catalysts required in this study. In this method pre-synthesised Co_3O_4 crystallites are deposited onto the alumina support. To tune the sizes of the cobalt oxide crystallites various w/o microemulsions with different water to surfactant mass ratios (ω) were prepared (see table 7.1) to yield different reverse micelle sizes (see chapter 5). The surfactant to oil ratio was kept constant in these preparations. A second variable changed in the preparation of the model catalysts was the concentration of the cobalt precursor ($\text{Co}(\text{NO}_3)_2 \cdot 6\text{H}_2\text{O}$) in the aqueous phase of the reverse micelle. Decreasing the concentration of cobalt nitrate in the water core of the reverse micelle decreases the availability of cobalt during the precipitation step and therefore limits the size of the precipitate particles. The naming of the samples relates to the respective volume weighted mean Co_3O_4 crystallite size obtained from transmission electron microscopy (see chapter 7.1.3).

Table 7.1: Composition of the microemulsions used to obtain nano-sized cobalt oxide crystallites.

Catalyst	Hexane (g)	PEGDE ^a (g)	Co-Sol. ^b (g)	Conc. ^c (mol/l)
CAT 9.6	500	68.4	29.24	0.15
CAT 8.6	1000	136.7	41.80	0.11
CAT 7.3	500	68.4	28.97	0.33
CAT 6.8	500	68.4	14.49	0.32
CAT 5.9	2000	273.6	14.46	0.32
CAT 4.8	1000	136.7	6.24	0.85
CAT 4.4	2000	273.6	55.50	0.08
CAT 4.0	500	68.4	7.62	0.67
CAT 3.1	4000	547.2	28.14	0.16

^a Penta-ethyleneglycol-dodecylether (anionic surfactant)

^b Cobalt solution.

^c Concentration of $\text{Co}(\text{NO}_3)_2 \cdot 6\text{H}_2\text{O}$ in the aqueous cobalt solution.

All prepared model catalysts were characterised with various methods including temperature programmed reduction and desorption, in-situ PXRD measurements, atomic absorption spectroscopy (AAS) as well as electron microscopy and atmospheric powder X-ray diffraction. The latter two methods were conducted with the freshly prepared, i.e. calcined, catalysts as well as after catalyst activation at elevated temperatures in pure hydrogen (samples were passivated in CO₂ after activation).

7.1.1 Atomic absorption spectroscopy (AAS)

For all catalysts prepared the targeted loading was 5 wt% of cobalt on the alumina support. To measure the actual loading the prepared catalyst samples were digested in a mixture of acids (see chapter 4.5.3) and the concentration of cobalt in the solution measured with atomic absorption spectroscopy. Each catalyst sample was digested twice and submitted for AAS analysis. Table 7.2 lists the experimentally obtained loadings of the synthesised model catalysts.

Table 7.2: Cobalt loadings of synthesised model catalysts measured via AAS.

Catalyst	Co-loading (wt%)
CAT 9.6	5.0 ± 0.02
CAT 8.6	2.1 ± 0.03
CAT 7.3	4.3 ± 0.01
CAT 6.8	3.1 ± 0.02
CAT 5.9	2.5 ± 0.04
CAT 4.8	2.2 ± 0.03
CAT 4.4	1.8 ± 0.02
CAT 4.0	3.3 ± 0.05
CAT 3.1	2.6 ± 0.11

For most of the model catalysts the measured cobalt loading is lower than the anticipated 5 wt%. This is a result of losses during the multistep preparation method. As described in chapter 4.1.1 the precipitate is washed extensively to remove residual surfactant from the cobalt hydroxide particles. The precipitate is then transferred to an open watch glass and spread out for calcination. The calcined Co₃O₄ crystallites are resuspended in water under ultrasonication and dried onto the alumina support. All these steps are possible sources of cobalt loss. This loss should be even more pronounced for small particles/crystallites as it is indeed the case in this study.

7.1.2 Temperature programmed reduction (TPR) and degree of reduction (DOR)

The reduction behaviour of the synthesised model catalysts was studied by means of temperature programmed reduction. The samples were heated under a flow of a 5 % H₂ in Ar to 950°C. The exhaust gas was analysed against the feed gas and the hydrogen consumption measured with a thermal conductivity detector (TCD). Figure 7.1 shows the spectra obtained from the TPR measurements

normalised for the amount of cobalt in the catalyst sample. All catalysts display two main reduction peaks indicating the two step reduction of Co_3O_4 via CoO to metallic cobalt (see equations 7.1 & 7.2). From the behaviour of the catalyst in the TPR the reduction/activation procedure prior to the FTS was determined. Slight differences in the position of the second reduction peak resulted in the choice of the corresponding reduction procedures (see table 7.3). While for the samples CAT 9.6, 8.6, 7.3, 6.8, 4.0 the second reduction displays maximum hydrogen consumption around 450°C , the remaining model crystallites (CAT 5.9, 4.8, 4.4, 3.1), all of which exhibit relatively small average crystallite diameters (see table 7.5), reduce at slightly lower temperatures (375°C).

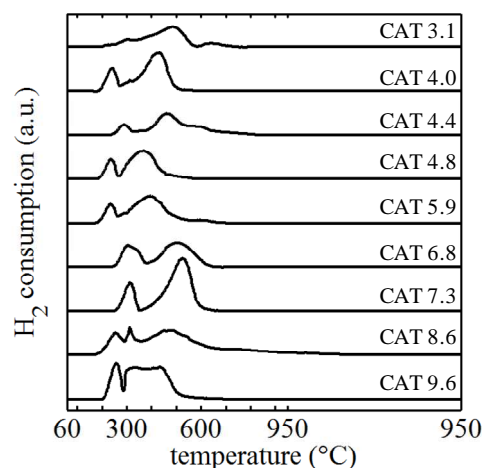


Figure 7.1: TPR spectra of synthesised model catalysts normalised for the respective cobalt loading (heating rate $10^\circ\text{C}/\text{min}$).

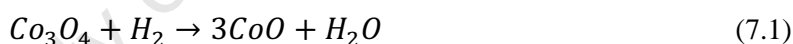


Table 7.3: Reduction conditions of supported nano-sized cobalt model catalysts under a flow of 40 ml/min (STP) H_2 per gram catalyst.

Sample	Red. Temp ($^\circ\text{C}$)	Hold. Time (h)	Ramp Rate ($^\circ\text{C}/\text{min}$)
CAT 9.6; CAT 8.6; Cat 7.3; CAT 6.8; CAT 4.0	450	6	1
CAT 5.9; CAT 4.8; CAT 4.4; CAT 3.1	375	6	1

Due to the nature of the preparation method of the model catalysts (see chapter 4.1.1) the surface of cobalt oxide crystallites, which are deposited on the alumina support, are likely to be partially covered with residual surfactant molecules. To test the extent of residual carbonaceous material, the exhaust gas stream was analysed during the TPR experiment using a mass spectrometer. Figure 7.2 A shows the formation of CH_4 , CO and CO_2 which was monitored during the temperature programmed reduction. As these carbonaceous species might influence catalyst activity and selectivity in the Fischer-Tropsch synthesis and/or cloud FT product analysis through their presence in the product gas stream, the formation of methane was monitored during the activation/reduction prior to the FT experiment. Figure 7.2 B shows the methane formation during the reduction (see table 7.3), reaching a

maximum at approximately 350°C and decreasing rapidly at higher temperatures. Two hours prior to the end of the reduction process no methane was detectable in the exhaust gas stream.

The effectiveness of the reduction, i.e. the degree of reduction, is measured by exposing a reduced catalyst sample (see conditions in table 7.3) to a further temperature ramp to 950°C and measure the hydrogen consumption. The difference in the hydrogen consumption in the TPR measurement and the consumption in this measurement gives the amount of cobalt present in the metallic state. All tested model catalysts show very high degrees of reduction, DOR > 95%. This indicates the absence of strong metal support interactions in form of cobalt aluminates as these are reported to only reduce at temperatures above 750°C [1-6]. Combined with the metal loading obtained from atomic absorption measurements (AAS) (see chapter 7.1.1) the content of metallic cobalt after activation and prior to exposure to Fischer-Tropsch conditions can be calculated (see table 7.4).

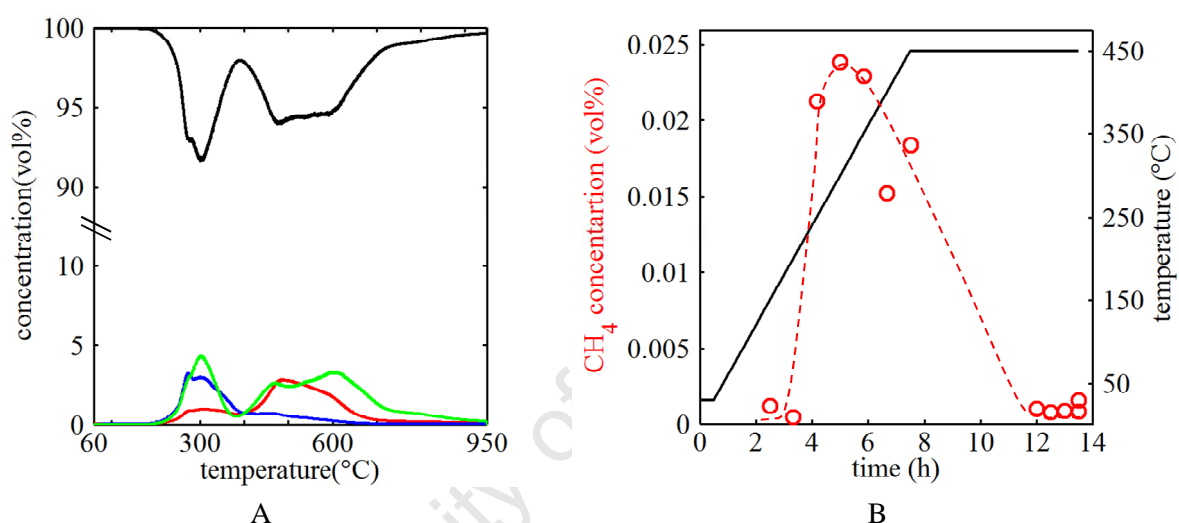


Figure 7.2: (A) formation of carbonaceous species during the TPR experiment of CAT 9.6 (H₂ ■, CO ■, CO₂ ■, CH₄ ■); (B) formation of methane during the activation/reduction of CAT 9.6.

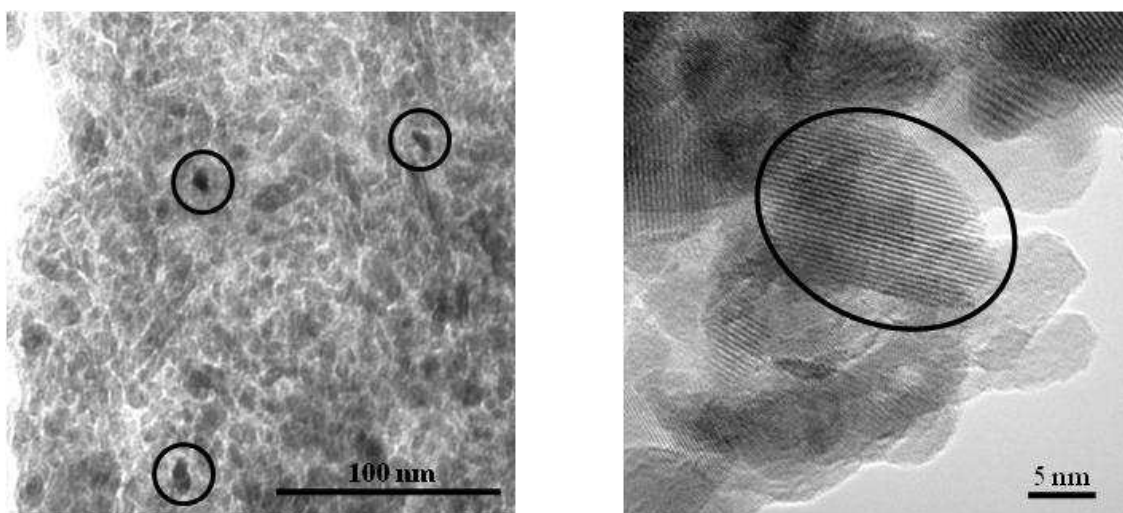
Table 7.4: Degree of reduction (DOR) and content of metallic cobalt after activation/reduction.

Catalyst	DOR (%)	Co metal (wt%)
CAT 9.6	97.6	4.9
CAT 8.6	95.6	2.0
CAT 7.3	97.6	4.2
CAT 6.8	95.0	3.0
CAT 5.9	98.3	2.5
CAT 4.8	97.4	2.1
CAT 4.4	97.6	1.7
CAT 4.0	98.9	3.2
CAT 3.1	98.1	2.5

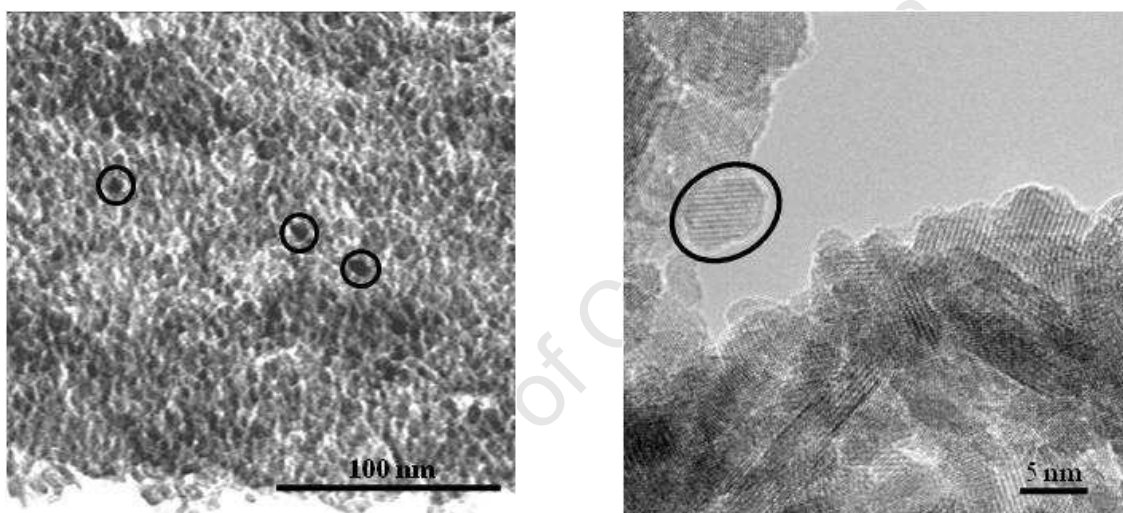
7.1.3 Transmission electron microscopy (TEM)

Transmission electron microscopy was used to image the model catalysts and to determine the average cobalt oxide and cobalt crystallite size. Samples were studied in the calcined state and after reduction and passivation in carbon dioxide. High resolution transmission electron microscopy (HRTEM) allowed the identification of cobalt species by comparison of the crystal lattice imaged to lattice parameters published in literature. Furthermore cobalt crystallites were identified by utilising energy dispersive X-ray spectroscopy (EDX). From the analysis of the TEM micrographs, crystallite size distributions for the model catalysts can be determined. In the following the model catalysts CAT 9.6, CAT 5.9 and CAT 3.1, representing the largest, a medium and the smallest crystallites prepared, are discussed in more detail.

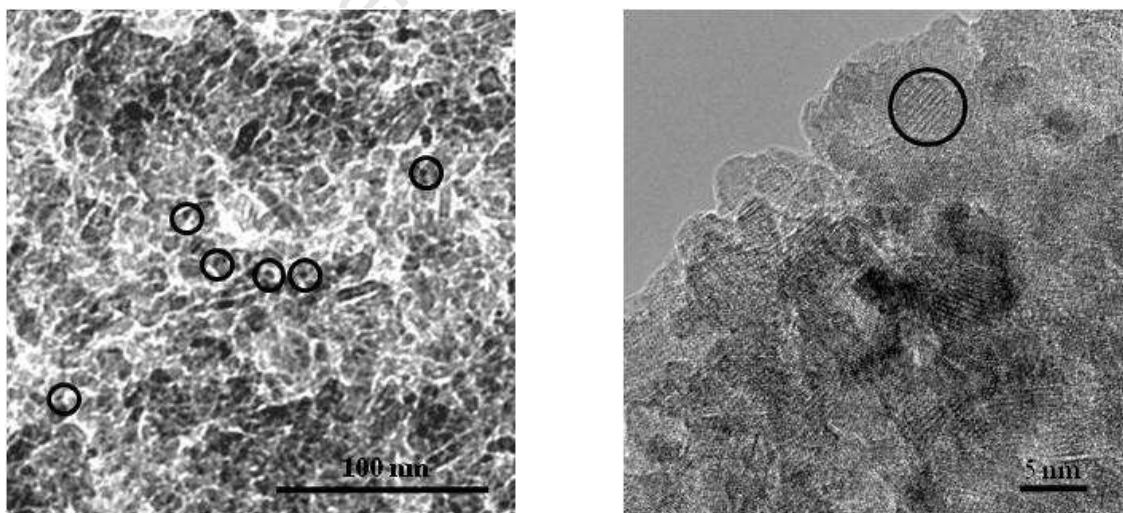
Figure 7.3 and 7.4 show TEM and HRTEM micrographs of the selected model catalysts in the calcined state and after reduction and passivation. Due to the similar densities of cobalt, Co_3O_4 and the alumina support ($\rho_{\text{Co}} = 8.98 \text{ g/cm}^3$; $\rho_{\text{Co}_3\text{O}_4} = 6.11 \text{ g/cm}^3$; $\rho_{\text{Al}_2\text{O}_3} = 3.95\text{-}4.10 \text{ g/cm}^3$ [7]) the contrast achieved in transmission electron microscopy is rather poor. The crystallites are predominately of ellipsoid shape and both radii are measured for the crystallites size distribution. HRTEM offers the possibility to measure the crystal lattice of imaged particles. Two different types of crystallites were identified by their crystallite lattices. One group displaying a distance of 4.6-4.8 Å while the other displays inter layer distances of 2.0-2.4 Å. Comparison with cobalt species in the International Centre for Diffraction Data PDF-2 database and literature results in a match with the [111] planes in Co_3O_4 (reported inter lattice parameter of 4.7 Å [8]). The lower measured inter layer distances are most probably due to the crystal lattice of alumina (reported inter lattice parameter of $\gamma\text{-Al}_2\text{O}_3$ 2.0 Å [400] plane). Metallic cobalt (hcp Co 1.9 Å [101] plane and fcc Co 2.0 Å [100] plane) displays very similar inter lattice spacings, however in the crystallites with smaller lattice parameter no cobalt was detected with dispersive X-ray spectroscopy (EDX). The reduced and passivated samples display the same lattice parameters as the calcined samples indicating that at least partial re-oxidation of the metallic cobalt during passivation and storage prior to HRTEM analysis did occur. This partial oxidation is most likely due to a surface oxidation forming in the passivation, i.e. treatment of the reduced catalysts with CO_2 . PXRD analysis of these samples showed the presence of metallic cobalt (see chapter 7.1.4), a bulk cobalt oxide phase could not be identified. It can therefore be assumed that the passivation with CO_2 results in a surface re-oxidation of the metallic cobalt crystallites, but not a bulk oxidation. A second identification possibility is the use of energy dispersive X-ray spectroscopy (EDX). In the scanning transmission electron microscopy (STEM) mode higher density material appears as brighter areas (see figure 7.5 A). Due to the small difference in density of cobalt/cobalt oxide and alumina however bright areas can also result from overlapping of alumina sheets and that is therefore not a fully conclusive identification tool for this catalyst system. However, by scanning areas on the sample grid with EDX, maps of the desired elements, i.e. Al and Co, can be obtained and therefore cobalt/cobalt oxide crystallites can be identified completely eliminating any uncertainties. A sample of these maps for CAT 9.6 in the calcined state is shown in figure 7.5. In image B the cobalt phase is displayed in green while the alumina is highlighted in yellow in image C. The HRTEM and the EDX identification methods confirm the average crystallite sizes obtained from the analysis of the TEM micrographs (see figure 7.6 and table 7.5).



CAT 9.6



CAT 5.9



CAT 3.1

Figure 7.3: TEM and HRTEM micrographs of CAT 9.6, CAT 5.9 and CAT 3.1 in the calcined state. Identified cobalt crystallites are encircled.

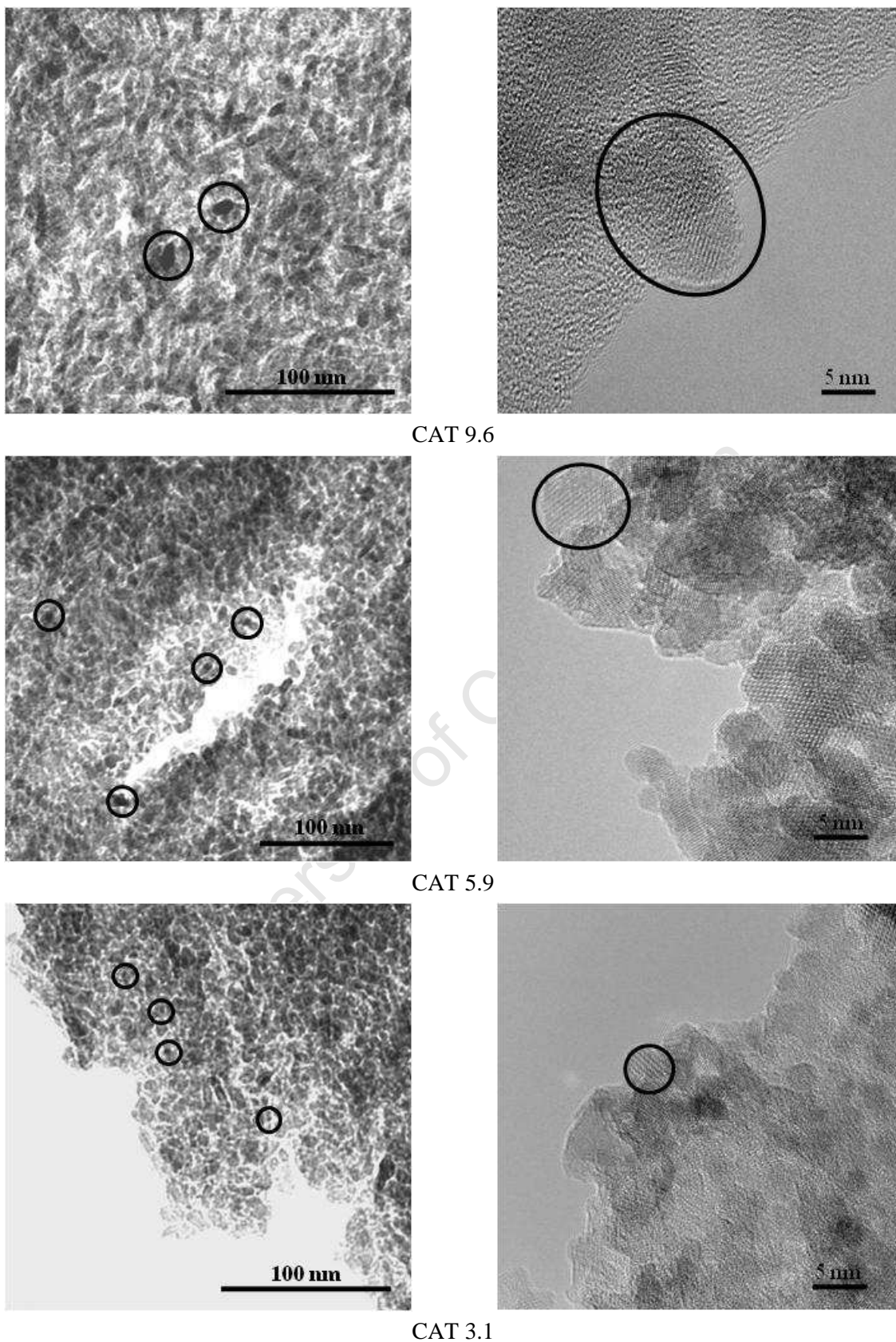


Figure 7.4: TEM and HRTEM micrographs of CAT 9.6, CAT 5.9 and CAT 3.1 after reduction and passivation in CO₂. Identified cobalt crystallites are encircled.

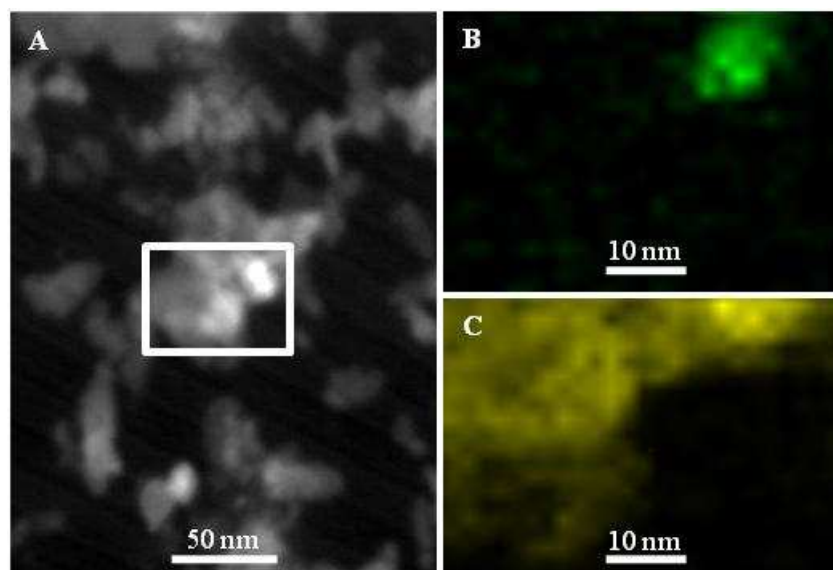


Figure 7.5: EDX maps of STEM micrograph of CAT 9.6 in calcined state: (A) STEM micrograph; (B) cobalt map of boxed area in (A); (C) aluminium map of boxed area in (A).

Table 7.5: Average crystallite size and standard deviation of cobalt oxide/cobalt crystallites in model catalysts calculated from a minimum of 300 crystallites in the calcined and in the reduced and passivated states. To allow comparison with values obtained from XRD analysis the volume weighted mean crystallite sizes are also given.

Catalyst	calcined state (Co_3O_4)				reduced and passivated (Co)			
	$d_{\text{num}}^{\text{a}}$ (nm)	σ^{b} (nm)	rel. dev. ^c (%)	$d_{\text{vol}}^{\text{d}}$ (nm)	$d_{\text{num}}^{\text{a}}$ (nm)	σ^{b} (nm)	rel. dev. ^c (%)	$d_{\text{vol}}^{\text{d}}$ (nm)
CAT 9.6	8.4	1.9	22.6	9.6	9.3	1.7	18.3	10.3
CAT 8.6	8.0	1.3	16.3	8.6	8.2	1.9	23.2	9.5
CAT 7.3	6.8	1.0	14.7	7.3	7.5	1.0	13.3	7.9
CAT 6.8	6.3	1.1	17.5	6.8	6.0	1.1	18.3	6.6
CAT 5.9	5.2	1.1	21.2	5.9	4.7	1.2	25.5	5.6
CAT 4.8	3.9	1.1	28.2	4.8	4.7	1.0	21.3	5.4
CAT 4.4	3.7	0.9	24.3	4.4	4.1	0.7	17.1	4.5
CAT 4.0	3.5	0.8	22.9	4.0	3.7	0.8	21.6	4.3
CAT 3.1	2.3	0.8	34.8	3.1	2.2	0.7	31.8	2.9

^a number weighted average crystallite size.

^b standard deviation of d_{num} .

^c relative deviation in % ($100 \cdot \sigma / d_{\text{num}}$).

^d volume weighted average crystallite size, assuming spherical crystallites.

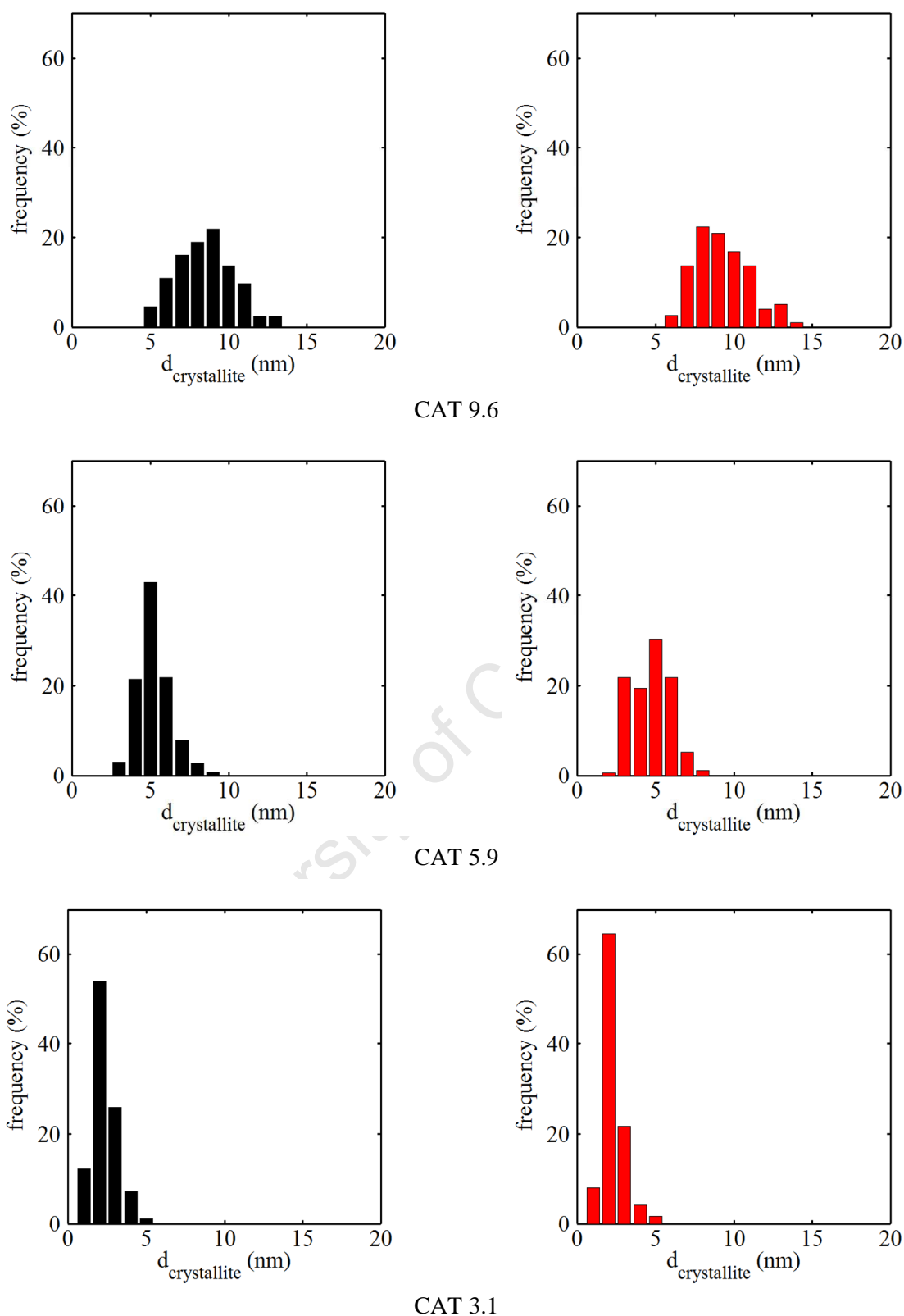


Figure 7.6: Crystallite size distributions (number based) of selected model catalysts calculated from a minimum of 300 crystallites (■ calcined; ■ reduced and passivated).

A minimum of 300 crystallites were measured and crystallite size distributions determined. Figure 7.6 shows the crystallite size distributions for the model catalysts CAT 9.6, CAT 5.9 and CAT 3.1 (for

crystallite size distributions of other model crystallites see appendix A6) in the calcined and in the reduced and passivated stages. Figure 7.6 as well as table 7.5 show that all studied model catalysts display a fairly narrow crystallite size distribution, with a maximum of 35 % relative deviation from the average value. This holds true for the calcined as well as for the reduced and passivated samples. From a comparison of the average crystallite sizes in the calcined and those in the reduced state, the stability of the model catalysts against sintering during reduction can be seen. From theoretical considerations, in absence of crystallite growth, the crystallite size of the metallic phase is expected to decrease by 25% from the calcined state due to the loss of oxygen. The model catalysts in this study do not show this decrease in crystallite size but rather show a slight increase or no change of the average crystallite size due to the reduction process.

7.1.4 Conventional and in-situ powder X-ray diffraction (PXRD)

Prior to the loading of the cobalt oxide crystallites onto the alumina support (see chapter 4.11 and figure 4.2), the nature and the size of the cobalt species is characterised by means of atmospheric powder X-ray diffraction. Figure 7.7 shows three exemplary PXRD scans of the unsupported cobalt oxide powder. From comparison with the reference pattern of Co_3O_4 in combination with Rietveld refinement it can be observed that during calcination of the cobalt hydroxide precipitate a pure Co_3O_4 phase was formed. Variations of the w/o microemulsion composition and cobalt nitrate concentration (see table 7.1) result in differently sized crystallites.

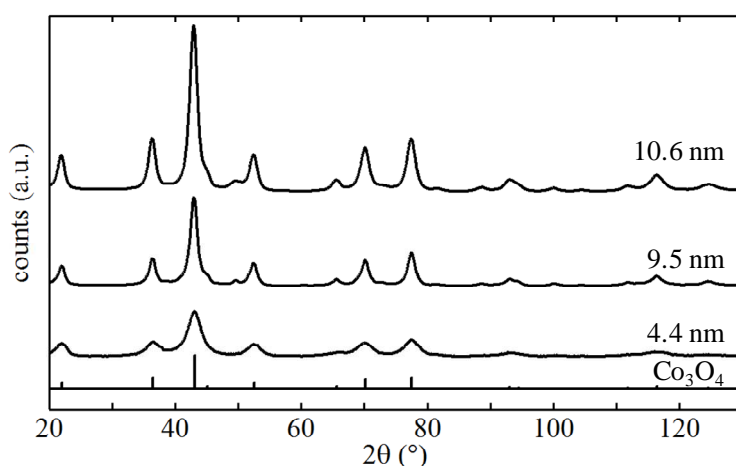


Figure 7.7: PXRD spectra of Co_3O_4 crystallites prior to their deposition on the Al_2O_3 support. Co_3O_4 diffraction pattern given as reference. Crystallite sizes were obtained via Rietveld refinement. For exact reference peak positions see table 7.7.

After the loading of the Co_3O_4 crystallites of different sizes onto the alumina support as well as after the ex-situ reduction of the so obtained model catalysts in a fluidised bed (for reduction conditions see table 7.3) the samples are studied again by means of PXRD (see figure 7.8 & 9). In both cases the diffraction pattern of the alumina support dominates the PXRD spectra of the model catalysts due to the low overall cobalt loadings (see table 7.2) and the relatively small cobalt-oxide/cobalt crystallites. The loading process (see chapter 4.1.1) does not result in phase changes in the cobalt oxide crystallites, therefore resulting in pure Co_3O_4 crystallites being dispersed on the

alumina carrier. The reduction of these model crystallites is very effective and degrees of reduction were achieved (see table 7.4). Remarkably, in the reduced and passivated catalysts face centred cubic cobalt could be identified as the only metal phase and no hcp cobalt could be detected. Using the Rietveld refinement methods with the PONKCS [9] approach, the crystallite sizes of the Co_3O_4 phase in the freshly prepared catalysts as well as the crystallite sizes of the fcc Co phase in the reduced and passivated model catalysts were calculated (see table 7.6). The so obtained crystallite sizes compare well with the volume weighted crystallite sizes determined by the analysis of TEM micrographs of the corresponding model catalyst sample (see table 7.5).

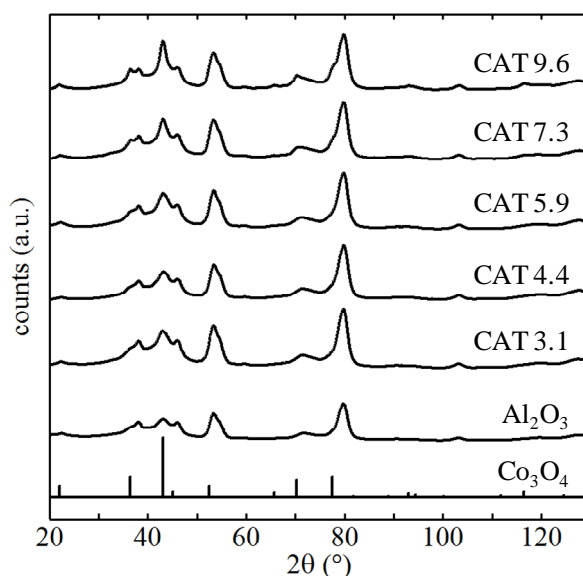


Figure 7.8: PXRD spectra of selected model catalysts in the calcined state with spectrum of pure Al_2O_3 and Co_3O_4 diffraction pattern as reference. For exact reference peak positions see table 7.7.

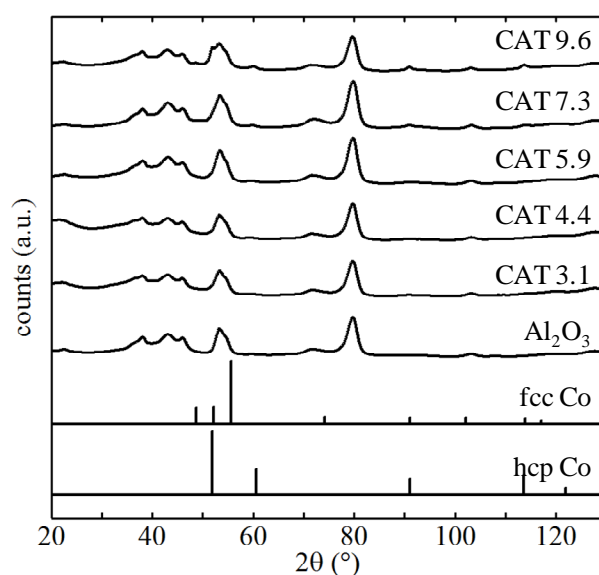


Figure 7.9: PXRD spectra of selected model catalysts in the reduced and passivated state with spectrum of pure Al_2O_3 and fcc Co and hcp Co diffraction pattern as reference. For exact reference peak positions see table 7.7.

Table 7.6: Crystallite sizes obtained via Rietveld refinement of PXRD scans of the calcined (d_{cal}) and reduced and passivated (d_{red}) model catalysts.

Catalyst	d_{cal} (nm)	d_{red} (nm)
CAT 9.6	10.6	9.5
CAT 8.6	9.5	7.9
CAT 7.3	7.4	7.7
CAT 6.8	6.1	5.5
CAT 5.9	5.3	5.1
CAT 4.8	4.8	4.8
CAT 4.4	4.4	4.5
CAT 4.0	4.1	4.5
CAT 3.1	3.6	3.4

The reduction behaviour (see reduction conditions in table 7.3) of the prepared model catalysts was studied by means of in-situ PXDR reduction. Figure 7.10 shows the obtained PXRD scans as well as the crystallite sizes of Co_3O_4 , CoO , fcc Co and hcp Co as a function of temperature for CAT 9.6 (for more in-situ PXRD scans see appendix A7). As discussed earlier (see chapter 6.6) the reduction in flowing hydrogen of model catalysts prepared by the reverse micelle method D (see chapter 4.1.1) results in a pure face-centred cubic cobalt metal phase. In the first step of the reduction Co_3O_4 is converted to CoO as can be seen by comparison of the PXRD scans (figure 7.10 A & B) with the reference patterns listed in table 7.7. The crystallite size evaluation, obtained using the Rietveld refinement method, shown in figure 7.10 C clearly indicates the start of the reduction process at 150°C resulting in a mixed phase of the two cobalt oxide species. The crystallite size of the Co_3O_4 crystallites decreases from this temperature on, while the size of the CoO crystallites increases but it remains smaller than the starting cobalt (II,III) oxide size, up to temperatures of 275°C . At this stage metallic fcc cobalt, forming in the second reduction step, can first be detected. After reaching 375°C only the metallic phase is observed. The slightly larger average crystallite size in the reduced state obtained from the in-situ PXRD studies compared to the measurements of external samples (see table 7.6) results from the necessity to conduct faster scans during in-situ measurements. In order to keep scan times short the scan range as well as the time per step was decreased resulting in a loss of resolution. This results in slight variations in the crystallite sizes obtained by Rietveld refinement as the source data of atmospheric PXRD scans allow a better quality of fit than the scans from in-situ work.

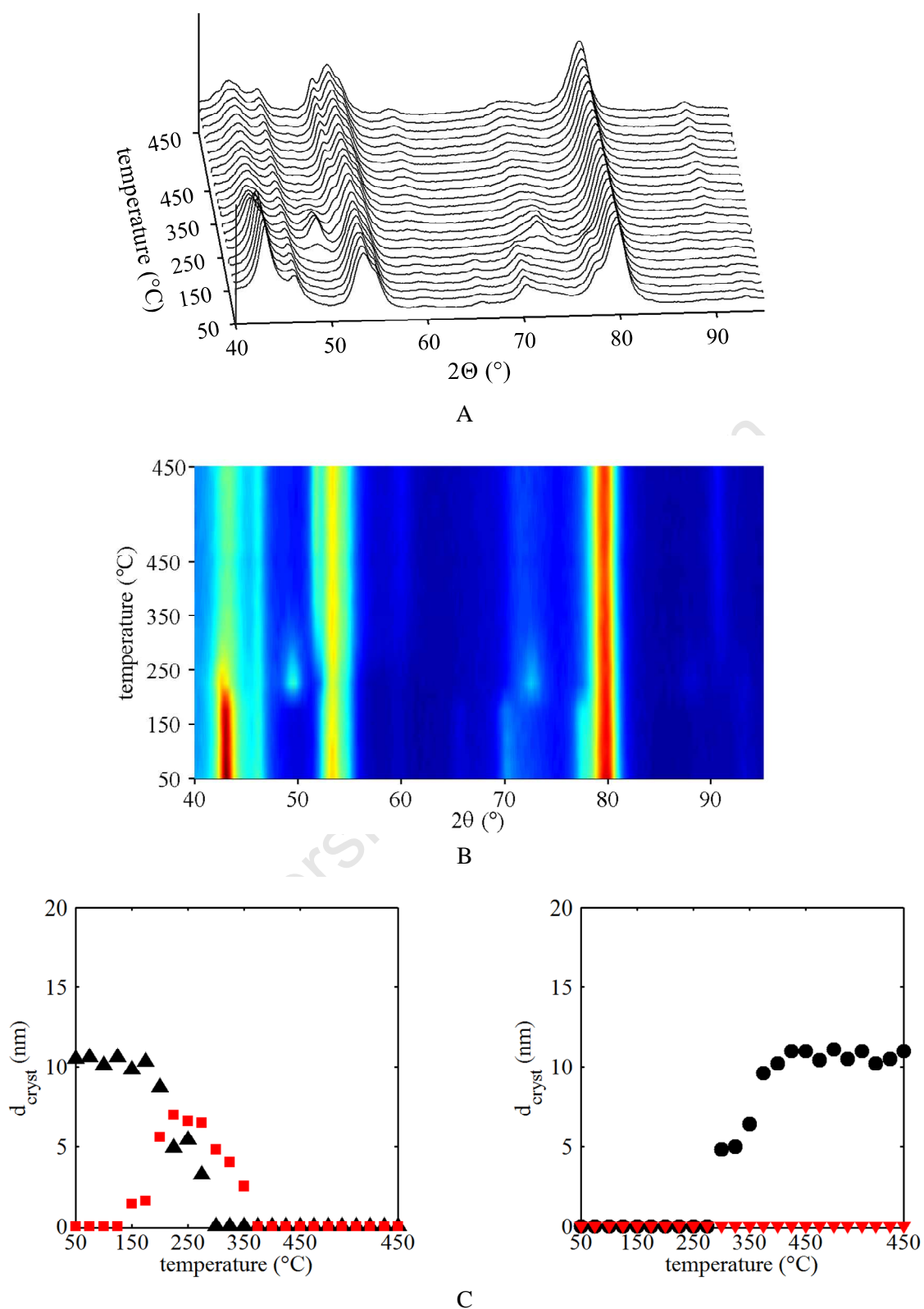


Figure 7.10: In-situ PXRD scans of CAT 9.6. A: diffraction patterns, 3D view; B: diffraction patterns on-top view; C: crystallite sizes of Co_3O_4 (▲), CoO (■), hcp Co (▼) and fcc Co (●) as function of temperature obtained via Rietveld refinement using POKKCS approach.

Table 7.7: Reference diffraction patterns of Co₃O₄, CoO, hcp Co and fcc Co in the relevant 2 θ range for a cobalt X-ray source ($\lambda = 1.78897 \text{ \AA}$). Values from International Centre for Diffraction Data PDF-2 database.

Phase	2 θ (°)	Int. (%) ^a	Phase	2 θ (°)	Int. (%) ^a	Phase	2 θ (°)	Int. (%) ^a	Phase	2 θ (°)	Int. (%) ^a
Co ₃ O ₄	43.07	100	CoO	42.65	65	Co (hcp)	48.68	27	Co (fcc)	51.83	100
	45.07	9		49.66	100		52.16	28		60.62	40
	52.54	19		72.87	50		55.69	100		91.08	25
	65.65	8		88.28	20		74.12	11			
	70.20	29		93.33	13		91.10	10			
	77.50	34									
	81.78	2									
	88.82	2									
	93.03	7									
94.44	4										

^a relative intensities in %

7.1.5 CO temperature programmed desorption (CO-TPD)

The interaction of the catalytic surface with gaseous carbon monoxide (CO) plays a crucial role in the Fischer-Tropsch synthesis. Recent studies in the field of theoretical catalysis emphasise the influence of the metal crystallite size of the CO dissociation [10-14]. The so called B5 site (see chapter 2.4), a group of 5 adjacent metal atoms in a geometric arrangement only present at kink and step sites, was identified as the most suitable site for the CO dissociation. To study the interaction of CO with the prepared model catalysts temperature programmed desorption of CO pre-adsorbed on the reduced surfaces (see chapter 4.5.8) was carried out on selected model catalysts CAT 9.6, CAT 8.6, CAT 6.8, CAT 5.9 and CAT 4.0. To identify effects originating from the support, pure alumina was also included in these measurements.

Figure 7.11 shows the TCD readings and the mass spectroscopy (MS) traces of CO, H₂ and H₂O monitored during CO TPD. While gaseous CO originates from the introduced gas pulse in the adsorption step of the TPD experiment, hydrogen originates from residual dissociated hydrogen from the preceding reduction procedure. Water was possibly confined in the porous support system and therefore not completely removed at a reduction temperature of 450°C or 375°C respectively (see table 7.3). The TCD spectra as well as all mass to charge (m/z) ratios shown in figure 7.11 also register peaks for the pure alumina support. A normalisation per gram of cobalt would therefore not be applicable, hence the obtained MS traces were normalised per gram of total model catalyst. This does not allow for a deconvolution of cobalt crystallite size and support effects.

However two more carbon species were detected and measured in the mass spectrometer: CH₄ (m/z = 15) and CO₂ (m/z = 44). Both species could not be observed in the exhaust gas stream of the TPD experiment with the pure alumina support and their formation rates can therefore be normalised with respect of the amount of metallic cobalt in the catalyst samples. The most probable source of

carbon dioxide is from CO via the Boudouard reaction (see equation 7.3) in which 2 moles CO disproportionate and form one mole of carbon dioxide and a carbon surface species. This carbon surface species can then react with dissociated hydrogen from the preceded reduction to form methane in a consecutive reaction (see equation 7.4). The water gas shift reaction (WGS) (see equation 7.5) could also play a role in the reaction scheme although no clear relationship between CO₂ and H₂ formation can be observed as to be expected in the case of the WGS reaction.

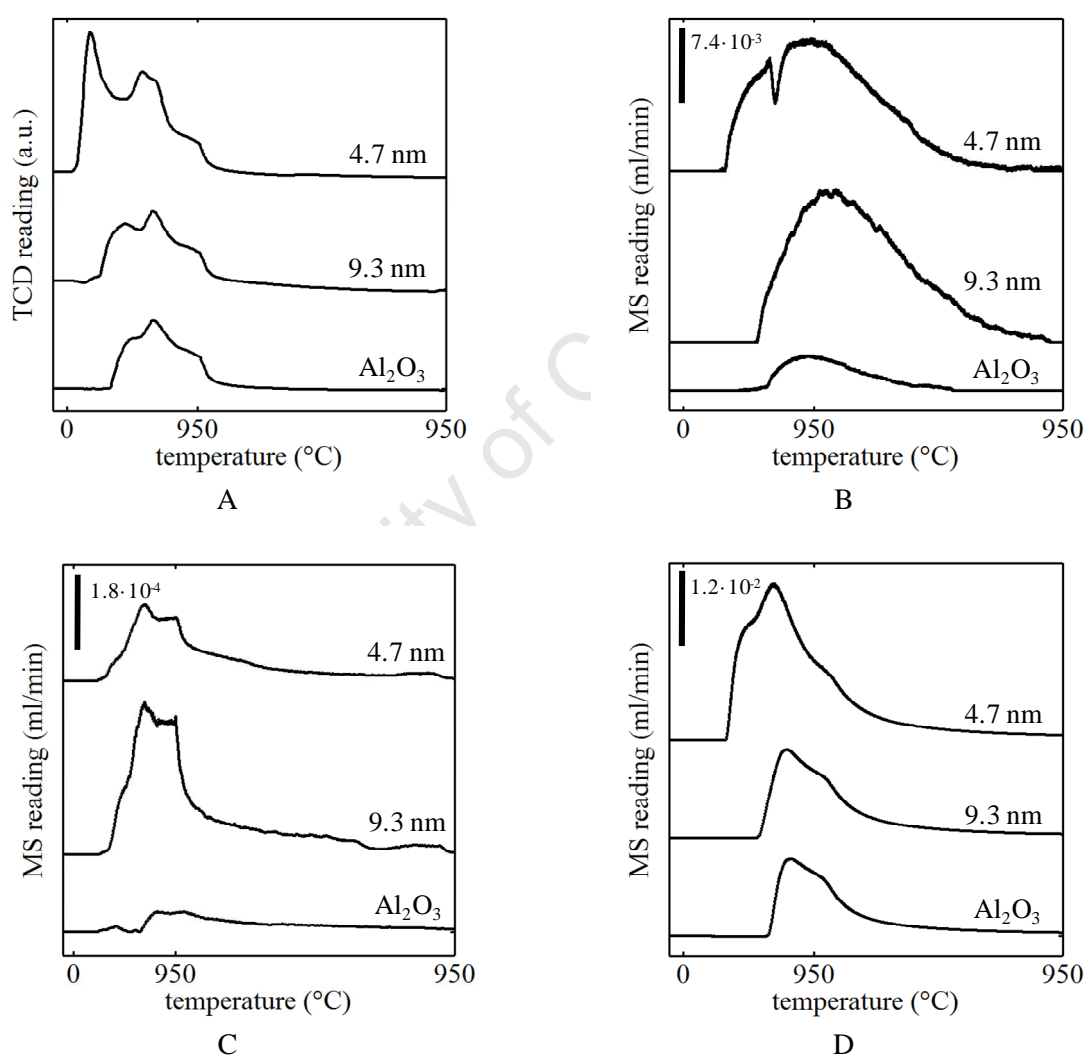


Figure 7.11: TCD reading and MS results from CO-TPD studies of Al₂O₃, CAT 9.6 ($d_{\text{num,red}} = 9.3$ nm) and CAT 5.9 ($d_{\text{num,red}} = 4.7$ nm). All scans normalised to 1 gram of model catalyst. Scales are indicated for B-D in the graph. A: TCD reading; B: CO flow (m/z = 28); C: H₂ flow (m/z = 2); D: H₂O flow (m/z = 18).

Figure 7.12 shows the MS traces of CO₂ and CH₄ in both cases normalised to one gram of metallic cobalt. CO₂ desorbs at up to 4 different temperatures indicating up to four different sites at which CO₂ is formed. A low temperature site with a peak onset around 100°C and three high temperature sites at 500-600°C, 650-750°C and 850-950°C. The amount of carbon dioxide formed at the high temperature sites increases with decreasing crystallite size, while the low temperature peak seems to go through a minimum as function of crystallite size. This trend culminates with CAT 5.9 (average crystallite size after reduction ($d_{\text{num,red}}$) of 4.7 nm; see table 7.5) displaying only one dominant desorption peak at an onset temperature of 575°C. The smaller cobalt crystallites of CAT 4.0 resemble the behaviour observed for the larger crystallites with four distinct desorption peaks. The methane formation is assumed to be due to a successive reaction to the formation of CO₂, therefore the CH₄ desorption peaks are expected to behave similarly to the ones of CO₂ but shifted to higher temperatures. In contrast to the CO₂ desorption spectra the low temperature site is not active towards methane formation. Methane formation rather seems to be associated with two of the ‘high temperature sites’ that also promote CO₂ formation. In table 7.8 all onset temperatures of the observed peaks are listed. Indeed in all cases the methane peaks show a slightly higher onset than the high temperature peaks of the corresponding CO₂ desorption. This correlates well with the hypothesised consecutive reaction of carbon monoxide to form methane (equation 7.4) via the Boudouard reaction (equation 7.3). The absence of a third high temperature methane desorption peak could be due to a lack of carbon or hydrogen, which is mostly desorbed or consumed at these temperatures (see figure 7.11 C) on the surface. As the carbon mass balance does not close completely and reheating of the samples under an oxygen flow leads to the formation of CO₂, most probably the lack of hydrogen limits the methane formation. Crystallites of an average diameter of 4.7 nm seem to display unique activity for carbon monoxide activation and methane formation. These are essential steps in the Fischer-Tropsch synthesis and these samples should therefore also display superior activity.

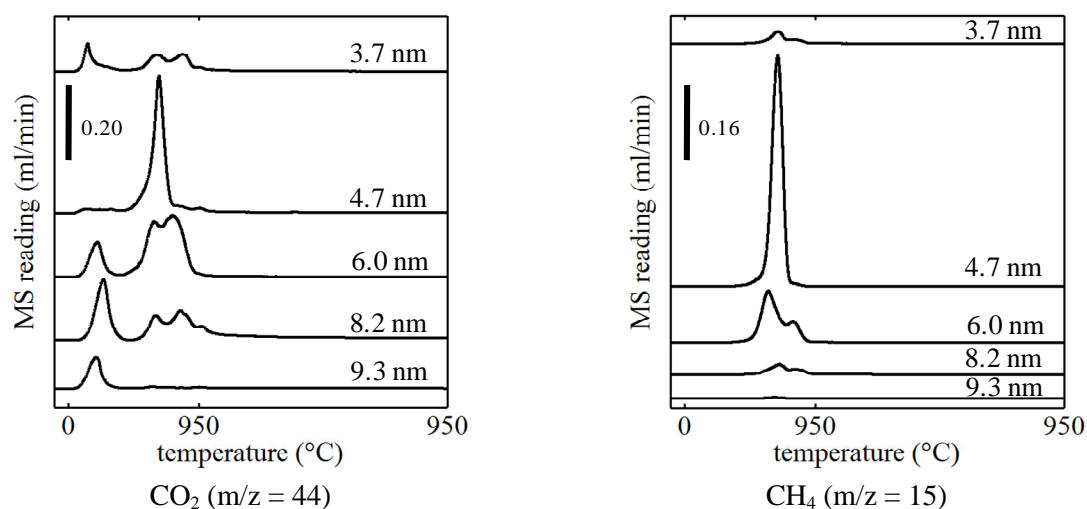


Figure 7.12: MS results from CO-TPD studies of CAT 9.6 ($d_{\text{num,red}} = 9.3$ nm), CAT 8.6 ($d_{\text{num,red}} = 8.2$ nm), CAT 6.8 ($d_{\text{num,red}} = 6.0$ nm), CAT 5.9 ($d_{\text{num,red}} = 4.7$ nm) and CAT 4.0 ($d_{\text{num,red}} = 3.7$ nm). All scans normalised to 1 gram of metallic cobalt. Scales are indicated in the graph.

Table 7.8: Onset temperatures for desorption peaks of CO₂ and CH₄.

Catalyst	Species	Peak onset temperature (°C)			
CAT 4.0	CO ₂	88	520	723	922
	CH ₄	-	570	737	-
CAT 5.9	CO ₂	-	576	-	-
	CH ₄	-	592	-	-
CAT 6.8	CO ₂	103	489	640	-
	CH ₄	-	491	663	-
CAT 8.6	CO ₂	139	531	682	850
	CH ₄	-	537	746	-
CAT 9.6	CO ₂	86	511	-	-
	CH ₄	-	539	-	-

7.1.6 Magnetic in-situ studies on supported cobalt crystallite model catalysts

Two of the prepared model catalysts (CAT 9.6 which has the largest cobalt crystallites and CAT 4.4 which has relatively small cobalt crystallites; see table 7.5) were studied for their magnetic behaviour under reduction, FT syntehsis (reaction conditions: T = 190°C, PP_{syn.gas} = 9.9 bar, SV = 7.2 ml_{syn.gas}/g_{catalyst}·min (STP)) and FT syntehsis at simulated high conversions (X_{CO-simulated} = 66%) conditions. An amount equivalent to 80 mg of cobalt was used with CAT 9.6 in the magnetometer (see chapter 4.8) while of catalyst CAT 4.4 only 1.17 g were available corresponding to 20 mg cobalt. The lower amount of cobalt in the case of CAT 4.4 resulted in an increased scatter in the obtained measurements.

The reduction of each model catalyst (for reduction conditions see table 7.3) was monitored by measuring the magnetisation of the samples at an external field strength of 20 kOe. From the calibration data of the magnetometer obtained with known amounts of pure metallic cobalt (see appendix A2) and the known amount of cobalt in each sample the degree of reduction (DOR) can be calculated as function of temperature (see figure 7.13). As expected from the DORs of the model catalysts measured via temperature programmed reduction (see chapter 7.1.2), for CAT 9.6 a degree of reduction of 97-98% was measured in the magnetometer. The first formation of metallic cobalt was measured at a temperature of 230-250°C corresponding well to the reduction behaviour measured in in-situ XRD studies (see figure 7.10). CAT 4.4, also reducing to 97% according to temperature programmed reduction measurements, only showed a degree of reduction of 60% at the reduction end temperature. At this point it is important to note that the hydrogen uptake in the TPR, which is correlated to the reduction process of the cobalt crystallites, is independent of crystallite size, while the measurement of the magnetisation of a sample in presence of an external field is strongly dependent on the crystallite size. Smaller crystallites require a higher external field strength to be magnetised [15,16] (it should be noted that at 20 kOe the following magnetisation relative to the corresponding saturation magnetisation of nano sized cobalt crystallites can be expected applying the Langevin equation (T=190°C): 93% (4 nm), 84% (3 nm), 52% (2 nm)). Indeed the hysteresis measured for this catalyst indicates incomplete saturation (see figure 7.14). The saturation magnetisation can be estimated from the linear extrapolation of a magnetisation (M) over inverse

external field strength ($1/H$) curve to values of $1/H = 0$. But even with this extrapolation the degree of reduction for CAT 4.4 is only 65%. This discrepancy of this measurement with the degree of reduction measured via TPR techniques may also be due to the relatively small amount of sample used in the magnetic measurements causing relatively large error.

A comparison of the reduction behaviour of the two catalysts indicates a slightly more facile reduction of the catalyst with the larger crystallites, CAT 9.6, as CAT 4.4 shows a delayed reduction behaviour at temperatures between 300 and 350°C. This is in qualitative agreement with the temperature programmed reduction measurement where the second reduction peak, i.e. the reduction from CoO to metallic cobalt, also occurs at higher temperatures for CAT 4.4 (see section 7.1.2).

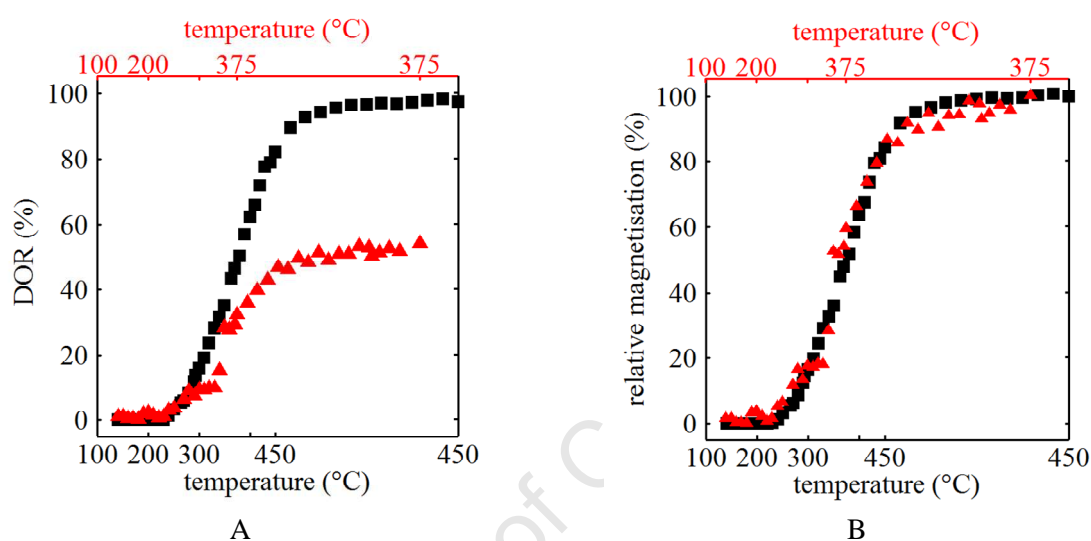


Figure 7.13: (A) Degree of reduction as a function of temperature for CAT 9.6 (■) and CAT 4.4 (▲) as calculated from the magnetic measurements; (B) Magnetisation relative to magnetisation at the end of the reduction process for CAT 9.6 (■) and CAT 4.4 (▲).

Prior to the start of the FTS experiments a full hysteresis (see chapter 4.5.10 and figure 4.4) was measured for both catalyst samples at reaction temperature under an argon atmosphere. As discussed in chapter 4.5.10 the shape of a hysteresis does give information on the average crystallite size and in the case of a superparamagnetic sample, i.e. no remnant magnetisation, even a crystallite size distribution can be calculated by superimposing a number of Langevin functions (see eq. 4.2) [15]. Figure 7.14 shows the obtained hystereses, normalised with respect to their saturation magnetisation. The magnetisation at lower field strength (H) is dominated by larger crystallites. In this case CAT 9.6 shows a larger magnetisation/steeper slope at the lower field strengths resulting from larger cobalt crystallites than CAT 4.4. CAT 9.6 furthermore is nearly saturated ($M/M_s = 1$) while CAT 4.4 is not fully saturated, again indicating the smaller cobalt crystallite size of CAT 4.4. The cut-out (figure 7.14 B) shows the cobalt crystallites of CAT 9.6 behave partially ferromagnetic, i.e. retain a remnant magnetisation upon removal of the external field, while CAT 4.4 is superparamagnetic. This allows the calculation of a crystallite size distribution for CAT 4.4 using Langevin functions (see figure 7.15 for extracted crystallite size distribution).

The average crystallite size (volume weighted) of CAT 4.4 calculated from magnetic measurements is 5.1 nm, which correlates well with the 4.5 nm obtained by means of TEM (see table 7.5) and XRD measurements (see table 7.6).

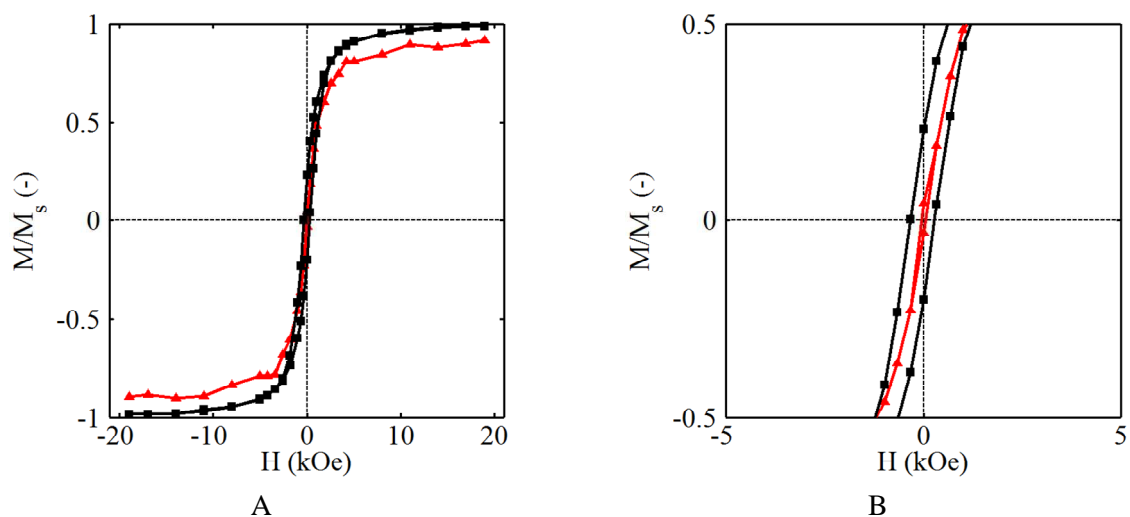


Figure 7.14: Relative magnetisation of CAT 9.6 (■) and CAT 4.4 (▲) as a function of external field strength (hysteresis). (A) full hysteresis; (B) cut-out at no external field ($H = 0$ kOe).

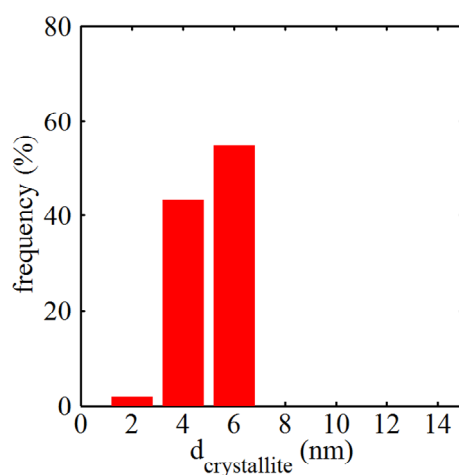


Figure 7.15: Crystallite size distribution of superparamagnetic sample CAT 4.4 calculated via superimposing Langevin functions.

Both model catalysts were exposed to the same FT conditions chosen in this study for the measurement of the activity and selectivity (reaction conditions: $T = 190^\circ\text{C}$, $PP_{\text{syn.gas}} = 9.9$ bar, $SV = 7.2$ $\text{ml}_{\text{syn.gas}}/\text{g}_{\text{catalyst}} \cdot \text{min}$ (STP), duration of run 25 h) and their magnetisation in an external magnetic field of 20 kOe was measured followed by a measurement at 0 kOe for the determination of the amount of ferromagnetic material (see figure 7.16 and 7.17). After 25 hours on stream the reaction was stopped and the catalyst was exposed to an argon atmosphere. To compare the freshly reduced catalyst to the one after 25 hours at FT conditions a full hysteresis measurement was conducted (for hystereses see appendix A8). After completion of this measurement the catalysts were again exposed to the same FT conditions but with an additional 6 bar of water partial pressure to simulate a CO conversion of 66%. This was achieved via co-feeding of water.

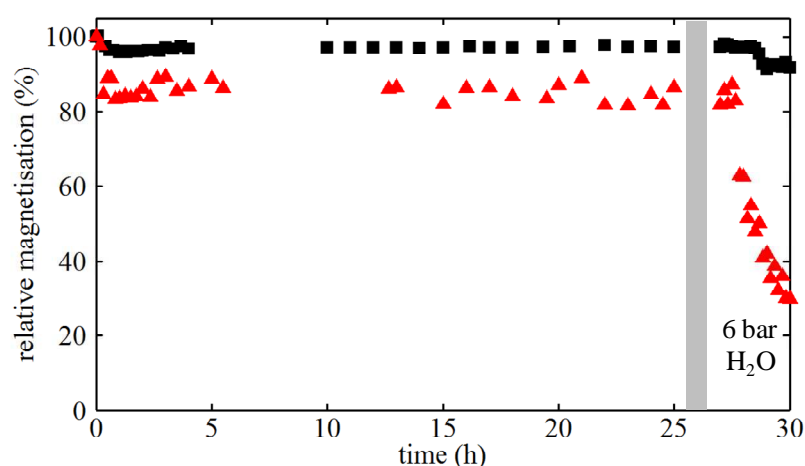


Figure 7.16: Relative magnetisation (normalised) as a function of time on stream for CAT 9.6 (■) and CAT 4.4 (▲) as calculated from the magnetic measurements under FT conditions and under FT conditions with co-fed water.

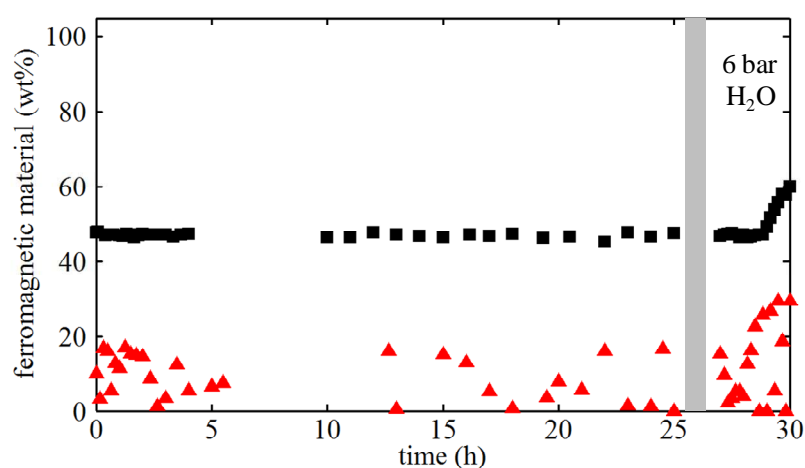


Figure 7.17: Percentage of ferromagnetic material as a function of time on stream for CAT 9.6 (■) and CAT 4.4 (▲) as calculated from the magnetic measurements under FT conditions and under FT conditions with co-fed water.

Figure 7.16 shows the degree of reduction as a function of time during the exposure of the catalyst to FT conditions with and without the addition of 6 bar water partial pressure. For both model catalysts the degree of reduction decreases slightly in the first 5-10 minutes on stream. This could be a result of a re-oxidation as well as a carbidisation during surface reconstruction [17, 18] of the metallic cobalt crystallites upon first exposure to synthesis gas. After the initial decrease, the degree of reduction remains constant during the first 25 hours of exposure to FT conditions. The percentage of ferromagnetic material (see equation 4.3), indicating the weight percentage of the magnetic material present in crystallite sizes allowing ferromagnetic in contrast to superparamagnetic behaviour, does not change upon the first 25 hours of exposure to FT conditions either (see figure 7.17). The larger scatter in data for catalyst sample CAT 4.4 resulted from the low absolute amount of cobalt in the magnetometer as well as the near superparamagnetic behaviour. Upon exposure to a water partial pressure of 6 bar both catalysts show a decrease of magnetisation, but while the magnetisation of CAT

9.6 only drops slightly that of CAT 4.4 decreases continuously. This is a strong indication of the re-oxidation of metallic cobalt into the Co^{2+} state in the presence of water as predicted by theoretical studies [19, 20]. These studies also suggest that the re-oxidation is more feasible for smaller crystallites (see figure 2.9). This could be confirmed in the here presented magnetic measurements. Furthermore an increase in the percentage of ferromagnetic material was measured for both catalysts, more extensive so for CAT 9.6. This increase results from smaller cobalt crystallites being re-oxidised while the larger crystallites remain in their metallic form. Concurrently crystallite sintering as caused by water may have occurred as water is also reported to support crystallite growth in form of sintering under FT conditions [21].

Crystallite size distributions of CAT 4.4 determined from hysteresis measurements after 25 hours and after the co-feeding experiment with water are shown in 7.18 (for corresponding hystereses see appendix A8). While the average crystallite size in the freshly reduced catalyst was 5.1 nm this average size decreased to 5.0 nm after 25 hour under FT conditions and to 3.6 nm after 3 hours of additional elevated water pressure. In this study the re-oxidation, and not sintering, seems to be the dominating effect on the cobalt phase.

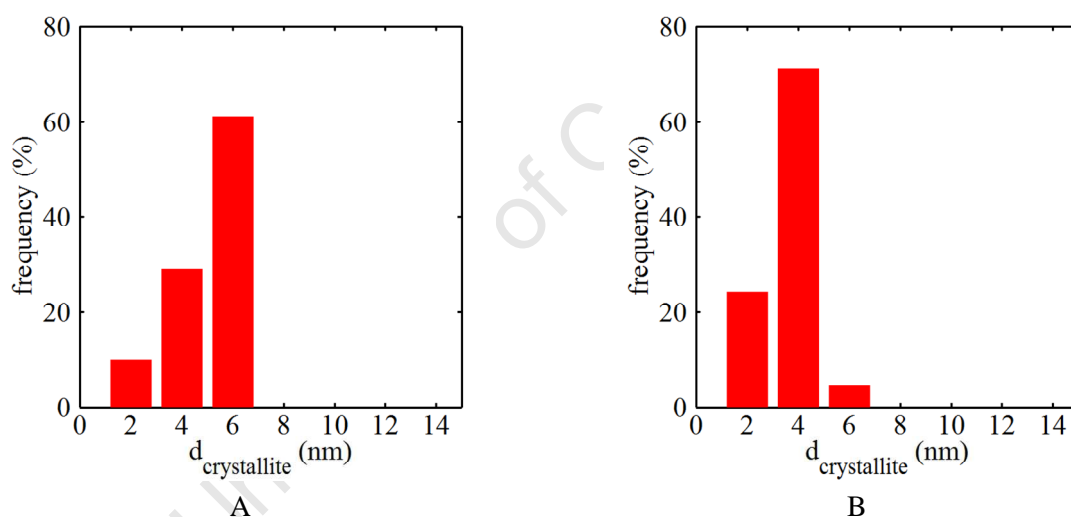


Figure 7.18: Crystallite size distribution of superparamagnetic sample CAT 4.4 calculated via superimposing Langevin functions (A) after 25 hours under conditions; (B) after 3 hours of additional co-feeding of 6 bar water.

A visual inspection of the spent catalysts after removal from the magnetometer indicated formation of cobalt aluminate, CoAl_2O_4 . CAT 4.4 had changed in colour from black to blue and in CAT 9.6 a slight blue touch could be seen. PXRD studies (see figure 7.19) of the spent catalysts were conducted to get clarity on the nature of the cobalt phases after exposure to elevated water pressures at FT conditions. While no CoO was found in these analyses, the alumina-oxide-hydroxide Bohmite ($\text{AlO}(\text{OH})$) was identified as the only new phase besides metallic fcc cobalt and the alumina support (see table 7.9). The absence of cobalt aluminates in the PXRD scans does indicate, that no bulk CoAl_2O_4 phase formed. However the colour change of the catalyst clearly confirms the presence of this spinel product. The only cobalt phase measurable is the fcc metallic cobalt and this only in CAT 9.6. For CAT 4.4., with a measured cobalt loading of 1.8 wt% (see table 7.2), a 60% decrease in the

degree of reduction (see figure 7.16) results in an effective cobalt metal loading of 0.6 wt% which is below the detection limit of the PXRD instrument.

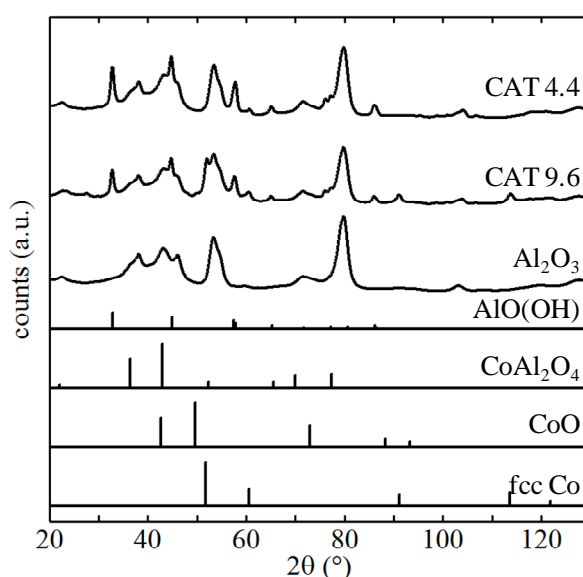


Figure 7.19: PXRD spectra of spent catalyst samples CAT 4.4 and CAT 9.6 as well as Al_2O_3 , with $\text{AlO}(\text{OH})$, CoAl_2O_4 , CoO and fcc Co diffraction patterns as reference.

Table 7.9: Calculated composition of spent model catalysts CAT 4.4 and CAT 9.6 obtained via Rietveld refinement (excluding alumina support).

Catalyst	fcc Co		CoO		Bohmite		CoAl ₂ O ₄	
Sample	wt%	d (nm)	wt%	d (nm)	wt%	d (nm)	wt%	d (nm)
CAT 4.4	0	n/a	0	n/a	18.8	18.5	0	n/a
CAT 9.6	4.4	10.5	0	n/a	13.5	19.3	0	n/a

Interestingly both model catalyst samples showed the alumina oxide hydroxide phase Bohmite ($\text{AlO}(\text{OH})$) after the treatment at elevated water partial pressures under Fischer-Tropsch conditions. The presence of this phase was verified with HRTEM analyses (see figure 7.20, showing the typical needle like structure of Bohmite [22]). Bohmite is known as a precursor in the preparation of $\gamma\text{-Al}_2\text{O}_3$ support material [23] and $\gamma\text{-Al}_2\text{O}_3$ is generally assumed to be stable under FT conditions, making it suitable as support material. Nishimura et al. [22] report the formation of Bohmite in gamma alumina supported copper catalysts during the water gas shift reaction. It was observed that catalysts with copper crystallites in the nanometer size range form more Bohmite. In this study we observed a similar effect, with CAT 4.4. forming 5.3 wt% more Bohmite than CAT 9.6 under the same conditions (see table 7.9). To test if the Bohmite formation was cobalt induced, a pure alumina sample was exposed to the identical reaction procedure as the model catalysts and then studied by means of PXRD. No change in its structure could be observed therefore suggesting, that upon the water induced oxidation and incorporation of cobalt atoms/ions into the alumina matrix, the $\gamma\text{Al}_2\text{O}_3$ support material can undergo a phase change to $\text{AlO}(\text{OH})$ in presence of water.

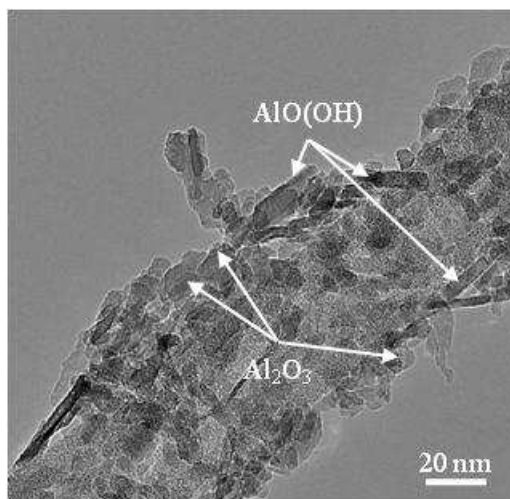


Figure 7.20: HRTEM image of CAT 4.4 after exposure to elevated water pressures under FT conditions. Examples of AlO(OH) and Al₂O₃ crystallites are indicated.

7.1.7 Conclusion and summary of the characterisation results of cobalt/cobalt oxide crystallites

The synthesised model catalysts were characterised extensively with in-situ as well as traditional techniques in the calcined and in the reduced state. From these characterisations it was determined that the catalyst preparation method D (see chapter 4.1.1) yields cobalt oxide crystallites (pure Co₃O₄ phase) supported on the alumina carrier. No extensive metal support interactions could be detected by means of temperature programmed reduction and XPS measurements (see chapter 6.4). The average sizes of the cobalt oxide crystallites were in the desired range (2-10 nm) and showed a very narrow size distribution. By strategically varying the w/o microemulsion composition, different sizes could be obtained.

Importantly upon reduction and exposure to FT conditions the crystallite sizes remained largely unchanged with similarly narrow size distributions, indicating the presence of only limited crystallite growth. The reduction process is composed of two steps: firstly the reduction of Co₃O₄ to CoO and secondly the reduction to metallic cobalt. Remarkably from X-ray diffraction the metal crystallites were identified to consist of a pure face-centred cubic phase. Residual surfactant is decomposed completely during the reduction process resulting in a clean hydrogen saturated metal surface after the activation. Upon exposure to FT conditions no re-oxidation of the cobalt crystallites could be observed under the chosen reaction conditions ($T = 190^{\circ}\text{C}$, $PP_{\text{syn.gas}} = 9.9 \text{ bar}$, $\text{H}_2/\text{CO} = 2$, $\text{SV} = 7.2 \text{ ml}_{\text{syn.gas}}/\text{g}_{\text{catalyst}} \cdot \text{min}$ (STP), reaction time 25 h). Only upon exposure to elevated water partial pressures, simulating a CO conversion of 66% a re-oxidation of the cobalt phase to mostly cobalt aluminates could be detected.

The differently sized cobalt crystallites display different CO activation as well as CO₂ and CH₄ formation behaviour during CO TPD, indicating the presence of various active sites on the different crystallites. Furthermore, certain active sites seem to be reaction specific, i.e. they show CO₂ but no corresponding CH₄ formation. Very high activity for CO activation and methane formation on one predominant site was measured for cobalt metal crystallites with an average crystallite diameter of 4.7 nm.

7.2 Organometallic cobalt complex

To study sub nanometer cobalt ensembles, an organometallic cobalt complex was synthesised [24]. This complex $((\text{CO})_9\text{Co}_3\text{CCOOH})$, see figure 7.21) was supported on the alumina carrier and tested for Fischer-Tropsch activity and selectivity. Due to the reported instability of cobalt carbonyls upon exposure to air, the supported complex was mainly characterised using in-situ techniques including diffuse reflectance infrared spectroscopy, powder X-ray diffraction and magnetic measurements.

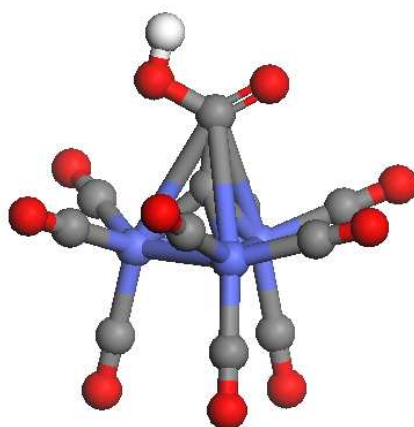


Figure 7.21: Ball and stick model of cobalt carbonyl complex $(\text{CO})_9\text{Co}_3\text{CCOOH}$ (Co blue, C grey, O red, H white).

7.2.1 Elemental analysis

The formed gaseous products of the combustion of the freshly synthesised cobalt complex are analysed and the content of carbon and hydrogen in the sample was determined. These contents were then compared to theoretical contents of C and H in $(\text{CO})_9\text{Co}_3\text{CCOOH}$ (see table 7.10). The experimental carbon and hydrogen contents correlate well with the theoretically calculated values for the desired cobalt complex. The slight deviations might result from residual reactants, for example acetic acid, which were used in the synthesis process.

Table 7.10: Carbon and hydrogen content of synthesised sample and theoretical contents of the desired cobalt complex and other common cobalt carbonyls.

	C (wt %)	H (wt %)
synthesised complex	26.6	0.3
$(\text{CO})_9\text{Co}_3\text{CCOOH}$	27.2	0.2
$\text{Co}_2(\text{CO})_8$	28.1	-
$\text{Co}_4(\text{CO})_{12}$	25.2	-

7.2.2 Mass spectroscopy (MS)

To further identify the synthesised material it was analysed using mass spectroscopy. Figure 7.22 shows the MS spectrum of the prepared cobalt complex. $(\text{CO})_9\text{Co}_3\text{CCOOH}$ has a molar mass of 485.8 g/mol. The absence of this mass in the MS spectrum underlines the instability of the complex.

However $m/z = 457.6$ represents the original complex with one CO ligand dissociated ($M_{\text{CO}} = 28$ g/mol). The following m/z values from 457.6 to 233.8 result from the step wise dissociation of the eight residual CO ligands. Between $m/z = 233.8$ and 188.8 possibly the carboxylic acid group decomposes while a loss of one cobalt atom ($M_{\text{Co}} = 59.93$ g/mol) could result in the m/z value of 129.9.

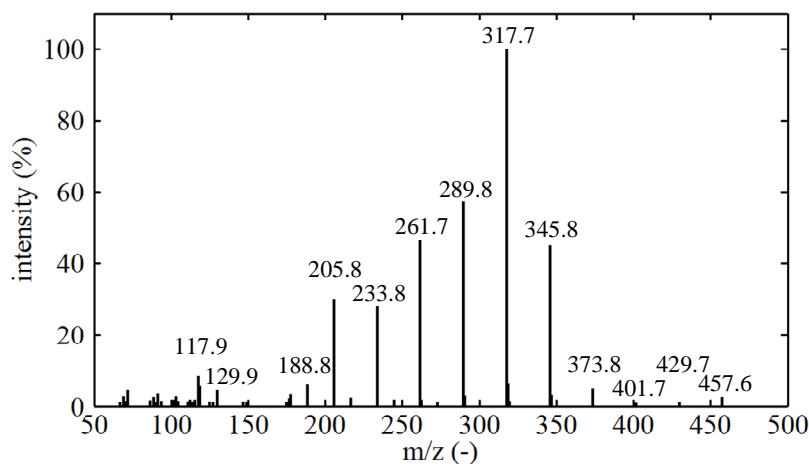


Figure 7.22: MS spectrum of synthesised cobalt carbonyl complex.

7.2.3 Fourier transform infra red spectroscopy (FTIR)

The freshly synthesised cobalt complex was studied with diffuse reflectance Fourier transform infra red spectroscopy (FTIR) (see figure 7.23). The most prominent feature in the pure complex is the group of peaks around wavenumbers in the range of $1900\text{--}2200\text{ cm}^{-1}$. These peaks are reported to result from the excitation of metal carbonyl bonds [25–29]. The number of slightly different peaks in this area indicates the presence of various different metal-CO bonds as is indeed to be expected in case of the studied complex $(\text{CO})_9\text{Co}_3\text{CCOOH}$. The intensity of the peaks in the discussed area decreased when the complex was put onto the support, mainly due to the dilution effect. Importantly however the position of the peaks remained unchanged. Therefore it can be assumed that the process of supporting the cobalt complex onto the alumina did not influence the nature of the complex.

The decomposition of freshly alumina supported $(\text{CO})_9\text{Co}_3\text{CCOOH}$ was studied in an in-situ FTIR reaction chamber. The temperature in the chamber was heated at $2^\circ\text{C}/\text{min}$ to 375°C and the decomposition of the complex was monitored by the changes in the metal carbonyl bands (at wavenumbers of $1900\text{--}2200\text{ cm}^{-1}$). As a reductive atmosphere, as is present in the Fischer-Tropsch synthesis, is likely to affect the decomposition process, the in-situ FTIR studies were conducted under 6 bar of N_2 (see figure 7.24) as well as under 6 bar of H_2 (see figure 7.25). Measurements using CO containing gas were not possible as the IR-spectra of the gaseous CO completely clouded the spectra due to the complex. As previously reported with gravimetric methods [30] the cobalt carbonyl complex decomposes fully below 200°C . In the case of the inert atmosphere, no metal carbonyl bands could be detected at temperatures above 141°C . In presence of the reductive atmosphere (H_2) a complete loss of the CO bonds is already observed at 92°C . It can be assumed that the presence of CO would have a stabilising effect on the cluster, but as mentioned above this could not be simulated in the FTIR set-up.

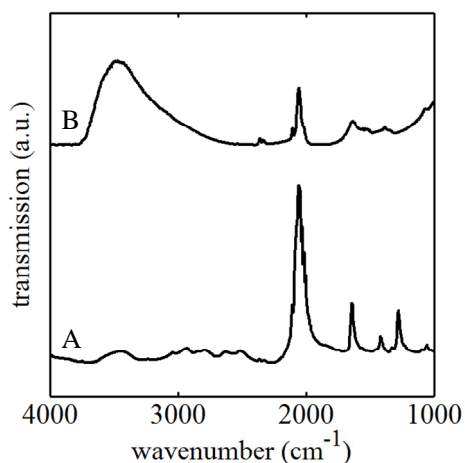


Figure 7.23: Diffuse reflectance FTIR spectra of freshly prepared $(\text{CO})_9\text{Co}_3\text{CCOOH}$ (A) and alumina supported $(\text{CO})_9\text{Co}_3\text{CCOOH}$ (B).

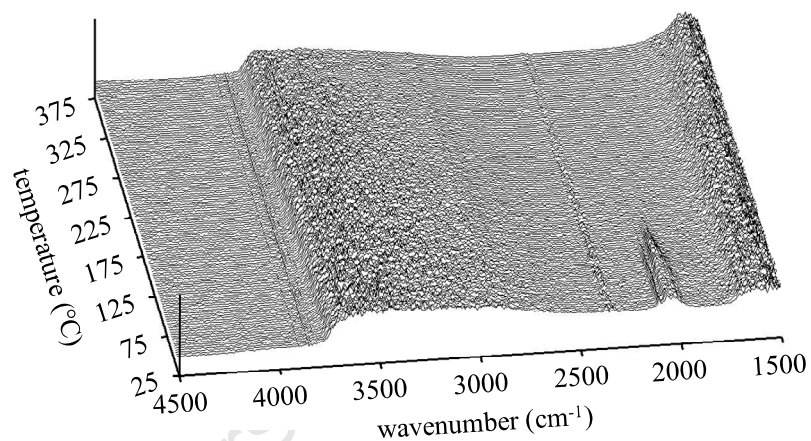


Figure 7.24: In-situ diffuse reflectance FTIR spectra of supported $(\text{CO})_9\text{Co}_3\text{CCOOH}$ at 6 bar and 40 ml/min (STP) N_2 flow. Heating rate $2^\circ\text{C}/\text{min}$.

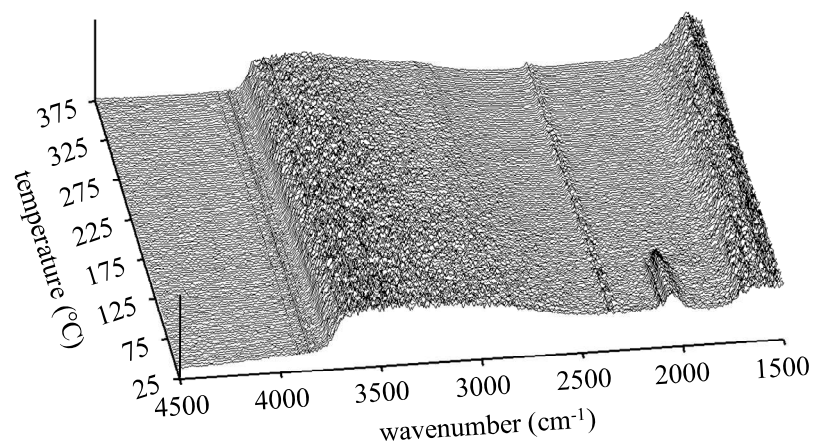


Figure 7.25: In-situ diffuse reflectance FTIR spectra of supported $(\text{CO})_9\text{Co}_3\text{CCOOH}$ at 6 bar and 40 ml/min (STP) H_2 flow. Heating rate $2^\circ\text{C}/\text{min}$.

7.2.4 Magnetic measurements

As described in chapter 4.2 the cobalt loading of the supported cobalt carbonyl complex was set to 3 wt%. In the magnetometer 1 g of this catalyst was exposed to the Fischer-Tropsch conditions as also applied in the reactivity and selectivity measurements in the Fischer-Tropsch test unit, i.e. $SV_{\text{syngas}} = 7.2 \text{ ml/g}_{\text{catalyst}} \text{ (STP)}$, $H_2/CO = 2$, $PP_{\text{syngas}} = 9.9 \text{ bar}$ (see chapter 4.7.4). Under these conditions the temperature was raised from 50°C to 400°C while measuring the saturation magnetisation at 20 kOe and the remnant magnetisation at 0 kOe in 10°C intervals (see figure 7.26). With calibration values obtained from known amounts of pure metallic cobalt (see appendix A2), the content of metallic cobalt can be calculated from the saturation magnetisation at 20 kOe (see figure 7.30). From the ratio of the remnant and the saturation magnetisation, the amount of ferromagnetic material in the metallic cobalt phase can be calculated (see equation 4.2). At room temperature cobalt crystallites are reported to display ferromagnetic behaviour above a crystallite size of 10-16 nm [31, 32] or from theoretical studies 8 nm for the fcc cobalt and 28 nm for the hcp cobalt phase [33]. At elevated temperatures these critical diameters increase. The presence of ferromagnetism would therefore indicate the formation of larger cobalt crystallites as a product of the cobalt carbonyl complex decomposition. With calibration values obtained from known amounts of pure metallic cobalt (see appendix A2), the content of metallic cobalt can be calculated from the saturation magnetisation values at 20 kOe.

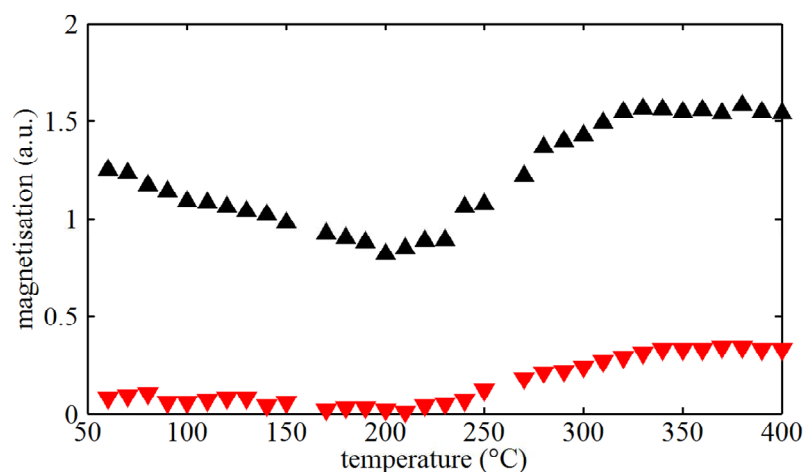


Figure 7.26: Saturation magnetisation (▲, at 20 kOe external magnetic field strength) and remnant magnetisation (▼, at 0 kOe external magnetic field strength) of the supported cobalt complex sample as function of temperature.

In the whole temperature range the saturation and remnant magnetisation remained very low resulting in a large scatter. Above 220°C a steady increase in saturation as well as remnant magnetisation could be measured (see figure 7.26). From in-situ FTIR studies (see chapter 7.2.3) it is known that no metal carbonyls can be expected to be present at these temperatures. A maximum of 0.15 wt% metallic cobalt was calculated above 340°C. Of this metallic phase 42 wt% was determined to be ferromagnetic, i.e. above the critical crystallite size (see figure 7.37). The percentage of ferromagnetic material at low temperatures is very low, which serves as an indication that no large metallic cobalt crystallites have formed at these conditions. 95% of the cobalt loaded can not be accounted for. Possibly the sizes of some formed cobalt crystallites/ensembles are too small to be magnetised or saturated at an external field strength of 20 kOe. Due to the colour change of the

catalyst after the magnetic measurements from black to pale blue it can further be assumed that cobalt is incorporated into the alumina matrix during the decomposition process forming cobalt aluminates of the very characteristic blue colour [34] (see figure 7.38).

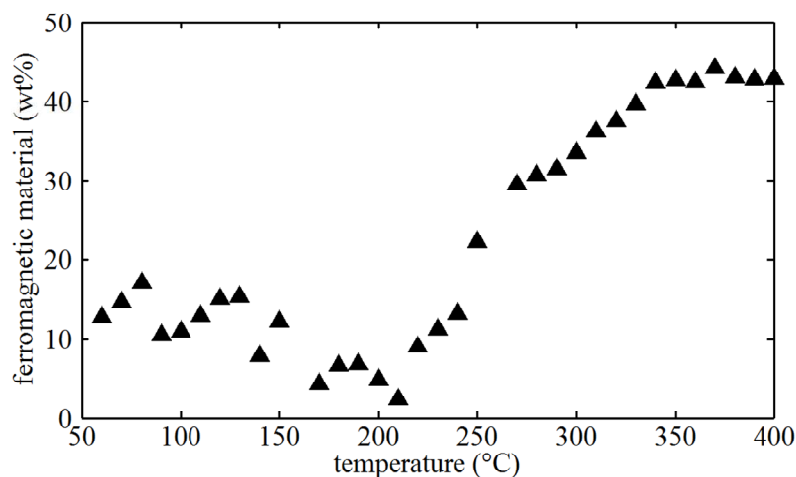


Figure 7.27: Percentage of ferromagnetic material in the supported cobalt complex sample as function of temperature.



A



B

Figure 7.28: (A) $(\text{CO})_9\text{Co}_3\text{CCOOH}$ freshly supported on alumina carrier; (B) supported $(\text{CO})_9\text{Co}_3\text{CCOOH}$ after exposure to high temperatures in synthesis gas in set-up for magnetic measurements.

7.2.5 In-situ powder X-ray diffraction (PXRD)

The decomposition of the supported cobalt carbonyl complex was further studied with in-situ powder X-ray diffraction. The temperature programmed magnetic measurements have shown a decomposition of the cobalt complex to a very small extent (~5 %) to metallic cobalt crystallites of sizes which should be measurable by means of PXRD. However, in in-situ PXRD 0.15 wt% cobalt is below the detection limit, so no formation of cobalt crystallites should be observed upon heating of the sample in 5 bar synthesis gas to 600°C. To ensure a synthesis gas atmosphere in the in-situ chamber, the volumetric flow rate of synthesis gas was set to 30 ml/min (STP) with a H_2/CO ratio of 2 resulting in a space velocity of $65 \text{ ml/min} \cdot \text{g}_{\text{catalyst}}$.

Figure 7.29 shows no formation of a metallic cobalt phase as to be expected from the magnetic measurements (for reference diffraction patterns see table 7.7). Above 300°C an increase in the peak intensity at $42\text{--}43^\circ 2\theta$ indicates the formation of a new phase or a phase change. The cobalt aluminate CoAl_2O_4 has a reported maximum intensity peak at $42.9^\circ 2\theta$. Combined with the observations from the magnetic measurement it is highly possible that the observed increase in peak intensity originates

from the formation of cobalt aluminates. Further peaks in the CoAl_2O_4 reference pattern in the scan range of the experiment are reported to be less intense and could therefore not easily be visible in the in-situ scans.

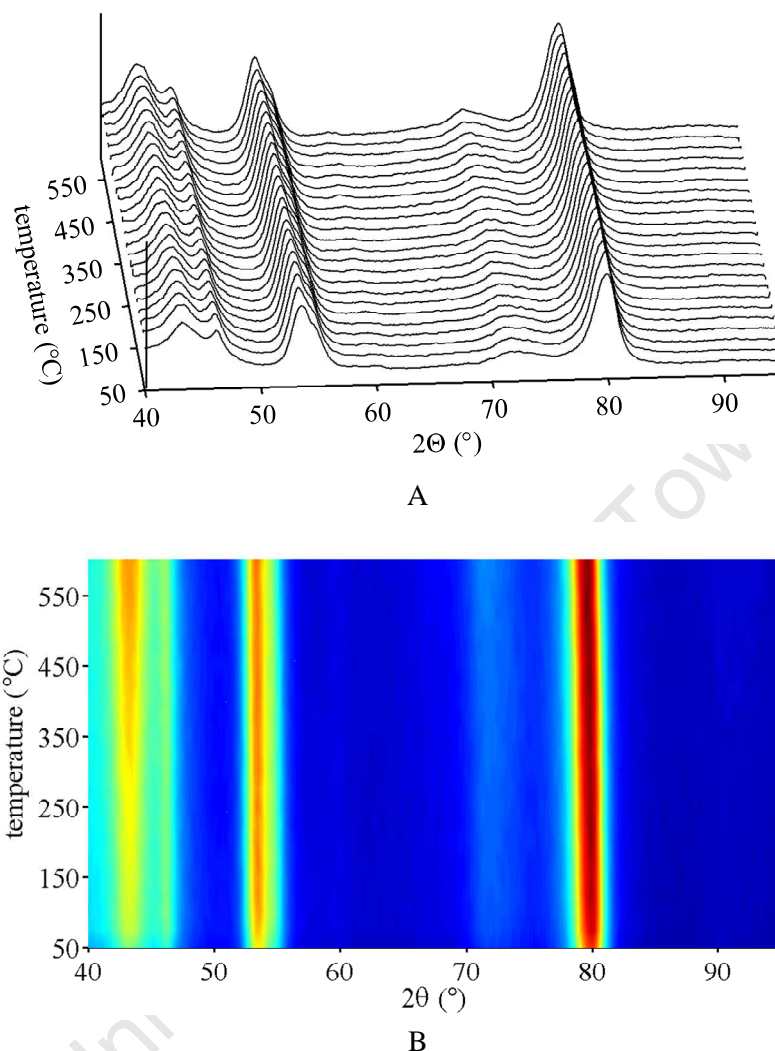


Figure 7.29: In-situ PXRD of supported $(\text{CO})_9\text{Co}_3\text{CCOOH}$ at 6 bar and 30 ml/min synthesis gas flow ($\text{H}_2/\text{CO} = 2$). Heating rate $2^\circ\text{C}/\text{min}$.

7.2.6 Conclusion and summary of the characterisation results of the organometallic cobalt complex

With elemental analysis (EA), mass spectroscopy (MS) and Fourier transform infra red (FTIR) studies it could be conclusively shown that the synthesised cobalt carbonyl complex is in fact the desired $(\text{CO})_9\text{Co}_3\text{CCOOH}$. The complex supported on the alumina carrier decomposes rapidly at elevated temperatures. The decomposition is even enhanced in a hydrogen atmosphere and no metal carbonyl bands can be observed with FTIR above temperatures of 92°C . Upon further increase of temperature above 200°C , a small amount of the decomposition products of the cobalt complex form a measurable cobalt metal phase with an increasing average crystallite size. As the utilised magnetometer is limited to a maximum external field of 20 kOe, the magnetic moments of very small cobalt metal crystallites

might not be aligned and therefore not visible in the magnetic measurements. Due to the colour change of the sample from black to pale blue during the magnetic measurement the formation of cobalt aluminates can be assumed to take place under synthesis gas at elevated temperatures. The absence of larger amounts (> 2 wt%) of metallic cobalt with crystallite sizes above 2 nm could be verified by in-situ powder X-ray diffraction. The formation of CoAl_2O_4 could be observed at temperatures above 300°C.

University of Cape Town

References

- [1] S.J. Tauster, *Accounts of Chemical Research*, 20 (1987) 389.
- [2] A.M. Saib, A. Borgna, J. van de Loosdrecht, P.J. van Berge and J.W. Niemantsverdriet, *Applied Catalysis A: General*, 312 (2006) 12.
- [3] A.M. Saib, D.J. Moodley, I.M. Ciobîca, M.M. Hauman, B.H. Sigwebela, C.J. Weststrate, J.W. Niemantsverdriet and J. van de Loosdrecht, *Catalysis Today*, 154 (2010) 271.
- [4] A. Tavasoli, R.M. Malek Abbaslou and A.K. Dalai, *Applied Catalysis A: General*, 346 (2008) 58.
- [5] S. Todorova, V. Zhelyazkov and G. Kadinov, *Reaction Kinetics and Catalysis Letters*, 57 (1996) 105.
- [6] G.S. Sewell, E. van Steen and C.T. O'Connor, *Catalysis Letters*, 37 (1996) 255.
- [7] C.R. Hammond, in D.R. Linde (Editor), *Handbook of Chemistry and Physics*, Vol. 73, CRC Press, Inc., Boca Ranton, Ann Arbor, London, Tokyo, 1993.
- [8] Z. Hui, W. Jinbo, Z. Chuanxin, M.W. Xiangyang, D. Ning, T. Jiangping and Y. Deren, *Nanotechnology*, 19 (2008) 035711.
- [9] N.V.Y. Scarlett and I.C. Madsen, *Powder Diffraction*, 21 (2006) 278.
- [10] I.M. Ciobîca, F. Frechard, R.A. van Santen, A.W. Kleyn and J. Hafner, *Journal of Physical Chemistry B*, 104 (2000) 3364.
- [11] I.M. Ciobîca and R.A. van Santen, *The Journal of Physical Chemistry B*, 107 (2003) 3808.
- [12] J.J. Mortensen, L.B. Hansen, B. Hammer and J.K. Nørskov, *Journal of Catalysis*, 182 (1999) 479.
- [13] V. Pallassana, M. Neurock, L.B. Hansen, B. Hammer and J.K. Nørskov, *Physical Reviews B: Condensed Matter and Material Physics*, 60 (1999) 6146.
- [14] S. Dahl, A. Logadottir, R.C. Egeberg, J.H. Larsen, I. Chorkendorff, E. Tornqvist and J.K. Nørskov, *Physical Review Letters*, 83 (1999) 1814.
- [15] J.A. Dalmon, in B. Imelick, Verdrine, J. (Editor), *Catalyst characterisation: Physical techniques for solid materials*, Chapter 21, Plenum Press, New York, 1994.
- [16] L. Weil, *Journal de Chimie Physique et de Physico-Chimie Biologique*, 51 (1954) 715.
- [17] J. van de Loosdrecht, B. Balzhinimaev, J.A. Dalmon, J.W. Niemantsverdriet, S.V. Tsybulya, A.M. Saib, P.J. van Berge and J.L. Visagie, *Catalysis Today*, 123 (2007) 293.
- [18] I.M. Ciobîca, R.A. van Santen, P.J. van Berge and J. van de Loosdrecht, *Surface Science*, 602 (2008) 17.
- [19] E. van Steen, M. Claeys, M.E. Dry, J. van de Loosdrecht, E.L. Viljoen and J.L. Visagie, *Journal of Physical Chemistry B*, 109 (2005) 3575.
- [20] J.C.W. Swart, A theoretical view on deactivation of cobalt-based Fischer-Tropsch catalysts, Department of Chemical Engineering, PhD, University of Cape Town, Cape Town, 2008.
- [21] G.L. Bezemer, T.J. Remans, A.P. van Bavel and A.I. Dugulan, *Journal of the American Chemical Society*, 132 (2010) 8540.
- [22] S. Nishimura, T. Shishido, K. Ebitani, K. Teramura and T. Tanaka, *Applied Catalysis A: General*, 387 (2010) 185.
- [23] J. Chandradass, D.S. Bae, and K.H. Kim, *Materials and Manufacturing Processes* 25 (2010) 919.

- [24] X. Lei, M. Shang, T.P. Fehlner, R. Werner, W. Haase, D. Hautot and G.J. Long, *Journal of Organometallic Chemistry*, 541 (1997) 57.
- [25] G. Prieto, A. Martínez, P. Concepción and R. Moreno-Tost, *Journal of Catalysis*, 266 (2009) 129.
- [26] D. Song, J. Li and Q. Cai, *The Journal of Physical Chemistry C*, 111 (2007) 18970.
- [27] L.E.S. Rygh, O.H. Ellestad, P. Klæboe and C.J. Nielsen, *Physical Chemistry Chemical Physics*, 2 (2000) 1835.
- [28] L.E.S. Rygh and C.J. Nielsen, *Journal of Catalysis*, 194 (2000) 401.
- [29] G. Blyholder, *The Journal of Physical Chemistry*, 68 (1964) 2772.
- [30] V.c. Calvo-Perez, A.S. Vega C, P. Cortes and E. Spodine, *Inorganica Chimica Acta*, 333 (2002) 15.
- [31] A. Barbier, A. Hanif, J.-A. Dalmon and G.A. Martin, *Applied Catalysis A: General*, 168 (1998) 333.
- [32] A. Barbier, G.-A. Martin, P.R. de la Piscina and N. Homs, *Applied Catalysis A: General*, 210 (2001) 75.
- [33] C.P. Bean and J.D. Livingston, *Journal of Applied Physica*, 30 (1959) 120.
- [34] L.D. Kock and D.D. Waal, *Journal of Raman Spectroscopy*, 38 (2007) 1480.

Chapter 8

Fischer-Tropsch Performance of the Model Catalysts

8.1 Supported nano-sized cobalt crystallites

The Fischer-Tropsch activity and selectivity of all prepared supported cobalt nano crystallites of different size was tested in a laboratory scale fixed-bed reactor (see chapter 4.7.2). An amount of 1g of catalyst was loaded into the u-tube reactor and a synthesis gas flow ($H_2/CO = 2$) of $7.2 \text{ ml/g}_{\text{catalyst}} \cdot \text{min}$ (STP) was used. The total pressure was kept at 11 bar, resulting in a synthesis gas partial pressure of 9.9 bar (rest argon). During reaction the reactor temperature was set to 190°C . These conditions result in very low carbon monoxide conversion, generally below 10 % (see appendix A9), which is desired to avoid the possibility of re-oxidation of the metallic cobalt crystallites due to the presence of product water (see chapter 2.2.4), which would result in a loss of activity due to the loss of catalytically active material. The product is collected from the exhaust gas stream using the ampoule method (see chapter 4.7.6) which can be used to obtain product samples at a high sampling frequency (in this work up to 1 sample/min). This results in a very high temporal resolution of the reported activity and selectivity trends therefore allowing a distinct differentiation between initial stages of the Fischer-Tropsch synthesis (and rapid changes that can occur during this stage) and steady state performance. In the following representative reaction data are shown. A full documentation of relevant reaction data is given in appendix A9.

8.1.1 Fischer-Tropsch activity and characterisation of the spent catalysts

Due to the very mild reaction conditions (190°C , 9.9 bar synthesis gas, $SV = 7.2 \text{ ml/g}_{\text{catalyst}} \cdot \text{min}$ (STP)) and the low cobalt loadings of the model catalysts (see table 7.4) the carbon monoxide conversion in the FTS could be kept below 10%. These low conversion levels can not be determined accurately via the analysis of the permanent gases (Ar, N_2 , H_2 , CO) in the exhaust gas stream using the online GC with TCD detection. The CO conversion was therefore calculated from the formation rates of hydrocarbons collected in the ampoule samples (see chapter 4.9) and analysed using an offline GC equipped with a flame ionisation detector (FID). Under the chosen reaction conditions hydrocarbons with carbon numbers of nine and higher can partially condense on the ampoule walls as is shown in theoretical calculations (see figure 4.10) and will therefore not be injected into the GC-

FID quantitatively. The product spectrum of these samples therefore does only follow the Anderson-Schulz-Flory (ASF) distribution (see chapter 2.1.2), specific for the FTS product spectrum, up to a carbon number of eight. To obtain the full CO conversion the linear behaviour of the ASF distribution, from carbon numbers of three to eight, is extrapolated to a carbon number of 50. From this extrapolated product spectrum the CO conversion (see appendix A9) is calculated. The formation of carbon dioxide (CO_2) due to the water gas shift (WGS) reaction (see equation 2.3) can be neglected at low CO conversions for cobalt based FTS.

To allow the comparison of the CO conversion/catalyst activity between the tested model catalysts, activity is either represented as mol CO converted per time unit and mass of metallic cobalt or as turn over frequency (TOF) (see chapter 4.9.2). The TOF is a surface specific activity defined as the moles of CO converted per time unit and exposed cobalt metal atom. The number of exposed cobalt metal atoms is calculated using the number weighted average crystallite sizes of the respective reduced model catalyst obtained from TEM analysis (see table 7.5), the amount of metallic cobalt present after reduction/activation (see table 7.4) and the statistic crystallite model for a face-centred cubic cubo-octahedron crystallite proposed by van Harveldt and Hartog [1] (for calculations see appendix A5). All cobalt atoms of the crystallite surface are assumed to be exposed and therefore able to contribute to the FT activity.

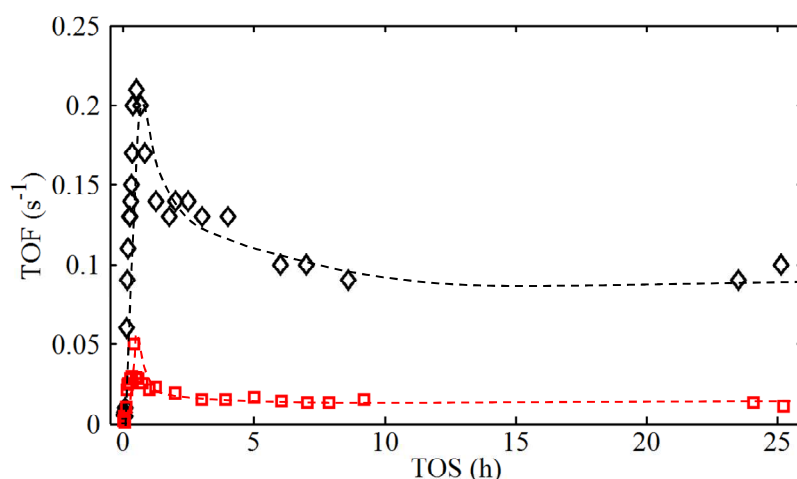


Figure 8.1: Turn over frequency (TOF) as a function of time on stream (TOS) for CAT 9.6 (◇) and CAT 3.1 (□). (Reaction conditions: $T = 190^\circ\text{C}$, $PP_{\text{syn.gas}} = 9.9 \text{ bar}$, $SV = 7.2 \text{ ml}_{\text{syn.gas}}/\text{g}_{\text{catalyst}} \cdot \text{min (STP)}$)

Figure 8.1 shows the TOF as a function of reaction time/time on stream (TOS) for the catalysts CAT 9.6 and CAT 3.1. All tested model catalysts display the same behaviour, with a sharp maximum activity after 30-50 minutes of reaction followed by a strong decrease before reaching steady state after approximately 10 hours on stream. The time when this maximum activity was reached is not crystallite size dependent and the ratios of the maximum TOF to the corresponding steady state TOF vary from 1.6-2.4. The position of the maximum activity (i.e. after 30-50 minutes) indicates that it is not a result of the residence time behaviour of the experimental set-up but a true effect of the catalytic process. The residence time in the reactor set up is in fact much shorter, namely around 10 min as determined in blank experiments. In studies on single crystal surfaces [2-4] and using Density Functional Theory (DFT) calculations [5] several researchers have shown that cobalt and nickel metal surfaces undergo a so called surface reconstruction upon exposure to FT conditions with elevated

temperatures, pressures and synthesis gas atmosphere. Carbon surface species have identified as the most likely cause for these reconstructions in these theoretical calculations [5]. Schulz and co-workers [6] hypothesised that the surface reconstruction of the freshly reduced catalyst is essential to form the sites required for the Fischer–Tropsch synthesis. These sites were labelled as Fischer-Tropsch ‘regime’. Welker [7] reports a rapid decrease in FT activity from minute one on nano-sized ruthenium crystallites supported on an alumina carrier before reaching steady state activity after approximately 100 minutes time on stream. This deactivation was proposed to be a result of the surface reconstruction taking place upon the first exposure of the catalyst to synthesis gas. By pre-exposing the freshly reduced ruthenium catalyst to CO for one hour at one bar at the reaction temperature (170°C) prior to the FT synthesis the high initial activity was not obtained, and the catalyst rather displayed the steady state activity and selectivity from the start of the reaction. In order to study the effect of carbon monoxide pre-exposure on the activity maximum for nano-sized cobalt crystallites in this work, the FTS experiment of CAT 7.3 was repeated. But in contrast to the normal experiments prior to the FT testing the freshly reduced catalyst was exposed to a carbon monoxide atmosphere at 3.3 bar (partial pressure of CO in FT experiment) for 1.5 hours at 190°C (reaction temperature of the FT synthesis in this study). The initial FT activity maximum was notably decreased (and so was the initial methane selectivity (see chapter 8.1.2 and figure 8.11)) upon exposure of this CO pre-treated catalyst to FT conditions (see figure 8.2). This decrease in initial activity supports the hypothesis published by Welker [7] that the initial deactivation is a result of the interaction of CO or surface carbon species with the freshly reduced metal surface. Which type of the theoretically calculated [5] surface reconstructions is responsible for this deactivation could not be determined. In contrast to the studies by Schulz and co-workers [6], who reported an increase in activity upon the initial exposure of the catalyst to FT conditions, in this work as well as in the work by Welker [7] the initial exposure to FT conditions, i.e. the proposed surface reconstruction, results in a deactivation of the catalysts. It can be speculated that these opposing observations are a result of fundamentally different catalyst structure at the start of the FT synthesis. While in this and Welker’s [7] study the metal crystallites have a very defined size in the nanometer range, the catalysts described by Schulz et al. [6] were exposed to high temperatures (600°C) during calcination and reduction probably resulting in large cobalt particles which display bulk metal behaviour.

With the time resolved reaction data the activity and selectivity results can be categorised into initial behaviour of the freshly reduced catalyst (maximum activity after 30-50 minutes TOS) and performance of the spent catalyst (after 25 hours under Fischer-Tropsch conditions). The freshly reduced catalyst, i.e. the catalyst responsible for the maximum activity and the initial catalyst behaviour, was characterised in detail (see chapters 7.1.1-7.1.4). To relate activity and selectivity data to the accurate crystallite sizes after 25 hours at Fischer-Tropsch conditions, after the experiment the catalysts were cooled down under argon to room temperature and passivated with CO₂ to avoid spontaneous re-oxidation upon exposure to air. Figures 8.3 and 8.4 show examples of TEM and HRTEM micrographs taken from spent catalysts and the calculated crystallite size distributions for the corresponding catalyst samples (for crystallite size distributions of other spent model catalysts see appendix A6). As discussed in the characterisation of the freshly reduced catalyst samples (see chapter 7.1.3), the lattice parameters measured from HRTEM imaging for the reduced cobalt crystallites of the spent catalysts (4.6 - 4.7 Å) are identical to the one expected for oxidic cobalt crystallites and not to the one of metallic cobalt (2.0 Å). As PXRD studies show only a metallic cobalt

phase present, it is assumed, that the passivation with CO₂ resulted in the formation of an oxidic layer on the cobalt crystallite but did not fully re-oxidise the metallic crystallites (see chapter 7.1.3). For purposes of comparison the crystallite size distributions of the freshly reduced and passivated samples are also given.

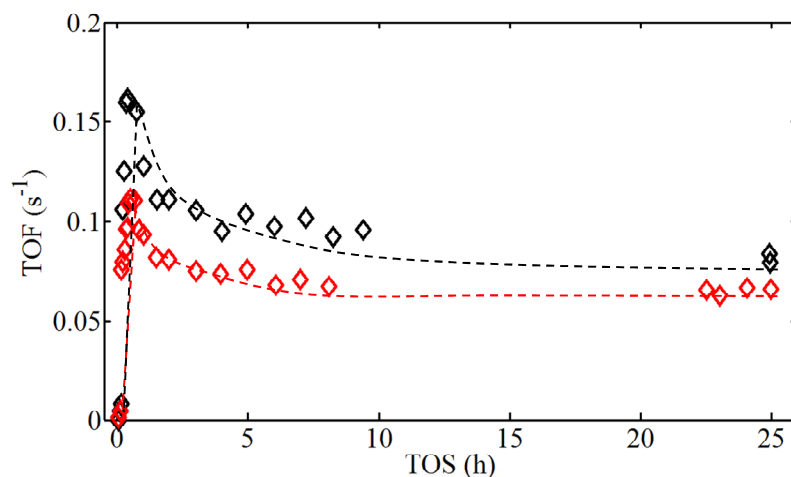


Figure 8.2: Turn over frequency (TOF) as a function of time on stream (TOS) for CAT 7.3 after normal activation process (\diamond) and CAT 7.3 after activation process followed by pre-exposure to 3.3 bar CO at 190°C for 1.5 hours. (\diamond). (Reaction conditions: $T = 190^\circ\text{C}$, $PP_{\text{syn.gas}} = 9.9$ bar, $SV = 7.2$ $\text{ml}_{\text{syn.gas}}/\text{g}_{\text{catalyst}} \cdot \text{min}$ (STP)).

Table 8.1: Average crystallite sizes and standard deviations of model catalysts calculated from a minimum of 300 crystallites in the spent state (after 25 hours at Fischer-Tropsch conditions and passivation with CO₂). For comparison with values obtained from PXRD analysis the volume weighted mean crystallite sizes are also given.

Catalyst	spent model catalyst (fcc-Co)				
	$d_{\text{num}}^{\text{a}}$ (nm)	σ^{b} (nm)	rel. dev. ^c (%)	$d_{\text{vol}}^{\text{d}}$ (nm)	$d_{\text{PXRD}}^{\text{e}}$ (nm)
CAT 9.6	10.1	2.3	22.8	11.7	11.3
CAT 8.6	8.7	1.7	19.5	9.7	8.2
CAT 7.3	7.5	1.1	12.6	8.6	7.7
CAT 6.8	6.3	1.1	17.4	6.3	6.3
CAT 5.9	7.4	1.7	23.0	8.6	9.2
CAT 4.8	5.3	0.9	17.0	5.8	6.7
CAT 4.4	6.8	1.3	19.1	6.8	7.6
CAT 4.0	3.6	0.7	19.4	4.1	5.3
CAT 3.1	2.5	0.5	20.0	2.8	3.6

^a number weighted average crystallite size.

^b standard deviation of d_{num} .

^c relative deviation in % ($100 \cdot \sigma/d_{\text{num}}$).

^d volume weighted average crystallite size, assuming spherical crystallites.

^e crystallite sizes obtained from PXRD spectra of the spent and passivated model catalysts using Rietveld refinement and the PONKCS approach.

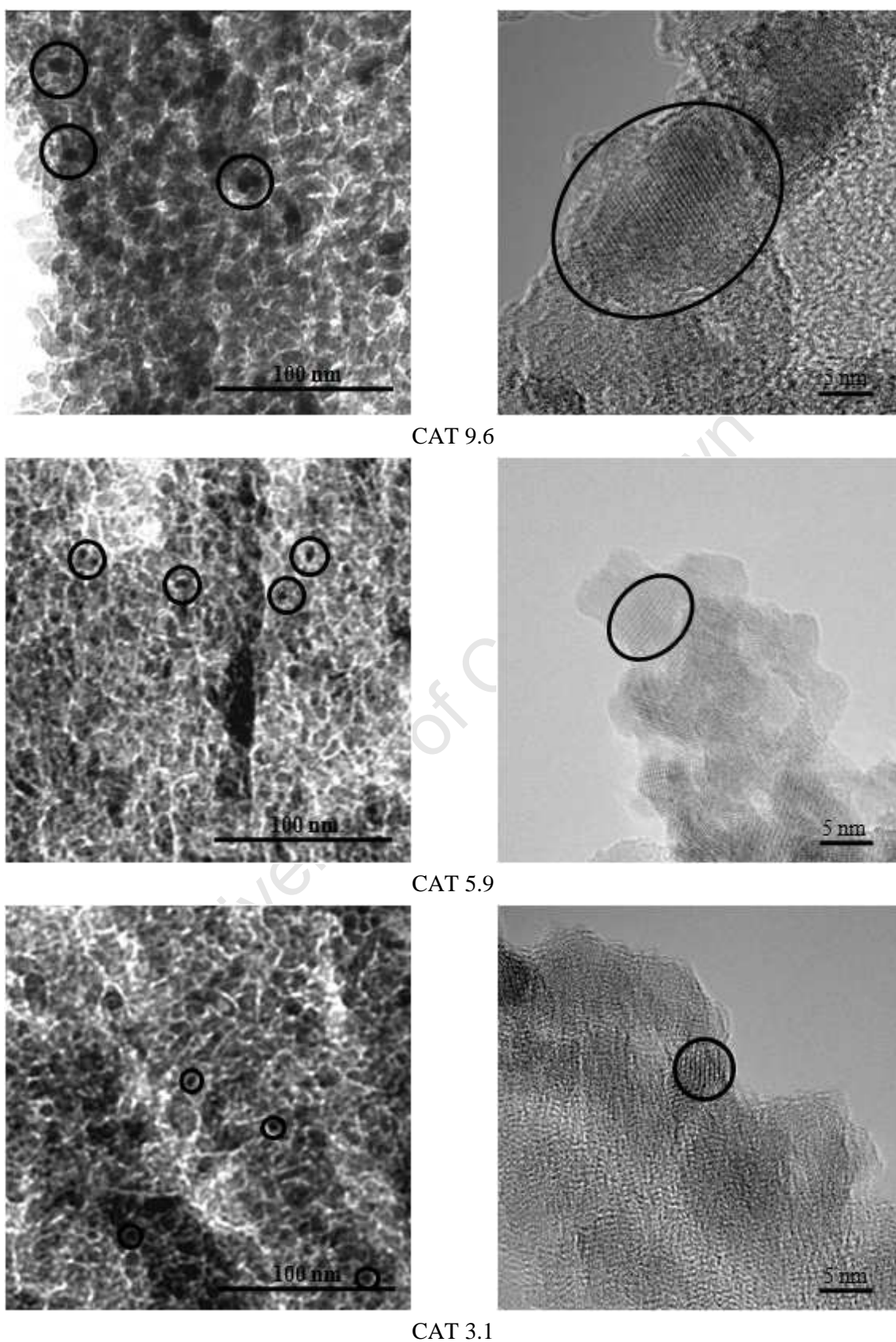


Figure 8.3: TEM and HRTEM micrographs of CAT 9.6, CAT 5.9 and CAT 3.1 after 25 hours under Fischer-Tropsch conditions and passivation in CO₂. Identified cobalt crystallites are encircled.

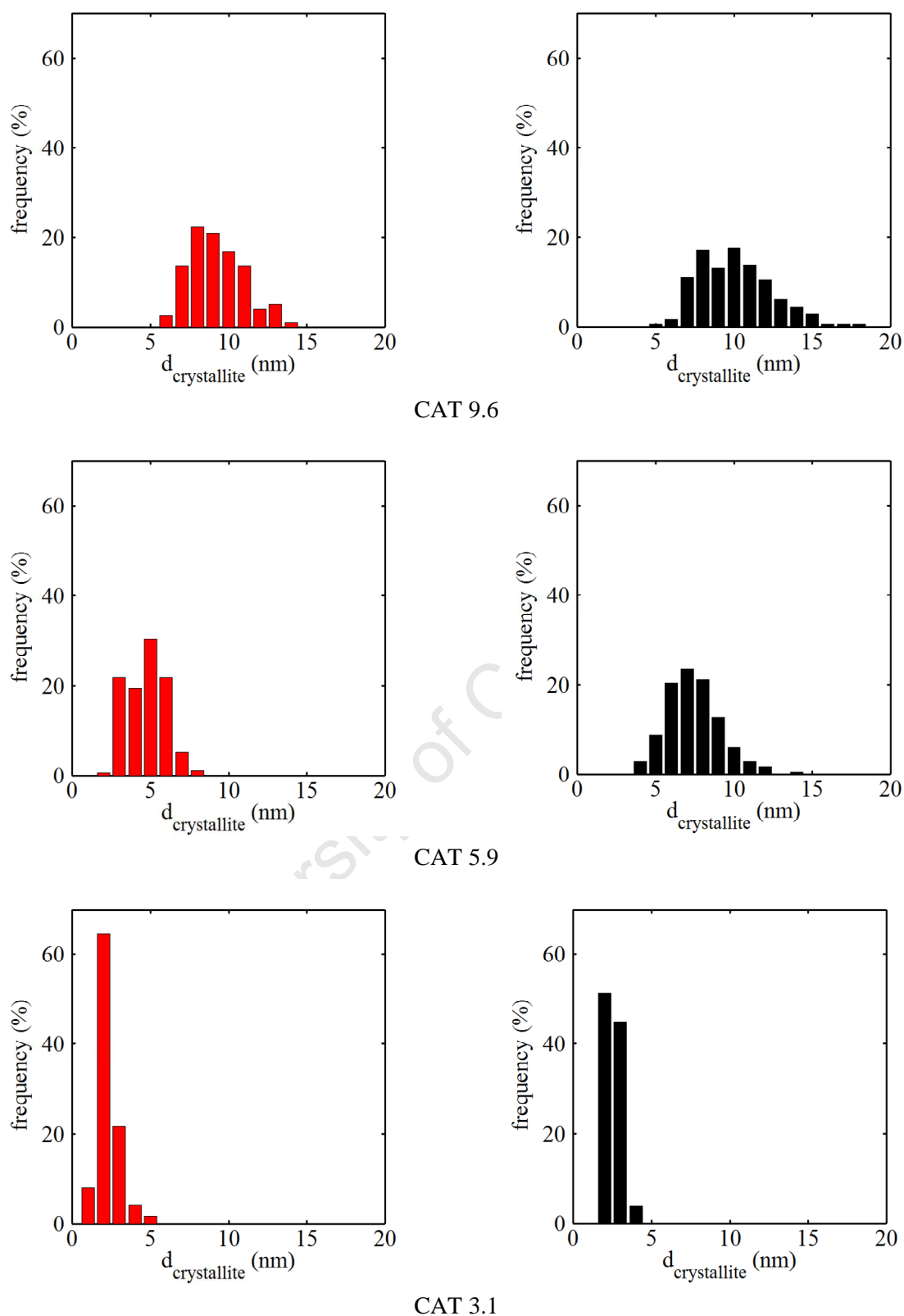


Figure 8.4: Crystallite size distributions (number based) of selected model catalysts determined from a minimum of 300 crystallites (■ reduced and passivated, ■ after 25 hours at Fischer-Tropsch conditions and passivated).

From the crystallite size distributions displayed in figure 8.4 as well as from the comparison of the sizes of the freshly reduced model catalyst (see table 7.5) and the spent catalysts (see table 8.1) it is evident that although the cobalt crystallites generally undergo slight to moderate crystallite growth during the FT synthesis (see table 8.2), the size distributions are still narrow and the relative standard deviation in all model catalysts is below 25 %.

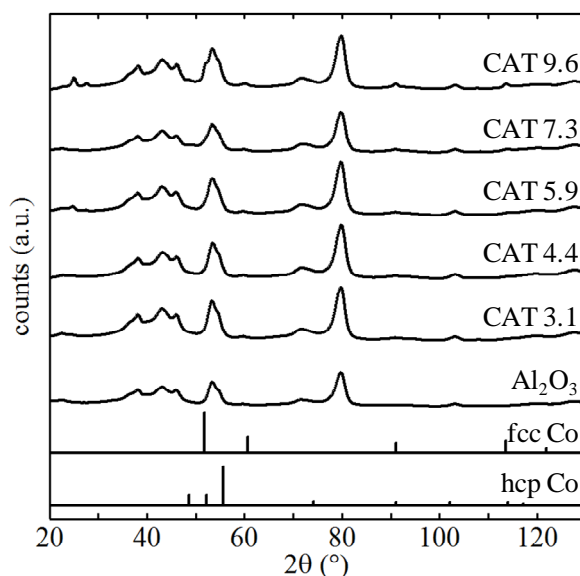


Figure 8.5: PXRD spectra of spent model catalysts, i.e. after 25 hours at Fischer-Tropsch conditions followed by passivation. The diffraction spectrum of Al_2O_3 and the reference patterns of face-centred cubic and hexagonal closest packed cobalt metal are given as reference.

In order to confirm the cobalt crystallite sizes of the spent catalysts (the model catalysts after 25 hours at Fischer-Tropsch conditions) as obtained by TEM/HRTEM analyses, the spent model catalyst samples were also characterised by means of powder X-ray diffraction (PXRD). The obtained diffraction spectra were compared to reported reference patterns and analysed using Rietveld refinement methods, more specifically the PONKCS approach proposed by Scarlett and co-workers [8] (see also chapter 4.5.2). All PXRD spectra of the spent model catalysts are dominated by the diffraction pattern of the alumina support as also previously pointed out for the calcined and freshly reduced catalysts (see chapter 7.1.4). From the comparison with reference patterns the only identifiable cobalt phase was the face-centred cubic metal phase (see figure 8.5) which was also the only detectable phase in the freshly reduced catalysts. The average crystallite sizes obtained from refinement of the PXRD scans correlate well with the results obtained from TEM/HRTEM analysis (see table 8.1). Based on the average crystallite sizes obtained by Rietveld refinement of the freshly reduced and the spent catalyst the cobalt crystallites undergo different levels of crystallite growth ranging from no growth to 80.7% (see table 8.2). To correct for these varying crystallite growth rates and to avoid the introduction of error in the analysis of the FT performance measurements of the model catalysts, all activity and selectivity comparisons are carried out at two specific points of the FT experiments. One being at the maximum activity, with the crystallite sizes assumed to be identical to the ones of the freshly reduced catalyst and one being after 24-25 hours under FT synthesis where the crystallite sizes obtained from the spent catalysts are relevant (see table 8.1).

Table 8.2: Relative crystallite growth (in %) during exposure to Fischer-Tropsch conditions, based on average crystallite sizes obtained from Rietveld refinement of PXRD spectra.

Catalyst	Growth (%)
CAT 9.6	19.5
CAT 8.6	3.4
CAT 7.3	0.0
CAT 6.8	13.9
CAT 5.9	80.7
CAT 4.8	40.7
CAT 4.4	68.9
CAT 4.0	16.7
CAT 3.1	7.1

Figure 8.6 shows the surface specific activity/turn over frequency (TOF) as function of the average cobalt crystallite diameter. The TOF is compared at the initial maximum activity with the crystallite sizes obtained from the analysis of the freshly reduced catalyst (see table 7.5) and after 24-25 hours under Fischer-Tropsch conditions with the crystallite sizes of the spent catalysts (see table 8.1). It should be noted that for the calculation of the number of cobalt surface atoms also the actual cobalt crystallite sizes were used, i.e. those of the freshly reduced catalyst and those of the spent catalysts respectively. As reported in previous studies on the crystallite size dependency of the Fischer-Tropsch synthesis [7, 9-16] the TOF decreases with decreasing crystallite size. In contrast to previous studies on cobalt [9-11], this decrease was observed for the whole range of crystallite sizes. Bezemer et al. [9] as well as Prieto et al. [11] reported a constant TOF for crystallites above a certain average diameter (6-8 nm in the work of Bezemer et al. [9], 12.8 nm in the work of Prieto et al. [11]). Van Santen [17] hypothesised, based on the work on surface reconstruction of metallic cobalt during exposure to synthesis gas by Wilson et al. [2], that a crystallite size effect on the CO activation would only be observed for cobalt crystallites below a size of 15 nm. Surfaces of larger metallic cobalt crystallites would be reconstructed to form islands in the size range of 15 nm (see figure 2.8) and would therefore all display a similar TOF at steady state.

The origin of the decrease in surface specific activity with decreasing crystallite sizes is widely discussed in literature. Several publications identify the re-oxidation of metallic cobalt to Co(II) as a possible deactivation mechanism [18-21]. Theoretical thermodynamic calculations [19, 22] indicate that, in the presence of water, small cobalt crystallites (< 6 nm) are more prone to undergo oxidation to Co(II)O, which is inactive for the Fischer-Tropsch synthesis (see figure 2.7). With water being a main product in the Fischer-Tropsch synthesis, higher water partial pressures correlate directly with higher conversions. Van de Loosdrecht and co-workers [23] compared the theoretical data with re-oxidation events or the lack thereof in FT synthesis studies reported in literature and found them to be in a good agreement. From these calculated data it can be concluded that for realistic cobalt based FT conditions, i.e. 170-240°C, 20 bar, H₂:CO = 2, X_{CO+H₂} = 50-70% [23], re-oxidation of metallic cobalt is only feasible for cobalt crystallites with a crystallite diameter of 4.5 nm and less. Due to the very mild Fischer-Tropsch conditions in this study (190°C, 10 bar synthesis gas, H₂:CO = 2, X_{CO} < 10%) the water partial pressure does not exceed 0.3 bar (value calculated with the idealistic assumption that H₂ and CO react solely to form C₃H₈ and H₂O) which is below the critical water concentration, which

would result in re-oxidation, even for cobalt crystallites that are smaller than 4-5 nm. The magnetic in-situ characterisation (see chapter 7.1.6) conclusively show that no oxidation of the odel catalysts did take place at the mild test conditions. In other words, the studies in this work are not affected by crystallite re-oxidation, and the observed crystallite size dependency should therefore have another cause.

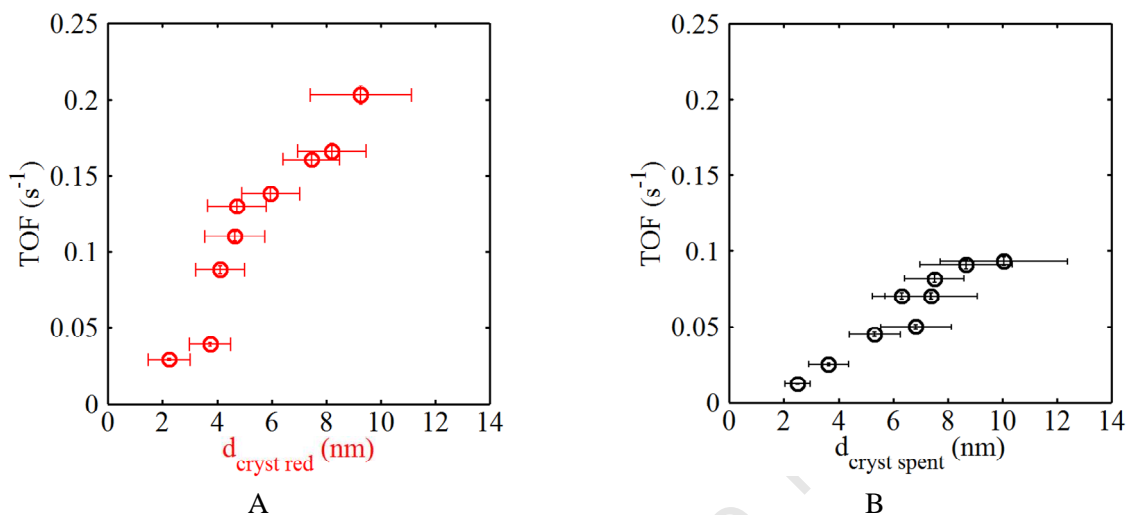


Figure 8.6: TOF as a function of average cobalt crystallite size; (A) at maximum activity versus the crystallite size of the freshly reduced catalyst; (B) at steady state versus the crystallite size of the spent catalyst, i.e. after 25 hours under Fischer-Tropsch conditions. (Reaction conditions: $T = 190^{\circ}\text{C}$, $PP_{\text{syn.gas}} = 9.9 \text{ bar}$, $SV = 7.2 \text{ ml}_{\text{syn.gas}}/\text{g}_{\text{catalyst}} \cdot \text{min (STP)}$).

In recent years a second theory, often referred to as the ensemble theory [1, 6, 17, 24-28], gained much attention as being the possible origin of the decreased surface specific FT activity with a decrease in crystallite size. This theory, first proposed in the late 60s by van Hardeveld and Hartog [1], states that complex surface reactions or reaction networks, as it is the case in the Fischer-Tropsch synthesis, can not be catalysed by a single metal atom but require a certain number of adjacent metal atoms in a set geometry. These ensembles or domains might be present on the reduced catalyst surface or only form during surface reconstruction at initial stages of the Fischer-Tropsch synthesis [6].

The ensemble theory was extensively studied in the field of theoretical catalysis [24, 25, 29-31]. In particular the dissociation of carbon monoxide on various surface sites was the focus of these studies. So called B5 sites (see figure 2.9 B) were identified as being the most suitable sites to facilitate the dissociation of the adsorbed gaseous carbon monoxide on the catalytic surface [24-26, 29-31]. These B5 sites are only present on kink or terrace sites on a metal surface [1] and they have been proposed to display different levels of activity depending on their surrounding, more specifically depending on the number of adjacent unsaturated metal atoms [17, 26]. More of these B5 sites can be expected for smaller crystallites due to the higher number of edges and kinks. Saib and co-workers [18] also postulate that during the process of surface reconstruction [2-5] more B5 sites are introduced. However if CO dissociation was the rate limiting step in the Fischer-Tropsch synthesis the methane selectivity would exceed 95% [32]. As this is in contradiction to experimental results, it is generally accepted that the product desorption and not the CO dissociation is the rate limiting step in the FTS [33, 34]. The B5 site is therefore unlikely to represent the whole Fischer-Tropsch ensemble but it probably constitutes a part of it. Due to the number of metal atoms forming the minimum required

ensemble displaying FT activity, their density on the catalyst surfaces is believed to decrease with decreasing crystallite sizes. A certain minimum crystallite size should therefore exist below which no FT activity can be sustained [27, 28]. The ensemble theory can conclusively explain the observed decrease in activity with decreasing crystallite size in this and previous studies [7, 9-16].

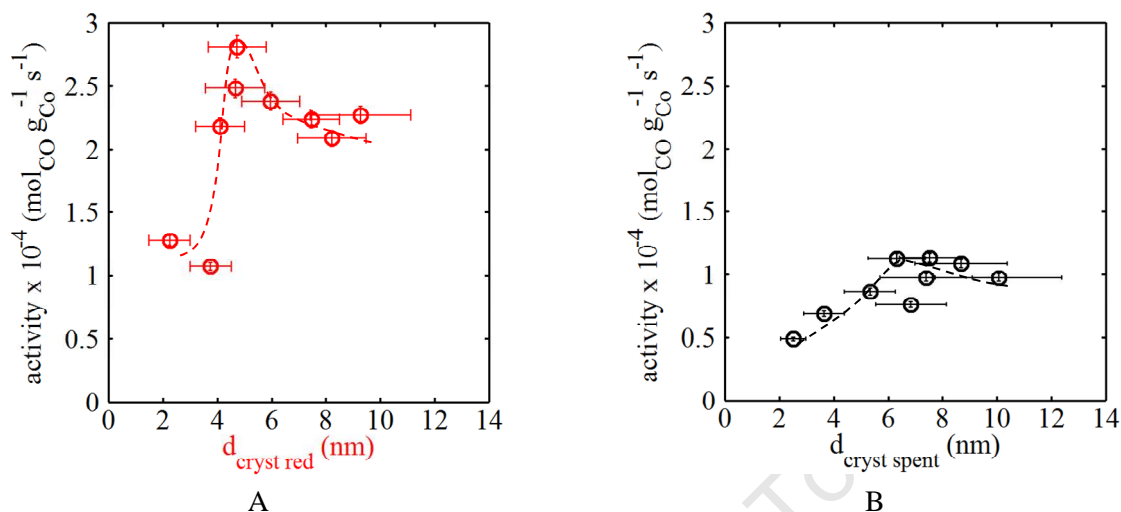


Figure 8.7: Mass specific activity as a function of average cobalt crystallite size; (A) at maximum activity versus the crystallite size of the freshly reduced catalyst; (B) at steady state versus the crystallite size of the spent catalyst, i.e. after 25 hours under Fischer-Tropsch conditions. (Reaction conditions: $T = 190^{\circ}\text{C}$, $PP_{\text{syn.gas}} = 9.9$ bar, $SV = 7.2$ ml_{syn.gas}/g_{catalyst}·min (STP)).

In figure 8.7 the Fischer-Tropsch activity of the tested model catalyst is expressed as mole carbon monoxide converted per gram metallic cobalt and unit time. The model catalysts at the initial stages of the FT experiment display a maximum activity at a crystallite size of 4.7 nm while at steady state the maximum is measured at around 6.3 nm. Bezemer et al. [9] reported this maximum to be in the same range in their study on the FT activity of nano-sized cobalt crystallites supported on carbon nano fibres.

As discussed in detail in chapter 7.1.5 selected model catalysts were characterised by means of temperature programmed desorption of carbon monoxide (CO-TPD). Of special interest is the formation of carbon dioxide and methane which desorb at various temperatures indicating the presence of different active surface sites. For a cobalt metal crystallite size of 4.7 nm, one site dominates in the formation of CO₂ and CH₄ (see figure 7.12). The highest amount of methane per gram metallic cobalt of all tested catalysts is formed on this site during CO-TPD. The same model catalyst (CAT 5.9) shows a maximum activity per gram cobalt in the Fischer-Tropsch synthesis at initial stages of the experiment, supporting the results obtained from the catalyst characterisation. Both sets of experiments indicate that for a cobalt crystallite size of 4.7 nm a maximum number of active sites or the ideal combination of active sites for the CO dissociation and CH₄ formation per mass of catalytic active material is present.

8.1.2 Methane formation and chain growth

Methane is the thermodynamically most stable [32, 35, 36] but at the same time the industrially least desired hydrocarbon product of the Fischer-Tropsch synthesis [37-39] as alternative routes to obtain

methane for industrial applications, for example directly from natural gas or from biogas, are much more cost effective. Furthermore, methane, in form of natural gas, is increasingly used as a feed stock for the generation of synthesis gas. According to the most commonly accepted Fischer-Tropsch mechanism, the alkyl mechanism (see chapter 2.1.2), methane is formed via the complete hydrogenation of a surface carbon species originating from the dissociative adsorption of carbon monoxide (see figure 8.8) [40]. The surface alkyl species can also act as a chain starter and induce chain growth via combination with a methylene species.



Figure 8.8: Schematic representation of the formation of methane and chain growth according to the alkyl mechanism (see chapter 2.1.2) (adapted from [40]).

Figure 8.9 shows the changes in methane selectivity as function of time during the FT experiments exemplary for CAT 9.6 and CAT 3.1. The methane selectivity for all tested model catalyst decreases rapidly from almost 100 C% in the first minute to a stable value of 15-20 C% after 30-50 minutes. It can be noted that the methane selectivity reaches steady state before the turn over frequency reaches steady values, even before the turn over frequency peaks (see chapter 8.1.1). The inversed trend of the methane selectivity can be observed for the selectivity for hydrocarbons with carbon numbers of 5 and higher ($S_{C_{5+}}$ see figure 8.10). $S_{C_{5+}}$ increases rapidly in the initial minutes of the FTS levelling off to a steady selectivity after 30-50 minutes on stream, again much earlier than steady state surface activity is reached. The decrease in activity from 1 to 10 hours under Fischer-Tropsch conditions (see figure 8.1) does not have any effect on the selectivities of methane or the selectivities of the higher hydrocarbons. This is further confirmed by the comparison of the chain growth probabilities (α) at maximum TOF and after 25 hours of FT testing which showed no change over time and which does not depend on crystallite size (see table 8.3). With a chain growth probability of approximately 80% (see table 8.3) the methane selectivity is expected, according to an ideal ASF product distribution, to be below 10 C%. The methane selectivities in this study are 50 to 100% higher. It has to be noted that the methane selectivity is calculated based on the extrapolated conversion (to a carbon number of 50) and is expressed as percentage carbon in this extrapolated product stream. It has been proposed in literature that besides the methane formed as a part of the FT product spectrum, further sites may be present on the catalysts surface which show activity towards the formation of methane but not towards chain growth [41, 42]. These simpler catalytic active sites result in increased methane selectivities without a decrease in chain growth probability. Schulz and co-workers [35] have studied the effect of the water partial pressure in the reaction system on the selectivity of cobalt catalysts in the FTS. They concluded that water inhibits the methanation reaction as an increase in water partial pressure from 1 to 9 bar resulted in an decrease in methane selectivity from approximately 15 to 5 C%. The water partial pressures in this study were deliberately kept low to avoid re-oxidation of the cobalt nanocrystallites to the FT inactive Co(II)O (see chapter 2.2.4). This lack of water could result in a higher methane selectivity than expected from FT experiments at higher conversions at the same chain growth probabilities.

Previous studies on Fischer-Tropsch synthesis with cobalt, iron, nickel and ruthenium [6, 7, 33, 43-45] have also reported higher initial methane selectivities. This was attributed to the absence of surface sites able to catalyse chain growth prior to a surface reconstruction [2, 6] under Fischer-Tropsch conditions. It is believed that these active regimes [6] or ensembles [28] form only upon exposure of the metallic catalyst surface to carbon surface species originating from dissociated adsorption of carbon monoxide [5, 18]. The formation of methane is believed to require a less complex active site [12] and therefore dominates the initial minutes of the FTS.

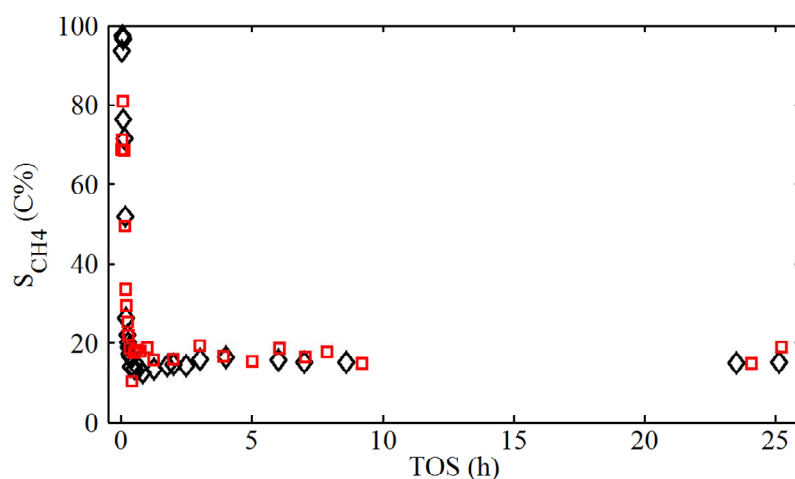


Figure 8.9: Methane selectivity as a function of time on stream (TOS) of CAT 9.6 (◇) and CAT 3.1 (□). Note that the methane selectivity is calculated based on the conversion obtained via product formation rates (extrapolated to a carbon number of 50) and is expressed as percentage carbon in this extrapolated product stream. (Reaction conditions: $T = 190^{\circ}\text{C}$, $PP_{\text{syn.gas}} = 9.9 \text{ bar}$, $SV = 7.2 \text{ ml}_{\text{syn.gas}}/\text{g}_{\text{catalyst}} \cdot \text{min (STP)}$).

In this study we have shown the effect of deactivation originating from CO induced surface reconstruction by pre-exposing the freshly reduced catalyst to 3.3 bar CO at reaction temperature for 1.5 hours (see figure 8.2). The deactivation process is measurable up to approximately 10 hours on stream. The selectivity changes of methane and the higher hydrocarbons do happen in the first 30 minutes after which the selectivities remain stable. High methane selectivities can also be expected for high hydrogen to carbon monoxide ratios in the synthesis gas stream and the resulting high concentration of dissociated hydrogen on the catalyst surface. From CO-TPD studies of the model catalysts (see chapter 7.1.5, especially figure 7.11 C) it could be shown that after reduction the cobalt metal surface of the catalysts is covered with strongly bound hydrogen (desorption temperatures up to 950°C) which can react to methane with dissociated carbon monoxide. Comparing the methane selectivities in the initial stages of the FT synthesis of CAT 7.3 without and with CO pre-exposure reveals the influence of this residual hydrogen coverage. Methane selectivity in the run without pre-exposure of the catalyst to carbon monoxide (see figure 8.11 A) shows initial values of more than 95 C% for approximately 10 minutes prior to the decrease to steady state selectivity. The catalyst pre-treated with CO (see figure 8.11 B) displays a maximum methane selectivity of 40 C% before decreasing to the same steady state methane selectivity as measured without additional CO pre-exposure FT conditions. The CO pre-exposure does not only allow the surface reconstruction to take place prior to the actual Fischer-Tropsch experiment but also allows the residual hydrogen on the

cobalt metal surface (originating from this reduction process) to partially react upon exposure to carbon monoxide atmosphere. The hydrogen concentration in the initial minutes of the experiment is therefore decreased resulting in less methane being formed.

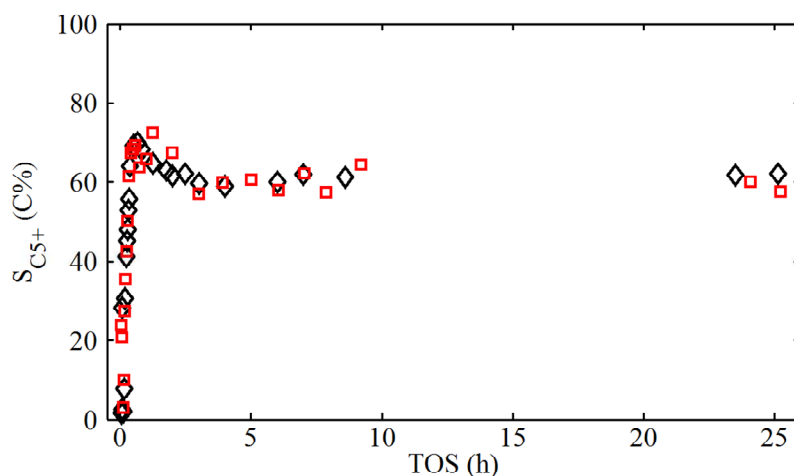


Figure 8.10: Selectivity towards hydrocarbons with a carbon chain length of five and higher ($S_{C_{5+}}$) as a function of time on stream (TOS) of CAT 9.6 (◇) and CAT 3.1 (□). Note that $S_{C_{5+}}$ is calculated based on the conversion obtained via product formation rates (extrapolated to a carbon number of 50) and is expressed as percentage carbon in this extrapolated product stream. (Reaction conditions: $T = 190^{\circ}\text{C}$, $PP_{\text{syn.gas}} = 9.9 \text{ bar}$, $SV = 7.2 \text{ ml}_{\text{syn.gas}}/\text{g}_{\text{catalyst}} \cdot \text{min (STP)}$).

Table 8.3: Chain growth probabilities for tested model catalysts at maximum turn over frequency and at steady state. The chain growth probabilities are calculated via linear regression from the ASF distribution (C_3 to C_8) of the measured FT products at the respective times.

Catalyst	Chain growth probability α (%)	
	max. TOF	steady state
CAT 9.6	78	75
CAT 8.6	72	69
CAT 7.3	76	76
CAT 6.8	73	75
CAT 5.9	76	75
CAT 4.8	77	76
CAT 4.4	75	75
CAT 4.0	73	73
CAT 3.1	79	77

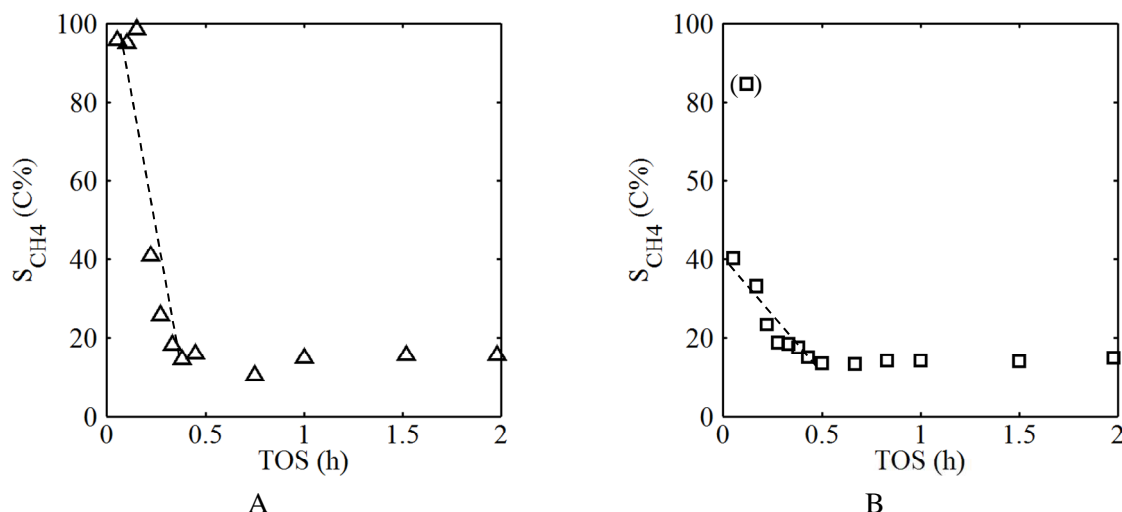


Figure 8.11: Methane selectivities in the first 2 hours of the FT experiment. (A) CAT 7.3; (B) CAT 7.3 after pre-exposure to 3.3 bar of CO at 190°C for 1.5 hours after reduction and prior to exposure to FT conditions. (Reaction conditions: $T = 190^\circ\text{C}$, $PP_{\text{syn.gas}} = 9.9$ bar, $SV = 7.2$ $\text{ml}_{\text{syn.gas}}/\text{g}_{\text{catalyst}} \cdot \text{min}$ (STP)).

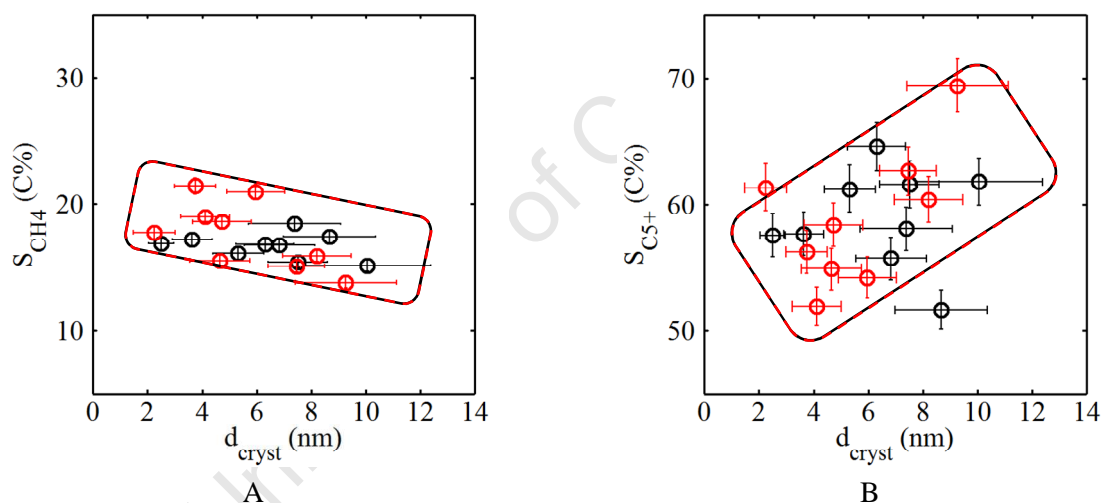


Figure 8.12: (A) Methane selectivities (S_{CH_4}) and (B) selectivities towards hydrocarbons of a carbon number of 5 and higher ($S_{\text{C}_{5+}}$) over cobalt crystallite sizes at initial maximum TOF (\circ) and after 25 hours under Fischer-Tropsch conditions (\circ). Note that both types of selectivities are calculated based on the conversion and product spectrum obtained via product formation rates (extrapolated to a carbon number of 50) FT product spectrum. (Reaction conditions: $T = 190^\circ\text{C}$, $PP_{\text{syn.gas}} = 9.9$ bar, $SV = 7.2$ $\text{ml}_{\text{syn.gas}}/\text{g}_{\text{catalyst}} \cdot \text{min}$ (STP)).

With respect to effects of the crystallite size on the methane selectivity in the FT synthesis, enhanced methane formation has been reported on cobalt, iron ruthenium and rhodium [7, 9, 10, 13-16] with decreasing crystallite size with a relative increase of up to 33% [9]. Due to the close relationship of the methanation reaction and chain growth on FT active sites/ensembles (see figure 8.9) an increasing methane selectivity with decreasing crystallite size results in a mirrored effect on the selectivity for higher hydrocarbons, i.e. hydrocarbons with a carbon number of 5 and higher. Similar to previous studies we could determine an increasing trend in the methane selectivity paired with a

decrease in $S_{C_{5+}}$ with decreasing crystallite size, although with some scatter of the data (see figure 8.12). As discussed above the deactivation of the model catalyst due to CO induced surface reconstruction does not affect the selectivities. Welker [7] reported the influences on the selectivities are more pronounced at more severe FT conditions, i.e. higher pressures and temperatures. Again the structure sensitivity of the FTS is identified as the origin of the crystallite size effect on the methane selectivity and the formation of long chain products [7, 9, 12]. The FTS is proposed to require a certain minimum number of adjacent metal atoms in a specific geometry in order to display activity [7, 9, 10, 12, 17, 24-28]. On smaller crystallites less of these minimum required ensembles [28] can be formed on the crystallite faces. As a result not only does the surface specific activity or TOF decrease with decreasing crystallite size, but also more metal surface atoms are available to take part in the less demanding methanation reaction [41, 42].

8.1.3 Olefin formation

The two main hydrocarbon classes formed as primary products in the Fischer-Tropsch synthesis are α -olefins and n-paraffins [36, 46-51]. According to the alkyl mechanism (see chapter 2.1.2) α -olefins are formed by β -hydrogen elimination from a surface alkyl species followed by desorption, while n-paraffins are formed through hydrogenation of a surface alkyl species (see figure 8.13). The composition of the primary products is between 70-90 mol% olefinic [49, 51, 52, 53]. Deviations from these selectivities indicate the presence of subsequent reactions of the primarily formed olefins. Most n-paraffins are formed via the re-adsorption of an α -olefin, followed by the hydrogenation of this surface alkyl species in a secondary reaction [49, 52] (see figure 8.14). Besides the hydrogenation and the formation of n-paraffins, the re-adsorbed α -olefins can also, normally to a lesser extent, be incorporated into further chain growth [45].

In the following, trends in olefin selectivity and product composition are shown. It should be noted that all displayed data are based on the hydrocarbon fraction (C_1 - C_8) analysed in the offline GC-FID, i.e. these are not based on the extrapolated product spectra (see chapter 8.1.2).

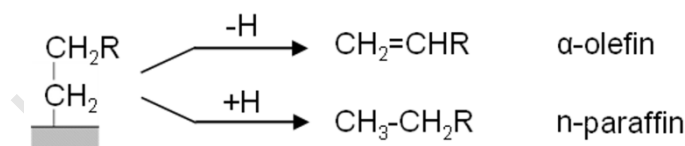


Figure 8.13: Proposed chain termination steps in the FTS according to the alkyl mechanism (see chapter 2.1.2) forming the primary products, α -olefins (predominant with 70-90 mol% [49, 51, 52, 53]) and n-paraffins (adapted from [40]).

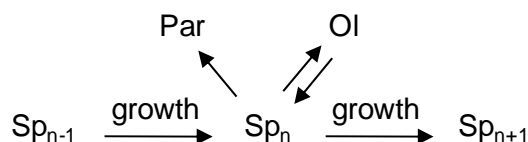


Figure 8.14: Non trivial surface polymerisation with chain growth, chain termination as n-paraffin (Par) and termination as α -olefin (Ol) and re-adsorption of α -olefins (adapted from [40]).

The studied model catalysts show three distinct phases of olefin formation during their exposure to Fischer-Tropsch conditions (see figure 8.15). In the first minutes, prior to the maximum turn over frequency (see figure 8.1), the selectivity towards olefins increases steeply from 0 C% to nearly steady state levels of approximately 40 C%. As previously discussed for the methane selectivity (see chapter 8.1.2) hydrogen originating from the activation process can be assumed to be present on the freshly reduced catalyst surface. High concentrations of hydrogen would clearly suppress the formation of olefins in the final product or enhance the primary and secondary reactions towards n-paraffins (in this case mainly methane, see figure 8.9). As the FTS is a rather slow reaction and requires time to form chain initiators and monomers (see chapter 2.1.2), the initial sharp increase of the olefin selectivity could also originate from this initial time delay in which mainly the thermodynamically most stable hydrocarbon, CH₄, is formed due to a lack of chain growth supporting surface species. Previous studies on cobalt, nickel and iron also show lower initial olefin selectivities which were explained by a higher hydrogen concentration on the catalyst surface and the higher possibility of an olefin to re-adsorb on a less populated surface to result in secondary hydrogenation [33, 44, 45, 53].

A second phase of olefin formation can be observed from 30-50 minutes into the run to 10 hours characterised by a slow but steady increase in olefin selectivity. Again possible higher hydrogen concentrations on the fresher catalyst might have an influence on the olefin selectivity. The increase in olefin content would then indicate the disappearance of this extra hydrogen source which contributed to the conversion of α -olefins to form paraffins. Alternatively, or in addition to this the surplus of hydrogen may even affect the primary product selectivity and paraffin desorption might be preferred over olefin formation. Schulz and co-workers [6, 50] have proposed that the cobalt metal surface reconstruction upon initial exposure to synthesis gas [2, 18] results in a decrease of sites which are active for secondary olefin reactions. These sites were hypothesised to be different and independent of the sites responsible for chain growth [53]. This would result in a higher steady state olefin selectivity than at initial stages prior to the surface reconstruction. Indeed the second phase of the olefin formation (see figure 8.15) correlates exactly with the deactivation behaviour observed with all studied model catalysts (see chapter 8.1.1 and figure 8.1). This deactivation process was overcome by pre-exposing a freshly reduced catalyst at reaction temperature to 3.3 bar carbon monoxide for 1.5 hours in an attempt to mimic carbon induced surface reconstruction. In the case of the pre-exposed catalyst, the olefin selectivity in the second stage of the experiment, i.e. the surface reconstruction, reaches higher initial values while displaying a less pronounced increase prior to reaching steady state (see figure 8.16). This behaviour coincides well with the hypothesis that upon the reconstruction of the metallic surface at FT conditions, the number of active sites for secondary olefin reactions decreases.

The third and last stage in the olefin formation trend coincides with the steady state activity (see figure 8.1) where no further changes in selectivity are expected nor observed. The steady state is reached independently of crystallite size after the same time on stream which is in line with studies on iron [14] but contrary to studies on ruthenium nano-crystallites in the FTS published by Welker [7] which indicate that larger crystallites reach steady state sooner than small ones.

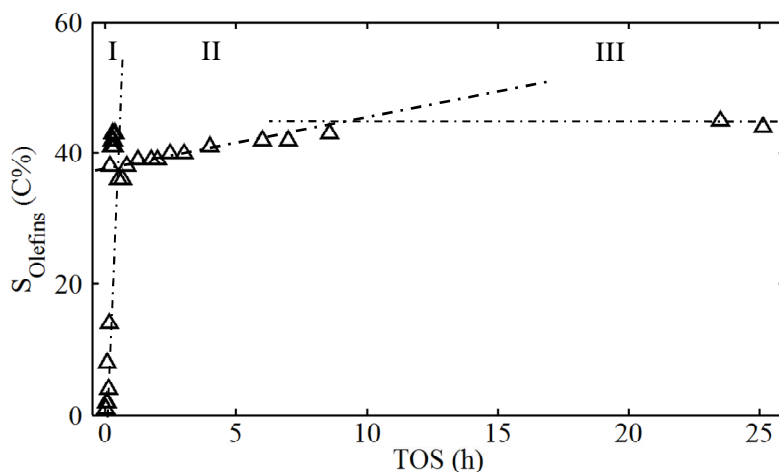


Figure 8.15: Selectivity (in C%) towards olefins in the C_1 - C_8 fraction as a function of time on stream for CAT 9.3 with different phases of the experiment indicated. (I) initial: high hydrogen concentration of the catalyst surface resulting in high methane selectivities and strong olefin hydrogenation; (II) surface reconstruction with increasing suppression of secondary olefin reactions resulting in an increase in olefin selectivity; (III) steady state. (Reaction conditions: $T = 190^\circ\text{C}$, $PP_{\text{syn.gas}} = 9.9$ bar, $SV = 7.2$ $\text{ml}_{\text{syn.gas}}/\text{g}_{\text{catalyst}} \cdot \text{min}$ (STP)).

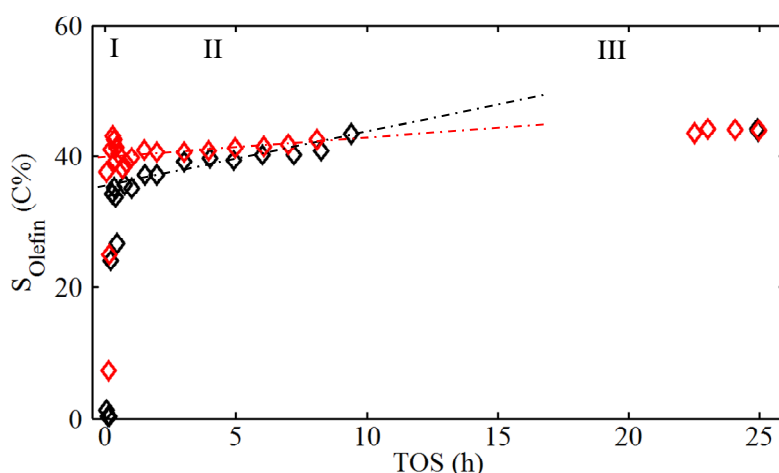


Figure 8.16: Selectivity (in C%) towards olefins in the C_1 - C_8 fraction as a function of time on stream for CAT 7.3 without CO pre-exposure (\diamond) and with CO pre-exposure (\diamond) at different phases of the experiment. (I) initial: high hydrogen concentration of the catalyst surface resulting in high methane selectivities and strong olefin hydrogenation; (II) surface reconstruction with increasing suppression of secondary olefin reactions resulting in an increase in olefin selectivity; (III) steady state. (Reaction conditions: $T = 190^\circ\text{C}$, $PP_{\text{syn.gas}} = 9.9$ bar, $SV = 7.2$ $\text{ml}_{\text{syn.gas}}/\text{g}_{\text{catalyst}} \cdot \text{min}$ (STP)).

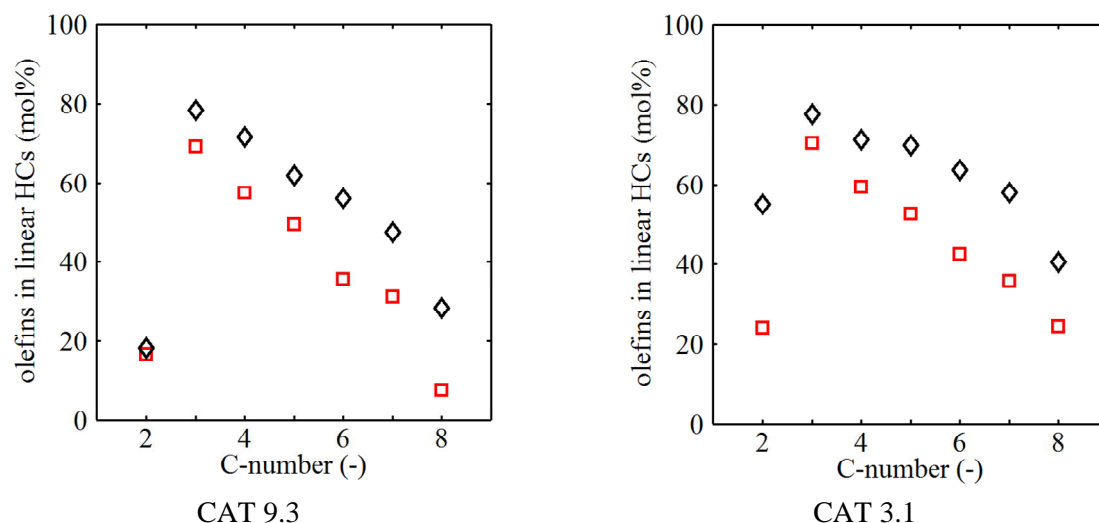


Figure 8.17: Carbon number dependent olefin fraction in the linear hydrocarbons for CAT 9.3 and CAT 3.1 at maximum TOF (□) and after 25 hours under Fischer-Tropsch conditions (◇). (Reaction conditions: $T = 190^{\circ}\text{C}$, $PP_{\text{syn.gas}} = 9.9$ bar, $SV = 7.2$ $\text{ml}_{\text{syn.gas}}/\text{g}_{\text{catalyst}} \cdot \text{min}$ (STP)).

In the absence of all secondary reactions the olefin content is expected to be carbon number independent at values of 70-90 mol% [49, 53]. In figure 8.17 the molar olefin concentrations in the corresponding linear hydrocarbon fractions are shown in dependency of the carbon number for catalysts CAT 9.3 and CAT 3.1 at the time of the maximum TOF and 25 hours at Fischer-Tropsch conditions. As discussed above the olefin selectivity increases with time on stream, be it due to initial higher hydrogen to carbon ratios on the catalyst surface or due to the partial disappearance of sites active for secondary reactions of α -olefins during the surface reconstruction [50]. It is however evident that even after the surface reconstruction secondary olefin reactions do take place as only the C_3 olefin fraction is in the concentration level expected for primary selectivity. The C_2 fraction is mostly paraffinic, while the concentration of higher olefins decreases with increasing carbon number. The low ethene concentration is attributed to its very high reactivity, while the olefin concentration decrease with increasing carbon number was proposed to be a result of carbon number dependent diffusion rates [54], solubility [53] and/or physisorption [55] leading to higher residence times of the longer chained olefins in the catalyst pores, therefore increasing the probability to undergo secondary reactions.

The molar ratios of olefins to paraffins of the C_2 , C_3 and C_5 fractions were chosen to compare the crystallite size effect on the olefin selectivity at maximum activity and after 25 hours of Fischer-Tropsch testing (see figure 8.18). The carbon number dependent olefin concentration at maximum TOF and at steady state is expected and discussed above. The increased olefin selectivity with time on stream due to initial high hydrogen concentration on the catalyst surface or through the disappearance of active sites for the secondary olefin hydrogenation during surface reconstruction processes [50] is also discussed in detail above. With changing crystallite size no change in olefin content could be measured in the different carbon number fractions. Biloen and co-workers [56] studied the reaction of propane dehydrogenation to propene on platinum and platinum-gold alloys. They concluded that the dehydrogenation of propane is catalysed by a single metal atom and does not require an ensemble.

From this study it can be proposed that the reverse reaction, i.e. the hydrogenation of α -olefins to *n*-paraffins, can also be catalysed on a single metal atom. Dorling and co-workers [57] studied the hydrogenation of ethylene on Pt/SiO₂ catalysts and could not find any signs of structure sensitivity. Therefore the secondary formation of paraffins from the primarily formed α -olefins can be regarded as structure insensitive, i.e. no crystallite size effects are expected. Previous studies on the crystallite size effects in the FT synthesis with cobalt [9] and ruthenium [7] reported a decrease of olefin selectivity with decreasing crystallite size. This trend was explained by the proposed preferred re-adsorption of olefins on metal atoms with a low coordination number [6] which are expected to be present in a higher density on smaller crystallites. It was further hypothesised that, through electronic effects, the dissociation of hydrogen on smaller crystallites is favoured over the dissociation of carbon monoxide. Besides the resulting higher hydrogen concentration it was also proposed that adsorbed CO does inhibit secondary olefin reactions [42]. It may be speculated that crystallite size effects on Fischer-Tropsch activity and selectivity are also dependent on the reaction conditions. Indeed Welker's study [7] using ruthenium catalysts showed more pronounced crystallite size dependency of the olefin selectivity at more severe testing conditions. The very mild conditions used in this study may therefore explain that no crystallite size dependency was observed with regard to molar olefin contents. Studies on iron are not conclusive with regard to crystallite size effects on the olefin selectivity as potassium promoted iron nano-crystallites have been reported to show no crystallite size effect [12, 16] while unpromoted iron crystallites showed a minimum olefin selectivity in the size range of 7-9 nm [14].

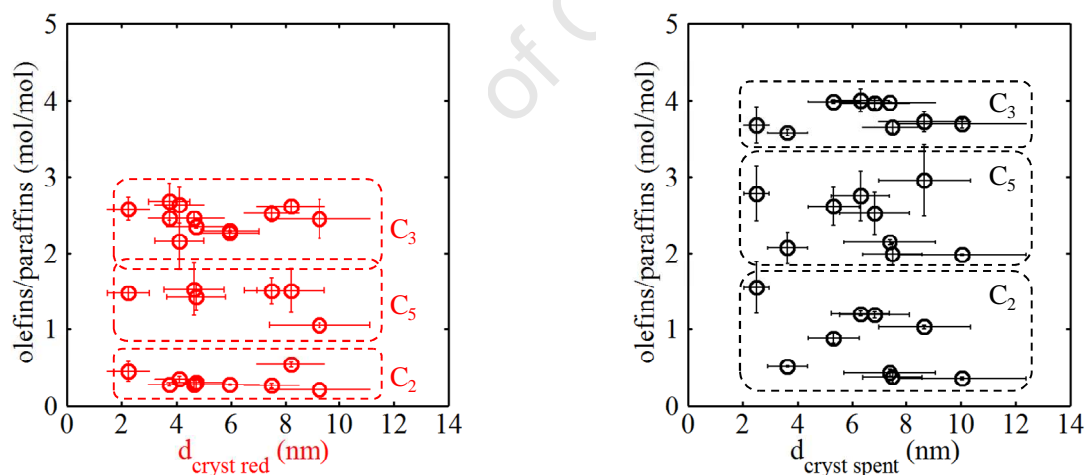


Figure 8.18: Molar ratio of olefins to paraffins for carbon numbers of 2, 3 and 5 as function of crystallite size at maximum TOF (○) and after 25 hours under Fischer-Tropsch conditions (○). (Reaction conditions: T = 190°C, PP_{syn.gas} = 9.9 bar, SV = 7.2 ml_{syn.gas}/g_{catalyst}·min (STP)).

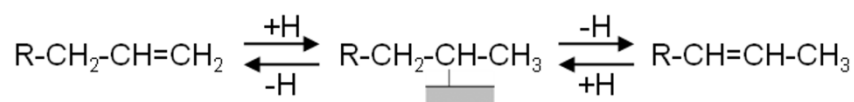


Figure 8.19: Schematic representation of the re-adsorption of an α -olefin and subsequent double bond isomerisation.

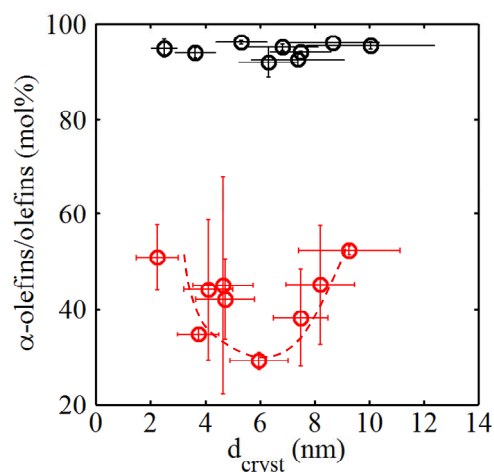


Figure 8.20: Molar content of primarily formed α -olefins in the fraction of C_5 olefins as function of crystallite size at maximum TOF (○) and after 25 hours under Fischer-Tropsch conditions (○). (Reaction conditions: $T = 190^\circ\text{C}$, $PP_{\text{syn.gas}} = 9.9$ bar, $SV = 7.2$ $\text{ml}_{\text{syn.gas}}/\text{g}_{\text{catalyst}} \cdot \text{min}$ (STP)).

In addition to hydrogenation to paraffins and incorporation into growing chains, re-adsorbed α -olefins can undergo a third type of secondary reaction: the double bond isomerisation (see figure 8.19). This reaction requires the α -olefin to re-adsorb non-terminally and it is known to occur on metal sites in the presence of hydrogen as well as on acid sites present on certain support systems [58]. As discussed earlier, 70-90 mol% of the primary FT product is expected to consist of α -olefins [49, 53]. Only a very small/negligible amount of olefins with internal double bond is believed to be formed as a primary product [49]. The molar content of α -olefins in the total fraction of C_5 olefins as a function of the different crystallite sizes of the studied model catalyst can therefore give evidence of the extend of secondary reactions for the tested catalysts. These molar α -olefin contents are depicted in figure 8.20 for the initial stages of the FTS, i.e. at maximum TOF, and at 25 hours of FT testing, i.e. at steady state. Schulz [50] proposed that during the initial surface reconstruction or formation of the FT regime on the catalytic surface, the sites active for undesired secondary reactions would decrease or even disappear. As discussed above the olefin hydrogenation indeed is suppressed at steady state conditions compared to early stages of the experiment (it should be noted that secondary olefin consumption via hydrogenation and incorporation can also occur on FT growth sites (see figure 8.14)). Interestingly the net olefin product at steady state is to 90-97 mol% primary, i.e. it consists mainly of α -olefins, while at initial stages of the FT experiment only 30-50 mol% α -olefins are present in the corresponding olefin fraction. In the de facto absence of double bond isomerisation at steady state no crystallite size dependency is expected or detected. At initial stages however a minimum α -olefin content or a maximum extent of isomerisation can be seen at medium crystallite sizes of approximately 6 nm (see figure 8.20). Similar maxima were observed by Cheang [14] for iron nano-crystallites for the hydrogenation activity and also for the double bond isomerisation. In Cheang's study these maxima were found at initial stages of the FTS as well as at steady state. Cheang [14] offers two possible explanations for this behaviour. One is an extension of the previously discussed ensemble theory (see chapter 8.1). It is based on the reported preferred re-adsorption of olefins on metal atoms with a low coordination number [6], i.e. corner or edge atoms, which are more prevalent on smaller crystallites (see figure 2.9 A). Assuming the double bond isomerisation requires a further active centre next to the site of olefin adsorption, these active sites could be an adjacent

planes, which in turn are more dominant on larger crystallites (see figure 2.9 A). These two opposing effects would result in an ‘ideal’ crystallite size for double bond isomerisation in a medium crystallite size range.

The second proposed mechanism to explain the minimum α -olefin selectivity is based on theoretical calculations and an analogy of the interaction of carbon monoxide with nano-sized gold crystallites [59]. An adsorbed olefin on a metal surface interacts in a classical HOMO-LUMO (highest occupied molecular orbital of the olefin – lowest unoccupied molecular orbital of the metal) interaction. The strength of the formed bond is inversely proportional to the energy difference between the HOMO and the LUMO of the metal surface, i.e. the Fermi level. Calculations of this difference for 1-pentene over iron nano-sized crystallites (1-20 nm) show a distinct minimum at an iron crystallite size of 3 nm indicating a maximum in the strength of the olefin-metal interaction. Such an increase in the strength of interaction would result in enhanced secondary reactions like the double bond isomerisation [14].

8.1.4 Formation of branched hydrocarbons

Branched hydrocarbons (mainly mono-methyl branched) are a minor product of the Fischer-Tropsch synthesis. None of the four major proposed reaction mechanisms (alkyl, alkenyl, enol and CO-insertion mechanism) does directly account for their formation (see chapter 2.1.2). Schulz and co-workers [60, 61] proposed a formation mechanism based on the previously discussed re-adsorption of a primarily formed α -olefin in the non-terminal position followed by further chain growth resulting in a mono-methyl branched hydrocarbon (see figure 8.21). This reaction pathway was evidenced by means of co-feeding of labelled olefins during the FT synthesis [62]. A primary reaction pathway for the formation of branched compounds was proposed by Lee and Anderson [63]. It is based on the reaction of a surface alkyldiene species with a surface methyl species (see figure 8.21).

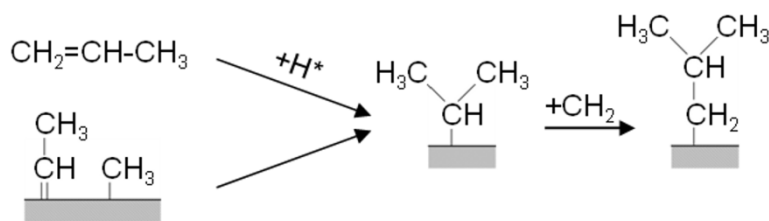


Figure 8.21: Schematic representation of proposed formation routes of branched hydrocarbons (adapted from [40]).

Again the representative C_5 fraction was chosen in this study to illustrate the crystallite size dependency, in this chapter with regards to the formation of branched hydrocarbons (see figure 8.22). It can be observed that no change in the selectivity to the branched hydrocarbons is detected from the stage of maximum TOF to the steady state at 25 hour under Fischer-Tropsch conditions. A clear increase (up to 3 fold) in the content of branched compounds can be measured with decreasing crystallite size. Above reported results on secondary reactions of olefins have clearly shown no influence of crystallite size, at least at steady state (see chapter 8.1.2). Schulz [50] proposed that sites active for undesired olefin re-adsorption do decrease during the initial stages of the FTS due to the surface reconstruction of the catalytic metal [2, 18]. As the selectivity towards branched compounds

does not change with time on stream and since it does change significantly with crystallite size, while all other secondary olefin reaction based selectivities are unaffected, it can be assumed that the here observed crystallite size effect is based on a primary branching reaction as, for example, proposed by Lee and Anderson [63]. Branched surface alkyl species are regarded to be more spatially demanding than straight chained alkyl species [36]. It can therefore be hypothesised that the primary formation of branched hydrocarbons is enhanced on smaller crystallites as these crystallites are expected to have a lower density of alkyl species on their surface and therefore the branching reaction is less inhibited.

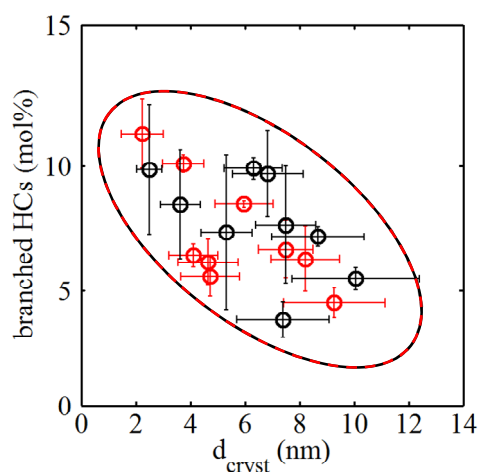


Figure 8.22: Molar content of branched hydrocarbons (HCs) in the C₅ fraction in mol% at maximum TOF (○) and after 25 hours under Fischer-Tropsch conditions (○). (Reaction conditions: T = 190°C, PP_{syn.gas} = 9.9 bar, SV = 7.2 ml_{syn.gas}/g_{catalyst}·min (STP))

Previous studies on the crystallite size effect on the Fischer-Tropsch synthesis for ruthenium [7] and iron [12] confirm the increased branching probability, though to a lesser extent, with decreasing crystallite size. In those two studies it was not possible to distinguish between primary and secondary branching reactions and the authors mainly argue with the increased probability of α -olefins to adsorb on smaller crystallites due to the higher concentration of low coordinated, i.e. edge and corner, surface atoms [6].

8.1.5 Formation of oxygenates

Oxygenates, mainly primary alcohols and aldehydes, comprise a minor but high value product group of the Fischer-Tropsch synthesis. Several formation routes have been proposed. Johnston and Joyner [64] proposed the incorporation of a surface hydroxyl species into an alkyl species to form primary alcohols (see figure 2.1). The enol mechanism proposed by Storch and co-workers [65] does account for the formation of aldehydes, alcohols, carboxylic acids as well as esters (see figure 2.4). The most accepted route for the formation of oxygenates is however the CO-insertion mechanism (see figure 2.5) proposed by Pichler and Schulz [66]. Similarly to the primarily formed α -olefins and n-paraffins the aldehydes are proposed to be the main primary product which can readily be converted to alcohols on the catalytic surface in a secondary reaction (see figure 2.7) [67, 68].

Previous studies on crystallite size effects on the FTS product spectrum on rhodium [15], cobalt [9] and iron [13] have shown an increase in the selectivity towards oxygenates with decreasing crystallite size. This was generally attributed to the proposed enhanced adsorption of CO on metal

sites with a low coordination number as present at a higher density on surfaces of smaller crystallites [6, 50]. This increase in CO adsorption could further enhance the proposed CO-insertion mechanism [66] on smaller metal crystallites. In particular metals such as rhodium and cobalt are known to promote such reactions, and homogeneous complexes of these metals are effective catalysts for the related olefin hydroformylation [69]. In studies on nano-sized ruthenium crystallites [7] a decrease in alcohol and aldehyde selectivity was reported with decreasing crystallite size. Aware of the contradictory results compared to previous studies, it was proposed that the secondary reactions of alcohols and aldehydes, i.e. hydrogenation and/or incorporation into chain growth, were enhanced on the smaller crystallites resulting in an overall decrease in the alcohol and aldehyde selectivity. Due to the very low conversions in this study no oxygenate formation/selectivity trends could be determined.

8.1.6 Conclusions and summary of the FT performance of the supported nano-sized cobalt crystallites

The here discussed results from the performance tests of the supported nano-sized cobalt crystallites show clear influences of the cobalt crystallite size on the Fischer-Tropsch activity. Trends in selectivity reveal differences in structure sensitivity of the different reactions occurring in the overall FT product formation mechanism. All effects were compared at initial stages of the FT synthesis, i.e. after 30-50 minutes on stream, and at steady state conditions after 25 hours.

The surface specific activity or turn over frequency (TOF) decreases linearly with a decreasing cobalt crystallite size at initial and at steady state conditions, this decrease is less pronounced at steady state where the activity is also lower. In contrast to previous studies on cobalt [9, 11] and iron [12] no constant turn over frequency above a certain crystallite size could be observed in the studied size range of this work. It is proposed that this levelling off results from the geometry of the cobalt metal surface after reconstruction showing the formation of islands in the size range of 7-15 nm [2]. Van Santen hypothesises that crystallite size effects in the FT synthesis can only be observed below this size range as the surface reconstruction of larger crystallites results in a surface resembling crystallites of the size range of 7-15 nm [17]. Studies conducted in the group of de Jong [9] further indicate that the crystallite size above which no further change in TOF is measurable is dependent on the reaction conditions. The inferior activity of small crystallites is explained with the structure sensitivity of the FT synthesis. Only certain metal atom ensembles or regimes are proposed to be able to show FT activity and chain growth [7, 9, 10, 12, 14, 15, 17, 26-28]. Expressing the activity per gram of reduced cobalt results in a maximum activity for a cobalt crystallite size of 4.7 nm at initial stages and 6.3 nm at steady state. It is proposed that on these crystallite sizes the ideal geometry for a maximum number of FT active ensembles on the cobalt surface is achieved. All studied model catalysts display a crystallite size independent deactivation before reaching steady state activity after approximately 10 hours on stream. This deactivation was attributed to the surface reconstruction upon exposure of the freshly reduced cobalt metal to FT conditions [2, 6, 18] as effects of sintering or re-oxidation of the metallic cobalt phase could be ruled out. This reconstruction could be mimicked by pre-exposing a reduced model catalyst to carbon monoxide, therefore highlighting the role of CO or carbon, respectively, in this surface transformation.

Steady-State Isotopic Transient Kinetic Analysis (SSITKA) studies by de Breejen and co-workers [10] show an increased residence time of CH_x and H species on nano-sized cobalt crystallites with

decreasing size. Along with these trends the CO residence time decreased with decreasing crystallite size. It is proposed that these changes in residence time result in a decrease in chain growth probability in the FT synthesis and an increase in methane selectivity. Van Santen postulated that the decrease of CO residence time with decreasing cobalt crystallite size is a result of an increased energy barrier for the CO dissociation on smaller crystallites [17]. Similar to previous studies on crystallite size effects in the FT synthesis on cobalt [9, 11], ruthenium [7], rhodium [15] and iron [12, 14], the methane selectivity in this study increased with decreasing crystallite size while the selectivity towards hydrocarbons with a carbon number of 5 and higher decreased, both trends were independent of time on stream. As there was no influence of the crystallite size on the chain growth probability, in line with previous studies on ruthenium [7] and iron [14], the increase in methane selectivity is proposed to be a result of the simpler ensemble requirements for the methanation reaction compared to the FT growth reaction. Smaller crystallites are expected to lack the ability to accommodate the more complex ensembles required for FT chain growth due to geometrical constraints while they are still able to support the formation of methane [41, 42].

With α -olefins being the main primarily formed products in the Fischer-Tropsch synthesis [36, 46-51] the olefin selectivity is governed by secondary reactions of the α -olefins, mainly the hydrogenation to n-paraffins and the double bond shift reaction [49, 52]. The hydrogenation of olefins has been shown to be structure insensitive, i.e. crystallite size independent, on noble metal catalysts [56, 57]. This study comes to an analogous conclusion. While with time on stream the olefin content per carbon number increases, no crystallite size dependency could be measured. The increase in olefin content with time on stream in the Fischer-Tropsch synthesis has previously been observed and can be attributed to a higher concentration of hydrogen on the freshly reduced metal surface and/or to the disappearance of sites active for secondary olefin reactions during the surface reconstruction process [6, 50]. Interestingly, previous studies generally report a decrease in olefin content with decreasing crystallite size [7, 9] or a minimum olefin selectivity at a medium crystallite size [14]. It may be speculated that differences in the observed trends are due to the choice of the reaction conditions, and crystallite size effects regarding olefin hydrogenation are generally less pronounced or even not present at milder conditions [7], as applied in this work. The extent of double bond isomerisation, as followed monitoring the amount of α -olefins in the olefin carbon number fractions, decreases with time on stream supporting the hypothesis that the number of sites for secondary olefin reactions decline upon surface reconstruction. While at initial stages of the FT experiments only 30-50 mol% of the olefin product consisted of primarily formed α -olefins, their concentration increases to over 95 mol% after 25 hours at FT conditions indicating almost complete absence of secondary double bond shift at steady state. At initial stages the tendency for the double bond shift reaction has a maximum at cobalt crystallite sizes around 6 nm. Similar trends have been observed for all secondary olefin reactions on nano-sized iron crystallites [14]. The origin of these trends is assumed to be either due to geometric or electronic effects.

A clear increase in selectivity for the formation of branched hydrocarbons was measured with decreasing crystallite size, independent of time on stream. As no crystallite size effect on the olefin double bond shift reaction was observed (at steady state), it can be assumed that the increase of branching probability is due to a primary reaction and not a secondary reaction pathway including olefins (see figure 8.21). Branched surface alkyl species are believed to have higher spatial requirements than straight chained alkyl species [36]. It can therefore be assumed that on smaller

crystallites the steric hindrance suppressing the primary formation of branched hydrocarbons in the FT synthesis is reduced.

8.2 Supported organometallic complex

The cobalt carbonyl based organometallic complex $(\text{CO})_9\text{Co}_3\text{CCOOH}$ (see figure 7.24) was synthesised and supported on the same alumina carrier material which was used for the nano-sized cobalt crystallites (see chapter 4.3). The supported organometallic complex was then studied under the same Fischer-Tropsch conditions as the other model catalysts in an attempt to obtain activity and selectivity information for sub nanometer cobalt ensembles (see chapter 8.1). No activation/reduction was required prior to the FT experiments. To avoid decomposition of the complex during slow heating up to reach the reaction temperature of 190°C in the experiment with the complex the reactor was placed in a pre-heated oil bath allowing the reaction temperature to be reached as fast as possible. As could be shown previously (see chapter 7.2) the cobalt complex decomposes upon exposure to elevated temperatures, especially in the presence of a hydrogen atmosphere. For this reason FT testing was conducted for 5 hours only.

8.2.1 Fischer-Tropsch activity and characterisation of the spent catalysts

Similar to organometallic ruthenium complexes [7] the Fischer-Tropsch activity or rates of product formation, respectively, of the supported organometallic cobalt complex are very low. Figure 8.23 shows the surface specific activity over time on stream. Here it is assumed that all cobalt atoms are exposed to the surface and therefore available for the reaction. For comparison, the steady state TOF of the model catalyst with the smallest cobalt crystallites (CAT 3.1) was 0.012 s^{-1} (see figure 8.6 B).

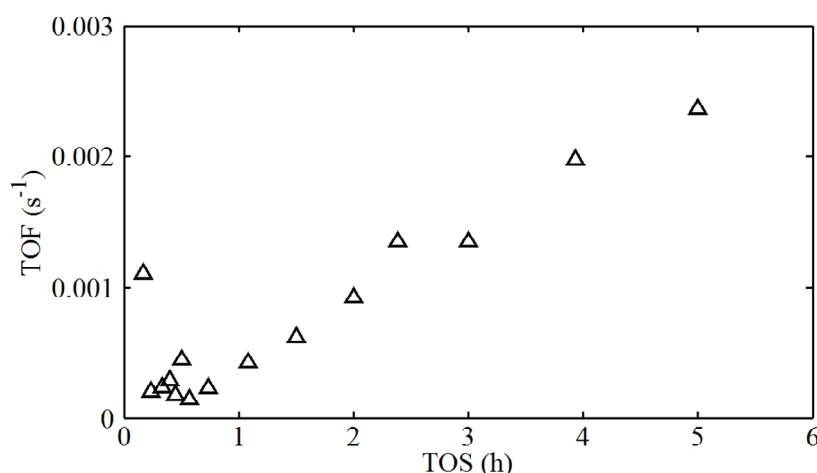


Figure 8.23: Turn over frequency (TOF) as function of time on stream (TOS) for alumina supported $(\text{CO})_9\text{Co}_3\text{CCOOH}$.

After the initial 20 minutes on stream where minimal activity (with formation of short chained products only, $\text{C}_1\text{-C}_5$) was detected, slowly a full FT product spectrum (up to C_7) could be measured in the GC-FID chromatograms using the off-line sampling technique (see chapter 4.7.6). From 20

minutes onwards until the end of the experiment (after 5 hours) the surface specific activity increased linearly. This increase in activity can be attributed to the decomposition of the cobalt complex forming small cobalt clusters and eventually cobalt metal crystallites. This behaviour has previously also been reported for ruthenium complexes, which were tested at somewhat higher temperatures, which was possible as organometallic ruthenium complexes show much higher stability towards decomposition than comparable carbonyl based cobalt complexes [7]. In contrast to the study on ruthenium no volatile cobalt complexes could be detected in the product gas stream using GC coupled with a mass spectrometer.

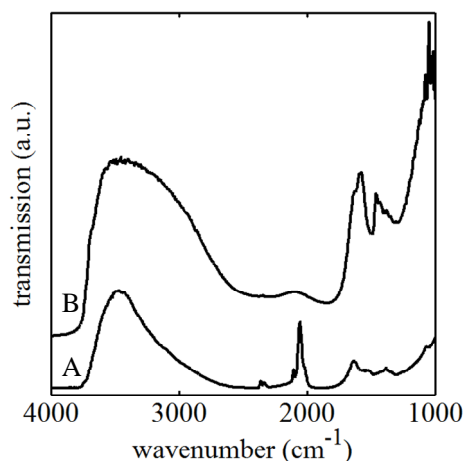


Figure 8.24 Diffuse reflectance FTIR spectra of fresh alumina supported $(\text{CO})_9\text{Co}_3\text{CCOOH}$ (A) and the spent catalyst after 5 hours under Fischer-Tropsch conditions (B).

The spent catalyst was passivated in CO_2 for 1 hour at room temperature. It was then attempted to characterise it by means of HRTEM, PXRD and FTIR. The colour of the catalyst changed from black to pale blue indicating the formation of small amounts of cobalt aluminates. This was expected based on the previous characterisation experiments in the magnetometer (see chapter 7.2.4) and with in-situ PXRD (see chapter 7.2.5). Attempts to identify cobalt crystallites, the assumed decomposition products of $(\text{CO})_9\text{Co}_3\text{CCOOH}$, with conventional PXRD and HRTEM were unsuccessful, probably due to the low loadings and the expected very small size of the cobalt crystallites (< 2 nm). Comparison of diffuse reflectance FTIR scans of the spent and the freshly supported cobalt complex (see figure 8.24) show a complete lack of the cobalt carbonyl vibration frequencies around 2000 cm^{-1} in the spent sample. It can therefore be concluded that the cobalt carbonyl structure (see figure 7.24) of the synthesised organometallic complex decomposes during the exposure to FT conditions and that cobalt gets partially incorporated into the alumina matrix forming cobalt aluminates, possibly CoAl_2O_4 (see chapter 7.2.5), which is strongly supported by the observed colour change of the sample. The extent of this aluminate formation and the nature of the residual cobalt can not be conclusively shown. From the activity trend shown in figure 8.23, keeping in mind that cobalt aluminates are not expected to show FT activity [18], it is hypothesised that the decomposition of $(\text{CO})_9\text{Co}_3\text{CCOOH}$ on the alumina support results in a small amount of cobalt which incorporates into the alumina matrix while the main decomposition product are sub two nanometer sized cobalt ensembles or crystallites which undergo continuous crystallite growth. As already stated above, in order to calculate the TOF it is assumed, due to a lack of suitable analysis methods, that all cobalt

atoms loaded onto the support in form of $(\text{CO})_9\text{Co}_3\text{CCOOH}$ are exposed and available for the FT reaction.

8.2.2 Methane formation and chain growth

As previously discussed for the supported cobalt nano-crystallites the methane and C_{5+} selectivities are expressed as percent carbon in the product spectrum, using the extrapolated ASF distribution up to a carbon number of 50 (see chapter 8.1.2).

A first FT specific product spectrum, including hydrocarbons with a carbon number higher than four, could be measured after 20 minutes. After approximately one hour a full product spectrum, up to a carbon number of seven, could be detected. Due to the very low conversion level no direct quantification for higher hydrocarbons (carbon number higher than 7) was possible. From four minutes up to one hour on stream the product spectrum is governed by methane and other short chain hydrocarbons (i.e. carbon number < 5). In the initial minutes methane is the only detectable hydrocarbon. Possibly these short chain hydrocarbons are a result of the hydrogenation of carbonyl groups of the original cobalt complex itself upon its decomposition. After 1 hour the selectivities towards methane as well as higher hydrocarbons reach a steady state like behaviour and do not change much until the termination of the experiment (see figure 8.25). During this stage the chain growth probability remains stable at values of 65-70 %. It can be noted that this probability is only slightly lower than those measured for the supported cobalt crystallites (see table 8.3).

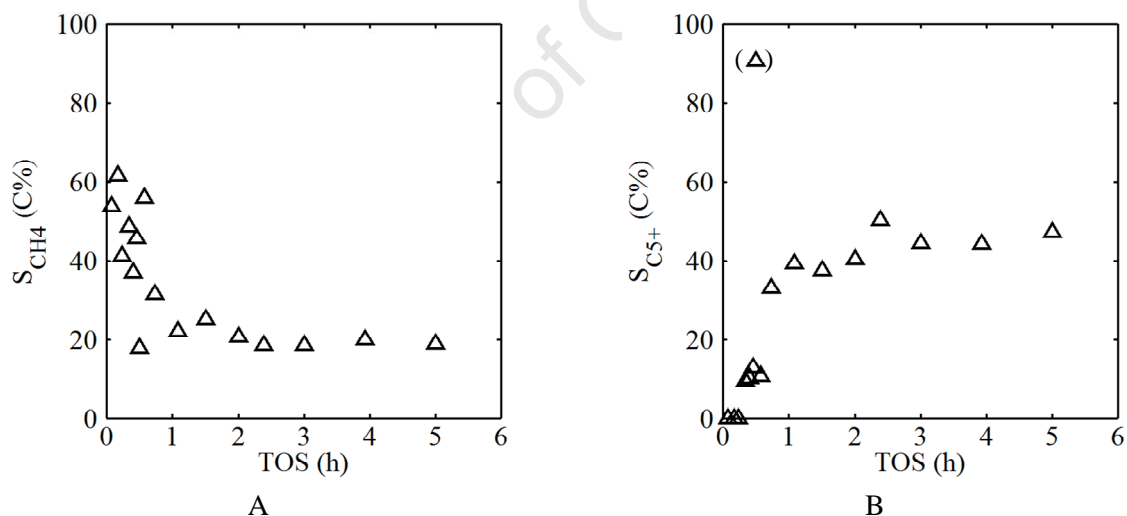


Figure 8.25: Methane (A) and C_{5+} (B) selectivity in carbon % as function of time on stream.

8.2.3 Olefin formation

As previously discussed olefins, more specifically α -olefins, are the dominant primary product in the Fischer-Tropsch synthesis [36, 46-51]. These primary olefins can however re-adsorb on the catalyst surface and undergo secondary reactions mainly to form paraffins via hydrogenation and olefins with internal double bonds via isomerisation reactions [49, 52] (for more details see chapter 8.1.2). In the absence of these secondary reactions the FT product spectrum would consist of 70-90 mol % olefins, independent of carbon number.

Figure 8.26 A shows the total olefin selectivity over time on stream in carbon percent. The olefin selectivity increases mainly due to the sharply decreasing methane selectivity, and then also reaches steady state like behaviour at approximately 50 C% olefin selectivity after one hour on stream. Note that the selectivities towards olefins are calculated from the experimental product spectrum obtained from GC-FID traces, i.e. up to a carbon number of seven, and these are not based on the extrapolated spectrum utilised to calculate the methane and C₅₊ selectivities in chapter 8.2.2. The carbon number dependent molar fraction of olefins in the hydrocarbon product shows a very primary distribution. The small deviations from carbon number independent primary product spectra originate from the carbon number dependent tendency for secondary hydrogenation to paraffins. While ethene is the most reactive olefin, the decrease of olefin content with increasing carbon number has been postulated to be due to carbon number dependent diffusion rates [54], solubility [70] and/or physisorption [55] resulting in a longer contact time of higher carbon number olefins with the catalytic surface therefore enhancing secondary reactions like the hydrogenation. Similar to the carbon number specific olefin content, the molar fraction of α -olefins in the total olefins remains constant from 1 hour on (at approximately 70 mol% for the C₅ fraction) indicating a limited extent of internal double bond shift reactivity. This value compares well to the initial stages of the FT experiments with the supported cobalt crystallites. At steady state these model catalysts displayed a higher molar fraction of α -olefins in the total olefins of approximately 95-97 mol%.

Due to the low product formation rates in the experiment with the cobalt complex double bond shift and chain branching could not be characterized.

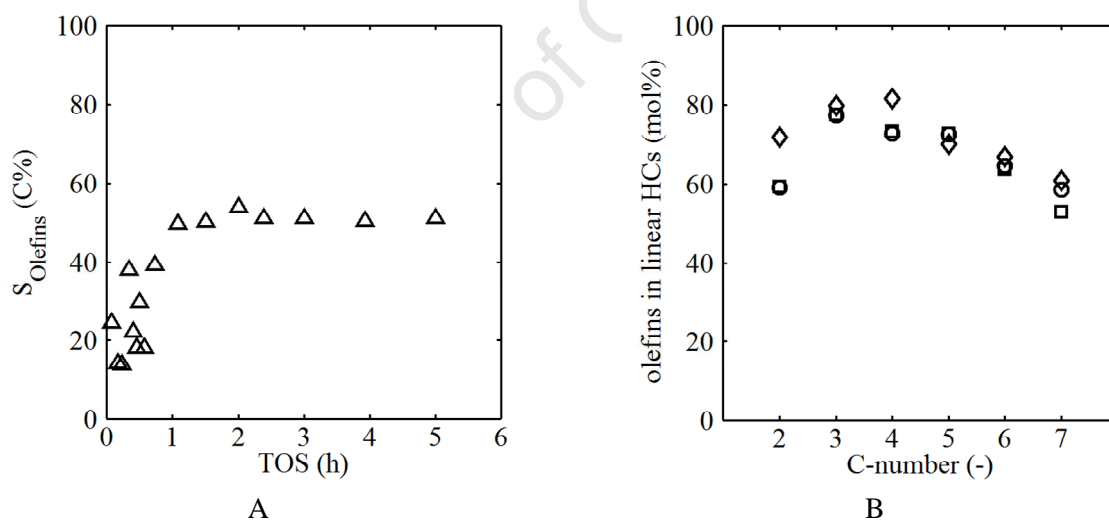


Figure 8.26: (A): Olefin selectivity in C% over time on stream; (B) Carbon number dependent olefin fraction in the linear hydrocarbons mol% at 1 h (\diamond), 3 h (\square) and 5h (\circ) on stream.

8.2.4 Activation of gaseous ¹³C

In previous studies on the Fischer-Tropsch tests with metal carbonyl based organometallic complexes [7] it was not conclusively determined if gas phase carbon monoxide was indeed incorporated into the Fischer-Tropsch product or whether the carbonyl ligands of the clusters provided the carbon source for the organic products that were formed. In order to gain insight into this aspect for the (CO)₉Co₃CCOOH on alumina system studied in this work, a three hour Fischer-Tropsch experiment

was conducted, exchanging the carbon monoxide with ^{13}CO . Due to its limited availability the experiments had to be carried out at atmospheric pressure. All other reaction parameters were kept the same as above. The product gas stream was not only sampled using the ampoule technique but also constantly analysed with an online mass spectrometer.

The co-fed cyclo-hexane, normally used as an internal standard for the quantitative analysis of the GC-FID traces (see chapter 4.9), and the mass over charge ratios (m/z) of all its fragments make it difficult to identify FT products at the very low conversions (see figure 8.27 A) with the mass spectrometer. However, methane with an incorporated ^{13}C atom has the distinct mass over charge ratio of 17. By studying this mass in the traces obtained from mass spectroscopy (see figure 8.28) we can show that ^{13}CO from the gas phase is clearly incorporated into the product. Strictly speaking it would be expected that the initial methane formation on the intact organometallic complex should not have ^{13}C incorporated but consists fully of carbon from the carbonyl bonds of the complex. Probably the complex does start losing carbonyl bonds, i.e. it decomposes, immediately upon its deposition onto the support or upon exposure to FT conditions so that the initial lag time expected for the formation of $^{13}\text{CH}_4$ is so short that it could not be detected. Temperature programmed CO desorption with the supported cobalt crystallites have shown that the support alone is not active towards the formation of methane (see chapter 7.1.5). It can therefore be assumed that the here measured C_1 fraction is indeed a product formed on the cobalt complex or its decomposition products. The initially high intensity of $m/z = 17$ correlates well with the methane selectivities obtained from GC-FID analysis of the product gas (see figure 8.27 B). Only trace amounts of CO_2 (mass over charge ratio of 44 (CO_2)) is by a factor of 10 lower than mass over charge ratio of 17 ($^{13}\text{CH}_4$) could be detected throughout the experiment.

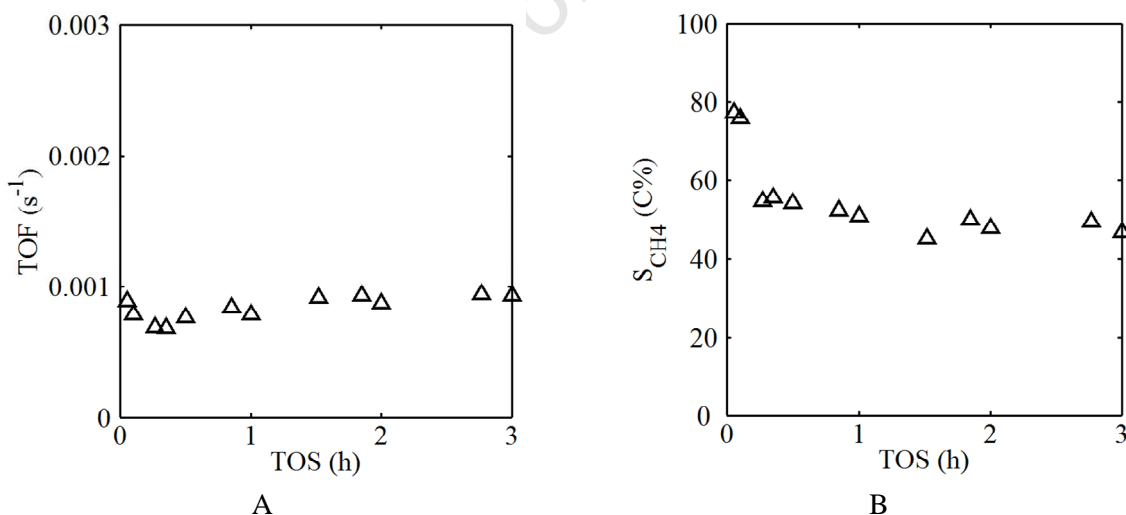


Figure 8.27: (A) Turn over frequency (TOF) as a function of time on stream; (B) Methane selectivity in C% as function of time on stream.

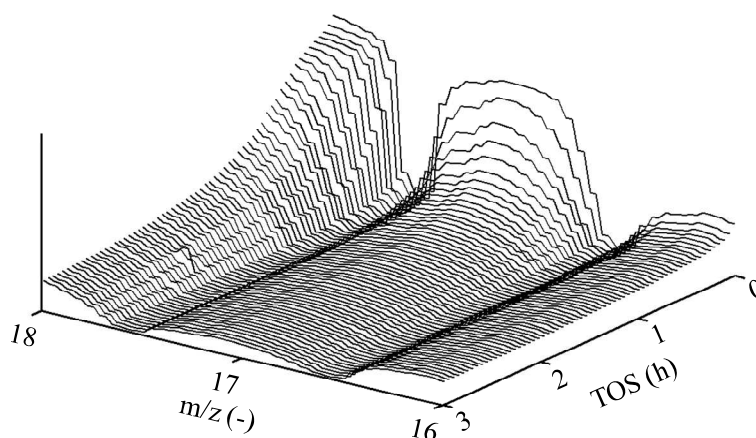


Figure 8.28: Mass over charge (m/z) ratio of 17 as a function of time on stream.

8.2.5 Conclusions and summary of the FT performance of the supported organometallic complex

After 4 minutes under Fischer-Tropsch conditions the first non C_1 hydrocarbons could be measured in the product gas stream indicating the possibility of C-C bond formation on the organometallic complex. Studies with ^{13}C O showed that from the start of the experiment gaseous carbon monoxide can be activated on the catalyst surface and be incorporated into the chain growth mechanism. Due to the rapid decomposition of the cobalt carbonyl complex it was not possible to exactly distinguish between activity originating from the original organometallic compound and its decomposition products. The linear increase in surface specific activity leads to the assumption that a large fraction of the cobalt bound in the complex undergoes ensemble/crystallite formation and growth during decomposition of the complex upon exposure to FT conditions. These ensembles/crystallites display full activity for the FTS with a decreased reactivity towards secondary olefin reactions compared to previous results obtained with supported cobalt crystallites (see chapter 8.1.3).

8.3 Consolidation of FT results of supported $(CO)_9Co_3CCOOH$ and supported cobalt crystallites

To compare the activity and selectivity results obtained from the FT experiments with the supported cobalt crystallites and the supported $(CO)_9Co_3CCOOH$, it first needs to be decided which stage of the experiment with cobalt crystallites the cobalt complex work can be compared to. Two distinct stages have been identified (see chapter 8.1.1): the maximum TOF after 20-30 minutes on stream and steady state behaviour after 25 hours under Fischer-Tropsch conditions. The first stage is assumed to represent the performance of the freshly reduced cobalt crystallites. In the latter stage the activity results from a reconstructed cobalt surface. Experiments in this study as well as theoretical calculations [5] indicate that carbon monoxide or the carbon species originating from the dissociation of carbon monoxide induce this surface reconstruction. As the organometallic cobalt complex synthesised in this study is based on a cobalt carbonyl and therefore saturated with CO ligands, the

activity and selectivity results of this compound needs to be compared to the steady state activity of the supported cobalt crystallites.

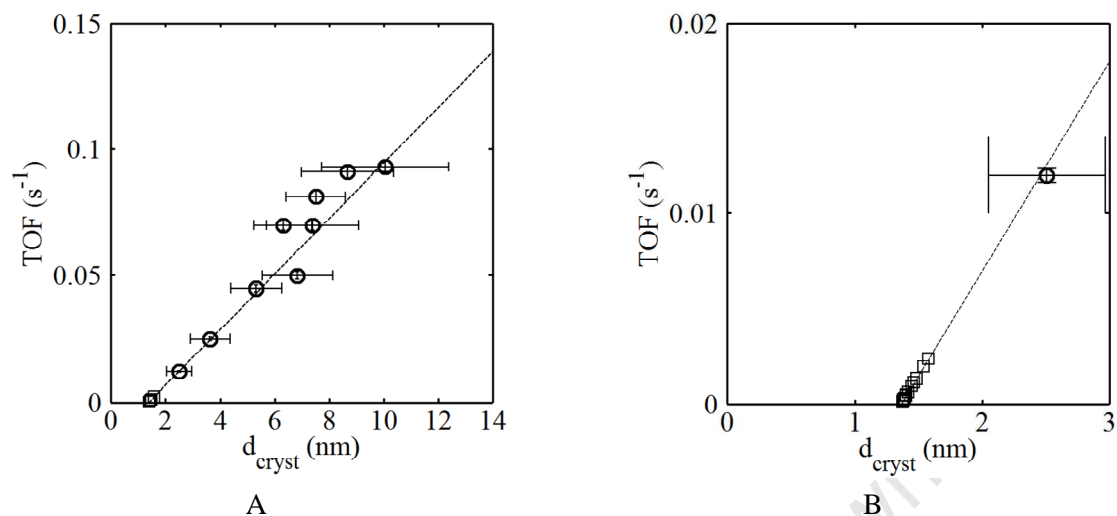


Figure 8.29: Steady state turn over frequency of supported crystallites (\circ) with extended trend and populated with turn over frequencies of supported organometallic cobalt complex (\square). (A) full view, (B) detailed view.

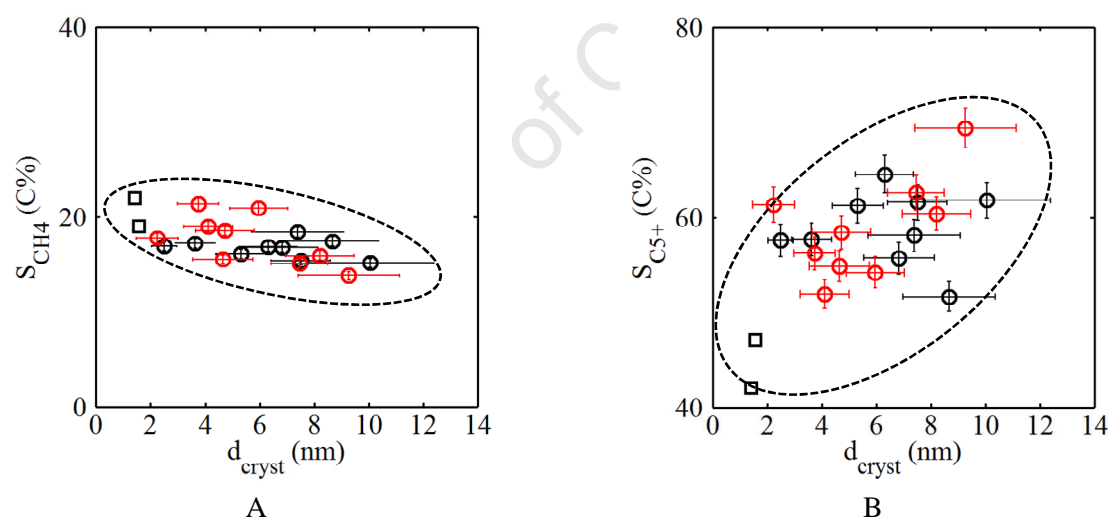


Figure 8.30: Selectivities of methane (A) and C_{5+} (B) for supported cobalt crystallites at maximum TOF (\circ) and after 25 hours under FT conditions (\circ) as well as for supported organometallic cobalt complex (\square). For clarity only the values of the organometallic complex experiment at 1 hour and at 5 hours TOS are shown.

It is assumed that the decomposition of the cobalt complex results in the formation of cobalt ensembles/crystallites which undergo further growth under FT conditions. The sizes of these ensembles/crystallites could not be determined with the available characterisation techniques. At steady state the surface specific activity (TOF) decreases approximately linearly with decreasing crystallite size. Assuming this trend does hold for crystallite/ensemble sizes smaller than the ones synthesised with the reverse micelle method, as shown for ruthenium [7], it is possible to linearly extrapolate the TOF for smaller crystallites. Populating this extrapolation with the turn over

frequencies obtained from the FT experiments with the supported organometallic complex results in crystallite sizes which can be assigned to the decomposition products at a certain time on stream (see figure 8.29). The so approximated crystallite sizes of the cobalt complex decomposition products for the different times on stream obtained are all between 1.4 and 1.6 nm. It should be borne in mind that for the calculation of the turn over frequencies of the complex derived catalyst it was assumed that all cobalt atoms are on the surface, i.e. available for the FT reaction. This assumption may however not hold true anymore for the crystallite sizes that may have formed, and above approximation may therefore be an underestimate. Nonetheless applying these estimated crystallite sizes on the methane and C₅₊ selectivity (see figure 8.30) and comparing them to the results obtained from the FT experiments with the supported cobalt crystallites shows a good agreement in the observed trends. With decreasing crystallite size the methane selectivity increases while the C₅₊ selectivity decreases.

University of Cape Town

References

- [1] R. van Hardeveld and F. Hartog, *Surface Science*, 15 (1969) 189.
- [2] J. Wilson and C. de Groot, *Journal of Physical Chemistry*, 99 (1995) 7860.
- [3] C. Klink, I. Stensgaard, F. Besenbacher and E. Laegsgaard, *Surface Science*, 360 (1996) 171.
- [4] J.E. Kirsch and S. Harris, *Surface Science*, 522 (2003) 125.
- [5] I.M. Ciobîca, R.A. van Santen, P.J. van Berge and J. van de Loosdrecht, *Surface Science*, 602 (2008) 17.
- [6] H. Schulz, Z. Nie and F. Ousmanov, *Catalysis Today*, 71 (2002) 351.
- [7] C.A. Welker, Ruthenium based Fischer-Tropsch synthesis on crystallites and clusters of different sizes, Department of Chemical Engineering, PhD, University of Cape Town, Cape Town, 2007.
- [8] N.V.Y. Scarlett and I.C. Madsen, *Powder Diffraction.*, 21 (2006) 278.
- [9] G.L. Bezemer, J.H. Bitter, P.C.E. Kuipers Herman, H. Oosterbeek, J.E. Holewijn, X. Xu, F. Kapteijn, A.J. van Dillen and K.P. de Jong, *Journal of the American Chemical Society*, 128 (2006) 3956.
- [10] J.P. den Breejen, P.B. Radstake, G.L. Bezemer, J.H. Bitter, V. Froseth, A. Holmen and K.P. de Jong, *Journal of the American Chemical Society*, 131 (2009) 7197.
- [11] G. Prieto, A. Martínez, P. Concepción and R. Moreno-Tost, *Journal of Catalysis*, 266 (2009) 129.
- [12] E.I. Mabaso, Nanosized iron crystallites for Fischer-Tropsch synthesis, Department of Chemical Engineering, PhD, University of Cape Town, Cape Town, 2005.
- [13] E.I. Mabaso, E. van Steen and M. Claeys, *DGMK/SCI-Conference "Synthesis Gas Chemistry"*, 4 (2006) 93.
- [14] V. Cheang, Effect of crystallite size and water partial pressure on the activity and selectivity of low temperature iron-based Fischer-Tropsch catalysts, Department of Chemical Engineering, PhD, University of Cape Town, Cape Town, 2009.
- [15] M. Ojeda, S. Rojas, M. Boutonnet, F.J. Pérez-Alonso, F. Javier García-García and J.L.G. Fierro, *Applied Catalysis A: General*, 274 (2004) 33.
- [16] D. Barkhuizen, I. Mabaso, E. Viljoen, C. Welker, M. Claeys, E. van Steen and J.C.Q. Fletcher, *Pure Applied Chemistry*, 78 (2006) 1759.
- [17] R.A. van Santen, Structure sensitivity of methane and CO activation, Lecture held at 9th Novel Gas Conversion Symposium (NGCS), Lyon, France, 2010.
- [18] A.M. Saib, D.J. Moodley, I.M. Ciobîca, M.M. Hauman, B.H. Sigwebela, C.J. Weststrate, J.W. Niemantsverdriet and J. van de Loosdrecht, *Catalysis Today*, 154 (2010) 271.
- [19] E. van Steen, M. Claeys, M.E. Dry, J. Van de Loosdrecht, E.L. Viljoen and J.L. Visagie, *Journal of Physical Chemistry B*, 109 (2005) 3575.
- [20] J.A. Moulijn, A.E. van Diepen and F. Kapteijn, *Applied Catalysis A: General*, 212 (2001) 3.
- [21] E. Iglesia, *Applied Catalysis A: General*, 161 (1997) 59.
- [22] J.C.W. Swart, A theoretical view on deactivation of cobalt-based Fischer-Tropsch catalysts, Department of Chemical Engineering, PhD, University of Cape Town, Cape Town, 2008.
- [23] J. van de Loosdrecht, B. Balzhinimaev, J.A. Dalmon, J.W. Niemantsverdriet, S.V. Tsybulya, A.M. Saib, P.J. van Berge and J.L. Visagie, *Catalysis Today*, 123 (2007) 293.

- [24] I.M. Ciobîca, F. Frechard, R.A. van Santen, A.W. Kleyne and J. Hafner, *The Journal of Physical Chemistry B*, 104 (2000) 3364.
- [25] I.M. Ciobîca and R.A. van Santen, *The Journal of Physical Chemistry B*, 107 (2003) 3808.
- [26] R.A. van Santen, *Accounts of Chemical Research*, 42 (2008) 57.
- [27] M. Claeys, M. Hearshaw, J.R. Moss and E. Van Steen, *Studies in Surface Science and Catalysis*, 130B (2000) 1157.
- [28] M. Claeys, M. Hearshaw-Timme, J.R. Moss and E. van Steen, *DGMK/SCI-Conference "Synthesis Gas Chemistry"*, 3 (2000) 95.
- [29] J.J. Mortensen, L.B. Hansen, B. Hammer and J.K. Nørskov, *Journal of Catalysis*, 182 (1999) 479.
- [30] V. Pallassana, M. Neurock, L.B. Hansen, B. Hammer and J.K. Nørskov, *Physical Reviews B: Condensed Matter and Material Physics*, 60 (1999) 6146.
- [31] S. Dahl, A. Logadottir, R.C. Egeberg, J.H. Larsen, I. Chorkendorff, E. Tornqvist and J.K. Nørskov, *Physical Review Letters*, 83 (1999) 1814.
- [32] R.B. Anderson, *The Fischer-Tropsch synthesis*, Academic Press, New York, 1984.
- [33] E. van Steen and H. Schulz, *Applied Catalysis A: General*, 186 (1999) 309.
- [34] P. Biloen and W.M.H. Sachtler, *Advances in Catalysis*, 30 (1981) 165.
- [35] H. Schulz, M. Claeys and S. Harms, *Studies in Surface Science and Catalysis*, 107 (1997) 193.
- [36] H. Schulz, E. van Steen and M. Claeys, *Studies in Surface Science and Catalysis*, 81 (1994) 455.
- [37] M.E. Dry, *Journal of Chemical Technology and Biotechnology*, 77 (2001) 43.
- [38] M.E. Dry and A.P. Steynberg, *Studies in Surface Science and Catalysis*, 152 (2004) 406.
- [39] J.J.C. Geerlings, J.H. Wilson, G.J. Kramer, H.P.C.E. Kuipers, A. Hoek and H.M. Huisman, *Applied Catalysis A: General*, 186 (1999) 27.
- [40] M. Claeys and E. van Steen, *Surface Science and Catalysis*, Vol. 152, 2004, p. 601.
- [41] F. Zaera, *Journal of Physics: Condensed Matter*, 16 (2004) S2299.
- [42] H. Schulz, E. van Steen and M. Claeys, *Topics in Catalysis*, 2 (1995) 223.
- [43] H. Schulz, *Studies in Surface Science and Catalysis*, 163 (2007) 177.
- [44] Z. Nie, *Anfangsaktivität und -selektivität von modifizierten Kobalt- und Nickelkatalysatoren*, Engler Bunte Institut, PhD, University of Karlsruhe (TH), Karlsruhe, 1996.
- [45] M. Claeys, *Selektivität, Elementarschritte und kinetische Modellierung bei der Fischer-Tropsch-Synthese*, Engler Bunte Institut, PhD, University of Karlsruhe (TH), Karlsruhe, 1997.
- [46] E. Iglesia, S.C. Reyes and R.J. Madon, *Journal of Catalysis*, 129 (1991) 238.
- [47] R.J. Madon, S.C. Reyes and E. Iglesia, *Journal of Physical Chemistry*, 95 (1991) 7795.
- [48] J. Gaube and H.F. Klein, *Journal of Molecular Catalysis A: Chemical*, 283 (2008) 60.
- [49] H. Gökcebay and H. Schulz, 1983, *Catalyst and process for the production of olefins, especially linear α -olefins*, European Patent Application, EP 71770 A2.
- [50] H. Schulz, *Topics in Catalysis*, 26 (2003) 73.
- [51] H. Schulz, S. Roesch and H. Gökcebay, *Internationale Kohlenwissenschaftliche Tagung*, Düsseldorf, Germany, (1981), 522.
- [52] H. Schulz, *C1 Molecule Chemistry*, 1 (1985) 231.

- [53] H. Schulz and M. Claeys, *Applied Catalysis A: General*, 186 (1999) 71.
- [54] E. Iglesia, S.C. Reyes, R.J. Madon and S.L. Soled, *Advances in Catalysis*, 39 (1993) 221.
- [55] E.W. Kuipers, C. Scheper, J.H. Wilson, I.H. Vinkenburg and H. Oosterbeek, *Journal of Catalysis*, 158 (1996) 288.
- [56] P. Biloen, F.M. Dautzenberg and W.M.H. Sachtler, *Journal of Catalysis*, 50 (1977) 77.
- [57] T.A. Dorling, M.J. Eastlake and R.L. Moss, *Journal of Catalysis*, 14 (1969) 23.
- [58] J.E. Germain, *Catalytic Conversion of Hydrocarbons*, Academic Press, 1969.
- [59] N.S. Phala and S.E. van, *Gold Bulletin*, 40 (2007) 150.
- [60] H. Schulz, K. Beck and E. Erich, *Fuels Processing Technology*, 18 (1988) 293.
- [61] H. Schulz, E. Erich, H. Gorre and E. van Steen, *Catalysis Letters*, 7 (1990) 157.
- [62] H. Schulz, B.R. Rao and M. Elstner, *Erdöl Kohle, Erdgas, Petrochemie*, 23 (1970) 651.
- [63] C.B. Lee, and R.B. Anderson, *Proceedings of the 8th International Congress of Catalysis, Bruxelles, Belgium, (1985) II15*.
- [64] P. Johnston, R.W. Joyner, F.S. L. Guzzi and T. P, *Studies in Surface Science and Catalysis*, 75 (1993) 165.
- [65] H.H. Storch, N. Golumbic and R.B. Anderson, *The Fischer-Tropsch and related syntheses*, John Wiley & Sons, 1951.
- [66] H. Pichler and H. Schulz, *Chemie-Ingenieurs-Technik*, 42 (1970) 1162.
- [67] R.A. Dictor and A.T. Bell, *Applied Catalysis*, 20 (1986) 145.
- [68] R.A. Dictor and A.T. Bell, *Journal of Catalysis*, 97 (1986) 121.
- [69] R.C. Ryan and C.U. Pittman Jr., *Journal of the American Chemical Society*, 99 (1977) 1986.
- [70] H. Schulz, *Applied Catalysis A: General*, 186 (1999) 3.

Chapter 9

Conclusions and Summary

The here presented work attempts to create an in depth understanding of the cobalt crystallite size effect on the activity and selectivity of the Fischer-Tropsch synthesis. The study can be divided into two main parts:

- The development of a novel catalyst preparation technique yielding the desired model catalyst systems. This includes the synthesis of nano-sized cobalt crystallites (average sizes 2-10 nm) utilising a modified reverse micelle approach and the synthesis of an organometallic cobalt complex to obtain information on the FT activity and selectivity of sub 2 nm sized cobalt ensembles. Besides the preparation of the model catalyst systems, a major emphasis was put on the full characterisation of the catalysts in the calcined/oxidic state as well as during and after reduction/activation prior to the exposure to Fischer-Tropsch conditions.
- The catalytic performance testing of the prepared model catalysts was conducted under mild Fischer-Tropsch conditions. In addition to the surface specific activity of the model catalysts with differently sized cobalt crystallites/ensembles, the selectivities towards the major FT product classes were also compared. With the ampoule off-line sampling technique [1] a high temporal resolution of product analyses was achieved allowing the comparison of the various model catalysts at different stages of the FT synthesis. A full characterisation of the spent catalyst further allowed a concise interpretation of the obtained activity and selectivity data.

With regards to **catalyst preparation** a novel w/o microemulsion [2-6] based synthesis method was developed. A cobalt hydroxide precursor was precipitated via direct addition of an ammonia solution to a single reverse micelle system containing an aqueous cobalt nitrate solution. The obtained precipitate was washed and dried before calcination in air which yielded nano-sized Co_3O_4 crystallites. These crystallites were re-suspended in water under ultrasonication and mixed with pre-dried alumina support powder. The water is removed from the slurry and the cobalt oxide crystallites are deposited onto the support structure under stirring and reduced pressure. The resulting calcined/oxidic cobalt catalyst precursors display very narrow size distributions. The sizes of the Co_3O_4 crystallites could be tuned by the w/o microemulsion composition, i.e. the water to surfactant ratio and/or the concentration of cobalt nitrate in the aqueous phase. The cobalt oxide phase reduced nearly to a 100% at elevated temperatures under a hydrogen atmosphere while largely maintaining its

average crystallite size and its narrow size distribution. Upon the reduction process no formation of metal support interaction, i.e. the formation of cobalt aluminates, could be detected and the resulting metallic cobalt phase was identified to consist purely of the fcc structure.

To obtain a model catalyst system with crystallites below the 2 nm range, which presents the lower limit achievable with the above discussed reverse micelle technique, the cobalt carbonyl based organometallic complex $(\text{CO})_9\text{Co}_3\text{CCOOH}$ [7] was synthesised and supported onto the alumina carrier for studies under Fischer-Tropsch conditions. The characterisation of this model catalyst showed a rapid decomposition of the cobalt carbonyl structure during exposure to a hydrogen atmosphere. The formation of cobalt aluminates during this decomposition of the complex could be shown, and it is further hypothesised that very small (< 2 nm) metallic cobalt ensembles/crystallites form and undergo further growth upon exposure to FT conditions.

The **Fischer-Tropsch testing** of all prepared model catalysts was conducted at very mild conditions ($T = 190^\circ\text{C}$, $\text{PP}_{\text{syn.gas}} = 9.9$ bar, $\text{SV} = 7.2 \text{ ml}_{\text{syn.gas}}/\text{g}_{\text{catalyst}}\cdot\text{min}$ (STP)) in a laboratory scale fixed bed reactor. The so achieved low conversions guaranteed the absence of elevated water partial pressures therefore minimising possible effects of re-oxidation and sintering of the nano-sized cobalt metal crystallites [8, 9]. Magnetic measurements conducted at these conditions further evidenced the absence of metal re-oxidation to Co(+II) which has been identified as possible reason for the crystallite size dependency in the Fischer-Tropsch synthesis in literature [10].

Two distinct stages during the FT experiments were observed in the tests with the supported nano-sized cobalt crystallites. After 30-50 minutes of time on stream (TOS) a maximum surface specific activity was measured, followed by a decrease before reaching steady state activity after approximately 10 hours. The initial maximum activity was related to the freshly reduced cobalt metal surface and crystallite size while the observed deactivation was identified to be due to carbon monoxide induced surface reconstruction [11-14].

The surface specific activity or turn over frequency (TOF) decreased with decreasing cobalt crystallite size at the initial stages of the experiment as well as at steady state. This decrease in TOF can be explained by the ensemble theory, which assumes that a complex reaction like the FT synthesis can not be catalysed by a single metal atom only but requires a certain number of adjacent metal atoms in a specific geometric orientation to display catalytic activity [15-19]. These adjacent atoms are referred to as a minimum required ensemble. The density of these ensembles on the metallic surface is hypothesised to decrease with decrease in crystallite size, resulting in a decrease of surface specific activity. The selectivity of methane increased with decreasing crystallite size concurrent with a decrease of the selectivity towards long chained hydrocarbons. This effect can also be explained with the ensemble theory. It is proposed that the methanation reaction has lower site requirements in order to show activity compared to the very demanding chain growth reaction [20, 21]. Therefore with the disappearance of FT active sites, or minimum required ensembles respectively, more surface atoms are available for the methane formation. The selectivity towards olefins is not influenced by the crystallite size in this study. α -olefins are the main primary product of the FT synthesis and they can react in secondary reactions [22] to form paraffins (via hydrogenation), longer chained and branched hydrocarbons (via incorporation) and internal olefins (via double bond shift). The dominating reaction is the secondary hydrogenation which has been shown to be structure insensitive [23, 24], as it can be catalysed by a single metal atom. Double bond shift reactions are only observed at the initial stages of

the experiment and not at steady state conversion. Possibly the active sites for this secondary olefin reaction are deactivated during surface reconstruction. Alternatively to an incorporation of α -olefins, branched hydrocarbons have been proposed to also form in a primary reaction mechanism [25]. In this study the selectivity towards branched hydrocarbons increased with decreasing crystallite size. As no effect on the olefin selectivity was observed (at steady state), it is hypothesised that the increased branching probability with decreasing crystallite size results from an enhancement of a primary branching reaction pathway. It is proposed that the steric hindrance [26] expected for the primary formation of branched hydrocarbons is lessened on smaller crystallites due to the decreased density of FT active sites and therefore less surface alkyl species.

Lastly, the test using the cobalt based organometallic complex suggest rapid decomposition of the complex under the formation of very small (below 2 nm) ensembles and crystallites. As to be expected the FT activity of these crystallites is lower than that of the larger crystallites, and, remarkably, the selectivity trends (methane selectivity, and olefin contents) observed with the larger crystallites could be confirmed for these very small crystallites therefore extending the understanding of crystallite size effects in cobalt based FT synthesis.

University of Cape Town

References

- [1] H. Schulz, W. Böhringer, C. Kohl, N. Rahman, A. Will, DGMK Forschungsbericht, 3 (1984) 320.
- [2] M. Boutonnet, S. Lögdberg and E. Elm Svensson, *Current Opinion in Colloid & Interface Science*, 13 (2008) 270.
- [3] S. Eriksson, U. Nylen, S. Rojas and M. Boutonnet, *Applied Catalysis A: General*, 265 (2004) 207.
- [4] M. Boutonnet, J. Kizling, P. Stenius and G. Maire, *Colloids and Surfaces*, 5 (1982) 209.
- [5] V. Uskokovic and M. Drofenik, *Advances in Colloid and Interface Science*, 133 (2007) 23.
- [6] V. Uskokovic and M. Drofenik, *Surface Review and Letters*, 12 (2005) 239.
- [7] X. Lei, M. Shang, T.P. Fehlner, R. Werner, W. Haase, D. Hautot and G.J. Long, *Journal of Organometallic Chemistry*, 541 (1997) 57.
- [8] E. van Steen, M. Claeys, M.E. Dry, J. van de Loosdrecht, E.L. Viljoen and J.L. Visagie, *Journal of Physical Chemistry B*, 109 (2005) 3575.
- [9] J.C.W. Swart, A theoretical view on deactivation of cobalt-based Fischer-Tropsch catalysts, Department of Chemical Engineering, PhD, University of Cape Town, Cape Town, 2008.
- [10] E. Iglesia, *Applied Catalysis A: General*, 161 (1997) 59.
- [11] I.M. Ciobîca, R.A. van Santen, P.J. van Berge and J. van de Loosdrecht, *Surface Science*, 602 (2008) 17.
- [12] I.M. Ciobica and R.A. van Santen, *The Journal of Physical Chemistry B*, 107 (2003) 3808.
- [13] J. Wilson and C. de Groot, *J. Phys. Chem.*, 99 (1995) 7860.
- [14] H. Schulz, Z. Nie and F. Ousmanov, *Catalysis Today*, 71 (2002) 351.
- [15] R.A. van Santen, Structure sensitivity of methane and CO activation, Lecture held at 9th Novel Gas Conversion Symposium (NGCS), Lyon, France, 2010.
- [16] C. Welker, J.R. Moss, E. van Steen and M. Claeys, DGMK/SCI-Conference "Synthesis Gas Chemistry", 4 (2006) 223.
- [17] M. Claeys, M. Hearshaw, J.R. Moss and E. van Steen, *Studies in Surface Science and Catalysis*, 130B (2000) 1157.
- [18] M. Claeys, M. Hearshaw-Timme, J.R. Moss and E. van Steen, DGMK/SCI-Conference "Synthesis Gas Chemistry", 3 (2000) 95.
- [19] V. Cheang, Effect of crystallite size and water partial pressure on the activity and selectivity of low temperature iron-based Fischer-Tropsch catalysts, Department of Chemical Engineering, PhD, University of Cape Town, Cape Town, 2009.
- [20] H. Schulz, E. van Steen and M. Claeys, *Topics in Catalysis*, 2 (1995) 223.
- [21] F. Zaera, *Journal of Physics: Condensed Matter*, 16 (2004) S2299.
- [22] H. Schulz and M. Claeys, *Applied Catalysis A: General*, 186 (1999) 71.
- [23] P. Biloen, F.M. Dautzenberg and W.M.H. Sachtler, *Journal of Catalysis*, 50 (1977) 77.
- [24] T.A. Dorling, M.J. Eastlake and R.L. Moss, *Journal of Catalysis*, 14 (1969) 23.
- [25] C.B. Lee, and R.B. Anderson, *Proceedings of the 8th International Congress of Catalysis, Bruxelles, Belgium, (1985) III15.*
- [26] H. Schulz, E. van Steen and M. Claeys, *Studies in Surface Science and Catalysis*, 81 (1994) 455.

Chapter 10

Recommendations and Future Work

In order to deepen the understanding on the cobalt crystallite size effects on the activity and selectivity in the Fischer-Tropsch syntheses further than already achieved in the here presented study, the following experimental approaches are recommended:

- Using the same type of supported nano-sized cobalt crystallites as model catalysts the effect of reaction water ("higher conversions") on the cobalt crystallite stability should be tested with in-situ techniques including PXRD and magnetic methods allowing the co-feeding of water. Depending on the obtained results, FT experiments can possibly be carried out at higher CO-conversions, i.e. higher water partial pressures, resulting in a broader product spectrum, allowing the better identification of minor product groups such as oxygenates, and clearer trends in selectivity and activity with changes in crystallite size. Moreover the threshold of the stability of these differently sized crystallites with regard to oxidation and sintering could be determined.
- Higher metal loadings could be aimed for in the catalyst preparation step, not only to achieve higher conversions (see above) but also to improve the quality of the catalyst characterisation results. However model catalyst systems with higher metal loadings would again need to be stable during reduction/activation and reaction, and agglomeration or sintering might be more difficult to prevent at higher loadings.
- The effect of the cobalt metal crystallite size on the adsorption/re-adsorption of carbon monoxide and other reaction gases/compounds, i.e. short chain olefins and alcohols, should be further studied by means of temperature programmed experiments or by means of in-situ FTIR studies.
- The nature of the metallic cobalt phase should further be verified. With the characterisation equipment which was available in this study the only crystallite phase identified was the face-centred cubic phase. Synchrotron based in-situ PXRD studies could give further insight on the purity of this phase.

- The influence of the cobalt metal phase (fcc, hcp and ϵ) on the activity and selectivity in the FTS should be investigated with similar model catalysts, i.e. similar cobalt crystallite sizes. The effect of the different phases on characterisation techniques like the magnetic measurements should be included in this study.
- Synchrotron based EXAFS studies on the decomposition of the supported cobalt organometallic complex, synthesised in this study, under Fischer-Tropsch conditions would give a clearer insight in the FT activity and selectivity of sub 2 nanometer cobalt ensembles.
- Decomposition based synthesis methods for nano-sized cobalt and cobalt oxide crystallites should be investigated to prepare model catalysts using alternative routes to the reverse micelle technique. These crystallites could either be supported and tested in a fixed bed reactor or be tested unsupported in a slurry reactor. The use of a slurry reactor might even allow the in-situ preparation of the cobalt crystallites in the same reaction vessel used for the FT synthesis. Using unsupported cobalt crystallites would also eliminate the influence of any kind of carrier material.

Appendix

A1 Composition of reverse micelles for stability measurements

Table A1.1: Composition of w/o microemulsions used to establish the reverse micelle stability region in the ternary phase diagram at 10, 25 and 45°C.

Sample	Mass (g)				ω	Sample	Mass (g)				ω
	PEGDE	Water	Hexane				PEGDE	Water	Hexane		
1	0.74	0.33	33.94		0.45	30	4.92	2.05	28.04		0.42
2	0.70	1.09	33.26		1.56	31	4.91	2.81	27.28		0.57
3	0.72	1.76	32.52		2.44	32	5.29	0.31	29.40		0.06
4	1.23	0.21	33.57		0.17	33	5.26	0.72	29.02		0.14
5	1.24	0.52	33.23		0.42	34	5.27	1.40	28.34		0.27
6	1.23	0.90	32.86		0.73	35	5.26	2.82	26.93		0.54
7	1.24	1.21	32.54		0.98	36	6.32	0.74	27.94		0.12
8	1.75	0.37	32.87		0.21	37	6.27	1.19	27.61		0.19
9	1.76	1.18	32.04		0.67	38	6.31	1.39	27.30		0.22
10	1.77	1.37	31.87		0.77	39	6.30	1.75	26.93		0.28
11	1.78	1.76	31.46		0.99	40	6.64	0.34	28.05		0.05
12	2.46	0.69	31.85		0.28	41	6.65	0.72	27.62		0.11
13	2.46	1.45	31.11		0.59	42	6.66	1.06	27.27		0.16
14	2.45	2.10	30.44		0.86	43	7.36	0.16	27.47		0.02
15	2.43	3.17	29.39		1.30	44	7.34	0.41	27.26		0.06
16	3.50	0.70	30.79		0.20	45	7.37	0.66	26.97		0.09
17	3.53	1.38	30.08		0.39	46	3.50	4.23	27.25		1.21
18	3.50	2.10	29.39		0.60	47	3.50	4.89	26.59		1.40
19	3.49	3.53	27.97		1.01	48	3.83	3.88	27.29		1.01
20	3.86	0.72	30.44		0.19	49	3.86	4.52	26.62		1.17
21	3.85	1.44	29.72		0.37	50	4.56	3.50	26.93		0.77
22	3.85	2.12	29.04		0.55	51	4.56	4.21	26.21		0.92
23	3.87	3.13	28.00		0.81	52	4.92	3.11	26.95		0.63
24	4.56	0.71	29.71		0.16	53	4.89	3.87	26.25		0.79
25	4.57	1.41	29.04		0.31	54	5.27	3.13	26.60		0.59
26	4.58	2.41	28.01		0.53	55	5.23	3.55	26.44		0.68
27	4.56	3.22	27.24		0.71	56	6.30	2.47	26.22		0.39
28	4.89	0.34	29.78		0.07	57	6.30	3.17	25.55		0.50
29	4.93	1.06	29.03		0.22	58	6.67	1.73	26.58		0.26

Appendix

Sample	Mass (g)				Sample	Mass (g)			
	PEGDE	Water	Hexane	ω		PEGDE	Water	Hexane	ω
59	6.65	2.45	25.90	0.37	100	13.31	2.43	19.24	0.18
60	6.65	3.17	25.18	0.48	101	11.91	3.88	19.19	0.33
61	7.35	1.43	26.22	0.19	102	10.52	5.27	19.18	0.50
62	7.34	1.76	25.89	0.24	103	9.09	6.67	19.26	0.73
63	7.38	2.10	25.54	0.28	104	16.79	0.74	17.48	0.04
64	8.04	0.35	26.61	0.04	105	16.12	1.40	17.46	0.09
65	8.04	1.07	25.87	0.13	106	14.73	2.75	17.51	0.19
66	8.06	1.74	25.19	0.22	107	13.28	4.23	17.47	0.32
67	8.74	0.35	25.89	0.04	108	11.93	5.55	17.50	0.47
68	8.75	1.04	25.21	0.12	109	10.52	6.97	17.55	0.66
69	0.75	2.74	31.52	3.65	110	1.41	7.09	26.52	5.03
70	1.24	2.96	30.79	2.39	111	2.79	7.02	25.24	2.52
71	2.46	3.85	28.72	1.57	112	3.48	7.03	24.48	2.02
72	3.85	5.25	25.90	1.36	113	4.21	7.01	23.79	1.67
73	4.90	4.91	25.18	1.00	114	4.88	7.00	23.16	1.43
74	6.34	3.82	24.86	0.60	115	5.59	7.02	22.37	1.26
75	7.34	2.82	24.85	0.38					
76	8.05	2.44	24.51	0.30					
77	8.74	1.74	24.54	0.20					
78	9.78	0.74	24.47	0.08					
79	10.52	0.33	24.14	0.03					
80	0.74	4.51	29.73	6.09					
81	1.24	5.43	28.33	4.38					
82	2.47	7.30	25.21	2.96					
83	3.86	6.28	24.85	1.63					
84	4.90	6.29	23.81	1.28					
85	6.35	5.55	23.09	0.87					
86	7.37	4.87	22.78	0.66					
87	8.06	4.19	22.77	0.52					
88	8.77	3.48	22.77	0.40					
89	9.79	2.44	22.77	0.25					
90	10.49	1.43	23.08	0.14					
91	11.19	0.36	23.44	0.03					
92	13.32	0.69	21.02	0.05					
93	12.58	1.49	20.92	0.12					
94	11.22	2.80	20.96	0.25					
95	9.79	4.22	21.04	0.43					
96	8.39	5.6	21.03	0.67					
97	6.99	7.04	20.97	1.01					
98	15.42	0.34	19.23	0.02					
99	14.72	1.06	19.25	0.07					

A2 Calibration of magnetometer

To calibrate the magnetisation reading obtained from the magnetometer the magnetisation of known amounts of metallic cobalt powder are measured at 20 kOe. Table A2.1 shows the obtained magnetisation results. Figure A2.1 illustrates the linear relationship of the mass of metallic cobalt and the measured magnetisation at an external field of 20 kOe. From the linear regression of the obtained experimental magnetisation the following relationship can be derived:

$$M_{20\text{ kOe}} = 0.0001007 \cdot m_{Co} + 0.0001928 \quad (\text{A2.1})$$

Where $M_{20\text{ kOe}}$ is the sample magnetisation measured at an external field strength of 20 kOe, and m_{Co} is the mass of metallic cobalt in mg.

Table A2.1: Calibration data obtained from magnetic measurements of various metallic cobalt masses.

Mass Co (mg)	Magnetisation at 20 kOe (a.u.)
150.3	0.014935
150.3	0.014916
150.3	0.014905
100.5	0.009967
100.5	0.009961
100.5	0.009970
50.8	0.004905
50.8	0.004903
50.8	0.004895

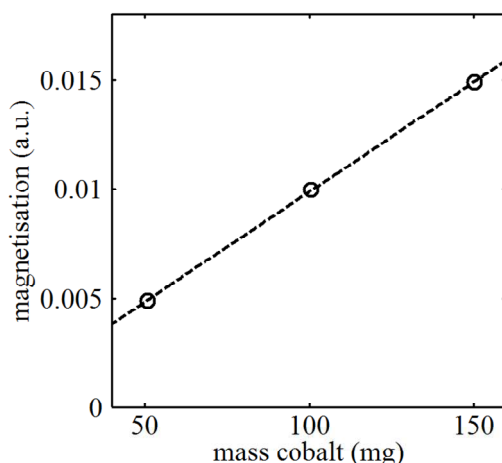


Figure A.2.1: Linear relationship of measured magnetisation at 20 kOe against amount of metallic cobalt.

A3 Conditions for off-line GC-FID analysis

Table A3.1: Off-line GC-FID conditions.

GC-Models	Varian CP 3900 Varian 3800		
Detector	Flame ionisation detector (FID)		
Detector temp.	200°C		
Column	Varian Capillary Column CP-Sil 5CB 25 m; 0.15 mm; 2 µm		
Column pressure	1.72 bar		
Flame gas	H ₂	30 ml/min (STP)	
Makeup gas	N ₂	25 ml/min (STP)	
Air flow	200 ml/min (STP)		
Temp programme	Ramp (°C/min)	Step (°C)	Time (min)
	-	-55	1.5
	20	0	0
	14	100	0
	16	280	2.36
Total time	25 min		
Coolant	CO ₂ (liquid)		

A4 Calculation of Kovats indices

Kovats indices¹ are component specific values which can be calculated for specific GC-column/conditions. Generally the n-paraffins are given the value of their carbon number multiplied by 100, i.e. methane = 100, ethane = 200, etc. From identifying the retention times of the n-paraffins in the GC trace the Kovats indices for all other peaks can be calculated (see equation A4.1) between two identified n-paraffin peaks.

$$KI = 100 \cdot \left[n + (N - n) \frac{\log(RT_{unknown}) - \log(RT_n)}{\log(RT_N) - \log(RT_n)} \right] \quad (\text{A4.1})$$

Where *KI* is the Kovats index, *RT* the retention time of an unknown peak and the smaller (carbon number = *n*) and larger (carbon number = *N*; with *N*=*n*+1) n-paraffin peak, which bracket the unknown peak in the chromatogram.

From a known product spectrum the positions of some compounds are identified (via mass spectroscopy or using standards) and the Kovats indices calculated (see table A4.1). From comparison of these reference indices with the calculated ones from the GC traces the unknown compounds can be identified. Note that this method is not 100% accurate due to changes in the retention times of some compounds and inspection of the obtained results is required.

¹ E.S. Kovats, Fresenius' Zeitschrift für analytische Chemie, 181 (1961) 351.

Table A4.1: Reference Kovats indices utilised in this study for most common FTS products up to a carbon number of 10.

Name	Kovats index	C-number	C=C	C-OH	R-CO-R	R-CO-H
Methane	100.00	1	0	0	0	0
Methanol	386.69	1	0	1	0	0
Ethane	200.00	2	0	0	0	0
Ethene	162.03	2	1	0	0	0
Ethanal	371.22	2	0	0	0	1
Ethanol	454.20	2	0	1	0	0
Propane	300.00	3	0	0	0	0
Propene	294.11	3	1	0	0	0
Propanol (1)	551.91	3	0	1	0	0
Propanone & Propanal	476.64	3	0	0	1	0
n-Butane	400.00	4	0	0	0	0
2-Me-Propane	369.55	4	0	0	0	0
Butene (1) & 2-Me-Propene (1)	392.97	4	1	0	0	0
t-Butene (2)	412.95	4	1	0	0	0
c-Butene (2)	428.47	4	1	0	0	0
Butadiene (1,3)	395.67	4	1	0	0	0
Butanal	578.81	4	0	0	0	1
Butanol (1)	639.16	4	0	1	0	0
Butanone (2)	574.88	4	0	0	1	0
n-Pentane	500.00	5	0	0	0	0
2-Me-Butane	477.42	5	0	0	0	0
Pentene (1)	490.45	5	1	0	0	0
2-Me-Butene (1)	496.37	5	1	0	0	0
3-Me-Butene (1)	460.96	5	1	0	0	0
t-Pentene (2)	509.15	5	1	0	0	0
c-Pentene (2)	517.77	5	1	0	0	0
2-Me-Butene (2)	522.65	5	1	0	0	0
Pentanal	661.51	5	0	0	0	1
Pentanol (1)	750.10	5	0	1	0	0
Pentanone (2)	642.90	5	0	0	1	0
n-Hexane	600.00	6	0	0	0	0
2-Me-Pentane	572.61	6	0	0	0	0
3-Me-Pentane	577.41	6	0	0	0	0
Hexene (1)	590.37	6	1	0	0	0
2-Me-Pentene (1)	585.46	6	1	0	0	0
t-Hexene (2)	603.85	6	1	0	0	0
c-Hexene (2)	611.97	6	1	0	0	0
Hexanal	780.05	6	0	0	0	1
Hexanol (1)	850.80	6	0	1	0	0
Cyclohexane (Ref)	670.14	6	0	0	0	0

Appendix

Name	Kovats index	C-number	C=C	C-OH	R-CO-R	R-CO-H
n-Heptane	700.00	7	0	0	0	0
2-Me-Hexane	656.96	7	0	0	0	0
3-Me-Hexane	669.19	7	0	0	0	0
Heptene (1)	690.00	7	1	0	0	0
2-Me-Hexene (1)	681.66	7	1	0	0	0
3-Me-Hexene (1)	643.89	7	1	0	0	0
t-Heptene (2)	704.36	7	1	0	0	0
c-Heptene (2)	714.06	7	1	0	0	0
z-Heptene (3)	696.54	7	1	0	0	0
Heptanal	883.08	7	0	0	0	1
Heptanol (1)	952.30	7	0	1	0	0
n-Octane	800.00	8	0	0	0	0
2-Me-Heptane	770.33	8	0	0	0	0
3-Me-Heptane	776.18	8	0	0	0	0
4-Me-Heptane	768.37	8	0	0	0	0
Octene (1)	789.31	8	1	0	0	0
2-Me-Heptene (1)	785.82	8	1	0	0	0
t-Octene (2)	802.93	8	1	0	0	0
c-Octene (2)	813.11	8	1	0	0	0
t-Octene (3)	794.68	8	1	0	0	0
t-Octene (4)	796.56	8	1	0	0	0
n-Nonane	900.00	9	0	0	0	0
2-Me-Octane & 4-Me-Octane	867.45	9	0	0	0	0
3-Me-Octane	875.13	9	0	0	0	0
Nonene (1)	889.63	9	1	0	0	0
t-Nonene (2)	901.88	9	1	0	0	0
c-Nonene (2)	913.09	9	1	0	0	0
Nonene (4) & z-Nonene (3) & c-Nonene (3)	894.83	9	1	0	0	0
Nonanal	1084.84	9	0	0	0	1
n-Decane	1000.00	10	0	0	0	0
2-Me-Nonane	967.09	10	0	0	0	0
3-Me-Nonane	974.40	10	0	0	0	0
4-Me-Nonane & 5-Me-Nonane	965.00	10	0	0	0	0
Decene (1)	989.51	10	1	0	0	0
c-Decene (2)	1013.72	10	1	0	0	0
t-Decene (4)	994.26	10	1	0	0	0

A5 Calculation of total and exposed cobalt atoms for specific crystallite sizes

Van Hardeveld and Hartog² published statistical methods of calculating the number of surface and total atoms in various crystal phases for distinct crystallite sizes. The size of these ideal crystallites is determined by the number of edge atoms. In this study we focus on the face-centred cubic cubo-octahedron cobalt crystallite (see model with 4 edge atoms in figure A4.1). For fcc structured phases the total number of atoms for a distinct crystallite size can be calculated as a first estimation by:

$$N_{Total} = \left[\frac{d_{cryst}}{d_{Co} \cdot 1.105} \right]^3 \quad (A5.1)$$

Where N_{Total} is the total number of atoms in a crystallite of a diameter of d_{cryst} and d_{Co} is the atomic radius of cobalt ($125.3 \cdot 10^{-3}$ nm).

This total number of atoms is then fitted to the number of edge atoms (m) dependent expression (see equation A5.2). With the correct number of edge atoms the number of exposed atoms can be calculated with equation A.5.3.

$$N_{Total} = 16 \cdot m^3 - 33 \cdot m^2 + 24 \cdot m - 6 \quad (A5.2)$$

$$N_{exp} = 30 \cdot m^2 - 60 \cdot m + 32 \quad (A5.3)$$

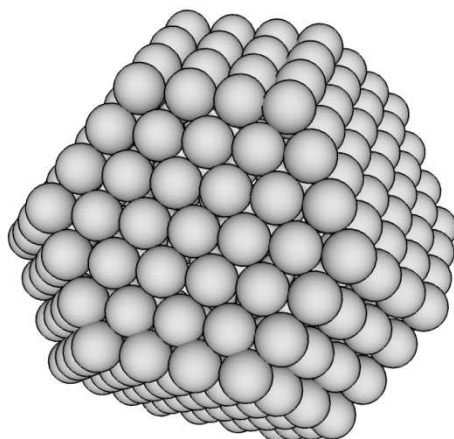


Figure A5.1: Model of a fcc cubo-octahedron with 4 edge atoms.

² R. van Hardeveld and F. Hartog, Surface Science, 15 (1969) 189.

A6 Crystallite size distributions from TEM analysis

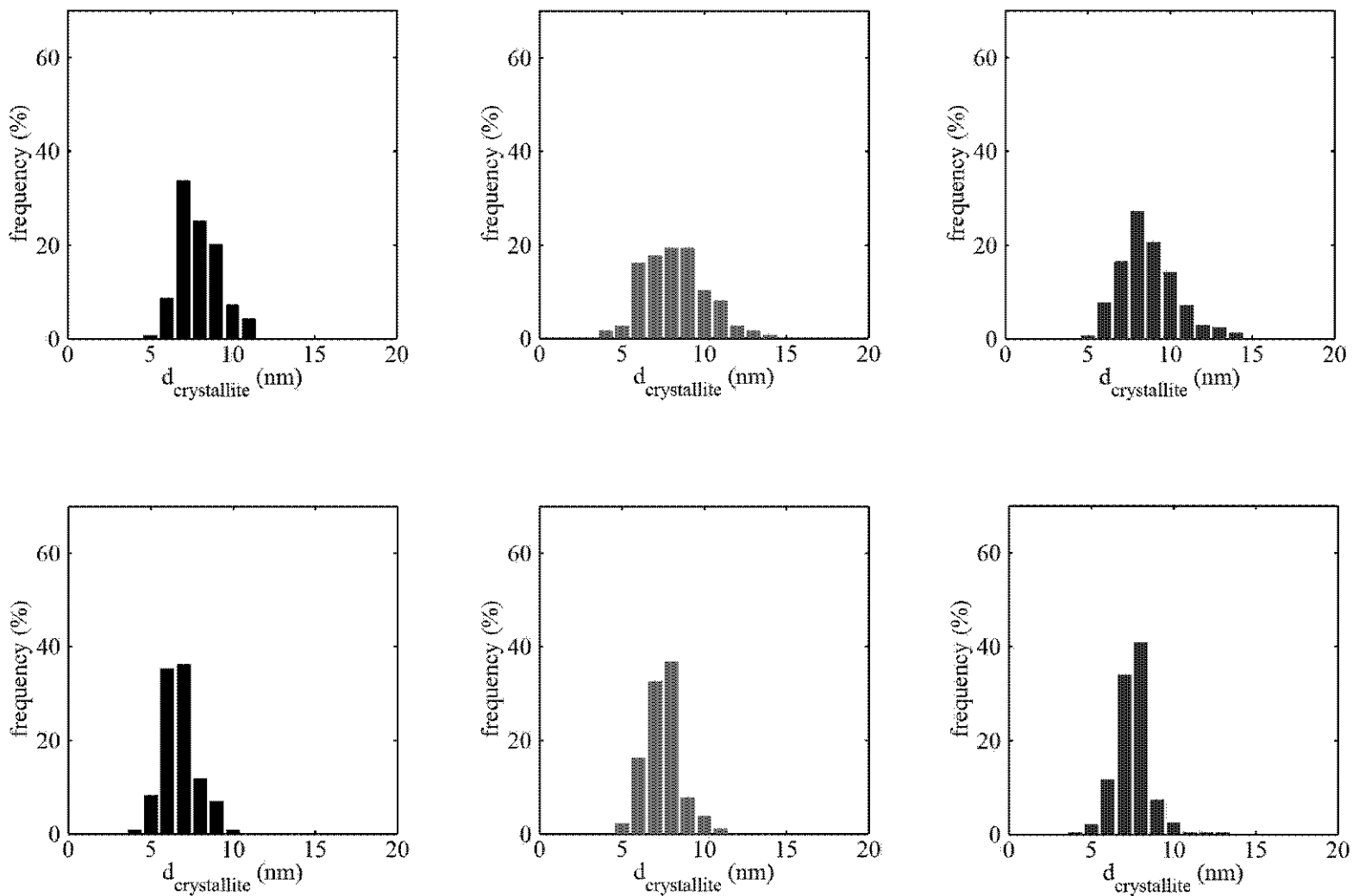


Figure A6.1: Crystallite size distributions (number based) of model catalysts (*top* CAT 8.6, *bottom* CAT 7.3) determined from a minimum of 300 crystallites (■ calcined; ■ reduced and passivated; ■ after 25 hours at FT conditions and passivated).

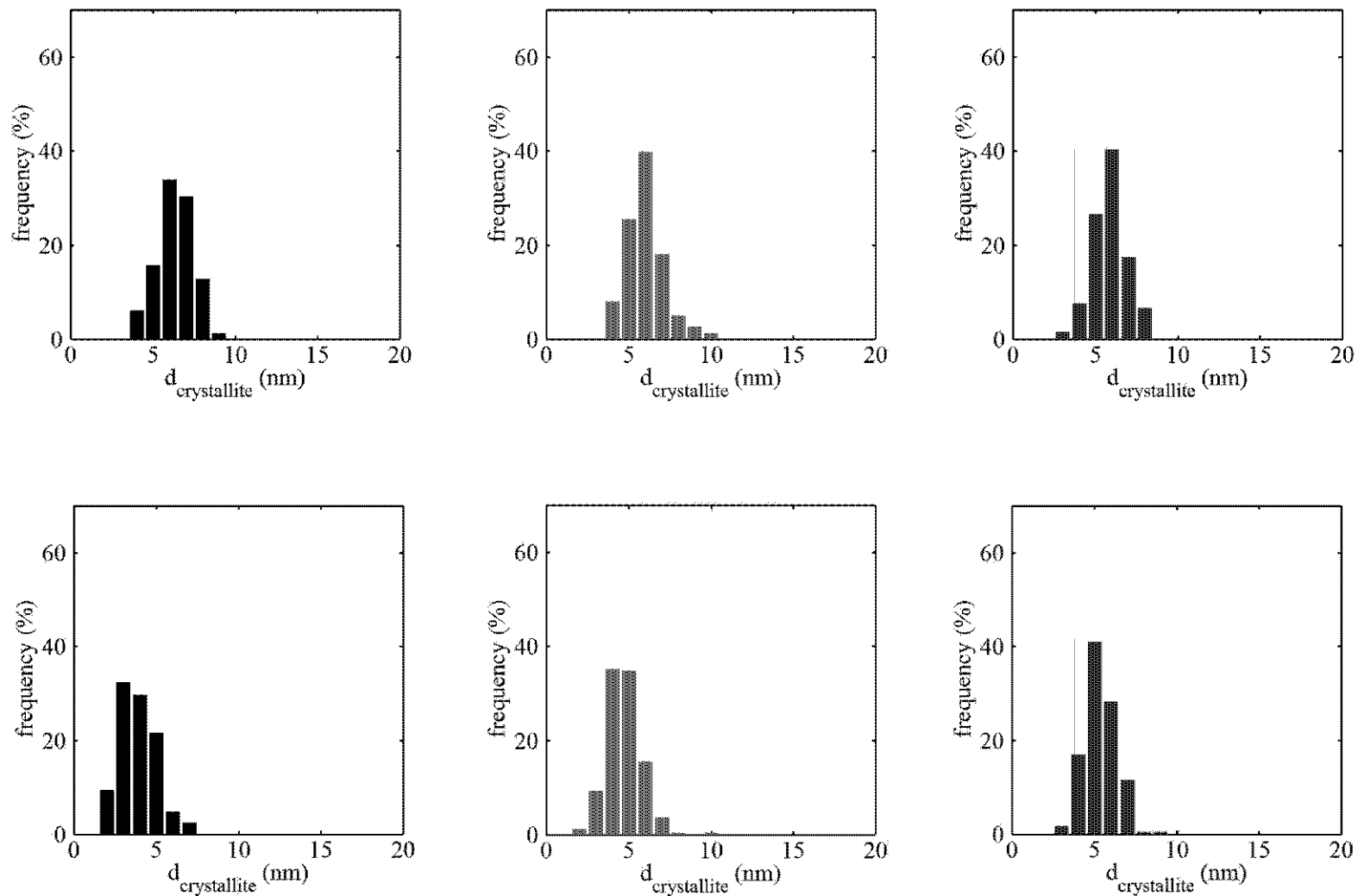


Figure A6.2: Crystallite size distributions (number based) of model catalysts (*top* CAT 6.8, *bottom* CAT 4.8) determined from a minimum of 300 crystallites (■ calcined; ■ reduced and passivated; ■ after 25 hours at FT conditions and passivated).

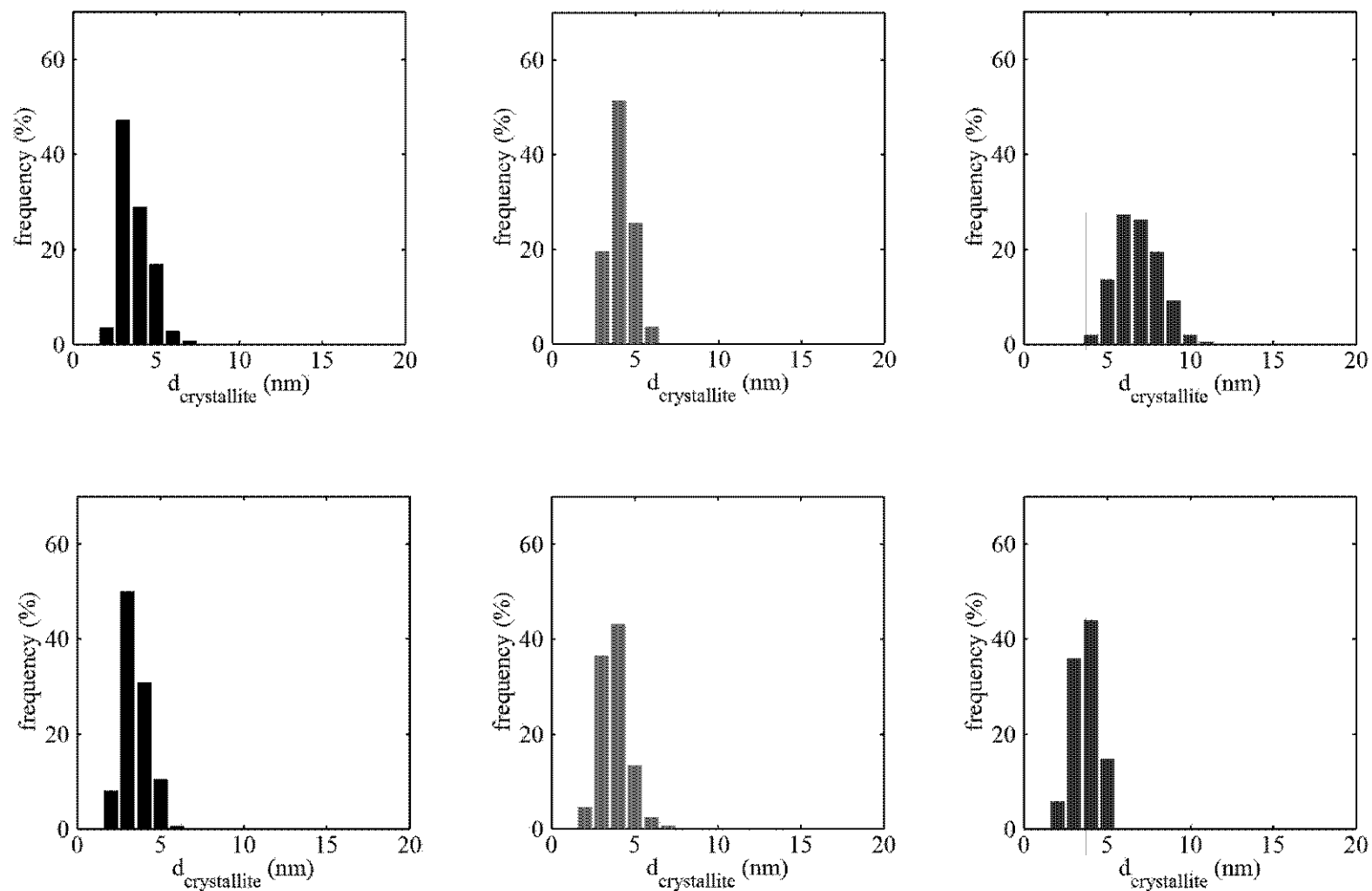


Figure A6.3: Crystallite size distributions (number based) of model catalysts (*top* CAT 4.4, *bottom* CAT 4.0) determined from a minimum of 300 crystallites (■ calcined; ■ reduced and passivated; ■ after 25 hours at FT conditions and passivated).

A7 In-situ PXRD scans

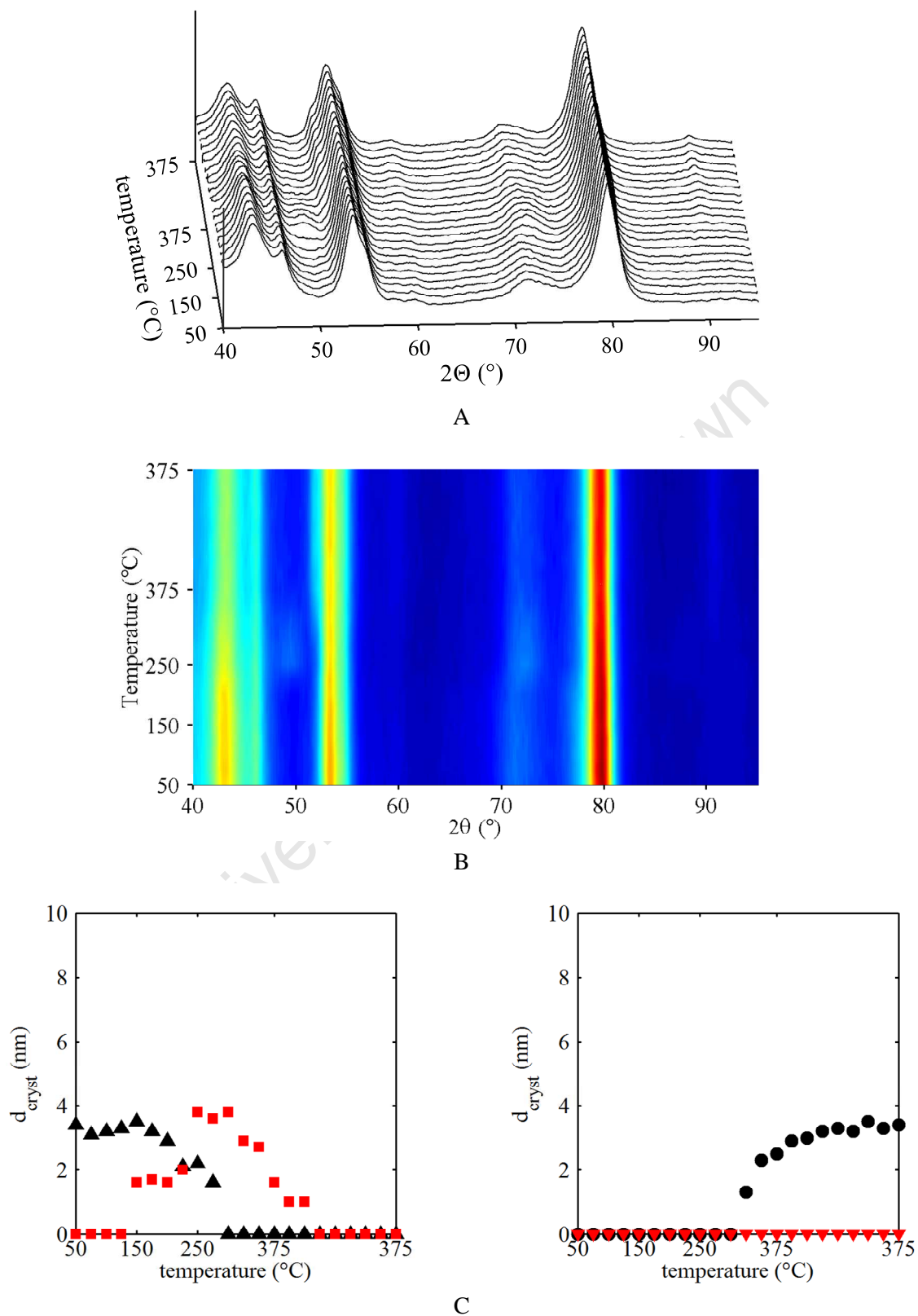


Figure A7.1: In-situ PXRD scans of CAT 3.1. A: diffraction patterns, 3D view; B: diffraction patterns on-top view; C: crystallite sizes of Co_3O_4 (▲), CoO (■), hcp Co (▼) and fcc Co (●) as function of temperature obtained via Rietveld refinement using PONKCS approach.

A8 In-situ magnetic measurements

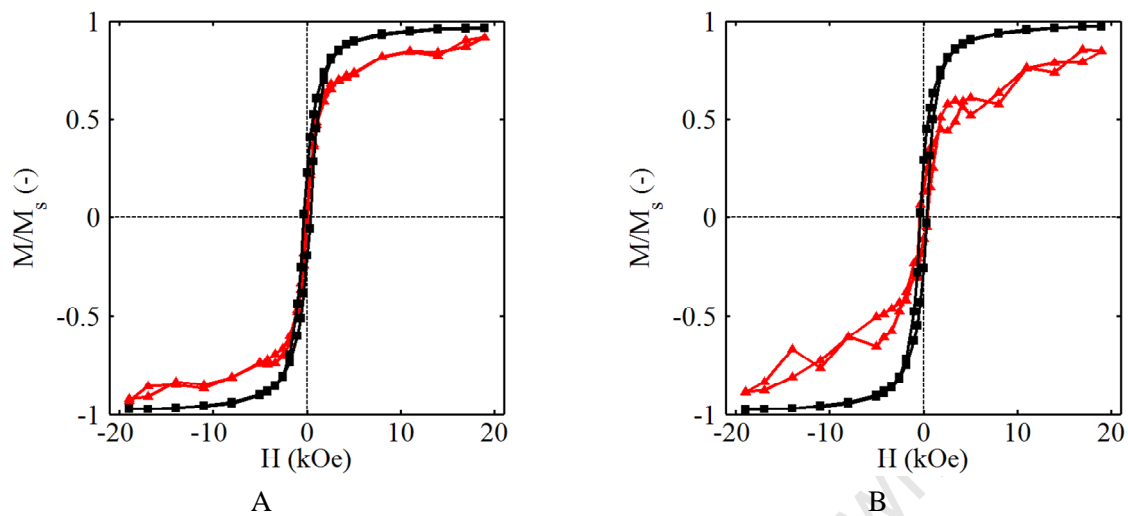


Figure A8.1: Relative magnetisation of CAT 9.6 (-■-) and CAT 4.4 (-▲-) as a function of external field strength (hysteresis). (A) after 25 hours under FT conditions; (B) after 3 hours of additional co-feeding of 6 bar water.

A9 Selected results of the FT testing

Table A9.1: Selected characterisation and FT activity and selectivity results for supported nano-sized cobalt crystallites at initial stages, i.e. at maximum TOF (Reaction conditions: T = 190°C, PP_{syn.gas} = 9.9 bar, SV = 7.2 ml_{syn.gas}/g_{catalyst}·min (STP)).

	CAT 9.6	CAT 8.6	CAT 7.3	CAT 6.8	CAT 5.9	CAT 4.8	CAT 4.4	CAT 4.0	CAT 3.1
d _{num,TEM} (nm)	9.3	8.2	7.5	6.0	4.7	4.7	4.1	3.7	2.2
σ (nm)	1.9	1.3	1.0	1.0	1.0	1.1	0.9	0.8	0.8
N _{surface} ^a	20330	15972	12864	8234	5084	4632	3792	3036	1052
N _{total} ^a	308463	215739	156617	81047	39887	34803	25969	18773	4061
d _{vol,TEM} (nm)	10.3	9.5	7.9	6.6	5.6	5.4	4.5	4.3	2.9
d _{PXRD} (nm)	9.5	7.9	7.7	5.5	5.1	4.8	4.5	4.5	3.4
X _{Co} (%) ^b	10.96	4.08	8.86	6.49	7.23	4.96	3.56	3.46	2.92
TOF (s ⁻¹)	0.203	0.166	0.160	0.138	0.130	0.110	0.088	0.039	0.029
r _{FT} · 10 ⁴ (mol _{CO} Co ⁻¹ s ⁻¹)	2.27	2.09	2.24	2.38	2.81	2.48	2.18	1.07	1.27
α (%)	78	72	76	73	76	77	75	73	79
TOS (m in) ^c	35	40	27	30	29	40	35	30	35
S _{CH4} (C%) ^d	13.8	15.9	10.6	21.0	18.6	15.5	19.0	21.4	17.7
S _{CH4} (mol%) ^d	48.1	48.6	44.4	58.7	56.1	50.0	56.1	50.5	55.3
S _{C5+} (C%) ^d	69.4	60.4	75.8	54.2	58.4	54.8	51.9	56.2	61.3
S _{C5+} (mol%) ^d	29.3	23.1	34.4	18.6	22.0	26.9	21.6	23.0	24.5
C ₂ Olefin/Paraffin (-)	0.21	0.53	0.26	0.27	0.29	0.27	0.34	0.27	0.44
C ₃ Olefin/Paraffin (-)	2.45	2.61	2.52	2.27	2.35	2.46	2.63	2.46	2.58
C ₅ Olefin/Paraffin (-)	1.05	1.51	1.51	2.29	1.42	1.52	2.16	2.68	1.48
C ₅ α-Olefin/total Olefin (-)	0.53	0.45	0.38	0.29	0.42	0.45	0.44	0.34	0.51
C ₅ branched HCs/n-HCs (-)	0.05	0.07	0.07	0.09	0.06	0.07	0.07	0.11	0.13

^a Number of surface and total atoms per crystallite based on d_{num,TEM}.

^b CO conversions based on product spectrum extrapolated to a carbon number of 50.

^c Time on stream at maximum TOF.

^d Selectivities based on product spectrum extrapolated to a carbon number of 50.

Table A9.2: Selected characterisation and FT activity and selectivity results for supported nano-sized cobalt crystallites at steady state, i.e. after 25 hours under Fischer-Tropsch conditions (Reaction conditions: T = 190°C, PP_{syn.gas} = 9.9 bar, SV = 7.2 ml_{syn.gas}/g_{catalyst}·min (STP)).

	CAT 9.6	CAT 8.6	CAT 7.3	CAT 6.8	CAT 5.9	CAT 4.8	CAT 4.4	CAT 4.0	CAT 3.1
d _{num, TEM} (nm)	10.1	8.7	7.5	6.3	7.4	5.3	6.8	3.6	2.5
σ (nm)	2.3	1.7	1.1	1.1	1.7	0.9	1.3	0.7	0.5
N _{surface} ^a	23196	17652	12864	9452	12864	6564	10754	3036	1052
N _{total} ^a	375143	250193	156617	99331	156617	58057	120177	18773	5333
d _{vol, TEM} (nm)	11.7	9.7	8.6	6.3	8.6	5.8	6.8	4.1	2.8
d _{PXRD} (nm)	11.3	8.2	7.7	6.3	9.2	6.7	7.6	5.3	3.6
X _{CO} (%) ^b	4.26	2.15	4.59	2.85	3.62	2.15	1.97	2.14	1.14
TOF (s ⁻¹)	0.093	0.091	0.081	0.070	0.070	0.045	0.050	0.025	0.012
r _{FT} · 10 ⁴ (mol _{CO} g _{Co} ⁻¹ s ⁻¹)	0.98	1.09	1.13	1.13	0.98	0.86	0.76	0.69	0.49
α (%)	75	69	76	75	75	76	75	73	77
S _{CH4} (C%) ^c	15.1	17.4	17.5	16.8	18.4	16.0	16.7	17.2	16.9
S _{CH4} (mol%) ^c	48.8	51.3	63.1	54.3	55.7	52.3	56.0	52.7	54.9
S _{C5+} (C%) ^c	61.8	51.6	50.2	64.5	58.0	61.2	55.7	57.6	57.5
S _{C5+} (mol%) ^c	25.2	21.1	26.1	22.6	21.9	24.0	20.5	23.4	24.1
C ₂ Olefin/Paraffin (-)	0.35	1.02	0.37	1.20	0.43	0.88	1.18	0.51	1.55
C ₃ Olefin/Paraffin (-)	3.70	3.73	3.65	4.00	3.97	3.98	3.97	3.58	3.68
C ₅ Olefin/Paraffin (-)	1.98	2.95	1.99	2.75	2.15	2.61	2.52	2.07	2.78
C ₇ Olefin/Paraffin (-)	0.94	1.12	1.21	1.43	1.00	1.36	1.18	0.85	1.49
C ₅ α-Olefin/total Olefin (-)	0.96	0.96	0.94	0.92	0.93	0.96	0.95	0.94	0.95
C ₇ α-Olefin/total Olefin (-)	0.87	0.80	0.81	0.81	0.87	0.90	0.87	0.86	0.89
C ₅ branched HCs/n-HCs (-)	0.06	0.08	0.08	0.11	0.04	0.08	0.11	0.09	0.11
C ₇ branched HCs/n-HCs (-)	0.02	0.05	0.05	0.04	0.04	0.04	0.08	0.07	0.05

^a Number of surface and total atoms per crystallite based on d_{num, TEM}.^b CO conversions based on product spectrum extrapolated to a carbon number of 50.^c Selectivities based on product spectrum extrapolated to a carbon number of 50.

A10 List of chemicals

Table A10.1: Table of chemicals used for the synthesis of model catalysts and for FT experiments.

Compound	Details
Acetic acid	Sigma Aldrich (>99.7 % purity)
Acetone	Kimix (Ar, 99.5 % purity)
Air, synthetic	Air products (21% O ₂ in N ₂ , 99.999 % purity)
Aluminium oxide	Puralox (Batch 9574), SCCa 5-150, Sasol Germany, S _{BET} = 162m ² /g, V _{pore} = 0.47 cm ³ /g, d _{pore} = 11.5 nm, particle size: 150-200 μm
Ammonia hydroxide	Kimix (25 %)
Ar	Air Liquide (99.999% purity)
Carbon dioxide	Air Liquide (99.999% purity)
Carbon monoxide	Afrox (99.97% purity)
Cobalt carbonyl (Co ₂ (CO) ₈)	Sigma Aldrich (purum, moistened with hexane 1-10%)
Cobalt nitrate hexahydrate	Sigma Aldrich (reagent grade 98% purity)
Cyclohexane	Sigma Aldrich (anhydrous, 99.5% purity)
Ethyl-trichloro-ethanoate	Sigma Aldrich (reagent grade)
Hydrazine hydrate	Sigma Aldrich (reagent grade, N ₂ H ₄ 50-60%)
Hydrochloric acid	Kimix (32 %)
Hydrofluoric acid	Sigma Aldrich (48 %)
Hydrogen	Air Liquide (99.999% purity)
Magnesium sulfate	Kimix (anhydrous, 99% purity)
n-Hexane	Kimix (Ar, 99.5 % purity)
Nitric acid	Kimix
Nitrogen	Air Liquide (99.999% purity)
Penta-ethylen-glycol-dodecylether	Akzo Nobel
Perchloric acid	Kimix
Sulfuric acid	Sigma Aldrich (95-98% purity)
Synthesis gas mixture	Afrox (10.0 ± 2 % Ar, 30 ± 2 % CO and 60 ± 2 % H ₂)
Tetrahydrofuran	Sigma Aldrich (anhydrous, > 99.9% purity)
Toluene	Sigma Aldrich (anhydrous, 99.8% purity)

A11 Curriculum vitae

Personal Information	
date of birth	22 nd of June 1983, Heidelberg, Germany
nationality	German
Education	
since 06/2011	Researcher Oxidation Catalysts BASF SE, Ludwigshafen, Germany
09/2007-06/2011	PhD thesis University of Cape Town, South Africa, Prof. Dr. M. Claeys & Prof. Dr. E. van Steen Thesis title: Preparation of nano- and ångström-sized cobalt ensembles and their performance in the Fischer-Tropsch synthesis.
10/2002-06/2007	Chemical engineering studies University of Karlsruhe (TH), Germany Majors: <ul style="list-style-type: none"> • technical biology • chemistry and engineering of fossil and renewable combustibles
12/2006-06/2007	Diploma thesis: Study of zeolite shape selectivity with Fischer-Tropsch (FT) products – FT synthesis and hydrocarbon reactions in one reactor.
10/2005-07/2006	Seminararbeit thesis: Evaluation of different methods to produce microbial rhamnolipids and commissioning of a parallel fermenting reactor system.
10/2004	Vordiplom
1994-2002	Helmholtz Gymnasium, Heidelberg, Germany
06/2002	Abitur
1989-1994	Colegio Alemán Alexander von Humboldt, Mexico, D.F. Mexico City
Industrial Experience	
05/2004-12/2006	Student trainee at the IAVF AG (Karlsruhe), division agion, www.iavf.de
since 06/2011	Research engineer oxidation catalysts at BASF SE, Ludwigshafen, Germany
International Experience	
1989-1994	Mexico, D.F. Mexico City
09/2007-06/2011	Cape Town, South Africa
Awards and Scholarships	
09/2007-06/2011	DST-NRF Centre of Excellence in Catalysis (c*change) bursary
05/2009	CATSA International Student Travel Grant, Catalysis Society of South Africa CATSA
09/2010	Best Oral Presentation Award, Nanosciences Young Researcher's Symposium 2010, Cape Town, South Africa
11/2010	Best Oral Presentation Award, Annual Conference of the Catalysis Society of South Africa CATSA 2010, Bloemfontein, South Africa

A12 List of publications

Journal Publications

2011

N. Fischer, E. van Steen & M. Claeys

“Preparation of supported nano-sized cobalt oxide and fcc cobalt crystallites”

Catalysis Today 171 (2011) 174.

N. Fischer, M. Minneman, M. Bäumer, E. van Steen & M. Claeys

“Metal support interactions in Co_3O_4/Al_2O_3 catalysts prepared from w/o microemulsions”

in preparation

N. Fischer, E. van Steen & M. Claeys

“Structure sensitivity of Fischer-Tropsch activity and selectivity on supported cobalt catalysts”

in preparation

N. Fischer, E. van Steen & M. Claeys

“Magnetic studies of alumina supported cobalt nanocrystallites in the Fischer-Tropsch synthesis”

in preparation

N. Fischer, E. van Steen & M. Claeys

“Fischer-Tropsch activity of alumina supported $(CO)_9Co_3CCOOH$ ”

in preparation

Conference Publications

2006

F. Leitermann, N. Fischer & C. Syldatk

“Advances on the production of microbial rhamnolipids based on vegetable oils”

Poster presented at the “Annual Conference of the Association for General and Applied Microbiology” 2006, Jena, Germany.

2008

N. Fischer, E. van Steen & M. Claeys

“Preparation of nano- and ångström-sized cobalt ensembles and their performance in the Fischer-Tropsch synthesis”

Lecture held at the “DST-NRF Centre of Excellence in Catalysis (c*change) Workshop” 2008, Parys, South Africa.

N. Fischer, E. van Steen & M. Claeys

“Preparation of nano- and ångström-sized cobalt ensembles and their performance in the Fischer-Tropsch synthesis”

Poster presented at the “Annual Conference of the Catalysis Society of South Africa CATSA” 2008, Parys, South Africa.

2009

N. Fischer, E. van Steen & M. Claeys

“Alumina supported nano-sized cobalt crystallites for the Fischer-Tropsch synthesis”

Lecture held at the “DST-NRF Centre of Excellence in Catalysis (c*change) Workshop” 2009, Rawsonville, South Africa.

N. Fischer, E. van Steen & M. Claeys

“Alumina supported nano-sized cobalt crystallites for the Fischer-Tropsch synthesis”

Lecture held at the “Annual Conference of the Catalysis Society of South Africa CATSA” 2009, Rawsonville, South Africa.

2010

N. Fischer, E. van Steen & M. Claeys

“Alumina supported nano-sized cobalt crystallites for the Fischer-Tropsch synthesis”

Lecture held at the “9th Novel Gas Conversion Symposium (NGCS9)” 2010, Lyon, France.

N. Fischer, E. van Steen & M. Claeys

“Alumina supported nano-sized cobalt crystallites for the Fischer-Tropsch synthesis”

Lecture held at the “Nanosciences Young Reseracher’s Symposium (NYRS)” 2010, Cape Town, South Africa.

N. Fischer, E. van Steen & M. Claeys

“Cobalt crystallite size effect on activity and selectivity in the Fischer-Tropsch synthesis”

Lecture held at the “DST-NRF Centre of Excellence in Catalysis (c*change) Workshop” 2010, Bloemfontein, South Africa.

N. Fischer, E. van Steen & M. Claeys

“Cobalt crystallite size effect on activity and selectivity in the Fischer-Tropsch synthesis”

Lecture held at the “Annual Conference of the Catalysis Society of South Africa CATSA” 2010, Bloemfontein, South Africa.

B. Clapham, N. Fischer & M. Claeys

“Development of an in situ XRD cell for Fischer-Tropsch catalyst characterisation”

Poster presented at the “Annual Conference of the Catalysis Society of South Africa CATSA” 2010, Bloemfontein, South Africa.

C. de Vries, N. Fischer, F. Rößner, E. van Steen, M. Petersen & M. Claeys

“Evaluation of the Mechanism and pathways of product formation when co-feeding ammonia during Fischer-Tropsch synthesis”

Poster presented at the “Annual Conference of the Catalysis Society of South Africa CATSA” 2010, Bloemfontein, South Africa.

N. W. Mungwe, N. Fischer, E. van Steen & M. Claeys

“Development and applications of rhodium nanocrystallites in the CO hydrogenation: oxygenates selectivity”

Poster presented at the “Annual Conference of the Catalysis Society of South Africa CATSA” 2010, Bloemfontein, South Africa.

Z. Chonco, N. Fischer, K. Bharuth-Ram, E. van Steen & M. Claeys

“Mössbauer characterisation of copper ferrite as a model system for the Fischer-Tropsch synthesis”

Poster presented at the “Annual Conference of the Catalysis Society of South Africa CATSA” 2010, Bloemfontein, South Africa.

2011

N. Fischer, E. van Steen & M. Claeys

“Preparation of nano-sized cobalt crystallites and their performance in the Fischer-Tropsch synthesis”

Lecture held at the “22nd North American Catalysis Society Meeting” 2011, Detroit, USA.

R. P. Mogorosi, N. Fischer, M. Claeys & E. van Steen

“Chemical promotion through strong-metal support interaction - silica as a chemical promoter in Fe-based Fischer-Tropsch catalysts”

Lecture held at the “22nd North American Catalysis Society Meeting” 2011, Detroit, USA.

M. A. Amod, L. Lodya, T. E. Feltes, N. Fischer, E. van Steen & M. Claeys

“Crystallite size effects on the carburization of unsupported iron Fischer-Tropsch catalysts”

Poster presented at the “EuroCat X” 2011, Glasgow, Scotland.

N. Fischer, E. van Steen & M. Claeys

“Cobalt crystallite size effect on activity and selectivity in the Fischer-Tropsch synthesis”

Poster presented at the “European summer school: Energy and materials from the sun” 2011, Kerkrade, Netherlands.